Efficient electronic structure methods applied to metal nanoparticles

Larsen, Ask Hjorth; Jacobsen, Karsten Wedel; Thygesen, Kristian Sommer

Publication date:
2011

Document Version
Publisher's PDF, also known as Version of record

Efficient electronic structure methods applied to metal nanoparticles

Ask Hjorth Larsen
October 2011

Ph.D. Thesis
Center for Atomic-scale Materials Design
Technical University of Denmark

Abstract

Nano-scale structures are increasingly applied in the design of catalysts and electronic devices. A theoretical understanding of the basic properties of such systems is enabled through modern electronic structure methods such as density functional theory. This thesis describes the development of efficient approaches to density functional theory and the application of these methods to metal nanoparticles.

We describe the formalism and implementation of localized atom-centered basis sets within the projector augmented wave method. Basis sets allow for a dramatic increase in performance compared to plane-wave or real-space methods, but sacrifice accuracy in doing so. This approach is implemented in the GPAW code where it complements the existing real-space approach. For both the real-space and basis set methods we implement parallel code to adapt GPAW for large-scale calculations on the BlueGene/P architecture.

Real-space calculations are performed to investigate the convergence of chemical properties of Au and Pt clusters toward the bulk limit. Specifically we study chemisorption of O and CO on cuboctahedral clusters up to 1415 atoms using up to 65536 CPU cores. Small clusters almost universally bind more strongly than large ones. This can be understood mostly as a geometric effect. Convergence of chemisorption energies within 0.1 eV of bulk values happens at about 200 atoms for Pt and 600 atoms for Au. Particularly for O on Au, large variations due to electronic effects are seen for smaller clusters.

The basis set method is used to study the electronic effects for the contiguous range of clusters up to several hundred atoms. The s-electrons hybridize to form electronic shells consistent with the jellium model, leading to electronic "magic numbers" for clusters with full shells. Large electronic gaps and jumps in Fermi level near magic numbers can lead to alkali-like or halogen-like behaviour when main-group atoms adsorb onto gold clusters.

A non-self-consistent Newns–Anderson model is used to more closely study the chemisorption of main-group atoms on magic-number Au clusters. The behaviour at magic numbers can be understood from the location of adsorbate-induced states relative to the Fermi level.

The relationship between geometric and electronic effects in Au is studied by rough first-principles simulated annealings with up to 150 atoms. Non-magic clusters are found to deform considerably, reducing the total energy through the creation of gaps. Clusters larger than 100 atoms can elongate systematically by up to 15 %. This demonstrates a complex interdependence between electronic and geometric structure in a size regime which in most cases has been studied semiempirically.

Resumé

Strukturer i nanoskala finder i stigende grad anvendelse inden for design af katalysatorer og elektroniske enheder. En grundlæggende teoretisk forståelse af sådanne systemer muliggøres af moderne elektronstrukturmetoder såsom tæthedsfunktionalteori. Denne afhandling omhandler udviklingen af effektive metoder inden for tæthedsfunktionalteori samt anvendelsen af disse metoder på metalnanopartikler.

Vi beskriver formalismen og implementationen af lokaliserede atomare basissæt i PAW-metoden. Basissæt muliggør betydeligt hurtigere udregninger end planbølge- eller realrumsgittermetoder, dog på bekostning af beregningsnøjagtighed. Metoden implementeres i programmet GPAW, hvor den supplerer den eksisterende gittermetode. For både realrums- og basissætmetoden implementeres parallelle metoder med henblik på afvikling af store beregninger på BlueGene/P-arkitekturen.

Ved hjælp af gitterbaserede beregninger undersøges konvergensen af kemiske egenskaber for store Au- og Pt-klynger. Specifikt udregnes kemisorptionsenergier for O og CO på kuboktahedrale klynger med op til 1415 atomer ved brug af 65536 CPU-kerner. Små klynger binder næsten universelt stærkere end store, hvilket kan forstås som en primært geometrisk effekt. Kemisorptionsenergien konvergerer inden for 0,1 eV af krystalgrænsen ved henholdsvis 200 og 600 atomer for Pt og Au. Der ses særligt for O på Au store variationer for de mindre klynger, som kan henføres til elektroniske effekter.

Basissætmetoden bruges til at undersøge disse elektroniske effekter for en sammenhængende følge af klynger op til flere hundrede atomer. s-elektronerne hybridiserer i elektronskaller i overensstemmelse med jelliummodellen, og disse fører til elektroniske "magiske tal" for klynger med fyldte skaller. Store elektroniske gab og hop i Fermienergi ved magiske tal kan medføre alkali- eller halogenagtig opførsel, når hovedgruppeatomer binder til guldklynger.

Der formuleres en ikke-selvkonsistent Newns–Anderson-model, som bruges til nærmere at undersøge kemisorptionen af hovedgruppeatomer på magiske guldklynger. Opførslen kan forstås ud fra placeringen af adsorbatinducerede tilstande i forhold til Ferminiveauet.

Forholdet mellem geometriske og elektroniske effekter i guldklynger undersøges ved hjælp af simulerede afkølinger baseret på tæthedsfunktionalteori med grove parametre op til 150 atomer. Energien af ikke-magiske klynger mindskes gennem en betydelig deformation hvorved der åbnes et elektronisk gab. Klynger på mere end 100 atomer kan således systematisk deformere med op til 15 %. Dermed vises en kompleks gensidig afhængighed af elektronisk og geometrisk struktur i et størrelsesregime som ellers primært har været behandlet med semiempiriske metoder.

Preface

This thesis is submitted for the degree of Ph.D. from the Technical University of Denmark. The work presented herein was carried out at the Center for Atomic-scale Materials Design between September 2008 and October 2011, with the exception that work on the localized basis set implementation was commenced in 2007. I am grateful for the help of my supervisors Karsten Wedel Jacobsen and Kristian Thygesen, and would further like to thank Jesper Kleis, Jens Jørgen Mortensen and Marco Vanin with whom I have worked at different stages of this project. Thanks to Marco Vanin, Jess Wellendorff and Kenneth Nielsen for proofreading parts of the thesis.

List of included papers

Paper I. Localized atomic basis set in the projector augmented wave method.

A. H. Larsen, M. Vanin, J. J. Mortensen, K. S. Thygesen, and K. W. Jacobsen.
Physical Review B, vol. **80**, p. 195112, 2009.

Paper II. Electronic structure calculations with GPAW: a real-space implementation of the projector augmented-wave method.

J. Enkovaara, C. Rostgaard, J. J. Mortensen, J. Chen, M. Dułak, L. Ferrighi, J. Gavnholt, C. Glinsvad, V. Haikola, H. A. Hansen, H. H. Kristoffersen, M. Kuisma, A. H. Larsen, L. Lehtovaara, M. Ljungberg, O. Lopez-Acevedo, P. G. Moses, J. Ojanen, T. Olsen, V. Petzold, N. A. Romero, J. Stausholm-Møller, M. Strange, G. A. Tritsaris, M. Vanin, M. Walter, B. Hammer, H. Häkkinen, G. K. H. Madsen, R. M. Nieminen, J. K. Nørskov, M. Puska, T. T. Rantala, J. Schiøtz, K. S. Thygesen, and K. W. Jacobsen.
Journal of Physics: Condensed Matter, vol. **22**, no. 25, p. 253202, 2010.

Paper III. Finite size effects in chemical bonding: From small clusters to solids.

J. Kleis, J. Greeley, N. Romero, V. Morozov, H. Falsig, A. Larsen, J. Lu, J. Mortensen, M. Dułak, K. Thygesen, J. Nørskov, and K. Jacobsen.
Catalysis Letters, vol. **141**, pp. 1067–1071, 2011. 10.1007/s10562-011-0632-0.

Paper IV. Electronic shell structure and chemisorption on gold nanoparticles.

A. H. Larsen, J. Kleis, K. Thygesen, J. Nørskov, and K. W. Jacobsen.
Submitted.

Paper V. In situ XAS of Pt monolayer model fuel cell catalysts: balance of nanostructure and bimetallic interactions.

D. Friebel, D. J. Miller, T. Anniyev, H. Ogasawara, V. Viswanathan, A. H. Larsen, C. P. O'Grady, J. Nørskov, and A. Nilsson.
In preparation.

Contents

Abstract iii

Danish abstract v

Preface vii

List of included papers ix

I Computational methods in quantum mechanics 1

1 Introduction 3

2 Theoretical methods 7
2.1 Quantum mechanics 7
2.2 The Hartree–Fock method 7
2.3 Density functional theory 8
2.4 Exchange–correlation functionals 9
2.5 Pseudopotentials 10
2.6 Basis sets 11

3 The projector augmented wave method 13
3.1 Transformation operator 13
3.2 Atomic corrections and expectation values 14
3.3 Compensation charges 15
3.4 Total energy 16
3.5 Basis set formalism 16
3.6 Overview 18
3.7 Atomic forces 19

4 Atomic basis sets 21
4.1 Generation of basis sets 21
4.2 Atomic orbitals 21
4.3 Multiple-ζ functions 23
4.4 Polarization functions 24
4.5 Basis set superposition error correction 25
4.6 Nonorthogonality and projected density of states 25

5 Development and parallelization **27**
5.1 Overview of parallelization 27
5.2 Linear algebra 28
5.3 Grids and localized functions 29
5.4 Two-center integrals and derivatives 30
5.5 Performance benchmarks 31
5.6 Real-space calculations and parallelization 33
5.7 Parallelization on BlueGene/P 34

II Electronic and chemical properties of metal clusters 37

6 Metal nanoparticles **39**
6.1 Packing and structural motifs in clusters 39
6.2 Jellium clusters 41
6.3 Noble metal clusters, relativity and gold 43

7 Chemical properties of large clusters **45**
7.1 Structure and calculation parameters 45
7.2 Adsorption energies 46
7.3 Geometric effects on adsorption 47

8 Electronic structure and chemisorption **51**
8.1 Construction of clusters 51
8.2 Calculation parameters 52
8.3 Adsorption energy and magic numbers 53
8.4 Main-group atoms on gold 56
8.5 Oxygen on transition metal clusters 58

9 Analysis of chemisorption on gold clusters **61**
9.1 The Newns–Anderson model 61
9.2 Newns–Anderson Hamiltonian from DFT 62
9.3 Binding energy from Newns–Anderson 63
9.4 Influence of d-band 65
9.5 Main-group elements 67

10 Electronic structure and geometry **71**
10.1 Molecular dynamics 71
10.2 Simulated annealing with EMT 72
10.3 First-principles global optimization 73

11 Conclusion **79**

Bibliography **81**

Paper I: Localized atomic basis set in the projector augmented wave method **91**

Paper II: Electronic structure calculations with GPAW: a real-space implementation of the projector augmented-wave method **103**

Paper III: Finite Size Effects in Chemical Bonding: From Small Clusters to Solids **129**

Paper IV: Electronic shell structure and chemisorption on gold nanoparticles **135**

Paper V: In situ XAS of Pt monolayer model fuel cell catalysts: balance of nanostructure and bimetallic interactions **151**

Part I

Computational methods in quantum mechanics

Chapter 1

Introduction

This thesis concerns the chemical properties of metal nanoparticles and the development of theoretical methods to describe them. In this work, a *nanoparticle* or *cluster* refers to an assembly of a few to a few thousand atoms of a chemical element which would normally form a bulk crystalline phase. A typical size of such a particle may be a few nanometres, small enough that quantum mechanical effects cause the particle to behave differently from the bulk material.

With modern computers and numerical methods it is possible to predict the behaviour of quantum mechanical systems using *ab initio* methods such as density functional theory (DFT).[1,2] The term ab initio or *first principles* signifies that a method is based on solving fundamental physical equations such as the Schrödinger equation. For systems with more than a few particles, the Schrödinger equation itself is too computationally demanding to solve directly, and computational methods must rely on a range of reformulations and approximations to make computations tractable. We describe one such approach, where an atomic orbital basis set is combined with the projector augmented wave method.[3,4] This approach is implemented in GPAW, an electronic structure code based on a more accurate but also more computationally expensive real-space representation of wavefunctions.[5–7] The localized basis set is similar to the SIESTA code, with the difference that SIESTA is based on simpler norm-conserving pseudopotentials.[8,9] The combination in GPAW of the high-performance localized basis set with the more accurate real-space method provides a number of advantages. In particular, the basis set is useful for calculating structures efficiently, while the real-space code can be used to evaluate binding energies which are less accurate with the basis set. The basis set is also useful for applications that mathematically emphasize a finite or localized basis set. For example the basis set is now used for Green's function based electron transport calculations.[10] Another development for the GPAW code is the parallelization of the real-space code for massively parallel calculations. The main advantage of real-space methods is the ability to parallelize over many quantities at the same time, which allows the calculations to scale efficiently up to thousands of processors.

The second part of this thesis applies these methods with the main objective of understanding the chemical behaviour of nanoparticles, focusing on gold. Gold is normally thought of as inert, but this really applies to *bulk* gold. The chemistry of gold is in fact extremely diverse.[11–13] Due to the large nuclear

charges, core electrons of the late transition metals exhibit relativistic behaviour, which alters the electrostatic screening felt by the remaining electrons. The relativistic effects lead to a contraction of the s electrons compared to d electrons, which in the end is responsible for most of the unusual properties of gold.[14–16] These relativistic effects, along with the full d-shell which places less energetic emphasis on atomic packing, cause gold clusters to form structures that differ not only from those of other late transition metal clusters, but also those of the other noble metals.[17] Small gold clusters of different size have been predicted to form a large variety of structures including flakes and cages.[18,19] A significant electronic effect of gold clusters is the organization of the s-electrons into global electronic shells that extend over the entire cluster. Such shell structure is found in many free-electron-like materials, particularly the alkali metals, and gives rise to electronic *magic numbers* where clusters have increased stability and large electronic gaps.[20–23] Many properties of clusters depend sensitively on the electronic shell structure including their chemistry.[24] However, limitations in available computational power has prevented thorough modelling of larger clusters.

The efficiency of the localized basis set allows us to study, at modest computational cost, such effects for contiguous ranges of typically 20–200 atoms. We find that large size-dependent variations in binding energy are associated with the shell structure of gold clusters. These calculations are performed for many different adsorbates, and comparisons are made between clusters of several different metals. A recurring theme in these calculations is the study of overall trends from large numbers of systems, although this happens at the sacrifice of accuracy of the individual calculations. This is probably the first computational study from first principles of such large ensembles of systems.

The thesis is structured as follows.

- Chapter 2 gives a brief introduction of computational methods in quantum theory, including density functional theory which practically all results in this work are based on.
- Chapter 3 describes the projector augmented wave method and the mathematical formalism of the atomic basis set expansion. An initial implementation was written in cooperation with Marco Vanin and documented in Refs. 25, 26, although many further developments have taken place since.
- The generation of basis functions from atomic reference calculations is described in Chapter 4 along with other issues of practical interest to basis sets.
- Chapter 5 discusses the efficiency and parallelization of the basis set code, and explains the implementation of some of the more important steps in a calculation. Performance benchmarks are included. Adaptation of the real-space code for massively parallel calculations is further described.
- Chapter 6 acts as an introduction to Part II of this thesis, wherein the properties of nanoparticles are investigated. Brief descriptions are given of the geometric structures of clusters and relevant theoretical methods.
- Large-scale DFT calculations of adsorption of O and CO on Au and Pt clusters with up to 1415 atoms are presented in Chapter 7, and the effect of facet size is discussed.

- The effect of electronic shell structure on the chemistry of clusters, focusing on gold, is studied in detail in Chapter 8 by considering adsorption of a range of adsorbates.
- In Chapter 9 a non-selfconsistent Newns–Anderson model is used to analyze the bonding of several adsorbates using Hamiltonian matrices obtained from DFT calculations.
- In Chapter 10, gold cluster structures are optimized using simulated annealing with simple EMT and DFT.
- Chapter 11 summarizes and concludes the work.

Chapter 2

Theoretical methods

This chapter gives a brief review of quantum mechanics from the perspective of computationally predicting the properties of an interacting system of electrons and nuclei.

2.1 Quantum mechanics

The properties of matter at small scales are described by the Schrödinger equation. For a system with N particles, the (time-independent) Schrödinger equation is a differential equation for the *many-body wavefunction* $\Psi(\mathbf{r}_1, \mathbf{r}_2, \ldots, \mathbf{r}_N)$ with a total of $3N$ spatial parameters, and this function entirely characterizes the system. The storage required to explicitly represent such an object in a computer is therefore exponential in the number of particles, making numerical calculations in this form impossible beyond a small number of particles. This is commonly referred to as the "exponential wall".[27] Computational approaches to quantum mechanics are therefore generally based on methods that recast the Schrödinger equation into more tractable forms by applying several approximations.

Because of the large ratio between electronic and nuclear masses, electrons and nuclei exhibit quantum mechanical behaviour on different length and time scales. The Born–Oppenheimer approximation assumes that the wavefunction of a combined electronic and nuclear system can be expressed as a product of an electronic and a nuclear wavefunction. Going one step further, the nuclei can for most purposes be assumed to behave like classical point particles. This reduces a quantum mechanical calculation to a purely electronic problem, which will be the subject of the next several sections.

2.2 The Hartree–Fock method

Electrons are by the symmetrization postulate *fermions*, meaning that electronic wavefunctions are antisymmetric with respect to the interchange of any two position variables $\mathbf{r}_i$ and $\mathbf{r}_j$. From any set of orthogonal single-particle states, an appropriately antisymmetric many-body wavefunction can be formed as a *Slater determinant* from the single-particle states. Any many-body wavefunction can be written as a linear combination of such determinants. In the

Hartree–Fock method it is assumed that the many-body wavefunction can be written as a single such determinant. This assumption leads to a set of equations, the Hartree–Fock equations, for each single-particle state minimizing the total energy. These equations can be solved numerically by iteratively adjusting wavefunctions and potential until obtaining self-consistent single-particle states and potential.

In the Hartree–Fock method, the electronic interaction energy can be understood as being comprised of two terms: the *direct* or *Hartree* term, and the *exchange* term. The Hartree term is the Coulomb energy of the full charge density, so it incorporates the Coulomb repulsion of every electron with every electron. Clearly, each electron interacts with every *other* electron, but not with the specific part of the charge distribution that it itself contributed. One term in the exchange contribution can be understood as a correction which compensates for this self-interaction part in the Hartree energy. The exchange term as a whole is a manifestation of Pauli exclusion.

While the Hartree–Fock approach is suited for numerical calculations, it is still an approximate many-body method. As mentioned, a general many-body wavefunction must be described as a linear combination of multiple Slater determinants. Any discrepancy between exact Hartree–Fock theory as compared to a full linear combination of Slater determinants, which yields the exact many-body wavefunction, is somewhat vaguely called *correlation*. Methods that improve on Hartree–Fock theory through various ways to include correlation are called *post-Hartree–Fock methods*. Within these methods, accuracy generally comes at the price that the computational cost scales with high powers of the number of electrons, and so these accurate methods are limited to small systems.

2.3 Density functional theory

Density functional theory (DFT) is an approach to solving the many-body problem using the electron density instead of the many-body wavefunctions. DFT evolved from the Thomas–Fermi theory, a more intuitive approach; Hohenberg and Kohn later developed the concept as a formally correct many-body method.[1]

The foundation of DFT is the insight that the ground-state electron density $n(\mathbf{r})$ of an electronic system is sufficient to entirely characterize that system. Thus any property which can be derived from the many-body wavefunction can in fact be derived knowing only the ground-state density. The total energy of a system of interacting electrons in a potential can be expressed as a functional of the electron density, and the ground-state density variationally minimizes this functional. All one has to do is, in principle, to perform such a minimization. This turns out to be tricky, since it is not known how to evaluate quantities such as the energy directly from an electron density without first using it to calculate the wavefunctions.

Kohn and Sham suggested an approach to solve this problem by introducing a fictional system of non-interacting particles represented by single-particle wavefunctions in a shared *effective potential*.[2] In this picture the potential must account for all interactions. Subject to a few representability issues, such as whether the true ground-state electron density *can* be expressed from single-particle wavefunctions, a universal form of the effective potential can be shown to exist which makes the method formally exact. Explicit expressions for phys-

ical quantities can then be written down in terms of the Kohn–Sham wavefunctions and the electron density, such as the energy:

$$E_{\mathrm{KS}} = \sum_n f_n \langle \psi_n | \hat{T} | \psi_n \rangle + \iint \frac{\rho(\mathbf{r})\rho(\mathbf{r}')}{\|\mathbf{r} - \mathbf{r}'\|} \,\mathrm{d}\mathbf{r}\,\mathrm{d}\mathbf{r}' + E_{\mathrm{xc}}[n]. \tag{2.1}$$

Here the energy is split into three terms. The first term is the single-particle kinetic energy of the Kohn–Sham states $|\psi_n\rangle$ weighted by their occupation numbers f_n. The second term is the Coulomb energy of the total charge distribution $\rho(\mathbf{r})$ in the system, including the electron density and the nuclear point charges. The third term $E_{\mathrm{xc}}[n]$ is a density functional which must describe the effect of the particle interactions otherwise neglected in the single-particle picture, and should therefore account for exchange, as considered in Hartree–Fock theory, and correlation. It is called the *exchange–correlation* (XC) functional. No one knows the true XC functional, and so it is generally approximated. This is a fundamental point of DFT as it is the only "uncontrolled" approximation.

From the energy expression one can, similarly to the Hartree–Fock method, derive a variational equation for the Kohn–Sham states. These Kohn–Sham equations can then be solved on a computer using an iterative procedure. Roughly speaking this involves choosing an initial electron density and repeating three steps:

- Calculate potential from density
- Calculate wavefunctions from potential by solving Kohn–Sham equations
- Calculate density by occupying the states with lowest energy

The procedure stops when density, potential and wavefunctions are self-consistent, in the sense that things no longer change on every iteration. At that point one has obtained the true ground-state density and energy of the system, at least if using the exact XC functional.

2.4 Exchange–correlation functionals

As previously mentioned, there exists a general XC density functional which makes the Kohn–Sham approach exact. No one knows what the exact functional looks like, so it is instead approximated.

A natural starting point for such an approximation is the homogeneous electron gas, which is entirely characterized by the constant density. In this simple case the exchange and correlation functional can be obtained. This case leads to the local density approximation (LDA): The assumption that each point in space contributes an XC energy which depends only on the density $n(\mathbf{r})$ in that point, and that this energy is the same as that of an electron gas with the same density.

A better approximation can be obtained by extending the LDA so that each point contributes an amount to the energy depending both on the value and the gradient of the density in that point. These approximations are called generalized gradient approximations (GGAs). The most widely used one is probably the Perdew–Burke–Ernzerhof (PBE) functional.[28]

A modification of the PBE functional, RPBE, is specifically designed to provide a better description of metal surfaces and adsorption (at the expense of a slightly worse description of bulk metals).[29] Throughout this work, calculations generally employ the RPBE functional.

2.5 Pseudopotentials

For all except the smallest atoms, electrons can be divided into tightly bound *core* states and loosely bound *valence* states. The strong Coulomb attraction from the nucleus localizes the core states so that they do not interact much with states on other atoms. Core states are therefore not essential to a numerical description of chemistry. However the valence states must be orthogonal to the core states, and therefore oscillate rapidly within the core region. Such oscillations are shown on Figure 2.1 for the 4s atomic orbital of iron (black line). The accurate representation of core states and oscillatory valence states in terms of real-space grids or plane-waves is expensive, and unnecessary in the sense that the chemical properties of an atom depend mostly on the behaviour of electrons far from the nucleus. *Pseudopotential* methods deal with this problem by replacing the steep potential of the nuclei as well as the core electrons with a smooth effective potential felt by the valence electrons. The exclusion of core states from the calculation procedure is called the *frozen core approximation*. Within the smooth potential, the oscillatory behaviour of valence states can be eliminated, resulting in smooth, nodeless *pseudowavefunctions* which are cheap to represent numerically. This is shown for the HGH pseudopotentials[30] on Figure 2.1 (green). The pseudowavefunctions are identical to the real ("all-electron" or AE) wavefunctions far from the nucleus, but are replaced by smooth functions close to it.

Clearly the pseudopotential approach makes sense only if it can be guaranteed that the pseudopotentials accurately reflect the behaviour of real atoms. A common way to do this is to add *Kleinman–Bylander projectors* to the Hamiltonian.[31] These are fixed functions which, by their scalar products with the pseudowavefunctions, adjust the energy of different states depending on their angular momentum and radial structure. These can be chosen to ensure that the atomic states have the correct energies and response to perturbations. The latter ensures better transferability of the pseudopotential between different systems.[32] While the pseudopotential approximation is conceptually simple, the generation of good pseudopotentials can be quite complicated due to the large number of parameters involved.[33]

There are two main kinds of pseudopotentials: norm-conserving and more recently "ultrasoft". With norm-conserving pseudopotentials it is expensive to represent highly localized states, such as the d-states of transition metals. From the figure, the 3d pseudowavefunction is significantly less smooth than the 4s one because the 3d state must be normalized to contain one electron. Ultrasoft pseudopotentials avoid the norm-conservation restriction through more complicated mathematics.[34] This allows smooth wavefunctions to be used also for localized states. The projector augmented wave method (red curves on Figure 2.1) is similar to ultrasoft pseudopotentials, but uses a transformation to also retain the all-electron information, thus eliminating pseudopotential transferability errors.

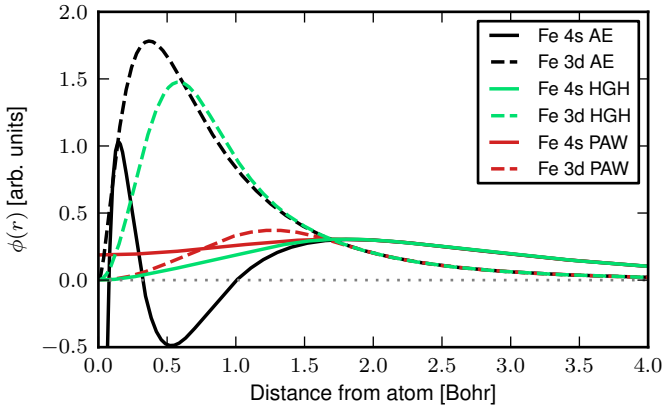

Figure 2.1: *Pseudopotential approaches for the 4s and 3d valence states of iron. Atomic orbitals (black) are replaced by smooth, norm-conserving pseudowave-functions (green). Localized states such as the 3d state can be made more smooth by ultrasoft pseudopotentials or the projector augmented wave method (red).*

2.6 Basis sets

To perform a DFT calculation one must choose a representation of the Kohn–Sham states, and this choice has significant implications on performance.

One way is to expand the wavefunctions as linear combinations of plane-waves, then variationally optimize the coefficients. Plane-waves are economical in the sense that relatively few plane-waves can represent a typical wavefunction well. Plane-waves are also complete, and a single parameter, namely the energy cutoff, can be used to control the quality of the basis set without any upper limit on precision. The number of plane-waves is generally large enough that iterative methods must be employed to solve the Kohn–Sham equations.[35] A disadvantage of plane-waves methods is that each plane-wave overlaps with atoms no matter their distance. Fast Fourier transforms, an integral element of plane-wave methods, are known to parallelize poorly, limiting the number of processors that can efficiently contribute to the same calculation.

More scalable methods must rely on localization to some extent. GPAW normally uses real-space grids to represent the wave-functions. These require significantly more memory than a plane-wave basis of equivalent quality, but are well suited for parallelization.[5,6] This allows efficient division of the system into spatial domains, with limited communication between adjacent domains. The real-space representation is similar to plane-waves since its quality can increased to any desired precision by reducing the grid spacing.

A different approach is to use atomic basis sets, where a limited set of fixed basis functions is assigned to each atom. Each function is chosen carefully so only few basis functions are required to represent the wavefunctions. This greatly speeds up the solution of the Kohn–Sham equations, and several operations which scale quadratically in plane-wave or real-space methods will scale linearly due to the localization of the basis functions. The main disadvantage of basis set approaches is that no single parameter can practically control the

accuracy, and the precision can only approach that of plane-wave or real-space methods. Atomic basis sets can be based on numerical atomic orbitals (NAO), where the actual orbitals are sampled on a grid and used as basis functions. They can also be based on simple analytic functions such as Gaussians or exponentials; commonly referred to as Gaussian-type orbitals (GTO) and Slater-type orbitals (STO). The advantage of such methods is that matrix elements can be calculated analytically, although more basis functions are needed than with NAO-based approaches.

The specific subject in the following is the implementation of a basis set of numerical atomic orbitals in GPAW, based on the projector augmented wave method.

Chapter 3

The projector augmented wave method

One of the main developments discussed in this thesis is the use of localized atomic orbitals as a basis set to describe electronic wave functions within the projector augmented wave method (PAW). In the light of the brief review in the previous chapter, it should be clear how this combination fits among the existing methods. A more complete and technical derivation of this specific method is given in this chapter.

The PAW method by Blöchl[3,4] is an approach to solving the Kohn-Sham equations which is based on a transformation $\hat{\mathcal{T}}$ between smooth, computationally convenient pseudowavefunctions $|\tilde{\psi}_n\rangle$ and the rapidly oscillating all-electron wavefunctions $|\psi_n\rangle$:

$$|\psi_n\rangle = \hat{\mathcal{T}}\,|\tilde{\psi}_n\rangle\,. \tag{3.1}$$

Numerical calculations are performed using the pseudowavefunctions $|\tilde{\psi}_n\rangle$, while the transformation $\hat{\mathcal{T}}$ ensures that the all-electron information is retained. This makes PAW calculations in many ways similar to ultrasoft pseudopotentials,[36] while PAW is in fact an all-electron method.

3.1 Transformation operator

The transformation operator $\hat{\mathcal{T}}$ is defined as the identity operator plus a local contribution around each atom a. It is defined to map a set of chosen smooth functions $|\tilde{\phi}_i^a\rangle$ for each atomic valence state i to the all-electron eigenstates $|\phi_i^a\rangle$:

$$\hat{\mathcal{T}} = \hat{1} + \sum_{ai} (|\phi_i^a\rangle - |\tilde{\phi}_i^a\rangle)\,\langle\tilde{p}_i^a|\,. \tag{3.2}$$

The functions $|\phi_i^a\rangle$ and $|\tilde{\phi}_i^a\rangle$ are called all-electron partial waves and pseudo partial waves, respectively. They are chosen to be equal outside a certain radius of a, so that the PAW transformation as a whole has no effect in regions far from atoms. The functions $\langle\tilde{p}_i^a|$ are Kleinman–Bylander projectors. They are localized, and the region in which they are nonzero is called the *augmentation*

region. Together with the pseudo partial waves they should form a complete orthonormal basis within this region:

$$\sum_i \langle \mathbf{r}|\tilde{\phi}_i^a\rangle \langle \tilde{p}_i^a|\mathbf{r}'\rangle = \delta(\mathbf{r}-\mathbf{r}') \quad \text{where} \quad \langle \tilde{p}_i^a|\tilde{\phi}_j^a\rangle = \delta_{ij}. \tag{3.3}$$

As an all-electron method, the PAW method is exact if projectors and partial waves form a complete basis around each atom, and the augmentation regions of distinct atoms do not overlap.*

3.2 Atomic corrections and expectation values

The expectation value of a local operator $\hat{O}$ can be written in terms of the pseudowavefunctions by inserting the PAW transformation (3.2) and industriously applying the completeness relation (3.3). Eventually

$$\begin{aligned}\langle \hat{O}\rangle &= \sum_n f_n \langle \tilde{\psi}_n|\hat{\mathcal{T}}^\dagger \hat{O}\hat{\mathcal{T}}|\tilde{\psi}_n\rangle \\ &= \sum_n f_n \langle \tilde{\psi}_n|\hat{O}|\tilde{\psi}_n\rangle + \sum_{aij}\left(\langle \phi_i^a|\hat{O}|\phi_j^a\rangle - \langle \tilde{\phi}_i^a|\hat{O}|\tilde{\phi}_j^a\rangle\right) D_{ji}^a + O_{\text{core}}\end{aligned} \tag{3.4}$$

where

$$D_{ji}^a = \sum_n \langle \tilde{p}_j^a|\tilde{\psi}_n\rangle f_n \langle \tilde{\psi}_n|\tilde{p}_i^a\rangle \tag{3.5}$$

are called *atomic density matrices*. The first term in (3.4) involves only the pseudowavefunctions and can be calculated efficiently with real-space grids or plane-waves. The second term involves the fixed atomic quantities $\langle \phi_i^a|O|\phi_j^a\rangle$ and $\langle \tilde{\phi}_i^a|O|\tilde{\phi}_j^a\rangle$. These calculations involve the rapidly oscillating all-electron wavefunctions, but they can be performed in a spherical coordinate system and stored once and for all for each type of atom. The only quantities in the second and third terms which depend on the system are D_{ij}^a. The scalar products $\langle \tilde{p}_i^a|\tilde{\psi}_n\rangle$ are cheap to evaluate since the projectors are localized, and since both functions are smooth. The last term in (3.4) is an extra, fixed contribution O_{core} due to the frozen core states.

The important implication of expression (3.4) is that the calculations are divided into an extended *pseudo*-part suitable for grid or plane-wave representations, which will account for most computational cost associated with the method, coupled to a set of constant, pre-evaluated *atomic corrections* only through the atomic density matrices D_{ij}^a. Most importantly the electron density is decomposed as

$$n(\mathbf{r}) = \tilde{n}(\mathbf{r}) + \sum_a n^a(\mathbf{r}-\mathbf{R}^a) - \sum_a \tilde{n}^a(\mathbf{r}-\mathbf{R}^a), \tag{3.6}$$

*Usually a couple of projectors are used for each atomic valence state. The necessary additional all-electron partial waves can be generated by radially integrating the atomic Kohn–Sham equations using an energy which is not an eigenvalue.

where

$$\tilde{n}(\mathbf{r}) = \sum_n f_n \langle \tilde{\psi}_n | \mathbf{r} \rangle \langle \mathbf{r} | \tilde{\psi}_n \rangle + \sum_a \tilde{n}_c^a(\mathbf{r} - \mathbf{R}^a), \tag{3.7}$$

$$n^a(\mathbf{r}) = \sum_{ij} \langle \phi_i^a | \mathbf{r} \rangle \langle \mathbf{r} | \phi_j^a \rangle D_{ji}^a + n_c^a(\mathbf{r}), \tag{3.8}$$

$$\tilde{n}^a(\mathbf{r}) = \sum_{ij} \langle \tilde{\phi}_i^a | \mathbf{r} \rangle \langle \mathbf{r} | \tilde{\phi}_j^a \rangle D_{ji}^a + \tilde{n}_c^a(\mathbf{r}). \tag{3.9}$$

Here an arbitrary pseudo-core density $\tilde{n}_c^a(\mathbf{r})$ has been included in (3.7) which is cancelled by the atomic correction (3.9).

3.3 Compensation charges

A recurring feature in the PAW method is the addition of something to a quantity, which is cancelled out by subtracting the atomic expansion of the same quantity. The reason for doing so is to make the wavefunctions, density and potential as smooth and well-behaved as possible. In this way, *compensation charges* $\tilde{Z}(\mathbf{r})$ are added around each atom to the charge distribution to eliminate the direct electrostatic interaction between atoms in favour of having a single smooth charge distribution which can be treated on a grid. Considering again the Kohn–Sham energy expression, the charge density is the sum

$$\rho(\mathbf{r}) = n(\mathbf{r}) + Z(\mathbf{r}) \tag{3.10}$$

of the all-electron density $n(\mathbf{r})$ and the atomic point charges $Z(\mathbf{r})$. The compensation charges are used to regroup the charge into two neutral distributions

$$\rho(\mathbf{r}) = \tilde{\rho}(\mathbf{r}) + \underbrace{\sum_a \rho^a(\mathbf{r} - \mathbf{R}^a) - \sum_a \tilde{\rho}^a(\mathbf{r} - \mathbf{R}^a)}_{\text{neutral}}, \tag{3.11}$$

such that the electrostatic singularities near the nuclei disappear in $\tilde{\rho}(\mathbf{r})$. The atomic charges are

$$\rho^a(\mathbf{r}) = n^a(\mathbf{r}) + Z^a(\mathbf{r}), \tag{3.12}$$

$$\tilde{\rho}^a(\mathbf{r}) = \tilde{n}^a(\mathbf{r}) + \tilde{Z}^a(\mathbf{r}). \tag{3.13}$$

Going one step further, the compensation charges are defined as a linear combination

$$\tilde{Z}^a(\mathbf{r}) = \sum_L Q_L^a \tilde{g}_L^a(\mathbf{r}) \tag{3.14}$$

of smooth localized functions $\tilde{g}_L^a(\mathbf{r})$ with real spherical harmonics $Y_L(\theta, \phi)$ as angular parts. L is a composite index for the usual angular indices (l, m). The coefficients Q_L^a are uniquely defined by requiring that the compensation charges must cancel out the multipole moments of the charges represented on radial grids. Thereby *all* electrostatic interactions between atoms are contained in $\tilde{\rho}(\mathbf{r})$ up to any chosen order. This makes the expansion coefficients Q_L^a a function of the atomic density matrices D_{ij}^a. A complete derivation is given by Rostgaard.[37]

3.4 Total energy

With these modifications, the total Kohn–Sham energy (2.1) can be written as three rather elaborate terms

$$E = \tilde{E} + \sum_a E^a - \sum_a \tilde{E}^a \tag{3.15}$$

with

$$\begin{aligned}\tilde{E} &= \sum_n f_n \langle \tilde{\psi}_n | \hat{T} | \tilde{\psi}_n \rangle + \frac{1}{2} \iint \frac{\tilde{\rho}(\mathbf{r}) \tilde{\rho}(\mathbf{r}')}{\|\mathbf{r} - \mathbf{r}'\|} \,\mathrm{d}\mathbf{r}\,\mathrm{d}\mathbf{r}' \\ &\quad + \sum_a \int \tilde{n}(\mathbf{r}) \bar{v}^a(\mathbf{r} - \mathbf{R}^a) \,\mathrm{d}\mathbf{r} + E_{\mathrm{xc}}[\tilde{n}], \end{aligned} \tag{3.16}$$

$$\begin{aligned}E^a &= \sum_{ij} \langle \phi_i^a | \hat{T} | \phi_j^a \rangle \, D_{ji}^a + \frac{1}{2} \iint \frac{\rho^a(\mathbf{r}) \rho^a(\mathbf{r}')}{\|\mathbf{r} - \mathbf{r}'\|} \,\mathrm{d}\mathbf{r}\,\mathrm{d}\mathbf{r}' \\ &\quad + E_{\mathrm{xc}}[n^a] + E_{\mathrm{kin}}^{\mathrm{core}}, \end{aligned} \tag{3.17}$$

$$\begin{aligned}\tilde{E}^a &= \sum_{ij} \langle \tilde{\phi}_i^a | \hat{T} | \tilde{\phi}_j^a \rangle \, D_{ji}^a + \frac{1}{2} \iint \frac{\tilde{\rho}^a(\mathbf{r}) \tilde{\rho}^a(\mathbf{r}')}{\|\mathbf{r} - \mathbf{r}'\|} \,\mathrm{d}\mathbf{r}\,\mathrm{d}\mathbf{r}' \\ &\quad + E_{\mathrm{xc}}[\tilde{n}^a] + \int \tilde{n}^a(\mathbf{r}) \bar{v}^a(\mathbf{r}) \,\mathrm{d}\mathbf{r}. \end{aligned} \tag{3.18}$$

Here $E_{\mathrm{kin}}^{\mathrm{core}}$ is the fixed kinetic energy of the frozen core states, and $\bar{v}^a(\mathbf{r})$ is an arbitrary localized potential which is "added and subtracted" similarly to compensation charges to make the total potential as smooth as possible. Note how the XC energy can be divided in this way only if it is assumed to be local, so that Eq. (3.4) applies. Non-local XC functionals can be incorporated but are considerably more complicated.[38]

A set of Kohn–Sham equations can be derived by requiring that the pseudowavefunctions should be simultaneously orthogonal and minimize the total energy, which will be done in the context of localized basis sets in the following.

3.5 Basis set formalism

The pseudowavefunctions $|\tilde{\psi}_n\rangle$ are expanded as linear combinations

$$|\tilde{\psi}_n\rangle = \sum_\mu |\Phi_\mu\rangle \, c_{\mu n} \tag{3.19}$$

of atom-centered, localized basis functions $|\Phi_\mu\rangle$ with coefficients $c_{\mu n}$. The coefficients shall be variational parameters, while the basis functions are fixed. To have a working ground-state calculation procedure, we must implement each of the Kohn–Sham steps, i.e. we must be able to calculate density from the wavefunctions, calculate the potential from the density (this step is unrelated to the basis), and be able to solve the Kohn–Sham equations. Most quantities are conveniently expressed in terms of the density matrix

$$\rho_{\mu\nu} = \sum_n c_{\mu n} f_n c_{\nu n}^* \tag{3.20}$$

The total energy, which we want to minimize, depends on the wavefunctions through the pseudodensity $\tilde{n}(\mathbf{r})$, the atomic density matrices D^a_{ij}, and explicitly through the smooth part $\tilde{T}$ of the kinetic energy in (3.16). These quantites are straightforwardly rewritten in terms of the density matrix:

$$\tilde{n}(\mathbf{r}) = \sum_{\mu\nu} \Phi^*_\mu(\mathbf{r})\Phi_\nu(\mathbf{r})\rho_{\nu\mu} + \sum_a \tilde{n}^a_c(\mathbf{r} - \mathbf{R}^a), \tag{3.21}$$

$$D^a_{ij} = \sum_{\mu\nu} P^a_{i\mu}\rho_{\mu\nu}P^{a*}_{j\nu}, \tag{3.22}$$

$$\tilde{T} = \sum_n f_n \langle\tilde{\psi}_n|\hat{T}|\tilde{\psi}_n\rangle = \sum_{\mu\nu} T_{\mu\nu}\rho_{\nu\mu}, \tag{3.23}$$

where we have defined

$$T_{\mu\nu} = \langle\Phi_\mu|\hat{T}|\Phi_\nu\rangle\,, \tag{3.24}$$

$$P^a_{i\mu} = \langle\tilde{p}^a_i|\Phi_\mu\rangle\,. \tag{3.25}$$

These are two-center integrals that can be evaluated before the start of a calculation once the atomic positions are known.

The Kohn–Sham equations can be obtained by requiring that the total energy (3.15) must be stationary with respect to the coefficients, and that the all-electron Kohn–Sham states must be orthogonal. The orthogonality condition is

$$\delta_{nm} = \langle\psi_n|\psi_m\rangle = \langle\tilde{\psi}_n|\hat{\mathcal{T}}^\dagger\hat{\mathcal{T}}|\tilde{\psi}_m\rangle = \sum_{\mu\nu} c^*_{\mu n}S_{\mu\nu}c_{\nu m}, \tag{3.26}$$

where $S_{\mu\nu}$ is the *overlap matrix*

$$S_{\mu\nu} = \langle\Phi_\mu|\hat{\mathcal{T}}^\dagger\hat{\mathcal{T}}|\Phi_\nu\rangle = \Theta_{\mu\nu} + \sum_{aij} P^{a*}_{i\mu}\Delta S^a_{ij}P^a_{j\nu}. \tag{3.27}$$

Here $\Theta_{\mu\nu} = \langle\Phi_\mu|\Phi_\nu\rangle$ are two-center integrals, and the numbers ΔS^a_{ij} are atomic constants depending on the partial waves. The orthogonality criterion is incorporated using the method of Lagrange multipliers. Differentiating the total energy plus Lagrange term by $c^*_{\mu n}$ leads to a generalized eigenvalue equation which can be solved for the coefficients $c_{\nu n}$ and eigenvalues ϵ_n:

$$\sum_\nu H_{\mu\nu}c_{\nu n} = \sum_\nu S_{\mu\nu}c_{\nu n}\epsilon_n. \tag{3.28}$$

Here we have defined the Hamiltonian matrix as the total derivative

$$H_{\mu\nu} = \frac{\mathrm{d}E}{\mathrm{d}\rho_{\nu\mu}} = \frac{\partial E}{\partial\rho_{\nu\mu}} + \int \frac{\delta E}{\delta\tilde{n}(\mathbf{r})}\frac{\partial\tilde{n}(\mathbf{r})}{\partial\rho_{\nu\mu}}\,\mathrm{d}\mathbf{r} + \sum_{aij}\frac{\partial E}{\partial D^a_{ji}}\frac{\partial D^a_{ji}}{\partial\rho_{\nu\mu}}, \tag{3.29}$$

which eventually leads to

$$H_{\mu\nu} = T_{\mu\nu} + V_{\mu\nu} + \sum_{aij} P^{a*}_{i\mu}\Delta H^a_{ij}P^a_{j\nu}. \tag{3.30}$$

The first term is the constant kinetic matrix (3.24). The second term is the matrix

$$V_{\mu\nu} = \int \Phi_\mu^*(\mathbf{r})\tilde{v}(\mathbf{r})\Phi_\nu(\mathbf{r})\,\mathrm{d}\mathbf{r} \tag{3.31}$$

of the total effective potential

$$\tilde{v}(\mathbf{r}) \equiv \frac{\delta E}{\delta \tilde{n}(\mathbf{r})} = \tilde{v}_{\mathrm{Ha}}(\mathbf{r}) + \tilde{v}_{\mathrm{xc}}(\mathbf{r}) + \sum_a \bar{v}^a(\mathbf{r} - \mathbf{R}^a). \tag{3.32}$$

The Hartree, XC and zero potential above emerge straightforwardly as derivatives of the corresponding energy terms in Eq. (3.16), with the Hartree potential obeying the Poisson equation

$$\nabla^2 \tilde{v}_{\mathrm{Ha}}(\mathbf{r}) = -4\pi\tilde{\rho}(\mathbf{r}). \tag{3.33}$$

The last term in (3.30) involves the *atomic Hamiltonian matrices* defined as

$$\Delta H_{ij}^a \equiv \frac{\partial E}{\partial D_{ji}^a}. \tag{3.34}$$

This derivative is horribly complicated[37] due amongst other things to atomic XC corrections. However it is basis set independent, and it suffices to note that ΔH_{ij}^a depend only on D_{ji}^a plus a large number of purely atomic constants. It is a special feature of PAW calculations compared to ultrasoft pseudopotential Hamiltonians that the atomic corrections can vary dynamically through changes in D_{ji}^a.

3.6 Overview

By now we can account for the entire self-consistency cycle. All two-center integrals such as $T_{\mu\nu}$ and $P_{i\mu}^a$ can be evaluated at the beginning, and a starting density (both $\tilde{n}(\mathbf{r})$ and D_{ij}^a) can be defined from the contributions of the isolated atoms. Then:

- The XC potential $\tilde{v}_{\mathrm{xc}}(\mathbf{r})$ is calculated from the density $\tilde{n}(\mathbf{r})$ depending on the relevant XC approximation.
- The total pseudocharge density $\tilde{\rho}(\mathbf{r})$ from (3.11) is calculated by adding the compensation charges $\tilde{Z}^a(\mathbf{r})$ using (3.14) chosen to cancel atomic multipole moments.
- The Hartree potential $\tilde{v}_{\mathrm{Ha}}(\mathbf{r})$ is calculated by solving the Poisson equation (3.33).
- The potential matrix $V_{\mu\nu}$ (3.31) is calculated by integrating the effective potential $\tilde{v}(\mathbf{r})$ (3.32) with the basis functions.
- The Hamiltonian matrix $H_{\mu\nu}$ (3.30) is calculated by adding kinetic, potential and atomic terms.
- The generalized eigenvalue problem (3.28) is solved for the coefficients $c_{\mu n}$ and energies ϵ_n, and the lowest states are occupied using a Fermi distribution.

- The density matrix $\rho_{\mu\nu}$ (3.20) is calculated from the coefficients and occupations.
- The pseudodensity $\tilde{n}(\mathbf{r})$ (3.21) and atomic density matrices D^a_{ij} (3.23) are recalculated.

Pulay mixing is generally used to stabilize changes in density, preventing "charge sloshing".[39]

3.7 Atomic forces

Aside from the self-consistency loop, structure optimizations and molecular dynamics simulations are formulated in terms of the force on an atom. The force on atom a is defined as the negative gradient

$$\mathbf{F}^a = -\frac{\partial E}{\partial \mathbf{R}^a} \tag{3.35}$$

of the total energy with respect to the position $\mathbf{R}^a$ of that atom. An expression for this gradient can be derived analytically from the energy expression. The gradient must be taken self-consistently in the sense that it should reflect the actual change in energy if two different energy evaluations were made with slightly different atomic positions, and it must differentially obey the orthogonality condition. Using the Hellman–Feynman force theorem and the chain rule carefully, the full force expression is

$$\begin{aligned}
\mathbf{F}^a = {} & 2\,\mathrm{Re}\sum_{\mu\in a;\nu}\frac{\mathrm{d}T_{\mu\nu}}{\mathrm{d}\mathbf{R}_{\mu\nu}}\rho_{\nu\mu} - 2\,\mathrm{Re}\sum_{\mu\in a;\nu}\left[\int\frac{\mathrm{d}\Phi^*_\mu(\mathbf{r})}{\mathrm{d}\mathbf{R}^a}\tilde{v}(\mathbf{r})\Phi_\nu(\mathbf{r})\,\mathrm{d}\mathbf{r}\right]\rho_{\nu\mu} \\
& - 2\,\mathrm{Re}\sum_{\mu\in a;\nu}\frac{\mathrm{d}\Theta_{\mu\nu}}{\mathrm{d}\mathbf{R}_{\mu\nu}}E_{\nu\mu} + 2\,\mathrm{Re}\sum_{\mu\nu}Z^a_{\mu\nu}E_{\nu\mu} - 2\,\mathrm{Re}\sum_{b;\mu\in a;\nu}Z^b_{\mu\nu}E_{\nu\mu} \\
& - 2\,\mathrm{Re}\sum_{\mu\nu}A^a_{\mu\nu}\rho_{\nu\mu} + 2\,\mathrm{Re}\sum_{b;\mu\in a;\nu}A^b_{\mu\nu}\rho_{\nu\mu} \\
& - \int\tilde{v}(\mathbf{r})\frac{\mathrm{d}\tilde{n}^a_c(\mathbf{r}-\mathbf{R}^a)}{\mathrm{d}\mathbf{R}^a}\,\mathrm{d}\mathbf{r} - \int\tilde{n}(\mathbf{r})\frac{\mathrm{d}\bar{v}^a(\mathbf{r}-\mathbf{R}^a)}{\mathrm{d}\mathbf{R}^a}\,\mathrm{d}\mathbf{r} \\
& - \int\tilde{v}_{\mathrm{Ha}}(\mathbf{r})\sum_L Q^a_L\frac{\mathrm{d}\tilde{g}^a_L(\mathbf{r}-\mathbf{R}^a)}{\mathrm{d}\mathbf{R}^a}\,\mathrm{d}\mathbf{r}
\end{aligned} \tag{3.36}$$

with

$$Z^a_{\mu\nu} = \sum_{ij}\frac{\mathrm{d}P^{a*}_{i\mu}}{\mathrm{d}\mathbf{R}_{a\mu}}\Delta S^a_{ij}P^a_{j\nu}, \tag{3.37}$$

$$A^a_{\mu\nu} = \sum_{ij}\frac{\mathrm{d}P^{a*}_{i\mu}}{\mathrm{d}\mathbf{R}_{a\mu}}\Delta H^a_{ij}P^a_{j\nu}, \tag{3.38}$$

$$E_{\mu\nu} = \sum_n c_{\mu n}f_n\epsilon_n c^*_{\nu n}. \tag{3.39}$$

The formula contains several extra terms compared to grid-based or plane-wave-based PAW force expressions[3,5] because an atomic displacement alters the atomic basis; such forces are called *Pulay forces*. A complete derivation of the formula can be found in the appendix of Paper I.[7]

Chapter 4

Atomic basis sets

By now we know how the self-consistency cycle in PAW works with a localized basis set. This chapter deals with the generation of basis sets and a few topics of more general utility.

4.1 Generation of basis sets

This section describes how basis functions are generated. Quite generally we use the form of a radial function times an angular function which is a spherical harmonic:

$$\Phi(\mathbf{r}) = \varphi(r)Y_L(\widehat{r}). \tag{4.1}$$

The spherical harmonics are the angular eigenfunctions of the laplacian operator, and emerge as factors in the solutions for any purely radial system. A perturbation of this potential changes both the radial and angular parts of a solution. Extra radial and angular degrees of freedom are therefore required to describe the perturbed atom well. Basis sets therefore consist of the following types of functions:

- One atomic orbital for each valence state. This is the minimal sensible basis set, called *single-ζ*.
- For each atomic orbital, extra functions can be added with the same angular part, but different radial parts. These are called "multiple-ζ" functions; these names comes from the tradition of enumerating them by their cutoff radius, called ζ.
- Polarization functions, which are extra functions with angular parts that are not present among the valence states.

The procedure by which these functions are chosen is explained below.

4.2 Atomic orbitals

In a radial coordinate system the Kohn–Sham equations are separable into a radial and an angular equation, with the angular equation having spherical harmonic solutions as mentioned. Due to the strong Coulomb attraction for the

heavier elements, particularly Au, the core electrons move at relativistic speeds, and must be described by the Dirac equation. In the scalar-relativistic approximation, the spin–orbit-coupling is neglected, which simplifies the solution procedure.[40] This results in the following radial equation:

$$-\frac{\mathrm{d}^2u(r)}{\mathrm{d}r^2}-\frac{1}{2Mc^2}\frac{\mathrm{d}v(r)}{\mathrm{d}r}\left[\frac{\mathrm{d}u(r)}{\mathrm{d}r}-\frac{u(r)}{r}\right] + \left[\frac{l(l+1)}{r^2}+2M(v(r)-\epsilon)\right]u(r)=0 \tag{4.2}$$

with

$$M=1-\frac{1}{2c^2}(v(r)-\epsilon), \tag{4.3}$$

where $v(r)$ is the effective potential, and $u(r)$ is related to the actual all-electron wavefunction $\mathrm{X}(r)$ by

$$u(r)=r\mathrm{X}(r). \tag{4.4}$$

GPAW already contains a radial atomic Kohn–Sham solver which is used to generate PAW setups. Eq. (4.2) is solved using non-equidistant grid representation with very fine grid spacing near 0. An initial guess for the energy is used to radially integrate the equation outward from 0 and inward from the outermost point. The two solutions must join smoothly in the middle; the energy guess is adjusted until they do. This way a solution is found for every atomic orbital $\mathrm{X}_{ln}(r)$, and a self-consistent density and potential are obtained.

The atomic orbitals in principle extend to infinity. Two things must be done before they can be used as basis functions: The functions must be localized, and they must look like pseudowavefunctions rather than all-electron wavefunctions. The simplest way to localize the solution is to solve the atomic problem with the outer boundary at the desired cutoff. This will however make the basis function non-differentiable at the boundary, which may cause the kinetic energy to depend sensitively on the exact location of grid points compared to the boundary. This is avoided by adding a smooth radial potential to the self-consistent potential. We use the same functional form as in SIESTA:[41]

$$v_{\mathrm{conf}}(r)=\begin{cases}0, & r\le r_{\mathrm{inner}}\\ \frac{A}{r_{\mathrm{cut}}-r}\exp\left(-\frac{r_{\mathrm{cut}}-r_{\mathrm{inner}}}{r-r_{\mathrm{inner}}}\right), & r_{\mathrm{inner}}<r\le r_{\mathrm{cut}}\\ \infty, & r_{\mathrm{cut}}<r\end{cases} \tag{4.5}$$

The radial equation is then non-self-consistently reintegrated to obtain functions that are localized. Since the different atomic orbitals have quite different range, they should have different cutoffs r_{cut} as well. Requiring a fixed increase $\Delta\epsilon$ of the confined orbital energy compared to the free atom universally defines reasonable cutoffs for all elements. In normal calculations we choose the confinement energy $\Delta\epsilon=0.1\,\mathrm{eV}$, which results in typical basis function cutoffs of 6–10 Bohr radii.

Next step is to convert the localized functions to pseudowavefunctions. The procedure is illustrated on Figure 4.1. It is done by solving

$$|\mathrm{X}\rangle=\hat{\mathcal{T}}\,|\Phi\rangle=|\Phi\rangle+\sum_i(|\phi_i\rangle-|\tilde{\phi}_i\rangle)\,\langle\tilde{p}_i|\Phi\rangle \tag{4.6}$$

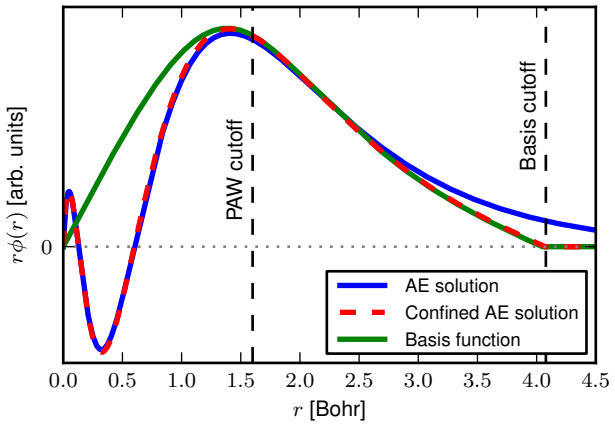

Figure 4.1: *Generation of atomic orbital basis function for S 2s-state. The all-electron partial wave is confined to a finite range ($\Delta\epsilon = 0.3\,\mathrm{eV}$), then transformed to a nodeless pseudowavefunction.*

for the basis function $|\Phi\rangle$ given the confined all-electron solution $|\mathrm{X}\rangle$, effectively inverting the PAW transformation. Applying a projector $\langle\tilde{p}_i|$ and using the completeness of the projector–partial wave basis within the augmentation region,

$$\langle\tilde{p}_i|\mathrm{X}\rangle = \sum_j \langle\tilde{p}_i|\phi_j\rangle \langle\tilde{p}_j|\Phi\rangle \,. \tag{4.7}$$

This equation can be solved for the partial-wave expansion coefficients $\langle\tilde{p}_j|\Phi\rangle$ which completely determine $|\Phi\rangle$ within the augmentation region. Note that if the coefficients $\langle\tilde{p}_j|\Phi\rangle$ are plugged directly into (4.6), the behaviour will be unstable near $r = 0$. This happens because the partial-wave basis is in reality slightly incomplete and does not entirely filter out the all-electron oscillations when inverted. It is more correct to use the partial-wave expansion of $|\Phi\rangle$ within the augmentation region and join it smoothly with $|\mathrm{X}\rangle$ at the boundary:

$$\Phi(\mathbf{r}) = \sum_i \phi_i(\mathbf{r}) \langle\tilde{p}_i|\Phi\rangle \quad \text{for small } r. \tag{4.8}$$

The basis function generation procedure is illustrated on Figure 4.1.

4.3 Multiple-ζ functions

The basis is improved by adding extra functions for each valence state. Fundamentally the goal is to have a basis set which is as complete as possible and at the same time cheap, with the basis functions being as localized as possible. It is natural to choose the confined pseudoatomic orbital $\Phi^0(r)$ as the longest-ranged basis function, since this function is physically justified. We then make up some

more functions $\Phi^\zeta(r)$ with smaller cutoffs. Define the function

$$\Delta\Phi^\zeta(r) = \begin{cases} r^l(a + br^2) & r < r_{\mathrm{cut}}^\zeta, \\ \Phi^0(r) & r_{\mathrm{cut}}^\zeta \leq r. \end{cases} \tag{4.9}$$

The prefactor r^l ensures that $\Delta\Phi^\zeta(r)$ has the correct radial behaviour of a wavefunction near $r = 0$ with angular momentum l. The parameters a and b are uniquely defined by requiring $\Delta\Phi^\zeta(r)$ to be continuous and differentiable at r_{cut}^ζ. The then define the actual basis function as

$$\Phi^\zeta(r) = \Phi^0(r) - \Delta\Phi^\zeta(r), \tag{4.10}$$

which is smooth and localized within r_{cut}^ζ. More functions can be added by selecting multiple cutoffs r_{cut}^ζ. We have found that a sensible first cutoff is obtained by defining r_{cut}^ζ such that 16 % of the norm of $\Phi^0(r)$ lies outside.

4.4 Polarization functions

Consider the lowest angular momentum l which does not correspond to any occupied valence state. This is typically a d-state for main-group elements or a p-state for transition metals. A perturbation of the valence state with angular momentum $l - 1$ will generally have a significant l-component (while it might have an $l - 1$ component, there would already be basis functions for this angular momentum channel). For this reason we add a *polarization function* with angular momentum l which, as we say, *polarizes* the preceding $l-1$ valence state.

The function is chosen to have the same cutoff as the orbital it polarizes. The approach used in SIESTA is to construct it as an actual perturbation.[9] Previous tests have not revealed any overwhelmingly importance of the exact form, and so we (still) use the rather primitive approach of defining a Gaussian-like function

$$\Phi_l^{\mathrm{pol}}(r) = Ar^l \exp(-\alpha r^2). \tag{4.11}$$

The decay constant α is chosen in terms of the norm of the tail of the polarized function. As the analytic form is not essential for our purposes, the function is modified slightly so it smoothly approaches zero at a finite range given in terms of the α.

Increasing the basis set will variationally decrease the energy of a system, with the lower limit being reachable by a grid-based GPAW calculation. Total energies tend to be much higher, while energy differences such as binding energies converge more quickly with the completeness of the basis set. Tests can be found in Paper I.[7] In general, a good compromise between efficiency and accuracy is obtained by a double-ζ polarized (dzp) basis set. This consists of the atomic orbitals plus one extra radial function each, and a single polarization function. As an example, the standard dzp basis set of gold is shown on Figure 4.2. Within a self-consistent calculation each radial function defined here contributes $2l + 1$ different spherical harmonics. Most elements have 13 or 15 such basis functions with a dzp basis set.

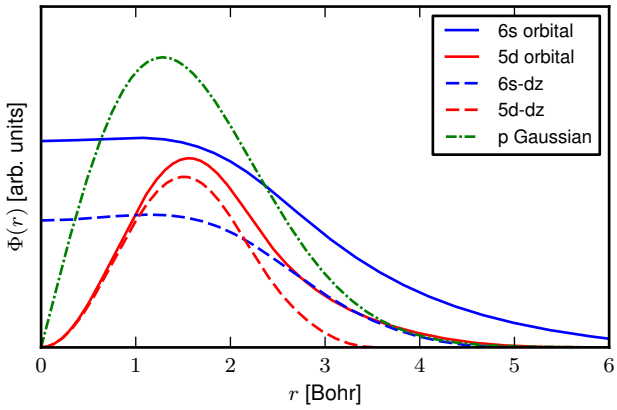

Figure 4.2: *Radial parts of basis functions of gold. Colours indicate angular momentum. Line styles indicate generation procedure. The total number of basis functions per gold atom is 15 if we count the azimuthal quantum number m.*

4.5 Basis set superposition error correction

The binding energy of some composite system with respect to its constituents is calculated by subtracting the sum of the energies of the isolated constituents from the energy of the composite system. In an atomic basis set, this introduces a *basis set superposition error* (BSSE): In the regions where basis functions overlap, atoms in the composite system effectively borrow unused degrees of freedom from one another, which artificially stabilizes the composite system. In other words, basis sets tend to produce too large binding energies.

The BSSE can be corrected by ensuring that the basis set of the composite system matches that of the isolated constituent systems. Therefore the calculation of the constituent systems should include basis functions on the sites where extra atoms would have been in the composite system. In GPAW this is implemented by adding an atom at that site equipped with the appropriate basis set, but without a pseudopotential. Such atoms are frequently called *ghost* atoms.

The BSSE is particularly large for isolated atoms. Since the basis functions are localized by truncation such that each orbital is 0.1 eV higher than on the free atom, this may, for a typical main-group atom, cause a combined increase of the total energy on the order of 0.5 eV, which the BSSE can partially "regain" in a composite system. The BSSE can therefore be several tenths of an eV for isolated atoms with the standard cutoff, but can be improved by decreasing the orbital confinement energy to e.g. $\Delta\epsilon = 0.01$ eV.

4.6 Nonorthogonality and projected density of states

We will later calculate the projected densities of states (PDOS) on various states. Within the PAW method the projected density of states on an atomic orbital,

given as an all-electron partial wave ϕ_i^a, can be approximated by[37]

$$\begin{aligned}\rho_i^a(\epsilon) &= \sum_n |\langle \phi_i^a | \psi_n \rangle|^2 \delta(\epsilon - \epsilon_n) \\ &\approx \sum_n |\langle \tilde{p}_i^a | \tilde{\psi}_n \rangle|^2 \delta(\epsilon - \epsilon_n). \end{aligned} \tag{4.12}$$

This is the standard definition used in GPAW. To the extent that the partial wave–projector basis is complete, and augmentation regions of distinct atoms do not overlap, the projected density of states integrated over all energies should yield 1. Thus it is in practice only approximate, as neither requirement is exactly fulfilled in normal calculations. This limits the use of this definition for electron-counting purposes, particularly when the objective is to filter out the total number occupation on a given atom or something similar. The atomic orbital basis set provides a natural definition of projected densities of states which is guaranteed to integrate to the right number of electrons provided that nonorthogonality is properly accounted for. Within the space spanned by the atomic basis set, the identity operator is given by

$$\hat{I} = \sum_{\mu\nu} |\Phi_\mu\rangle \, [S^{-1}]_{\mu\nu} \, \langle \Phi_\nu| \,, \tag{4.13}$$

as can be verified by applying the operator on an arbitrary linear combination of atomic orbitals. Suppose we are interested the projected density of states on an arbitrary subset M of orbitals, such as all the orbitals on atom a, or all d-type orbitals on all Au atoms. A projection operator onto that space is given by

$$\hat{P}_M = \sum_{\mu\in M, \nu\in M} |\Phi_\mu\rangle \, [P_M^{-1}]_{\mu\nu} \, \langle \Phi_\nu| \,, \tag{4.14}$$

where $[P_M^{-1}]_{\mu\nu}$ is the inverse of the submatrix of $S_{\mu\nu}$ corresponding to the subspace M (not to be confused with a submatrix of the inverse). Then we define the projected density of states on M as

$$\rho_M(\epsilon) = \sum_n \langle \tilde{\psi}_n | \hat{P}_M | \tilde{\psi}_n \rangle \, \delta(\epsilon - \epsilon_n). \tag{4.15}$$

In the case where the subspace M corresponds to a single state, the normalization is simply a division by the squared norm $\langle \Phi_\mu | \Phi_\mu \rangle$ of the basis function.

Chapter 5

Development and parallelization

This chapter describes aspects of the implementation and parallelization of localized basis set calculations and to a lesser extent real-space calculations.

GPAW is implemented in a combination of Python and C. Python is a high-level language which allows complicated tasks to be programmed quickly and with high clarity. C, as a low-level language, is well suited for number crunching. Most code is therefore written in Python using the Numpy array library, while only expensive operations are delegated to C functions or external libraries such as BLAS.

Input files for DFT calculations are written as Python scripts using the Atomic Simulation Environment (ASE).[42] This provides enough flexibility that any calculated quantity, such as Hamiltonians or overlap matrices which we will use later, can be extracted directly from an input file without special-purpose compilation or intermediate file storage. MPI is used for parallelization. This is a distributed-memory framework where each CPU core runs a separate copy of the programme.

5.1 Overview of parallelization

GPAW supports parallelization over several quantities. For real-space grid calculations, the computational cost will normally be dominated by real-space operations on the wavefunctions $\tilde{\psi}_n^{\sigma k}(\mathbf{r})$. Roughly in order from the most efficient to the least efficient, parallelization can be performed over k-points, spins σ, real-space $\mathbf{r}$ and Kohn–Sham states n. Spin parallelization for many purposes resembles k-point parallelization, and we will only distinguish between these when necessary. These parallelization modes can be used in any combination simultaneously: to each CPU is assigned a particular set of k-points/spins, a real-space domain and a set of states. The latter two parallelization modes are normally called *domain decomposition* and *band parallelization*. For medium-sized real-space calculations one usually maximizes k-point parallelization and then uses domain decomposition with the remaining CPUs. However the computational cost within a single domain increases with the number of electrons.

Operation	Parallelization	Complexity	Eq.
Poisson, multigrid	$\mathbf{r}$	$\mathcal{O}(N)$	(3.33)
Density $\tilde{n}(\mathbf{r})$	$\mathbf{r}$, σ	$\mathcal{O}(N)$	(3.21)
XC potential $\tilde{v}_{\mathrm{xc}}(\mathbf{r})$	$\mathbf{r}$, σ	$\mathcal{O}(N)$	—
Atomic XC / ΔH^a_{ij}	$\mathbf{r}$, σ	$\mathcal{O}(N)$	—
Potential matrix $V_{\mu\nu}$	ν, $\mathbf{r}$, σ, k	$\mathcal{O}(N)$	(3.31)
Diagonalization of $H_{\mu\nu}$	μ, ν, σ, k	$\mathcal{O}(N^3)$	(3.28)
Density matrix $\rho_{\mu\nu}$	μ, ν, σ, k	$\mathcal{O}(N^3)$	(3.20)

Table 5.1: *Important operations in the self-consistency cycle and how the relevant data structures are distributed over domains* $\mathbf{r}$*, spins* σ*, basis functions* μ *and* ν *and* k*-points* k*. Only operations with the most significant computational cost have been included.*

For sufficiently large systems it therefore becomes increasingly relevant to parallelize over bands.

With the introduction of the localized basis set, or *"LCAO mode"*, the same degrees of parallelization can be used (band parallelization in this case then corresponds to parallelization over orbitals). However most of the computational cost will be associated with very different operations, particularly for large systems where the cubically scaling linear algebra operations, namely diagonalization of the Hamiltonian and calculation of the density matrix, will eventually dominate.* Since these are pure matrix operations, they not parallel over domains. Many other operations are only, or almost only, parallel over domains. An overview of the different operations and how they can be parallelized is shown in Table 5.1. Clearly, for sufficiently large systems a sparse method would be faster since the Hamiltonian and overlap matrix are in fact sparse.

The implementation of the more important individual steps of the calculation procedure will be described in the following.

5.2 Linear algebra

We parallelize matrix operations using *Scalable Linear Algebra PACKage*, a software library for parallel dense linear algebra.[44,45] ScaLAPACK relies on standard standard BLAS libraries for local operations and BLACS,[46] *Basic Linear Algebra Communication Subroutines*, for parallel communication.

Matrices in ScaLAPACK are distributed among CPU cores according to a *2D block cyclic* scheme: A matrix is divided into rectangular blocks of equal size. Each core holds a set of blocks from distinct parts of the matrix, and the ownership of consecutive blocks *cycles* between the available CPUs. The CPUs are *themselves* divided into a 2D grid such that rows and columns are blocks are shared by rows and columns of CPUs in the CPU grid. The distribution is illustrated on the left in Table 5.2. The algorithms in ScaLAPACK are optimized to emphasize communication between adjacent CPUs in the CPU grid.

*The Hamiltonian and overlap matrices are both sparse, and sparse methods will therefore be favourable for the larger systems. The advantage of the sparsity of the Hamiltonian is however limited by the lack of sparsity of the coefficients $c_{\mu n}$, as the Kohn–Sham formulation is inherently global in nature. True $\mathcal{O}(N)$ methods must be formulated by alluding to locality of e.g. the spatial density matrix $\rho(\mathbf{r}, \mathbf{r}')$, resulting in a quite different formalism.[43]

0	2	4	6	0	2	4	6
1	3	5	7	1	3	5	7
0	2	4	6	0	2	4	6
1	3	5	7	1	3	5	7
0	2	4	6	0	2	4	6
1	3	5	7	1	3	5	7

0	2	4	6

Table 5.2: *The two main matrix distributions used in calculations. Left: 2D block cyclic matrix distribution. A matrix is divided into 6×8 blocks, each represented by a cell. The cells are shared by a grid of 2×4 CPUs numbered 0–7. The number in each cell indicates which CPU stores that block. Each CPU stores 6 blocks in total. Adjacent CPUs in the grid should have fast interconnect. Right: 1D column distribution, perhaps of the same matrix. Only four of the eight CPUs are used in this case.*

Thus, operations on the matrix in the example will be fast if CPU 1 has a fast interconnect to CPUs 0, 3 and 7, but it does not need a fast interconnect to the other CPUs. A simpler distribution using only half the CPUs is shown to the right in Table 5.2. Such a column-based distribution is useful for calculations that are parallel over real-space domains and orbitals at the same time. CPUs 0, 2, 4 and 6 would in this case be responsible for one domain while 1, 3, 5 and 7 would have a copy of the same matrix, but apply it to a different domain.

Parallel operations can be invoked from Python through an object oriented Python interface with the following classes, each of which relies on the underlying parallel libraries:

- Communicator: An object resembling the standard MPI communicator interface for a set of CPUs.
- BLACS grid: Represents a 2D grid of CPUs. Each BLACS grid is associated with a communicator.
- BLACS descriptor: A template for matrices with a specific 2D block cyclic layout (matrix size, block size). Provides utility methods to build and perform operations on arrays. Each BLACS descriptor is associated with a BLACS grid.
- Redistributor: Redistributes matrices between different BLACS grids or descriptors. Is associated with two BLACS grids.

Python interface functions for diagonalization and matrix multiplication are implemented in terms of the above classes.

5.3 Grids and localized functions

The calculation of the density $\tilde{n}(\mathbf{r})$ and the potential matrix elements $\tilde{v}(\mathbf{r})$ involves basis functions as well as extended real-space functions. Because the basis functions are localized, these operations are $\mathcal{O}(N)$. In terms of grid points G, the potential matrix is calculated as

$$V_{\mu\nu} = \sum_G \Phi^*_{G\mu} \tilde{v}_G \Phi_{G\nu} \tag{5.1}$$

using an explicit outer loop over G and an inner loop over all pairs (μ, ν) of locally nonzero basis functions. The density, sampled on a grid, is calculated with a similar loop over grid points G, for each of which a similar inner loop

$$\tilde{n}_G = \sum_{\mu\nu} \Phi^*_{G\mu} \Phi_{G\nu} \rho_{\nu\mu} \tag{5.2}$$

is carried out.

The basis function values $\Phi_{\mu G}$ in each grid point are pre-tabulated during initialization by explicitly evaluating radial parts times spherical harmonics. Loops over pairs of nonzero basis functions are possible by first registering, for each basis function, the grid coordinates G_{z_1} to G_{z_2} along the z axis between which the basis function is nonzero, for all pairs of grid coordinates G_x, G_y along the other axes. This metadata allows us to maintain a list of locally nonzero basis functions when looping over grid points: Basis function indices are dynamically added and removed from this list as the loop enters and leaves their localization areas. The entry/exit point metadata is stored in one buffer, while the actual basis function values are stored in a different (much larger) buffer, in an order consistent with the list of currently nonzero basis functions for easy indexing.

The operations (5.1) and (5.2) are naturally parallel over domains. They are further parallelized over orbitals ν in $V_{\mu\nu}$ or $\rho_{\nu\mu}$ using the column layout from Table 5.2. Each CPU is responsible for one domain/column combination. After $V_{\mu\nu}$ is calculated, it must be redistributed from column form to block cyclic form, where it is used to construct the Hamiltonian. After the diagonalization and calculation of $\rho_{\mu\nu}$ from the coefficients, which happens in block cyclic form, $\rho_{\mu\nu}$ is then distributed back to column form to apply (5.2).

In the force expression (3.36), the derivative of the potential matrix $V_{\mu\nu}$ with respect to a rigid displacement of a basis function must be calculated. This can be done with a similar loop, except it is the derivatives

$$\frac{\mathrm{d}\Phi(\mathbf{r} - \mathbf{R}^a)}{\mathrm{d}\mathbf{R}^a} = -\frac{\mathrm{d}\Phi(\mathbf{r} - \mathbf{R}^a)}{\mathrm{d}\mathbf{r}} \tag{5.3}$$

which are evaluated through

$$\frac{\mathrm{d}\Phi(\mathbf{r})}{\mathrm{d}\mathbf{r}} = \frac{\mathrm{d}\varphi(r)}{\mathrm{d}r} \bar{Y}_L(\mathbf{r}) \widehat{\mathbf{r}} + \varphi(r) \frac{\mathrm{d}\bar{Y}_L(\mathbf{r})}{\mathrm{d}\mathbf{r}}. \tag{5.4}$$

Circumflex denotes a unit vector. The notation $\bar{Y}_L(\mathbf{R}) = R^l Y_L(\widehat{\mathbf{R}})$ refers to the real solid spherical harmonics, which are polynomials in the cartesian coordinates. Their derivatives are therefore straightforward to evaluate.

5.4 Two-center integrals and derivatives

The geometry-dependent but otherwise constant overlap integrals $T_{\mu\nu}$, $S_{\mu\nu}$ and $P^a_{i\nu}$ are calculated through the procedure described by Sankey and Niklewsky[47] which is also used by SIESTA.[9] The matrices consist of two-center integrals between localized functions which are in all cases represented as a radial part on a one-dimensional grid times a spherical harmonic which is implied from an angular momentum quantum number.

Each localized function is Fourier transformed. The two-center integrals can then can be evaluated cheaply as convolutions between a pair of Fourier transformed functions. This function is then transformed back into real-space. Due to the Fourier transform of the spherical harmonics it becomes a sum of many spherical harmonics times different radial parts:

$$\int \Phi^*(\mathbf{r})\mathrm{X}(\mathbf{r}-\mathbf{R})\,\mathrm{d}\mathbf{r} \equiv \Theta(\mathbf{R}) = \sum_L \Theta_L(R)\bar{Y}_L(\mathbf{R}). \tag{5.5}$$

See also the master thesis by Vanin.[25] Overlap matrices such as $T_{\mu\nu}$ or their position derivatives are constructed by looping over all pairs of atoms which are close enough for the localized functions to overlap. This operation is parallelized according to where atoms reside: the overlap between atom a and atom b with $a \leq b$ is calculated on the CPU responsible for the domain in which a resides. $T_{\mu\nu}$ and $S_{\mu\nu}$ are then immediately distributed on the block cyclic grid.

The force expression (3.36) involves a number of derivatives of overlaps. These are evaluated as

$$\frac{\mathrm{d}\Theta(\mathbf{R})}{\mathrm{d}\mathbf{R}} = \widehat{\mathbf{R}}\sum_L \frac{\mathrm{d}\Theta_L(R)}{\mathrm{d}R}\bar{Y}_L(\mathbf{R}) + \sum_L \Theta_L(R)\frac{\mathrm{d}\bar{Y}_L(\mathbf{R})}{\mathrm{d}\mathbf{R}}. \tag{5.6}$$

The actual overlap derivative matrices in the force formula (3.36) are evaluated this way, except they must also be antisymmetric, reflecting that interchange of two basis functions changes the sign of $\mathbf{R}$ above.

5.5 Performance benchmarks

A few performance benchmarks are presented below. These are meant to provide an idea about the performance on real systems, and are applied to some of the clusters studied in later chapters.

Figure 5.1a shows a benchmark of localized basis set calculations on Au clusters. The figure is based on structure relaxations of Au clusters generated by simulated annealing with EMT. The precise procedure is described in Chapter 10. The tests run on one 8-core xeon node on Niflheim.[48] Performance is recorded on the master core. Parallelization is used with $2 \times 2 \times 2$ domain decomposition and a 4×2 core BLACS grid. The diagonalization uses the *divide & conquer* algorithm.

A breakdown of the walltime for different operations is shown on Figure 5.1b, accounting for the total relative time spent with each operation. ScaLAPACK is invoked for clusters larger than $N = 50$ explaining the sudden shift. Some parts of the calculation, most importantly the force calculations, have not yet been optimized well in combination with ScaLAPACK. *Grid ops* refers to the calculation of $V_{\mu\nu}$ and $\tilde{n}(\mathbf{r})$, which take roughly the same time; *network* represents communication including waits due to load imbalance; *atomic* represents PAW corrections, which is dominated by radial XC; *matrix ops* refers to calculation of $\rho_{\mu\nu}$ plus smaller operations such as two-center integral evaluation.

Figure 5.2 shows scaling of computational time of individual functions measured per self-consistency step (whereas the previous figure refers to an entire self-consistency loop; the number of necessary self-consistency steps increases weakly with system size). Scaling powers are calculated by logarithmic fitting

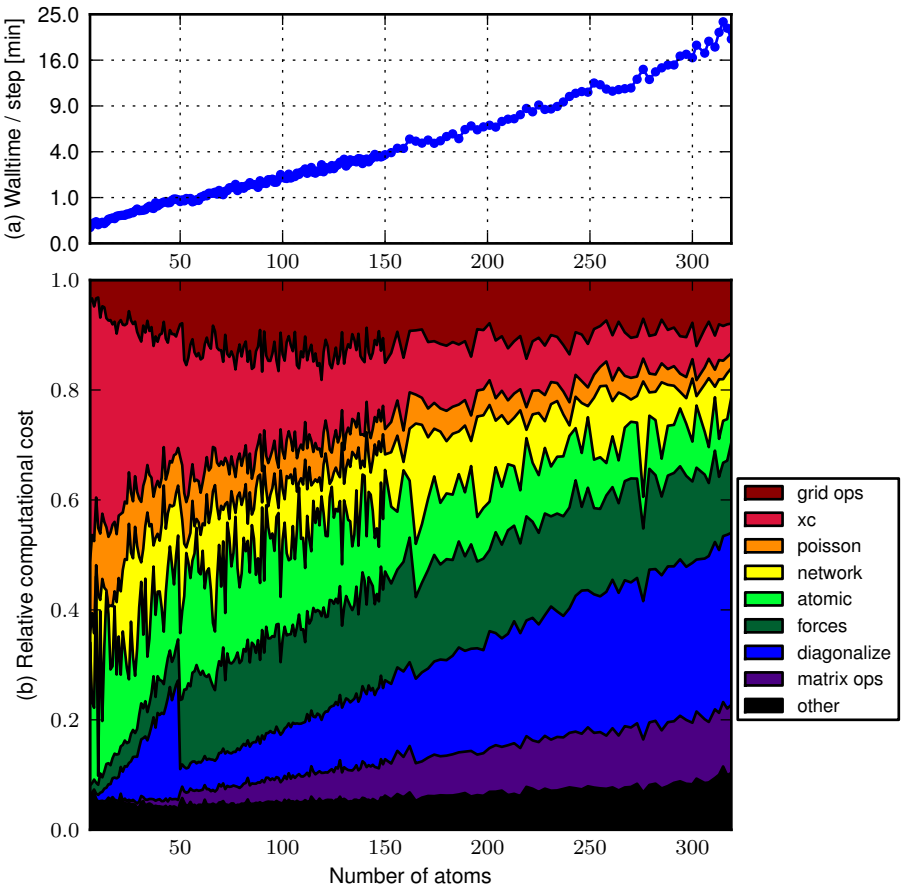

Figure 5.1: *Performance of basis set calculations on gold clusters. Top: Wall-clock time in minutes of one step in a structural optimization as a function of number of atoms. Note that the axis is quadratic. Below: Relative time spent in different parts of the code. The qualitative change at 50 atoms is due to a switch to parallel diagonalization.*

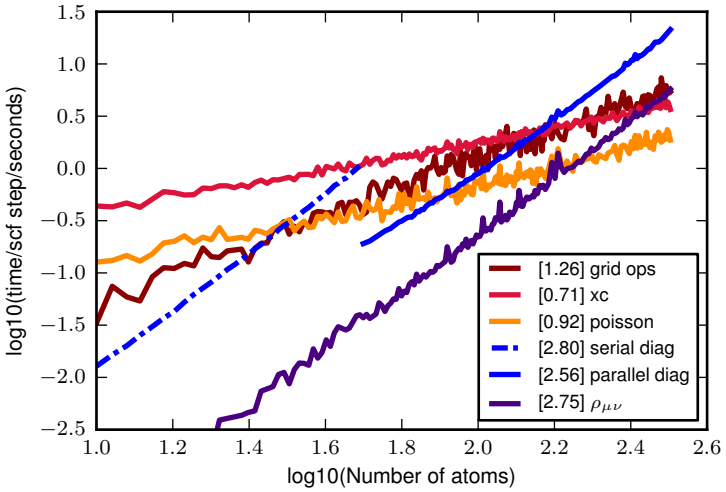

Figure 5.2: *Doubly logarithmic plot of time per SCF iteration for different operations. The scaling powers are indicated in the legend. Colours are consistent with Figure 5.1.*

for $N > 50$ except for the serial diagonalization. "Grid ops" is nominally linear, but superlinear in this case because of a gradual increase in the ratio of bulk to surface atoms with N. The increased density of orbitals around bulk atoms increases the cost. XC and Poisson performance appears sublinear because of the non-proportinal relationship between volume and number of atoms; for example, a system with one atom needs about as much vacuum as a system with two atoms.

Overall, the main limitation on parallel performance is the matrix diagonalization, as its non-local character implies significant communication. While calculations even for systems beyond 1000 atoms have been tested and are indeed faster than the real-space code, the time-consuming diagonalization is an obstacle which makes the approach practical only for systems up to around 400–600 atoms on the Niflheim cluster with the current interconnect.

5.6 Real-space calculations and parallelization

In real-space calculations, the number of variational degrees of freedom is too large to directly diagonalize the Hamiltonian like in the localized basis set. Instead an iterative procedure is used. For each self-consistency iteration, guesses for the pseudowavefunctions are improved until they converge alongside the density and potential.

The Hamiltonian is applied to the pseudowavefunctions in the real-space basis using a finite-difference stencil for the Laplacian:

$$\langle \mathbf{r}|\hat{\tilde{H}}|\tilde{\psi}_n\rangle = -\frac{1}{2}\nabla^2\tilde{\psi}_n(\mathbf{r}) + \tilde{v}(\mathbf{r})\tilde{\psi}_n(\mathbf{r}) + \sum_{aij}\tilde{p}_i^a(\mathbf{r})\Delta H_{ij}^a\,\langle\tilde{p}_j^a|\tilde{\psi}_n\rangle\,. \qquad (5.7)$$

The Hamiltonian in the basis of the current pseudowavefunctions, $\langle\tilde{\psi}_n|\hat{\tilde{H}}|\tilde{\psi}_m\rangle$, is then constructed by real-space integration. The operation involves all pairs of bands n and m, and hence the entire pseudowavefunction arrays must be passed around between band-parallelizing cores; this is why band parallelization is usually more expensive than domain decomposition, which involves communication at the domain boundaries. Following this step, the Hamiltonian matrix is diagonalized using the ScaLAPACK implementation described previously, involving redistribution to block cyclic form and back. The coefficients obtained from this diagonalization are then used to rotate the wavefunctions within their subspace so that they have definite eigenvalues.

The wavefunctions are improved by calculating the residual

$$R_n(\mathbf{r}) = \hat{\tilde{H}}\tilde{\psi}_n(\mathbf{r}) - \hat{S}\tilde{\psi}_n(\mathbf{r})\epsilon_n \tag{5.8}$$

and applying the residual minimization method described by Kresse and Furthmüller.[35] The wavefunctions are explicitly orthogonalized by constructing the overlap matrix $\langle\tilde{\psi}_n|\hat{S}|\tilde{\psi}_m\rangle$, and performing the rotation

$$\tilde{\psi}_n(\mathbf{r}) \leftarrow \sum_m \tilde{\psi}_m(\mathbf{r})[L^{-1}]_{mn}, \tag{5.9}$$

where L_{mn} is the Cholesky decomposition of S_{mn}. ScaLAPACK is used again for this inverse Cholesky decomposition of the overlap matrix. The remaining steps of the self-consistency cycle have for the most part been discussed in the previous chapter.

The computational cost for large systems is dominated by the cubically scaling and communication-intensive matrix element calculations, plus the subsequent rotations. Provided that the diagonalization is parallelized, it is not among the most expensive operations. Parallel diagonalization is also important for another reason: The double-precision floating point representation of a bands-by-bands matrix in a 10000-electron system (e.g. 1000 Pt atoms) requires about 200 MiB RAM. This is clearly unacceptable on a BlueGene/P with 512 MiB RAM per core.

This is the calculation procedure for the large-scale DFT calculations presented in later chapters. A scaling benchmark can be found in Paper II.[6]

5.7 Parallelization on BlueGene/P

It is our intention to perform DFT calculations on very large gold clusters using the accurate but expensive real-space grid methods in GPAW. For this purpose we use the IBM BlueGene/P supercomputer located at Argonne National Laboratory. In the limit of very large systems, some of the otherwise innocuous operations become quite expensive and must be taken into account in the implementation.

Supercomputers of small to medium size typically contain a number of distinct *nodes*, each containing a small number of CPU cores. The nodes might be connected by means of network switches, providing the usual star-shaped network topology where all CPUs can communicate with each other directly. For sufficiently large computers a network of this type will, however, suffer congestion because all data must pass through the same switch. An indefinitely

scalable computer therefore cannot have a star-shaped topology, but must make use of localization. The parallel structure of a programme must then take into account the network topology of the supercomputer on which it runs, so that communication takes place if possible only between neighbouring nodes.

In the BlueGene/P supercomputer which is our specific target, the nodes are connected in a three-dimensional grid. Each core is assigned a set of coordinates XYZT, where XYZ designate the position of the node in the grid, and T enumerates the cores within a node (and acts as a very short fourth dimension). A core is connected directly to its immediate neighbours along each of these four grid directions. The first and last CPUs in each direction are also directly connected. The network topology is therefore a four-dimensional torus, which has a maximal of size $40 \times 32 \times 32 \times 4$ cores, or 163840 CPUs. Calculations generally involve smaller sets (or *partitions*) of CPUs which are also wired to form a torus. Since solution of the Kohn–Sham equations is parallel over both the three spatial directions (x, y, z) and states n, the logical parallelization is to let the XYZT network torus correspond some permutation of x, y, z and n.

Part II

Electronic and chemical properties of metal clusters

Chapter 6

Metal nanoparticles

This chapter provides a short introduction to metal nanoparticles. An overview of the geometric structures formed by nanoparticles is given, and different simple models for their structure and properties are discussed.

Nanoparticles have important applications in catalysis, where size-dependent changes in chemical properties can have a big impact on catalytic activity. For example gold clusters become effective catalysts under some conditions. Of particular note is the ability of gold clusters, when deposited on surfaces of certain transition metal oxides, to oxidize CO at very low temperatures.[49] This has been observed for gold particles of around 4 nm in size.[50] The high catalytic activity has been attributed to a number of effects, such as non-metallic behaviour associated with flat islands.[51] Others attribute the increase in reactivity mainly to the availability of low-coordinated atoms and surface roughness, although many effects are understood to be involved.[52–56] Understanding the catalytic activity is part of the motivation for this work, although we focus on understanding the more fundamental properties of free-standing nanoparticles, which are much simpler systems than the complicated nanoparticle/support-based systems used in catalysis.

6.1 Packing and structural motifs in clusters

The lowest-energy shapes of very large nanoparticles are characterized by the combination of crystal planes which yields the lowest total surface energy, and can be obtained by the Wulff construction method. For smaller clusters, size effects will allow several different structural motifs to compete. A few such structures of particular relevance will be described below.

A number of highly symmetric structures can be constructed by successively adding shells of atoms. A simple such structure is the *cuboctahedron*. The first cuboctahedron is formed by adding 12 neighbours around a central atom forming part of an fcc lattice. Further cuboctahedral structures can be formed by adding further such shells, resulting in clusters with 13, 55, 147, 309, 561, 923, 1415,... atoms. The first few cuboctahedral clusters are shown on Figure 6.1. The cuboctahedra are simple fcc-based clusters with (111) and (100) surfaces. By adjusting the number of (111) versus (100) surface layers, one can also obtain cubes, truncated cubes, cuboctahedra, truncated octahedra and octahedra—see

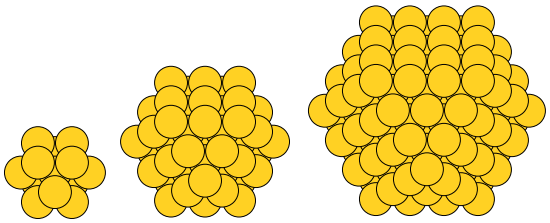

Figure 6.1: *The first three cuboctahedral clusters, having 13, 55 and 147 atoms.*

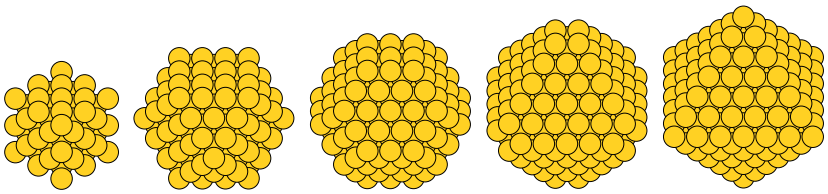

Figure 6.2: *A family of fcc clusters: 63-atom cube, 147-atom cuboctahedron, 201 and 225-atom truncated octahedra and 231-atom octahedron.*

Figure 6.2. Truncated octahedra are frequently the most stable structures for large clusters, including those of Au.[57]

The close-packed (111) surfaces of fcc structures tend to have the lowest surface energy. It is possible to form clusters with *only* close-packed surfaces, although this happens at the expense of internally straining the cluster by breaking the fcc structure. This is the case for the icosahedral series of clusters. Like the cuboctahedra, these are generated by adding successive layers of atoms around a single atom, resulting in the same geometric shell closings at 13, 55, 147, ... atoms. The first few icosahedra are shown on Figure 6.3. The distance between atoms in neighbouring icosahedral shells differs from the distance between atoms within the same shell. This causes an overall $\mathcal{O}(N)$ increase in energy, while the decrease in energy from the change in surface structure must be proportional to the amount of surface $\mathcal{O}(N^{2/3})$. The icosahedral motif is therefore a likely structure for medium-sized clusters. Many other lattice-based structures can be imagined, of which the most important for gold are probably truncated decahedra[58,59] which are, like icosahedra, internally strained. A thorough classification of atomic shell structures has been written by Martin.[60] The

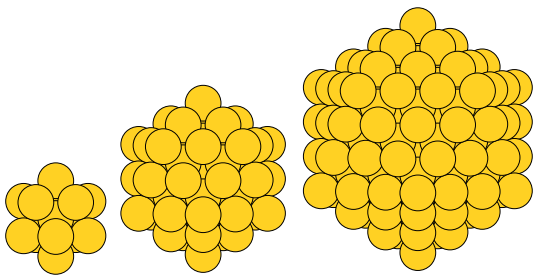

Figure 6.3: *Icosahedral clusters with 13, 55 and 147 atoms.*

free energy of different structural motifs depends on size as well as temperature, leading to complicated phase diagrams with temperature-dependent preference for different structures.[61–63]

Due to the high computational cost of ab-initio methods, the structural properties of large metal clusters are usually studied through simple models. Several such models are based on pair potentials with energy terms that model the attractive and repulsive parts of atomic interactions formulated e.g. as an energy contribution for each pair of atoms. For example, the Sutton–Chen[64] and Gupta[65] potentials both predict highly stable clusters with 13 (icosahedral), 38 (truncated octahedral), 55 (icosahedral) and 75 (decahedral) structure.[66] Such many-body potentials can be well suited to describe the specific properties they were designed for, but make no reference to electronic structure, which limits their ability to describe small clusters.

6.2 Jellium clusters

A simple model of materials can be obtained by entirely neglecting atomic structure, and instead assuming that electrons are interacting in a smeared-out background charge so that the whole system is neutral. This fictitious material is called *jellium*. Jellium models of clusters have been studied extensively since the discovery that alkali metal clusters with specific "magic" numbers of electrons are particularly stable and can be understood through jellium models.[20,21,67–73] Below we describe the simplest imaginable jellium model of clusters, namely that of independent electrons in an infinite spherical well.

Assume that a cluster with N electrons is described by an infinite spherical well potential with radius $R = N^{1/3}$. By separation of variables one obtains distinct equations for radial and angular parts of the eigenstates, quite like in the atomic problem from Section 4.1, except for the shape of the radial potential. The radial equation is the spherical Bessel equation with zero boundary conditions, whose solutions are spherical Bessel functions $j_l(r)$ of the first kind.* The angular equation as always yields spherical harmonics $Y_{lm}(\theta, \phi)$. Thus

$$\psi_{lnm}(r, \theta, \phi) = \alpha_{ln} j_l \left(\frac{z_{ln} r}{R} \right) Y_{lm}(\theta, \phi), \tag{6.1}$$

where α_{ln} is a normalization factor and z_{ln} is the n'th zero of j_l. The energies of these solutions ares

$$\epsilon_{ln} = \frac{1}{2} k_{ln}^2 = \frac{1}{2} \frac{z_{ln}^2}{R^2}. \tag{6.2}$$

Thus there exists a set of degenerate solutions for each zero z_{ln} of each spherical Bessel function $j_l(r)$, with degeneracy $2(2l + 1)$, counting spin. The energy levels are ordered the same way as the zeros of the spherical Bessel functions. This results in an *Aufbau* rule like in the periodic table, except a higher angular momentum tends to be relatively more favourable for jellium clusters than additional radial nodes. Configurations with a full shell are particularly stable. In order of increasing energy, the eigenstates are 1s, 1p, 1d, 2s, 1f, 2p, 1g, ..., which results in magic numbers at the shell fillings N=2, 8, 18, 20, ..., as illustrated on Figure 6.4; see also Table 6.1.

2	**8**	**18**	20	**34**	40
58	68	90	**92**	106	132
138	168	**186**	196	198	232
254	268	306	312	**338**	380
398	428	**438**	**440**	486	508
542	556	562	612	638	...

Table 6.1: *Magic numbers of spherical non-interacting jellium clusters. Major magic numbers, having particularly large electronic gaps at the Fermi level, are highlighted.*

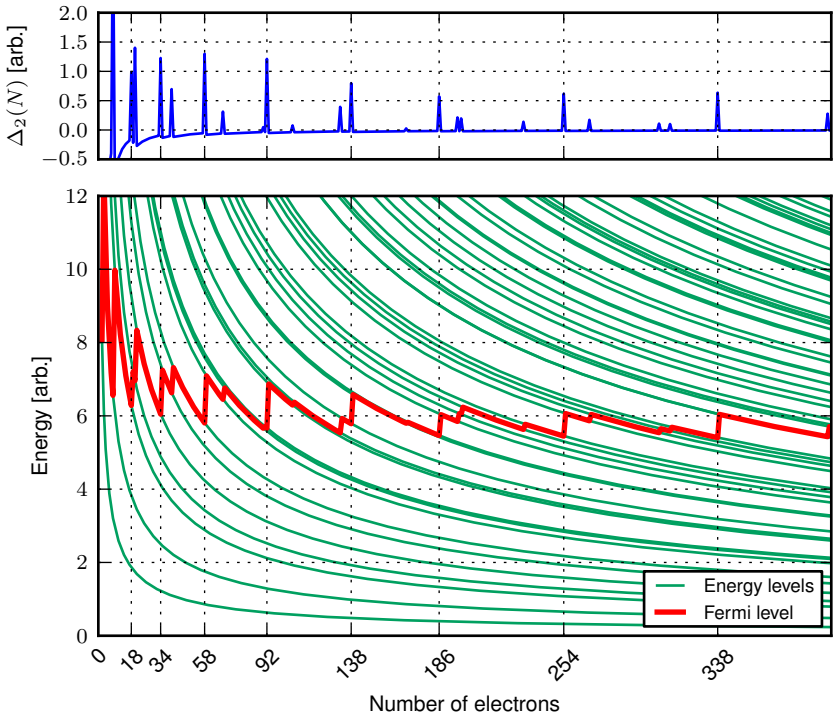

Figure 6.4: *Below: Energy levels and Fermi level of spherical-well jellium clusters as a function of number of electrons. Major magic numbers are indicated. Above: Second-order energy differences* $\Delta_2(N) = E(N-1) - 2E(N) + E(N+1)$*, a measure of the curvature of the total energy.*

The spherical-well model above is the simplest possible jellium model. Many other jellium-based models have been formulated to describe alkali metal clusters. The inclusion of electronic interactions, typically through the solution of the Kohn-Sham equations using the local density approximation, yields magic numbers similar to those we found in the previous non-interacting model. The relative importance of the different magic numbers may shift depending on the exact model used, but the spherical shell closings are almost universally reproduced as listed in Table 6.1. More insight is gained by considering jellium clusters of different shapes. Commonly, the jellium clusters are allowed to deform under some specified set of rules.[71,74–77] An important result is that jellium clusters with a non-magic number of electrons will deform into prolate (elongated along one axis) and oblate (flattened) shapes depending on the number of electrons. This allows non-magic clusters to obtain lower energies, which we will also see in Chapter 10 using DFT calculations. Different highly symmetric shapes such as tetrahedra also lead to strong magic numbers.[78]

The previously mentioned pair potentials are formulated only in terms of atomic separations, while jellium models completely neglect atomic structure. Both electronic and structural effects can be combined in tight-binding models, such as the Hückel model.[79–82] This model predicts electronic magic numbers in agreement with the jellium model.[83,84]

6.3 Noble metal clusters, relativity and gold

Since the noble metals have a fully occupied d-band, they are electronically similar to alkali clusters. Jellium-like magic numbers have been observed in the mass spectra of noble metal clusters, indicating particular stability of clusters with closed electronic shells.[22] While clusters of the three noble metals show similar electronic shell structure, gas-phase gold clusters form particularly remarkable geometric structures. The smallest gold clusters are predicted to be planar, with a transition between planar and 3-dimensional structures usually put between 8–15 atoms depending on charge and other circumstances.[18,85,86] The exact transition between planar and 3-dimensional clusters of various charge states has been discussed extensively within DFT methods and depends strongly on the XC approximation.[19,87–89] The stability of planar structures, along with practically all the peculiarities of subsequent Au clusters as compared to Ag or Cu, can be attributed to relativistic behaviour of the core electrons which, through changes in screening of the outer electrons, increase the range and hybridization with the d-states.[17] Larger gold clusters form many more exotic structures, such as cages and tubes even beyond 30 atoms, with the 32-atom cluster being a cage.[19,90,91] Gold in particular has a tendency to form low-symmetry structures.[92] Even the 55-atom Au cluster does so rather than forming an icosahedron as has been found for Ag.[93,94] Due to the high computational cost of such global structure optimizations of clusters, the determination of globally optimal structures of most larger clusters must to some extent rely on simpler methods, although limited studies of large clusters have been made.[95]

*The spherical Bessel functions are related to the ordinary ("cylindrical") Bessel functions by $j_l(r) = \sqrt{\frac{\pi}{2r}} J_{l+\frac{1}{2}}(r)$.

Chapter 7

Chemical properties of large clusters

In this chapter we examine the convergence of chemical properties of gold clusters with respect to cluster size. This is done by calculating binding energies of simple adsorbates on cuboctahedral clusters up to 1415 atoms. The cuboctahedra are not lowest-energy structures,[57,96] and particularly the small clusters Au_{13} and Au_{55} are known to form entirely different structures in the gas phase. However the cuboctahedra provide a simple geometry which can be compared at different sizes and with different metals.

7.1 Structure and calculation parameters

We calculate the binding energy of O and CO, each on two different adsorption sites, and on Au as well as Pt cuboctahedra. The motivation for specifically considering O and CO is the relevance of these adsorbates as intermediates in CO oxidation, although we make no attempt to model actual catalytic systems at this time. Figure 7.1 shows the adsorption sites. They are:

- O on the fcc hollow site closest to the center of an (111) facet
- O on the bridge site closest to the center of an edge

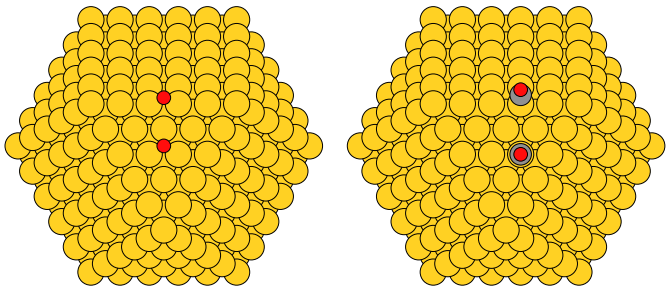

Figure 7.1: *Adsorption sites, shown two at a time, of O and CO on the Au_{561} cuboctahedron.*

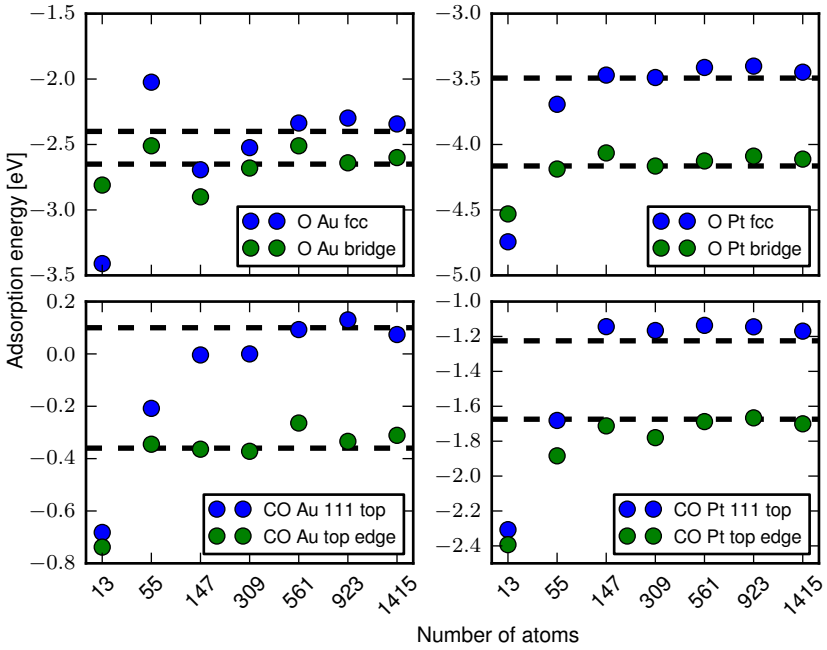

Figure 7.2: *Binding energy of O and CO on cuboctahedral Au and Pt clusters of different size. For each series of datapoints, the bulk limit is indicated.*

- CO on top of the atom closest to the center of an (111) facet
- CO on top of the atom closest to the center of an edge, with O pointing away from the cluster

The distance between adsorbate and metal atoms is in each case based on a relaxation of the adsorbate on an infinite metal surface locally similar to the cluster. Since no relaxation of the cluster is performed, we do not care to deeply about the exact geometry of the adsorbate either. In the limit of infinitely large clusters, the environment around each adsorbate approaches either that of a clean surface or a step configuration. Such configurations are used to obtain values for the bulk limits. The calculations are performed using the RPBE XC-functional with the real-space grid implementation in GPAW. A grid spacing of 0.175Å is used for Au clusters, and 0.140Å for Pt clusters. The lattice constants 4.218 Å for Au or 3.999 Å for Pt are used in the cluster construction. No structure relaxation is performed in these calculations. The effects of structure optimization on the adsorption energies to Au cuboctahedra has been found to be small; see Paper III.[97]

7.2 Adsorption energies

The calculated adsorption energies as a function of cluster size are shown on Figure 7.2. A common feature of both Pt and Au clusters is that small clusters

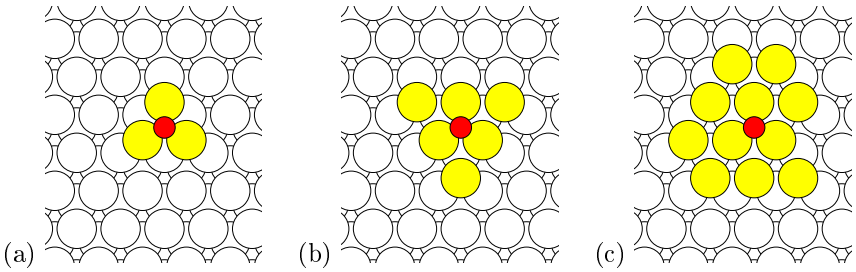

Figure 7.3: *O adsorption on adatom plateaus of sizes 3, 6 and 11 atoms. The colouring only serves to distinguish adatoms from surface atoms; adatoms and surface atoms are the same type.*

tend to bind the adsorbates more strongly. A notable deviation from this trend is that the O on both (111) facet and bridge site of the Au_{55} binds extremely weakly, weaker even than the bulk limit (upper left on Figure 7.2). The low reactivity towards O of Au_{55} is consistent with existing observations,[98,99] although the real free-standing Au_{55} is known to have a quite different low-symmetry structure.[93,95] CO on Au exhibits a much more smooth convergence towards the bulk limit.

For Pt, the overall size-dependent change in adsorption energies is more uniform than for Au. Almost all variation stops after $N = 147$, except a slight fluctuating tendency which is slowly damped.

Variation in the cluster size will necessarily change both the local structure around of the adsorbate, and the overall cluster size. The changes in local structure can be studied separately from calculations on extended surfaces. This will be done in the next section. In the next chapter we will study electronic effects more closely.

Further analysis of the large-scale results for Pt are in progress (unpublished). A more thorough discussion of the results for Au can be found in Paper III.[97]

7.3 Geometric effects on adsorption

Part of the size trend in the previous calculations must be attributable to the change in size of the facets. To investigate this local, geometric effect we compare cluster adsorption energies with adsorption energies calculated on infinite surfaces with plateaus of various size. We concentrate here on O adsorption on Au and Pt.

We consider an fcc (111) surface slab with four layers of atoms and lattice constants 4.218 Å for Au or 3.999 Å for Pt, as before. On top of the slab we construct plateaus with different numbers of adatoms forming part of an extra surface layer. We start with an adatom trimer whose central (111) fcc site is locally consistent with the previously considered O adsorption site. The plateau is then expanded by adding one atom at a time on sites consistent with the lattice. A few of the geometries are shown on Figure 7.3. Each time, the atom is added as close as possible to the adsorbate such that the adsorbate will always be close to the center of the plateau. In order to fit a plateau with 50 atoms

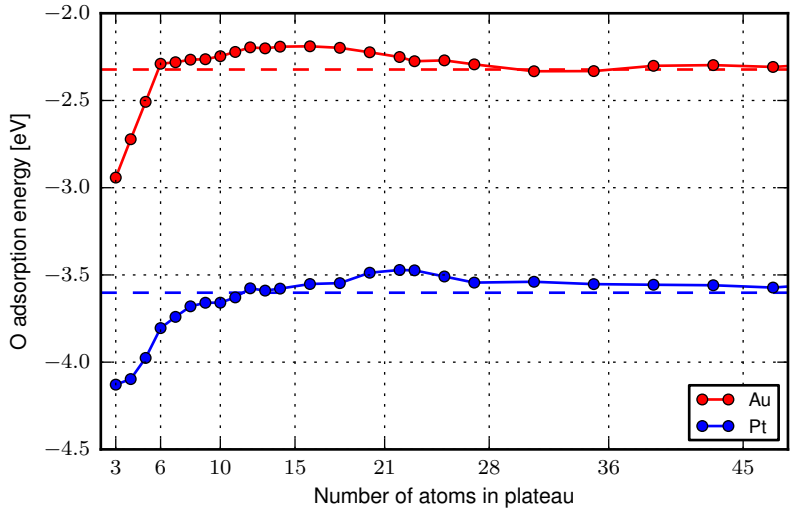

Figure 7.4: *Binding energy of O on central fcc site of Au and Pt one-layer adatom plateaus as a function of the number of atoms in the plateau. The bulk limit is indicated by a dashed horizontal line. Ticks on x axis are placed so they correspond to sizes of cluster facets (the 55-atom cuboctahedron or icosahedron has 6 atoms in an (111) facet).*

in the cell (the 1415-atom cuboctahedral (111) facet contains 36 atoms), it is necessary to include a total of 365 atoms in the calculation. We use the localized basis set with the standard double-ζ polarized basis sets.

For each of these geometries we then calculate the adsorption energy without any structure relaxation. O is put at a fixed perpendicular distance of 1.37 Å (Au) or 1.28 Å (Pt) from the plateau atoms which is consistent with the fixed cluster geometries.

The adsorption energy of O as a function of the number of adatoms is shown on Figure 7.4. For Au the adsorption energy increases swiftly and linearly between plateau sizes of 3–6 atoms. Once the triangular 6-atom plateau on Figure 7.3 is completed, the energy remains largely constant. The 6-atom plateau is identical to the (111) facet on the Au_{55} cluster which binds O very weakly, but the geometric trend here is insufficient to explain the spectacularly weak binding on Au_{55}. Medium-sized plateaus up to 28 atoms (like the 923-atom cluster) bind slightly more weakly than bulk Au, after which the difference from bulk is tiny. This geometric trend thus accounts (partially) for the strong binding on the 13-atom cluster compared to subsequent clusters, but agrees with *none* of the behaviour of other clusters until near the bulk limit at 561 atoms and larger.

For Pt the smallest plateaus also bind strongly, but the trend differs from that of Au since the binding energy varies much more smoothly over the small plateaus. The convergence of the Pt binding energy with respect to plateau size

matches roughly that of the Pt clusters: after a plateau size of 10 atoms (147-atom cluster), most of the variation has stopped, and only weak oscillations remain.

In the next chapter we will consider the effect of electronic structure on adsorption energies.

Chapter 8

Electronic structure and chemisorption

The variations in adsorption energies for smaller clusters, and in particular the very weak adsorption of O on the Au_{55} cluster, remains to be explained. To study electronic effects on adsorption in greater detail, we will in this chapter construct a contiguous range of clusters up to several hundred atoms. This implies a quite large number of calculations. Since we are not interested in binding energies with high accuracy, but rather the overall variation of binding energies, the localized basis set method is ideally suited for these calculations.

8.1 Construction of clusters

Consider two consecutive cuboctahedral clusters. We can get a contiguous range of intermediate clusters by stripping off the outermost shell of atoms in the larger cluster one atom at a time, so that eventually only the smaller cluster remains. The atoms can be removed in any order. To obtain reasonably realistic geometries, we choose to always remove at random one of the atoms with lowest coordination. Since we want to calculate an adsorption energy for each size of cluster, and since we are interested in overall electronic size effects rather than the effects of geometry, the local geometry around the adsorption site should remain unchanged during this procedure. This can be managed by effectively removing two shells from the side of the cluster opposite the adsorption site. This procedure is shown on Figure 8.1. Since atoms are removed at random, a pseudorandom number generator can be used to generate several series of clusters. This reveals how sensitive the procedure is to detailed structural differences, although the strictly cuboctahedral clusters always have the exact same geometry. The procedure can be used to generate any structure based on geometric shells, and we will use this to compare to icosahedral clusters. However because of the internal straining of icosahedra, the local geometry around the adsorbate cannot be conserved for all sizes of clusters. For convenience we therefore limit this study to cuboctahedra with the central (111) fcc site on Figure 8.1, which was also the subject of our previous studies. The Au_{13} cuboctahedron does not have an (111) fcc site (only an hcp site), so this cluster cannot be generated from the discussed procedure; instead we use a 19-atom cluster which is the result

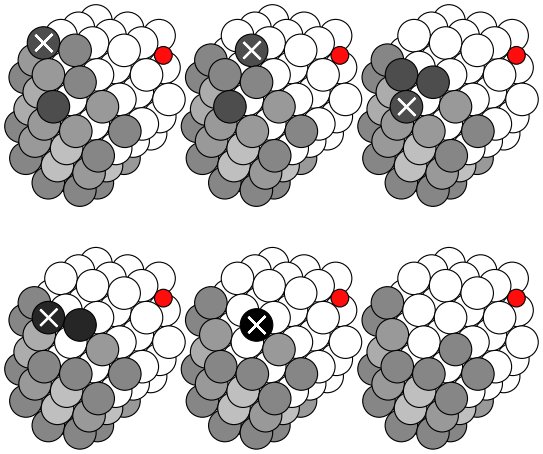

Figure 8.1: *Construction of clusters with arbitrary number of atoms. Atoms in the 55-atom cuboctahedron are white, while removable atoms are coloured according to their coordination. At each step, one of the removable atoms with lowest coordination is removed. An O atom is shown at the (111) fcc site.*

of removing most of the atoms from the Au_{55} cuboctahedron without changing the immediate environment around the adsorbate.

Over the next sections we perform calculations on clusters up to 200 or 320 atoms in size. For clusters larger than 150 atoms we skip two thirds of the clusters to save CPU time. This may appear as pixelation in some of the figures, but does not represent any physical effect.

8.2 Calculation parameters

For four different series of randomly generated Au clusters we calculate the adsorption energy of O using the localized basis sets in GPAW. The calculations use somewhat coarse parameters to improve efficiency. The grid spacing is 0.2Å, and 5.0Å vacuum is added in all directions. Each atom has the standard double-zeta polarized basis set and the standard PAW setup package supplied with GPAW. The RPBE XC functional is used as in the previous calculations. A Fermi temperature of 0.01 eV is used. We do not consider spin-polarization except in atomic reference calculations.

For each cluster a structure optimization is performed with O located at the central (111) fcc site. The implementation of the BFGS structure optimization algorithm from ASE is used.[42] Structure optimizations terminate when the forces are no greater than 0.075 eV/Å.

Since we are not interested in high accuracy, but rather in a broad size-comparison of different clusters, we calculate adsorption energies in a more rough way than normal. First a structure relaxation of the combined system, cluster plus adsorbate, is performed, yielding a total energy. The binding energy is then calculated by subtracting the total energy of the isolated atom and the total energy of the isolated cluster. In the calculation of the isolated cluster we do *not* perform a separate structure relaxation. Aside from saving time, the benefit

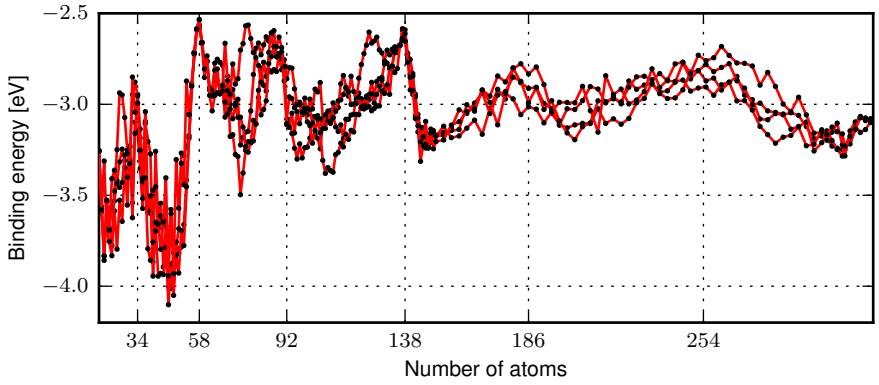

Figure 8.2: *Binding energies of O on Au clusters. Major jellium magic numbers are indicated.*

of this procedure is that we do not have to worry about the *egg-box effect*: If we relaxed both the combined and the isolated clusters, the atoms would have moved slightly relative to the grid points, which causes a small difference in evaluated energies. For large systems such an error will easily be significant compared to a one-atom binding energy. The overall effect of not relaxing the isolated cluster is that *all binding energies are overestimated*. Furthermore, we shall not care to apply a basis set superposition error (Section 4.5). This error is similar for all the clusters, since the local environment around the atom is similar, and therefore only shifts the energies by a constant.

8.3 Adsorption energy and magic numbers

Figure 8.2 shows the adsorption energy of O on the central fcc site on Au cuboctahedra as a function of number of atoms. Four different series of randomly generated clusters are shown. The binding energy oscillates with an amplitude of 0.5–1.0 eV. Minima in binding occurs at or close to the jellium magic numbers $N = 34, 58, 92, 138$ and 186.

Figure 8.3 shows the density of states (DOS) of the Au cuboctahedra. The d-band lies between -10 and -6, eV and changes relatively little. The s-states, however, split up into distinct electronic shells separated by gaps. As cluster size increases, shells are filled one electron at a time. When a shell is full, electrons must be filled into the next higher shell, resulting in an abrupt increase in Fermi level at the magic numbers 34, 58, 92 and 138 matching the jellium model. Figure 8.4 shows DOS close to the Fermi level of cuboctahedra compared to icosahedra. The icosahedra are generated by the same procedure by stripping off atomic shells one atom at a time. The two types of structure have highly similar shell structures in agreement with potential-well models.[100] In small jellium clusters the magic numbers are also known to be robust to geometric variations as long as the gaps between shells are large compared to the effect of distortion.[101]

The loosely bound electrons just after a magic number are easily donated to O, causing an abrupt increase in O binding energy at the magic numbers.

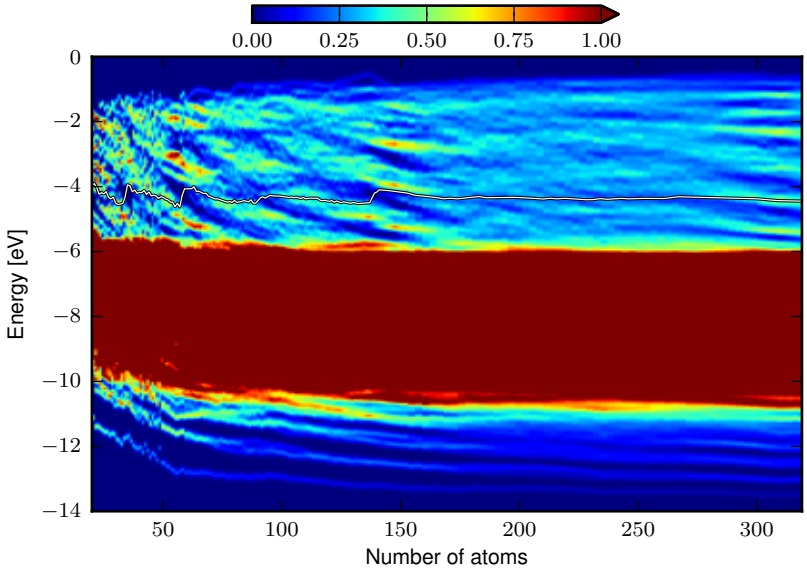

Figure 8.3: *DOS of Au clusters based on the cuboctahedral series as a function of cluster size and energy. The Fermi level is indicated. Magic numbers are associated with abrupt jumps in the Fermi energy.*

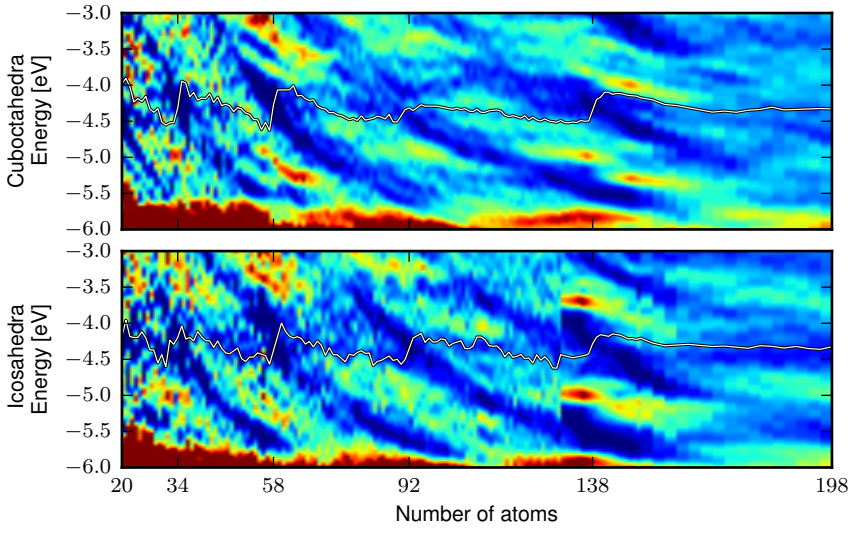

Figure 8.4: *DOS of cuboctahedral (top; a subset of the data in Figure 8.3) and icosahedral (bottom) Au clusters near Fermi level. The Fermi level is indicated.*

Clusters with full shells are generally unreactive.

As cluster size increases further, the energetic distance between subsequent shells decreases, causing the shell structure to become less well resolved. However we still see from Figure 8.2 how the magic numbers 186 and 254 correspond to particularly weak binding, even if no well-resolved magic number is immediately visible in the spectrum from Figure 8.3. In general, the electronic shell structure is most well-resolved close to the geometric shell fillings (55 and 147 for both cuboctahedra and icosahedra), and for smaller clusters where the energetic separation between shells are large. Au_{55} is just below a magic number, while Au_{147} os slightly above one. This accounts for the observations in the previous calculations.

Intermediate clusters such as the $N = 92$ cluster may be deformed significantly due to the generation procedure. This is probably why the magic number appears at a slightly lower cluster size. The structure relaxation tends to enhance the shell structure, and the magic number at $N \approx 92$ is only visible for cuboctahedra due to this relaxation.

While variations in the oxygen binding energy tend to correlate with in the Fermi level or HOMO, this correlation is far from perfect. A large DOS near the Fermi level tends to increase adsorption as well. A more complete picture would be that the overall accessibility of loosely bound electrons from the adsorption site plays an important role. Such an effect has previously been pointed out for the adsorption of molecular oxygen on Au clusters.[53]

On a side note, the clear relationship between the electronic shell structure clusters and the chemical properties of gold clusters raises the question of whether the previous conclusions, placing the convergence of adsorption energies with cluster size at about 600 atoms, might be wrong due to magic numbers in between the cuboctahedral geometric shell closings. The spectra of icosahedral and spherical potential wells have been found to be highly similar as high as 1000 atoms, while cuboctahedral potential wells deviate much more quickly beyond a few hundred atoms.[100] Au clusters have been predicted to form fcc structures from somewhere around 500 atoms and above, preceded by decahedral clusters.[59] The lower symmetry of fcc clusters as well as decahedra compared to icosahedra make it less likely that large gaps can be found at those sizes. Thus the expected structures in the relevant size ranges do not favour the formation of gaps. Another effect which works to disfavour highly magic numbers for clusters much larger than 500 atoms, at least to the extent that the clusters can still be considered vaguely spherical, is the supershell structure. The relationship between electronic shells of different radial and angular dependencies is expected to result in a beat phenomenon such that major shell effects are mostly extinguished between 500-900 atoms.[102] The supershell effect once again allows for well-resolved magic numbers for clusters larger than 1000 atoms, although at this point the truncated octahedral[57] structure of gold clusters would be less likely to display such behaviour. Electronic shell structure has been observed in alkali metal clusters up to 1500 atoms, after which point geometric magic numbers corresponding to cuboctahedral or icosahedral shell closings take over.[103] This shift in character of magic numbers was attributed to solidification of the clusters. Another study has observed electronic shell structure as high as 3000 atoms.[104]

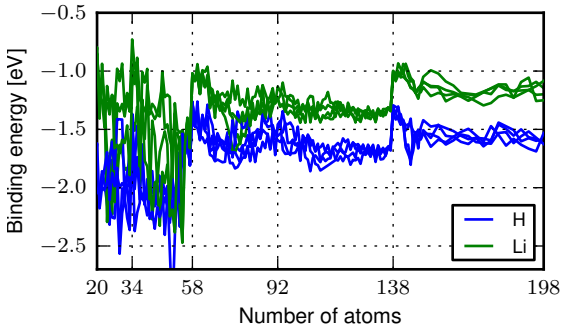

Figure 8.5: *Adsorption energy of H and Li on Au cuboctahedra as a function of cluster size. Clusters are generated with several different pseudorandom seeds.*

8.4 Main-group atoms on gold

We investigate the electronic shell effects more thoroughly by considering adsorption of several different elements.

The binding energies of H and Li on Au clusters are shown on Figure 8.5. Again, magic-number clusters are universally unreactive. H and Li follow the opposite behaviour of O: past a magic number, a sharp *decrease* in binding takes place. This is not surprising for Li which has a loosely bound electron. However H would sooner be expected to receive partial charge, so this behaviour is somewhat perplexing. An existing study of H adsorption on very small Au clusters has found a similar behaviour which was deemed "anomalous".[105] We will look further into this in Chapter 9.

Figure 8.6 shows the adsorption energy of ten 2p and 3p elements. Again, magic-number clusters are universally unreactive. The behaviour near magic numbers is consistent with the picture of electron donation or electron acceptance: For a cluster slightly smaller than a magic number the Fermi level is low, and so the donation of an electron to an electronegative adsorbate is associated with very low adsorption energy, while the acceptance of an electron leads to high adsorption energy. The opposite is the case after a magic number. The 2p elements, as can be expected, exhibit a more electronegative behaviour than the 3d ones. In general, Au clusters near magic numbers can therefore be viewed as alkali-like or halogen-like. For the halogens F and Cl, the increase in energy just past a magic number is quite abrupt. For less electronegative elements (O and S) the change in energy is larger but more gradual, happening over the addition of several atoms to the cluster. This can be interpreted as a transfer of several electrons gaining more energy, but is more likely to represent a covalent character of the bond as has been found for Au–S.[106]

In all cases, completion of the triangular 6-atom facet causes a sharp decrease in binding leading up to the $N = 55$ cuboctahedron. As before, $N = 92$ is not distinguishable as an electronic magic number, but weak binding is generally found around $80 < N < 90$. The overall amplitude of variation can be several eV and tends to be higher for the electropositive adsorbates.

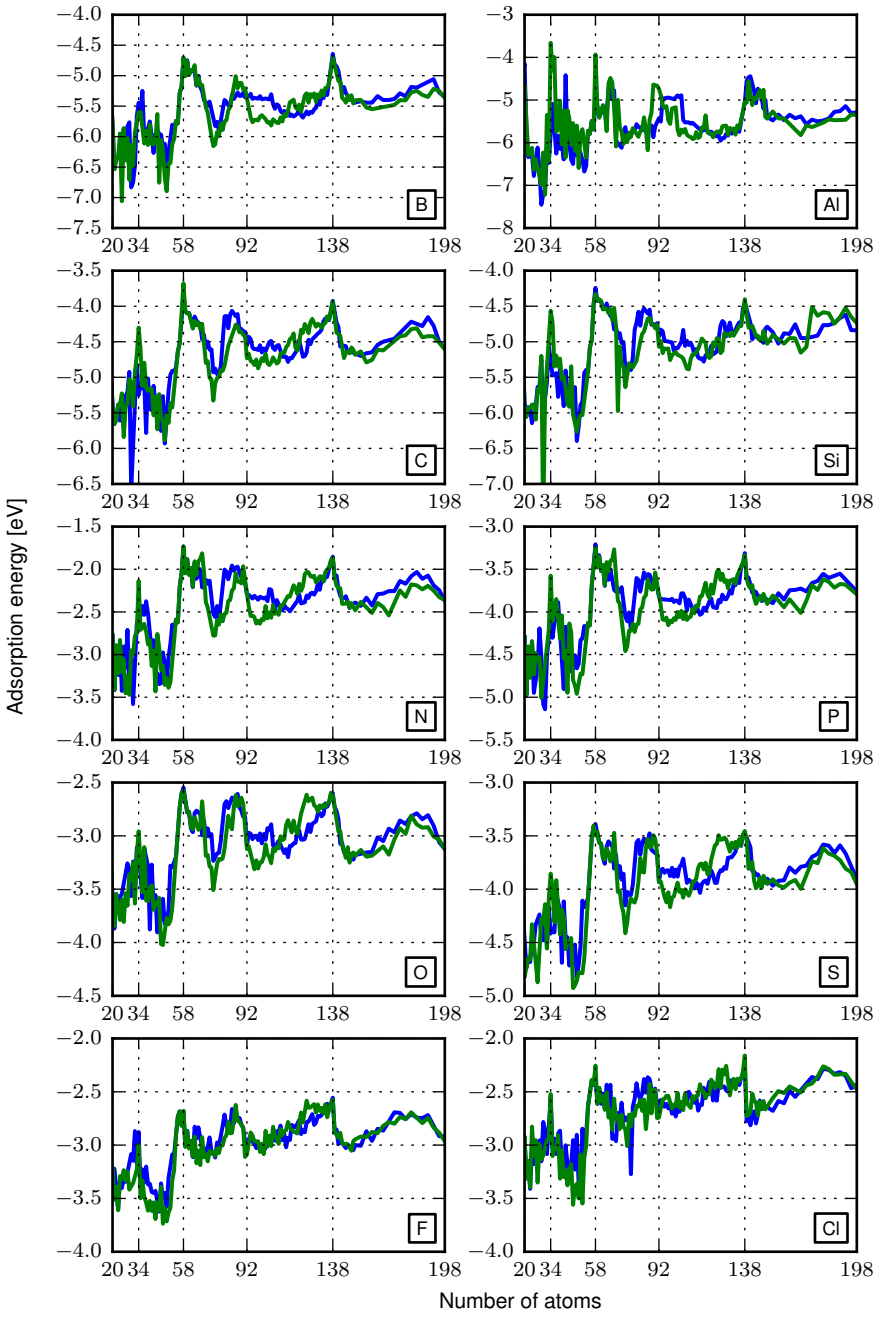

Figure 8.6: *Adsorption energy of main group elements on Au cuboctahedra as a function of cluster size. Two series of generated clusters are shown on each figure.*

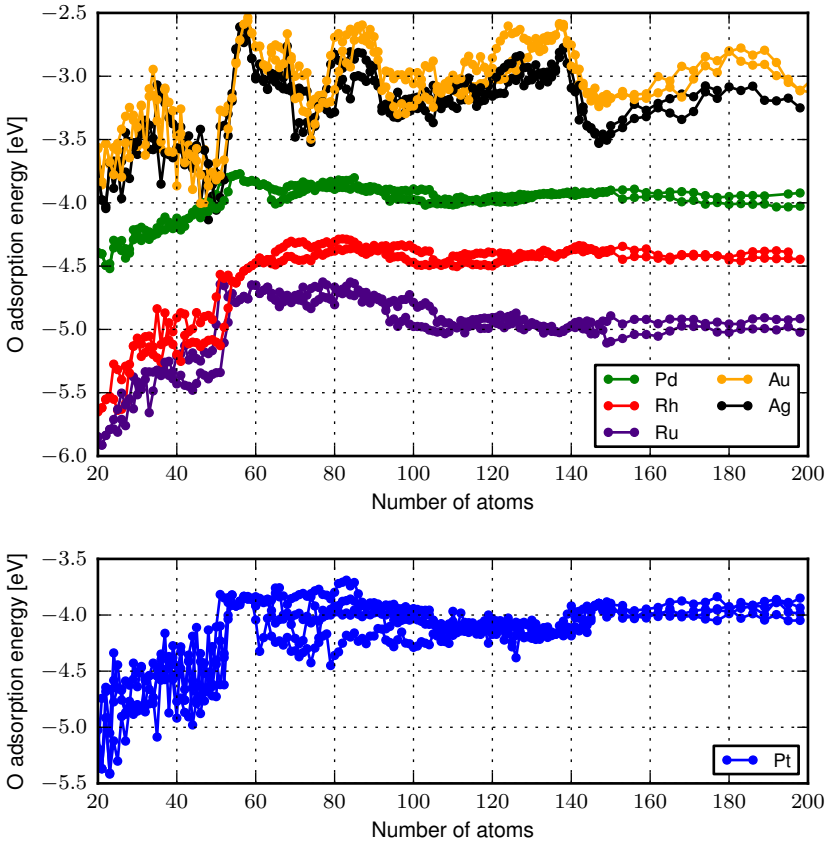

Figure 8.7: *Binding energy of O on cuboctahedral clusters of different metals.*

8.5 Oxygen on transition metal clusters

To expand our study in a slightly different direction, let us consider the trends in O adsorption for clusters of different metals. We compare the noble metals Au and Ag, plus several other transition metals with unfilled d-bands, using the same geometric series of clusters.

Figure 8.7 shows the adsorption energy of O on cuboctahedral clusters of various fcc transition metals. Pt adsorption energies are shown separately since some of the Pt clusters frequently reconstruct considerably, which causes a much more noisy trend. Structure optimizations of these Pt clusters require around three times as many steps as the 4d metals due to these massive reorganizations.

Au and Ag, having similar electronic structure, behave almost identically, with Au binding more weakly as expected. Evidently the relativistic effects of Au do not cause significant changes in the reactivity trend towards O on cuboctahedra (however the relativistic effects are known to have profound implications on cluster *structure*, and so would therefore be indirectly important in any case; relativistic effects could also be related to the tendency of Pt clusters to restructure much more than other d-band metals, although this has not been

investigated).

The transition metals Ru, Rh, Pd and Pt show much simpler trend than the noble metals. Three overall size regimes can be identified.

- From around 160 atoms and above, the binding energy is mostly constant, varying by about 0.1 eV. This agrees well with the previous real-space calculations, where the changes in adsorption energy on Pt converged more smoothly with cluster size than for Au. In the d-band model, the binding energies of adsorbates is predicted to vary among transition metals. For the largest clusters, the binding strength for the series Ru–Rh–Pd/Pt–Ag/Au very closely follows the filling of the d-band, with higher filling leading to weaker binding in agreement with the d-band model (see however the discussion below).

- Between 55–100 atoms the binding is generally weaker than for smaller or larger clusters, but without large variations (except for Pt). In this region the O atom binds to a 6-atom (111) facet. This specific site on that facet is apparently particularly unreactive: The increase in binding energy for larger clusters happens when the facet is further expanded, and the very steep change at $N \approx 50$–55 happens when the 6-atom facet is completed.

- Before the 6-atom facet is formed, the binding energy becomes much stronger, and generally binding energy increases steeply in the limit of small clusters. This can be a combination of several effects. In this region, the Fermi level and absolute d–band center both change in a similar way. The exact cause for this change may be attributable to some combination of movement of the d-band, the Fermi level and geometric nearest-neighbour changes. The variation of d-band location, and hence Fermi level which is pinned to the upper part of the d-band, takes place over roughly this same size range. For some reason Pd has a much weaker such variation than Ru, Rh and Pt.

The crucial chemical difference between the noble metal clusters and the remaining transition metals is clearly the electronic shell effects. Figure 8.8 shows the DOS of Pt clusters as a function of cluster size. The overall DOS is remarkably similar to that of Au, with the s-electrons forming gradually broadening subshells. However the Fermi level is located within the d-band where the DOS is very high, which locks it in place and this prevents the creation of any gaps. Note that the atomic basis set is not expected to be accurate for high-lying unoccupied states, and so these results do not conclusively prove persistence of shell structure among the unbound states.

It is natural to ask to what extent the size-dependence of adsorption energies within a series of clusters of the *same* metal can be understood from the d-band model. The d-band model predicts that binding energies of adsorbates on surfaces are related to the filling of antibonding states on the adsorbate, with a high filling causing low binding energies. A descriptor for the tendency of such states to be filled is usually taken to be $\epsilon_F - \epsilon_d$, the difference in energy between the Fermi level and the weighted center of the d-projected density of states on the atoms next to the adsorbate. If the Fermi level is high compared to the location of the d-band, antibonding states resulting from the hybridization of adsorbate states with the d-band will tend to lie below the Fermi level, which

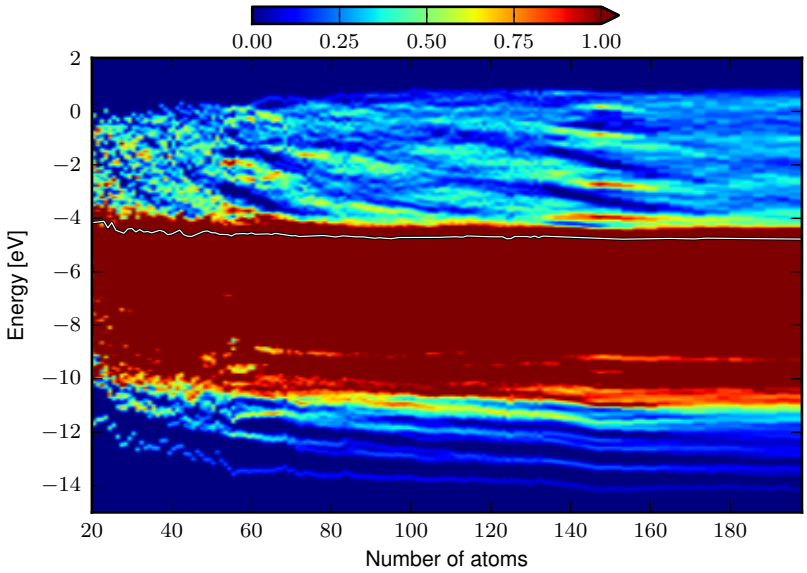

Figure 8.8: *DOS of Pt cuboctahedra. The Fermi level is indicated.*

amongst other things explains the low reactivity of noble metals.[107] This model can clearly not be a *sufficient* explanation for noble metals, where most of the trend is explained by s-electron shell effects. However the Pt d-band, as seen from Figure 8.8, clearly rises in energy for small clusters where adsorbates also bind more strongly. The same is true for the Fermi level. For noble clusters we have seen so far that variations in the Fermi level are important factors in the determination of adsorption energies on clusters as compared to bulk materials, and the *simple* descriptor $\epsilon_F - \epsilon_d$ does not explain the size variation of binding energies even for the metals with partially filled d-bands. The conclusion so far is that a number of different size effects participate, thus making the common $\epsilon_F - \epsilon_d$ descriptor less useful than in bulk systems.

Chapter 9

Analysis of chemisorption on gold clusters

We have seen how magic numbers affect the binding energy of various adsorbates on gold clusters, with clusters appearing alkali-like or halogen-like depending on the number of atoms. However a few questions are not resolved by the simple previous analysis. In particular the apparent donation of an electron by H, which would be expected to attract charge, is perplexing. A Newns–Anderson model will be applied below to better understand the bonding of different adsorbates.

9.1 The Newns–Anderson model

The Newns–Anderson model describes the chemisorption of an atom on a metal surface.[108] It is a tight-binding model which describes the hybridization of a single state $|a\rangle$ on an atom with the continuum of states $|k\rangle$ of a surface characterized by a Fermi energy ϵ_F. The model considers the Hamiltonian

$$\hat{H} = \hat{H}_0 + \hat{V}, \tag{9.1}$$

where $\hat{H}_0$ is the Hamiltonian of the uncoupled metal and adsorbate, and $\hat{V}$ describes the coupling. In the basis of uncoupled eigenstates $|k\rangle$ and $|a\rangle$, the Hamiltonian takes the form

$$\mathbf{H} = \left[\begin{array}{ccc|c} \ddots & & 0 & \vdots \\ & \epsilon_k & & v_{ka} \\ 0 & & \ddots & \vdots \\ \hline \cdots & v_{ak} & \cdots & \epsilon_a \end{array}\right], \tag{9.2}$$

where $\hat{H}_0$ and $\hat{V}$ correspond to the diagonal and off-diagonal blocks, respectively. The parameters are the uncoupled energy of the adsorbate ϵ_a, the energies ϵ_k of the metal states, and the adsorbate–metal couplings v_{ak}.

The strength of this model is, as we shall see in the following, that it can be used to attribute parts of the binding to different energy ranges, providing qualitative information which is not easily obtained from a DFT calculation. While DFT calculations themselves can provide accurate results, the self-consistency

procedure eventually results in every quantity depending on every other quantity. What we would like is a simple, more qualitative understanding, which is more easily obtained through a non-self-consistent model.

In the following we will describe a method to extract a Hamiltonian matrix from a DFT calculation using the localized basis set, which can be used within the Newns–Anderson model.

9.2 Newns–Anderson Hamiltonian from DFT

The Hamiltonian matrix calculated in the localized basis set is far from the Newns–Anderson form (9.2). In order to apply the model, we must find a way to transform the matrix.

Suppose we have calculated a Hamiltonian using DFT and apply a "small" perturbation which self-consistently would change both the Hamiltonian, density and wavefunctions. By the force theorem, since both wavefunctions and density are at variational minima, the change in energy due to this perturbation corresponds specifically to the change in Hamiltonian. Thus, from a small perturbation of a self-consistent Hamiltonian we can obtain the changes in adsorption energy knowing only the change in the Hamiltonian.

We will use this to perform a DFT calculation for a combined system including both cluster and adsorbate, then modify this Hamiltonian to obtain expressions for the uncoupled cases.

In the localized basis, the Hamiltonian calculated by DFT will consist of blocks $\mathbf{H}^M, \mathbf{H}^A, \mathbf{H}^{AM}$ and $\mathbf{H}^{MA}$ pertaining to the basis functions on the metal atoms, adsorbate and the interaction:

$$\mathbf{H}_{\mathrm{DFT}} = \begin{bmatrix} \mathbf{H}^M & \mathbf{H}^{AM} \\ \mathbf{H}^{MA} & \mathbf{H}^A \end{bmatrix}. \tag{9.3}$$

The metallic and the atomic submatrices can each be brought on diagonal form by diagonalizing them independently. Since the localized basis set is non-orthogonal, we solve the generalized eigenvalue equations involving also the overlap matrix $S_{\mu\nu}$:

$$\sum_\nu H^M_{\mu\nu} c^M_{\nu k} = \sum_\nu S^M_{\mu\nu} c^M_{\nu k} \epsilon_k, \tag{9.4}$$

$$\sum_\nu H^A_{\mu\nu} c^A_{\nu a} = \sum_\nu S^A_{\mu\nu} c^A_{\nu a} \epsilon_a. \tag{9.5}$$

Since the solutions $c^M_{\nu k}$ and $c^A_{\nu a}$ diagonalize each of the submatrices H^M and H^A, they can be used to transform the interaction blocks H^{AM}_{ak} and S^{AM}_{ak}:

$$v_{ak} = \sum_{a'k'} c^{A*}_{a'a} H^{AM}_{a'k'} c^M_{k'k}, \tag{9.6}$$

$$s_{ak} = \sum_{a'k'} c^{A*}_{a'a} H^{AM}_{a'k'} c^M_{k'k}. \tag{9.7}$$

By now the DFT-based Hamiltonian has been brought on the form (9.2) except for two issues: First of all there are several states on the atom, whereas Eq. (9.2) only allows one. We will assume that each of the atomic states hybridizes

independently, resulting in a separate Hamiltonian for each such state. This method has been used previously to describe the interaction of several molecular orbitals with metal surfaces. Second, the basis functions on the atom have an overlap $s_{ak} = \langle a|k\rangle$ with the metal states. Grimley has solved this problem in a non-orthogonal basis, and that approach will be used in the following.[109]

9.3 Binding energy from Newns–Anderson

The energy of the uncoupled metal can be written in terms of the metallic density of states $\rho(\epsilon)$, as an integral up to the Fermi level

$$E = 2\int_{-\infty}^{\epsilon_F} \rho(\epsilon)\epsilon \,\mathrm{d}\epsilon, \tag{9.8}$$

where the factor 2 denotes spin-degeneracy. Suppose now that a single atomic state couples to the metal surface, causing a change $\delta\rho(\epsilon)$ in the density of states. The change in energy can then be obtained by integrating $\delta\rho(\epsilon)\epsilon$ over the occupied states, except care must be taken to ensure that the right number of electrons is counted in this integration. First of all the adsorbate contributes a number n_a of electrons (probably 1 or 2), whose initial energy $n_a\epsilon_a$ must be subtracted. These electrons are deposited at the Fermi level ϵ_F.

Consider the integral of the induced density of states

$$\Delta N = \int_{-\infty}^{\epsilon_F} \delta\rho(\epsilon)\,\mathrm{d}\epsilon. \tag{9.9}$$

This is the number of states that have, by the chemisorption event, been introduced below the Fermi level. If this is nonzero, a number of electrons will have moved from the Fermi level down into these newly available states. Thus, a number $2\Delta N$ (counting spin) of electrons has been removed from the Fermi level. Taking these electron counting corrections into account, the adsorption energy can be written as

$$E_{\mathrm{ads}} = 2\int_{-\infty}^{\epsilon_F} \delta\rho(\epsilon)\epsilon \,\mathrm{d}\epsilon - 2\Delta N\epsilon_F + n_a(\epsilon_F - \epsilon_a). \tag{9.10}$$

The induced density of states, and thus the energy, can be calculated using Green's functions. The theory behind this will be briefly sketched next.

The Green's operator $\hat{G}(z)$ is defined for some Hamiltonian $\hat{H}$ by

$$(z - \hat{H})\hat{G}(z) = \hat{I}, \tag{9.11}$$

where $z = \epsilon + i\lambda$ is a complex number. The retarded Green's function is defined by taking the limit $\lambda \to 0+$, which will be implicit in all expressions from now on. With this convention, the matrix element $G_\alpha(\epsilon) \equiv \langle\alpha|\hat{G}(\epsilon)|\alpha\rangle$ corresponding to some state $|\alpha\rangle$ is related to the projected density of states $\rho^\alpha(\epsilon)$ through*

$$\mathrm{Im}\,\langle\alpha|\hat{G}(\epsilon)|\alpha\rangle = -i\pi\rho^\alpha(\epsilon). \tag{9.12}$$

*This uses the relation $\lim_{\lambda\to 0}\frac{1}{x+i\lambda} = \frac{\mathcal{P}}{x} - i\pi\delta(x)$, where $\mathcal{P}$ is the Cauchy principal value, known from complex analysis.

Therefore the full density of states can likewise be obtained from the trace as $\operatorname{Im}\operatorname{Tr}\hat{G}(\epsilon)$, allowing us to actually calculate binding energies. We need to calculate the Green's function $\hat{G}(\epsilon)$ of the combined system in order to be able to integrate the induced density of states and obtain a binding energy, a task which is made more complicated by the fact that the basis is non-orthogonal.

By making use of the projection operator for non-orthogonal basis sets, (4.13), the matrix elements of (9.11) are

$$\sum_{\xi\lambda} \langle\Phi_\mu|\epsilon - \hat{H}|\Phi_\xi\rangle\, S^{-1}_{\xi\lambda}\, \langle\Phi_\lambda|\hat{G}(\epsilon)|\Phi_\nu\rangle = \langle\Phi_\mu|\Phi_\nu\rangle = S_{\mu\nu}, \tag{9.13}$$

and hence in matrix notation

$$(\epsilon\mathbf{S} - \mathbf{H})\tilde{\mathbf{G}}(\epsilon) = \mathbf{I}, \quad \tilde{\mathbf{G}}(\epsilon) = \mathbf{S}^{-1}\mathbf{G}(\epsilon)\mathbf{S}^{-1}, \tag{9.14}$$

where $\tilde{\mathbf{G}}(\epsilon)$ is the usual non-orthogonal Green's function.[110] This can be rewritten as a perturbation series

$$\tilde{\mathbf{G}}(\epsilon) = \mathbf{G}^0(\epsilon) + \mathbf{G}^0(\epsilon)\mathbf{X}(\epsilon)\tilde{\mathbf{G}}(\epsilon), \tag{9.15}$$

with $\mathbf{G}^0(\epsilon)$ being the known Green's function of the uncoupled system, and

$$\mathbf{X}(\epsilon) = \mathbf{V} - \epsilon\mathbf{s}, \quad \mathbf{S} = I + \mathbf{s}. \tag{9.16}$$

Then $\mathbf{X}(\epsilon)$ contains only elements that couple between adsorbate and metal. Using the perturbation series, all matrix elements G_a, G_k, G_{ka}, G_{ak} are relatively straightforward to write down. With this change, the remaining part of the calculation mostly resembles the non-orthogonal case,[108] where the binding energy (9.10) becomes an integral

$$E_{\text{ads}} = \frac{2}{\pi}\int_{-\infty}^{\epsilon_F} \eta(\epsilon)\,\mathrm{d}\epsilon + n_a(\epsilon_F - \epsilon_a) \tag{9.17}$$

over a *phase shift* $\eta(\epsilon)$ calculated from the real and imaginary parts $\Lambda(\epsilon)$ and $\Delta(\epsilon)$ of the self-energy:

$$\tan\eta(\epsilon) = \frac{\Delta(\epsilon)}{\epsilon - \epsilon_a - \Lambda(\epsilon)}. \tag{9.18}$$

These functions are given by

$$\Delta(\epsilon,\epsilon') = \sum_k |X_{ak}(\epsilon)|^2\delta(\epsilon' - \epsilon_k), \tag{9.19}$$

$$\Lambda(\epsilon) = \mathcal{P}\!\int_{-\infty}^{\infty} \frac{\Delta(\epsilon,\epsilon')}{\epsilon - \epsilon'}\,\mathrm{d}\epsilon', \tag{9.20}$$

with the short-hand $\Delta(\epsilon) = \Delta(\epsilon,\epsilon)$.[109] The notation $\mathcal{P}\!\int$ refers to the Cauchy principal value. The ϵ and ϵ'-dependent factors in $\Delta(\epsilon,\epsilon')$ can be calculated directly from the couplings of the transformed DFT Hamiltonian and overlap matrix, and used to evaluate the rest of the quantities.

The phase shift $\eta(\epsilon)$, which determines the entire chemisorption energy except for the charge transfer terms, is related to the *cumulative induced DOS*

$$N(\epsilon) = \int_{-\infty}^{\epsilon} \delta\rho(\epsilon')\,\mathrm{d}\epsilon' = -\frac{\eta(\epsilon)}{\pi} \tag{9.21}$$

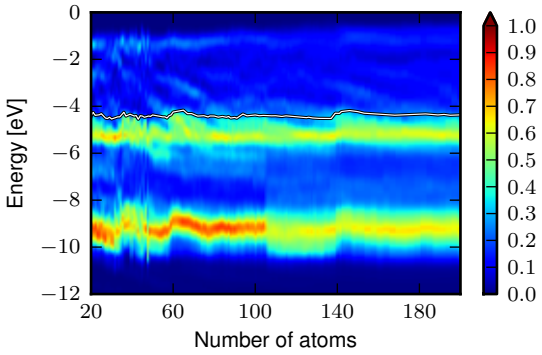

Figure 9.1: *PDOS (arb. units) for O on Au clusters as a function of energy and cluster size. The Fermi level is indicated. The most visible changes, such as the one at $N \approx 105$, happen when the local facet is modified. However the impact on binding energy is small compared to that of shell structure.*

The projected density of states on the adsorbate, which will be used in the following, can be calculated from

$$\rho_a(\epsilon) = \frac{\Delta(\epsilon)}{(\epsilon - \epsilon_a - \Lambda(\epsilon))^2 + \Delta^2(\epsilon)}. \tag{9.22}$$

9.4 Influence of d-band

Before using the full non-orthogonal model on DFT Hamiltonians, we can obtain a qualitative understanding of this model by playing around with a simple chemisorption function. The overall reactivity of different metals is well described by the d-band model, which attributes the variations to the position or filling of the d-band.

To do this we must choose the adsorbate level ϵ_a and the chemisorption function $\Delta(\epsilon)$. We will choose these values such that the projected density of states (PDOS) on the adsorbates match those calculated with DFT. Figure 9.1 shows the PDOS on the atomic basis functions of O using (4.15). The O states split into states on either side of the d-band, which can be understood as bonding and antibonding. The PDOS does not qualitatively change with cluster size, although some variations are seen near the magic numbers. In all cases, the antibonding states are largely occupied.

Assume first that the adsorbate couples to an idealized metallic s-band and d-band, where the coupling to each band can be approximated as semielliptic contributions $V_s^2\rho_s(\epsilon)$ and $V_d^2\rho_d(\epsilon)$ to $\Delta(\epsilon)$, where $\rho_s(\epsilon)$ and $\rho_d(\epsilon)$ integrate to 1. Thus

$$\Delta(\epsilon) = \pi V_s^2 \rho_s(\epsilon) + \pi V_d^2 \rho_d(\epsilon). \tag{9.23}$$

V_s and V_d determine the coupling strength. s and d bandwidths are chosen to roughly match those of real Au. On Figure 9.2a, $\Delta(\epsilon)$ (full lines) and corresponding $\Lambda(\epsilon)$ (broken lines) are shown for two different choices of semielliptic d-band.

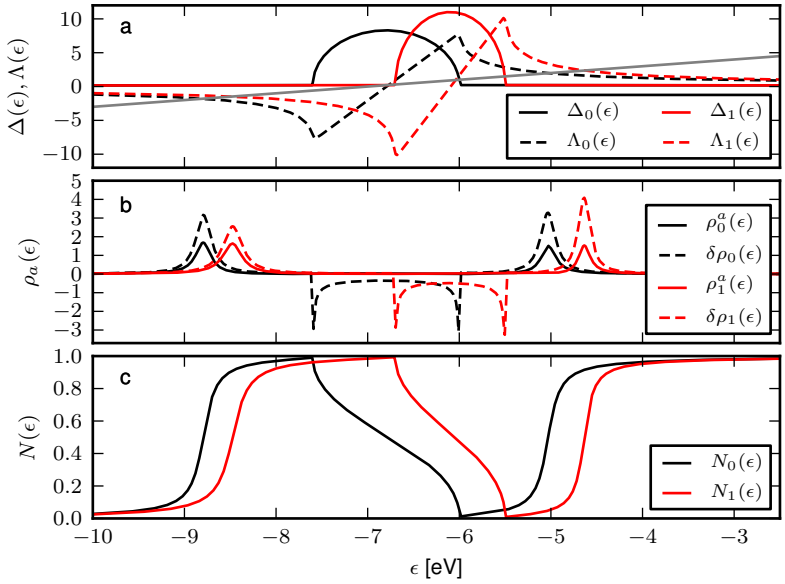

Figure 9.2: *(a) Two choices of semielliptic $\Delta(\epsilon)$ (full lines) and resulting $\Lambda(\epsilon)$ (broken lines). Bonding and antibonding states appear at intersections between $\Lambda(\epsilon)$ and the shown line $\epsilon - \epsilon_a$. (b) The projected density of states on the adsorbate showing bonding and antibonding states. (c) The cumulative induced DOS $N(\epsilon)$. (d) The adsorption energy as a function of the location of the Fermi level. If the Fermi level is located above the antibonding PDOS peak, d-band location no longer affects adsorption energy.*

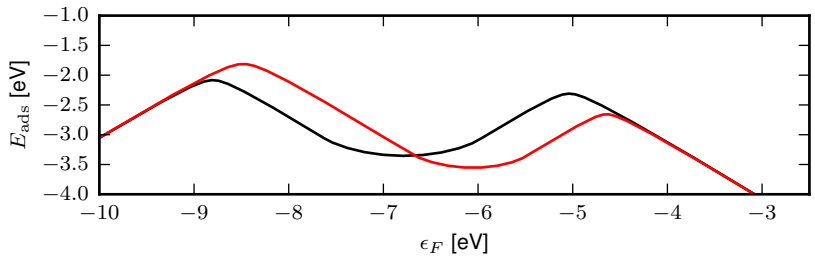

Figure 9.3: *Binding energy as a function of Fermi level for two different d-band locations.*

One represents an ordinary Au surface while the other is shifted higher in energy and made more narrow, representing e.g. an undercoordinated site such as may be found on a cluster. The adsorbate energy level is set to $\epsilon_a = -7\,\mathrm{eV}$.

The coupling results in two states with the PDOS shown on Figure 9.2b. They correspond to clear bonding and antibonding states broadened into resonances by the s-band. Also shown is the induced DOS $\delta\rho(\epsilon)$. The bonding and antibonding states are, together and counting spins, capable of accepting four electrons. However a single state is eliminated from within the d-band, so that a total of only two extra electrons is induced. The cumulative induced DOS is shown on Figure 9.2c.

We can now calculate the binding energy, shown on Figure 9.3 as a function of the Fermi level. Clusters close to a magic-number cluster will presumably have almost the same chemisorption function, and vary only by having different Fermi levels. Considering the variation of the energy as a function of Fermi level therefore corresponds to the transition past a magic number. Since the Fermi level is located at approximately $-4.5\,\mathrm{eV}$ for Au, the binding energy varies with the Fermi level but is locally independent of the location and width of the d-band. In fact, in this simple case, *the location of the d-band affects the adsorption energy only if the Fermi level lies between the bonding and the antibonding states.*

This variation of binding energy with Fermi level agrees with the behaviour of O on Au clusters close to magic numbers. The adsorption of an O atom with two empty p-states creates states below the Fermi level that can accept two electrons in total. These two electrons are removed from the Fermi level, and therefore an increase of the Fermi level corresponds to an increase in adsorption energy by twice as much. An analysis of the occupation of the O p-states (using the DOS expression in terms of the basis functions, (4.15)) reveals that the effect of increasing the Fermi level on the cluster is not to transfer significantly more charge to the atom. Instead the increase in binding due to a higher Fermi level happens because the electrons which would *anyway* be going from the Fermi level into the induced states, can now do so from a higher-lying Fermi level.

9.5 Main-group elements

We now use the full non-orthogonal model with DFT Hamiltonians. Consider O as a first example. A DFT calculation is performed on one of the previously

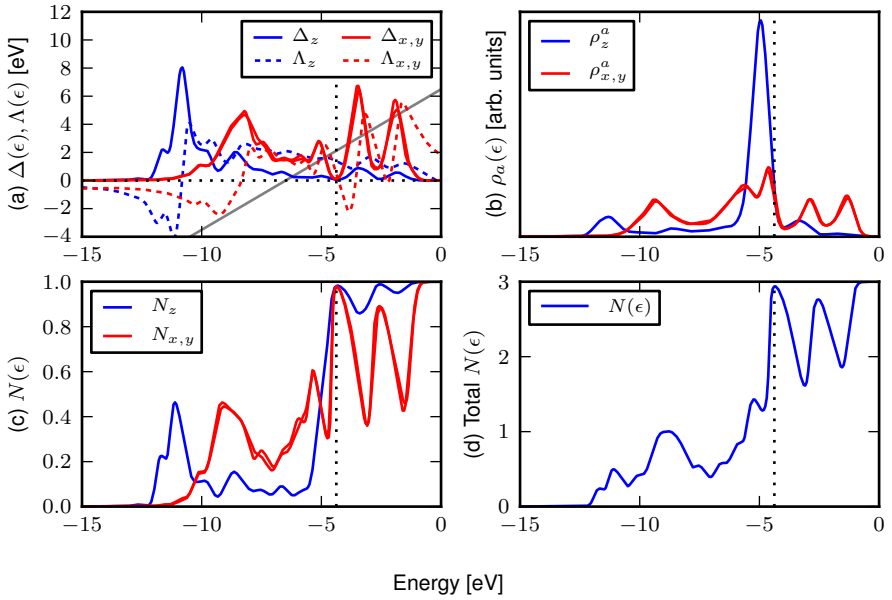

Figure 9.4: *Newns–Anderson model applied to O on Au_{58}. (a) $\Delta(\epsilon)$ and $\Lambda(\epsilon)$ for the three p states, with x and y being almost identical. The grey line is $\epsilon - \epsilon_a$ (ϵ_a of the three states lie close). The Fermi level is indicated. (b) PDOS. (c) Cumulative induced DOS for each state. Total cumulative induced DOS $N(\epsilon) = N_x(\epsilon) + N_y(\epsilon) + N_z(\epsilon)$.*

relaxed Au_{58} clusters with O adsorbed on it. The DFT calculation uses the usual parameters, except we use only a single-ζ basis set for the atoms such that we only have functions for the actual atomic orbitals. From this calculation we export the overlap matrix and Hamiltonian and calculate chemisorption function and other quantities. We consider only the 2p states.

$\Delta(\epsilon)$ and $\Lambda(\epsilon)$ are shown on Figure 9.4a for the p_z state (blue) and the p_x and p_y states (red), which are degenerate and have the same coupling. The p_z state couples strongly in the region $\epsilon \approx -11\,\text{eV}$ while the two other states couple to higher energies, including the two peaks above the Fermi level that correspond to electronic shells. The resulting PDOS (Figure 9.4b) shows a clear state just below the Fermi level, like previously in Figure 9.1. Note that the exact behaviour of the PDOS above the Fermi level may not be realistic, as the atomic basis set is not well suited for higher-lying unbound states, and because the PDOS plotted here is based on (9.22) which does not account for non-orthogonality. The PDOS therefore does not cannot represent numbers of electrons, but does show in a sense the presence of states. Higher-lying peaks are generally exaggerated due to this effect.

The cumulative induced DOS $N(\epsilon)$ for each of the states is shown on Figure 9.4c. They behave in a manner consistent with the simple model considered previously: The additional states introduced into the spectrum with the bonding

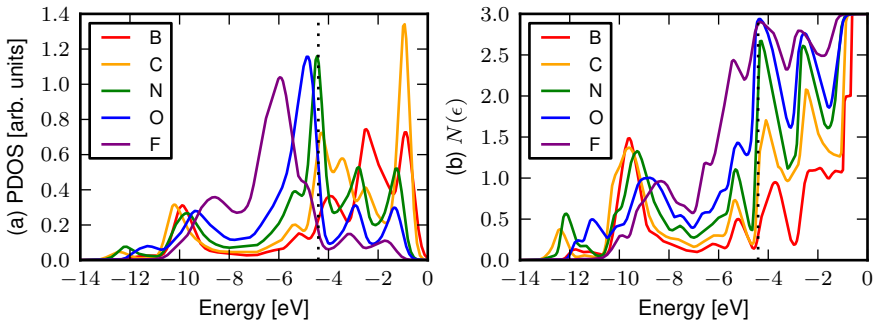

Figure 9.5: *(a) PDOS calculated as a sum over p_x, p_y and p_z for elements B–F. Splitting of the adsorbate state generally decreases with 2p filling. (b) Total $N(\epsilon)$ of the three 2p states for each of the elements B–F.*

peaks are cancelled out by the elimination of metallic states, so that the $N(\epsilon)$ remains low e.g. at $\epsilon = -7.5\,\text{eV}$. The antibonding states, however, all lie below the Fermi energy which means a total of three extra states have been introduced in the spectrum below the Fermi level. The four electrons from O fill only two of these, and thus two electrons can be moved from the Fermi level down to the induced states. Increasing the Fermi level would thereby increase binding by twice that amount. The hybridization of each state with the unfilled electronic shells above the Fermi level can be understood as a slight movement of the states within the electronic shells. If the Fermi level had been located within these, the relationship between Fermi level and adsorption energy would have been more complicated. Thus, the simple relationship exists only because of the gap at the Fermi level. Figure 9.4d shows the sum of the cumulative induced DOS for each state, which therefore reaches 3.

Figure 9.5 shows the behaviour for the 2p elements B–F. The PDOS (Figure 9.5a) very high splitting between bonding and antibonding states for B, decreasing towards F which has only a fully occupied resonance peak. The filling of antibonding states is normally taken as the primary reason why Au binds adsorbates weakly. It is seen here that it is really $N(\epsilon)$ which contains all quantitative information, and from which conclusions can be drawn.

Finally the PDOS and $N(\epsilon)$ for H and Li are shown on Figure 9.6. Li induces a state above the Fermi level from which one electron is contributed, consistently with expectations. The H coupling is so strong that a low-lying bonding state appears at$-12\,\text{eV}$, the bottom of the s-band (a similar effect has been described in Ref. 111, while the antibonding state is above the Fermi level. Since one state is eliminated from the metallic DOS (at approximately $-10\,\text{eV}$), the total induced DOS up to the Fermi level integrates to approximately zero. The electron introduced by H therefore effectively goes on top of the Fermi level, explaining why it behaves like Li.

In conclusion, we understand from this model that the shift in adsorption energy across a magic number can be positive or negative depending on whether states are induced above or below the Fermi level. If excess states are introduced below the Fermi level, the increase in Fermi level associated with a magic

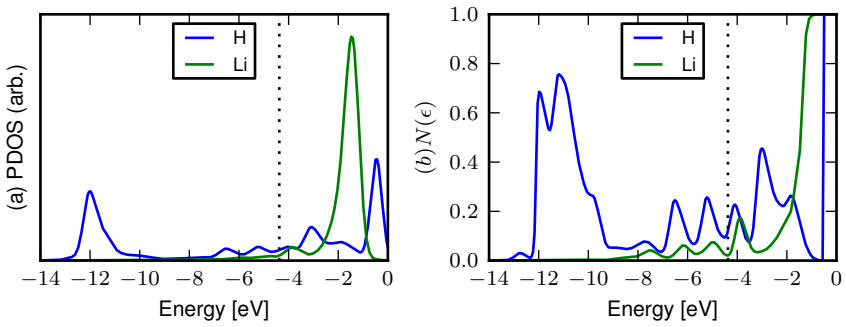

Figure 9.6: *(a) PDOS of H and Li (b) Cumulative induced DOS.*

number will allow electrons to transfer from the higher Fermi level, leading to stronger adsorption. If states are introduced above the Fermi level, the electrons controbuted by the atom must be deposited onto the Fermi level, instead leading to weaker adsorption. The case of hydrogen is explained by a strong splitting with the introduction of a low-lying bonding state far below the Fermi level, but the elimination of effectively one state from the metal below the Fermi level. Therefore hydrogen behaves like Li, though a more appropriate picture is that of a covalent bond.

Chapter 10

Electronic structure and geometry

Until now we have considered Au clusters which are based on regular structures. While these structures make it easy to compare adsorption energies since the local geometry around the adsorbate can be retained across different cluster sizes, it is not certain how well our conclusions apply to clusters with realistic structures. As previously mentioned, small Au clusters in particular form quite varied structures that are far from the regular structures considered previously. Optimizations of cluster structures based on ab-initio methods with the objective of finding the globally optimal structures are prohibitively expensive in the range of cluster sizes we are considering. However if our objective is to obtain a qualitative idea about the behaviour of real clusters (or even a realistic idea, given that finite-temperature ensembles will naturally consist of mixtures), then the exact determination of strict lowest-energy structures is not essential. In the following we perform simulated annealings on Au clusters using the simple EMT potential[112,113] implemented in ASAP,[114] and then with DFT using the localized basis sets.

10.1 Molecular dynamics

We will in the following use simulated annealing within molecular dynamics (MD) as a means to globally optimize structures. This method simulates that a collection of atoms is cooled down from above its melting point until it completely freezes, allowing the atoms to gradually arrange themselves the same way they would in nature. There exist much more efficient global optimization algorithms than simulated annealing, but since this method simulates a physical process, it will be guaranteed to produce structures which are at least in some sense physical. We acknowledge that due to the limited annealing employed here, there is a possibility that the determined shapes of clusters may be more like those found at higher temperatures. In particular the creation of regular lattices is disfavoured by this procedure.

MD simulations solve Newton's equations of motion for the atomic positions as a function of time. This requires subsequent calculations of the forces on each atom to update momenta and positions, and will preserve the total energy

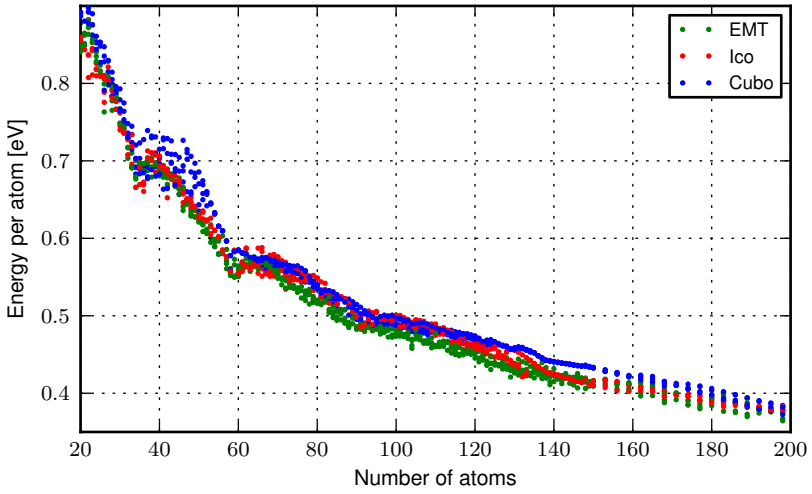

Figure 10.1: *Energy per atom of Au clusters with different structural motifs.*

of the system, but not necessarily the temperature which it is more desirably for us to control. The temperature can be regulated or fixed by applying an artificial adjustment of atomic velocities on each iteration. Such a correction is called a *thermostat*. Here we use Langevin dynamics, adding a first-order damping term to Newton's equations, which for each iteration slightly adjusts the temperature towards the desired value.

10.2 Simulated annealing with EMT

For clusters of 6–200 atoms we perform a simulated annealing using the empirical potential in the ASAP code.[114] Since this is a classical potential, we would expect it to favour atomic packing. The potential makes no reference to the concept of electrons, so the electronic structure for this series of clusters will strictly be a function of the geometric packing. The simulated annealing is performed from a starting temperature above the bulk melting point, down to 200 K. The temperature is lowered by 1 K for each 600 MD steps. After the annealing we perform a DFT structure optimization using the localized basis set to obtain spectrum and energies.

Figure 10.1 compares the energies of structures obtained with EMT to those of the regular cuboctahedra and icosahedra generated by the procedure from Chapter 8. The EMT structures generally have the lowest energies, with icosahedra being favourable to cuboctahedra within this size range. The magic numbers 34, 58 and 92 are clearly visible as kinks with particularly low energies for all types of clusters.

Figure 10.2 shows the spectra, with shell structures in agreement with those found in previous chapters. For comparison, a similar series of Pt clusters is shown. Jumps in the Fermi level of Au stop beyond 92 atoms due to the reduced regularity compared to the icosahedra and cuboctahedra, although shell

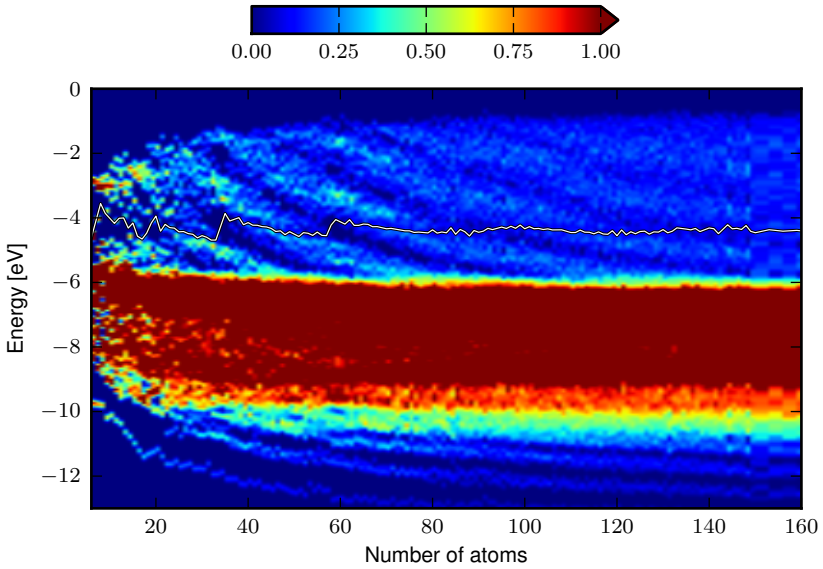

Figure 10.2: *DOS of Au clusters obtained by simulated annealing using EMT. The white line indicates the Fermi level.*

structure as a whole persists longer.

10.3 First-principles global optimization

Due to the prodigious amount of calculations necessary, we have to make certain sacrifices of numerical precision. Several parameters lend themselves for such compromise. The annealing process itself can be shortened, the time step increased, and the temperature range narrowed. Also the DFT parameters can be sacrificed: most importantly the grid spacing and basis set quality. The amount of vacuum surrounding the cluster must however be kept high to prevent systematically biasing compact structures. The choices described below are based on test runs for clusters about 30 atoms in size with the specific objective of determining the coarsest parameters that still yield a sane behaviour.

An MD simulation aiming for realism might use a time step of only a few fs. Higher time steps make it difficult to ensure energy conservation because of the large atomic movements with every step. We choose to increase the time step and leave it to the thermostat to damp any energy instabilities by using a high friction coefficient of 0.06 with the Langevin implementation of ASE. Tests with the EMT potential have revealed that with a time step larger than about 30 fs, atoms will be randomly ejected from the cluster at high speed due to the poor detailed description of collisions. We have therefore chosen a time step of 24 fs, which does not exhibit such behaviour even during long simulations.

We choose the EMT-optimized clusters as starting points for the DFT annealing. The temperature must be high enough, and the number of MD steps large enough, for the end result to be independent of the initial structure. Au clusters melt at considerably lower temperatures than bulk Au. The thermodynamics of clusters have been investigated in many works, mostly based on MD

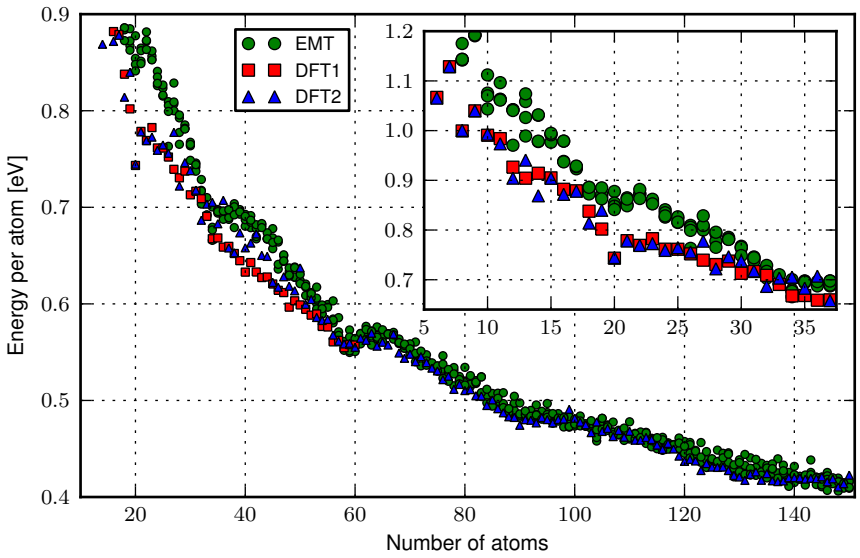

Figure 10.3: *Energy per atom for clusters obtained with simulated annealing with DFT and EMT. Inset: Magnified view of smaller clusters.*

simulations with empirical potentials.[61,115] The largest cluster we optimize has 150 atoms and melts at around 625 K,[63] so we start the annealing at 750 K and end it at 300 K. The temperature is high enough to entirely remodel the surface structure in all cases.

Two series of MD annealings are performed:

- A "high-quality" series for N=6–60 with grid spacing 0.24 Å and the standard dzp basis set. The temperature is lowered by 1 K every $5 + N/2$ MD steps.
- A "low-quality" series for N=6–150 with grid spacing 0.25 Å, and a basis set which excludes the d-type split-valence wavefunction. The temperature is lowered by 1 K every 20 MD steps.

Tests with further reduced basis set or grid quality tend to yield some highly picturesque structures, albeit of little scientific value. At the end of the annealing procedure, a structure relaxation is performed with the standard DFT parameters.

Many of the clusters exhibit recognizable structural motifs. The clusters with 6–9, 12 and 13 atoms are found to be planar. The clusters from 19–23 atoms consist of the extraordinarily stable Au_{20} tetrahedron[78,116,117] plus or minus a few atoms. Several of the larger clusters involve structures suggestive of tetrahedra in spite of many structural irregularities. The energy per atom as a function of the number of atoms is shown on Figure 10.3, comparing the two series of annealed clusters with the four previous series obtained from EMT. The small DFT-based clusters are, as can be expected, far lower in energy than those of EMT. The difference is smaller for larger clusters, where the short DFT annealing times are expected to produce many imperfections*.

*An extremely long EMT annealing yields energies that are better than the DFT-based

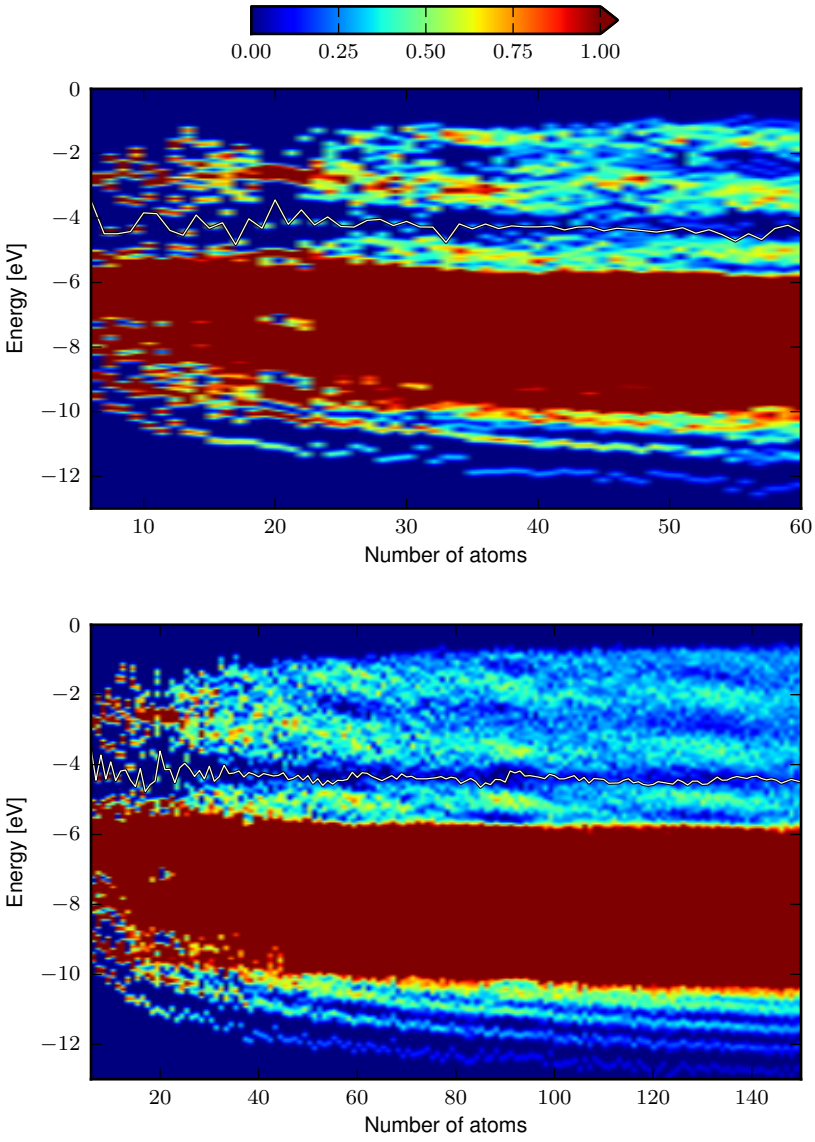

Figure 10.4: *DOS of Au clusters obtained by simulated annealing. The white line indicates the Fermi level.*

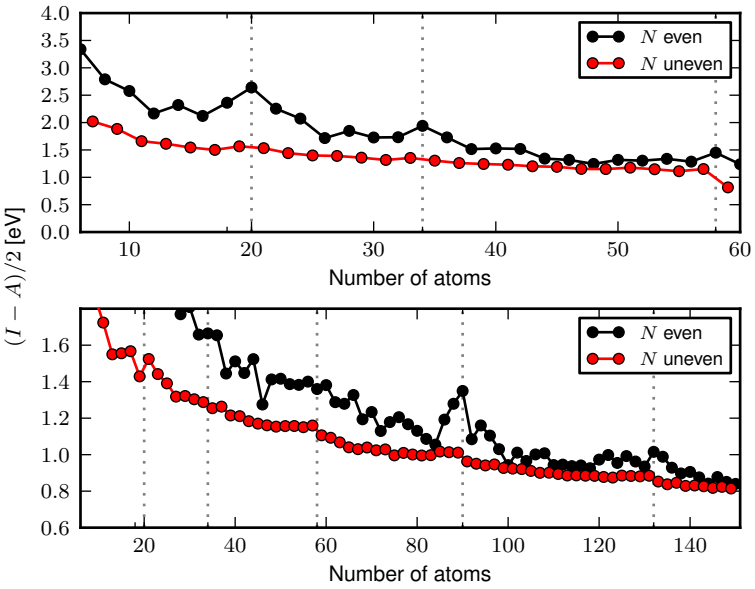

Figure 10.5: *Gaps, calculated as chemical hardness. This is the difference* $(I - A)/2$ *in ionization potential, for the two series of DFT structures. Top: The 6–60-atom series. Bottom: The 6–150-atom series. For clarity, separate graphs for even and uneven clusters are shown. The dotted lines indicate the magic numbers 20, 34, 58, 90 and 132. The last two magic numbers differ from the usual major spherical jellium shell closings.*

Figure 10.4 shows the DOS as a function of cluster size and energy for the 6–60-atom series (top) and the 6–150 series (bottom). The optimization procedure tends to yield large gaps not only at the magic-number clusters, but for almost *every* cluster. For uneven-numbered clusters, the half-filled state at the Fermi level is located in the middle of a gap between fully occupied and fully empty states. The same phenomenon has been found for other monovalent clusters.[82,118–120] The creation of such a gap is consistent with the *principle of maximum hardness*.[121,122] The energy is lowered by pushing all occupied states down, while unoccupied states are pushed up at no cost. The principle behind Jahn–Teller deformations is in many ways similar. Of particular note is the qualitative feature of the DOS that the electronic shells stay at constant energy levels for all sizes, rather than move continuously down as seen for the EMT structures and regular geometries. The shell structure is greatly enhanced close to the magic numbers, resolving here into the same bands as in EMT-based or regular structures.

Figure 10.5 shows the gaps of the clusters calculated as a difference between

clusters from about 80 atoms, although the DFT clusters still prevail close to the magic numbers 92 and 138. However this procedure yields *worse* energies than those of the EMT annealings presented here for most smaller clusters. The structures obtained in this range from long annealing times are generally decahedral, with icosahedra close to $N = 147$

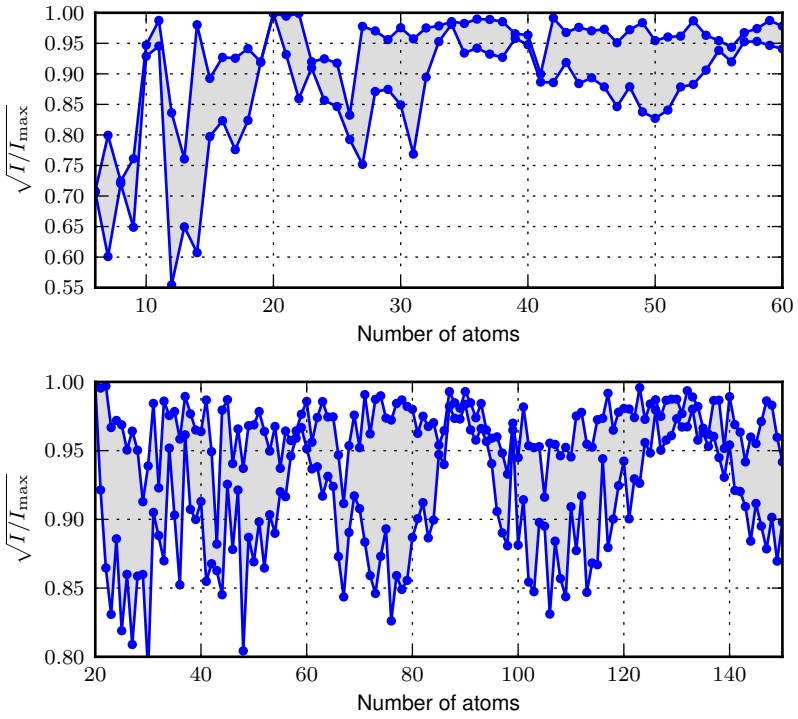

Figure 10.6: *Ratios of moments of inertia for the 6–60 (top) and 6–150 series (bottom) of DFT-annealed Au clusters. The area between the larger and the smaller moments is shaded for clarity.*

states of charge +1 and −1. This reveals that the real magic numbers of these structures are, surprisingly, 90 and 132 rather than the expected 92 and 138. Both 90 and 132 are minor spherical shell closings of the simple jellium model presented in Chapter 6, differing by an s orbital and a p orbital from the subsequent major shell closings. There are strong odd–even alternations due to the half-filled state for uneven clusters. These are well-known from a multitude of theoretical models.[123,124] The alternations can exist as long as the creation of a gap is possible, implying that they may be found in larger clusters as well. Alternations have been also shown in molecular adsorption energies for small clusters.[125–127]

Structural trends of the optimized clusters are revealed by considering their moments of inertia. For each cluster we calculate the three principal moments of inertia, $I_1 \leq I_2 \leq I_3$. Figure 10.6 shows the quantities $\sqrt{I_1/I_3}$ and $\sqrt{I_2/I_3}$ as a function of cluster size for the two series of clusters. Large deformations are characterized by large deviations of either ratio from 1. Small deformations indicate spherical or otherwise symmetric structures such as the Au_{20} tetrahedron. These deformations are similar to the well-known distortions of jellium clusters,[74] and can also emerge from tight-binding models.[118] The deformation due to shell structure is however a fundamentally non-local phenomenon which cannot be accounted for using simple atomic potentials. Recall from Figure 10.3 how the EMT potential generates structures of about the same energy as

DFT *near magic numbers*, while the intermediate EMT-structures, particularly between 34 and 58 atoms, are systematically higher in energy. Shell structure effects are essential to the determination of correct geometries of clusters well above hundred atoms in size.

Chapter 11

Conclusion

A localized basis set implementation in GPAW has been presented which provides a very efficient alternative to the real-space code, as demonstrated by most of the results presented later in this work. More systematic testing of further of basis sets beyond dzp is desirable in the future. $\mathcal{O}(N)$ or other low-scaling methods would also be a logical next step to improve performance on systems beyond 200–300 atoms.

Using the real-space representation of GPAW, we have performed large-scale DFT calculations on Au and Pt clusters with up to 1415 atoms using 65536 cores on the BlueGene/P supercomputer at Argonne National Laboratory. From these calculations it appears that the size-dependent chemical properties of clusters, as measured by adsorption of O and CO, roughly converge with size at 600 atoms for Au and 200 atoms for Pt, although small variations within 0.1 eV of the bulk limit exist. The tendency of small clusters to bind more strongly can to some extent be understood as a geometric effect attributable to small facet sizes, although variations of adsorption energy on Au do not correlate with geometry because of profound electronic effects.

Using the basis set code, we have studied the trends in adsorption energy of atomic adsorbates on full ranges of Au cuboctahedron-based clusters, usually up to 200 atoms. It is revealed that electronic size effects relating to the jellium-like electronic structure entirely dominates the chemical properties of noble-metal clusters in this size range, with oscillations in adsorption energy on the order of 1 eV depending on adsorbate. While the DOS of the d-states varies little beyond 50 atoms, the s-states split into electronic subshells that fill one by one as cluster size increases. From calculations with several different atomic adsorbates, Au clusters can be categorized as alkali-like, noble or halogen-like depending on their number of atoms relative to magic numbers. At a magic number, the Fermi level jumps across the electronic gap into the next electronic shell, from which it is more easily donated to an adsorbate.

Transition metal clusters of Ru, Rh, Pd and Pt exhibit similar shell structure of the s-electrons, but the Fermi level is lodged within the d-band preventing any significant variation. Adsorption energies on such clusters therefore show no trace of shell structure. The main variation in binding energy on these clusters stops around 50–60 atoms when facets are sufficiently large that the local geometry around the adsorbate does not change anymore.

Using a Newns–Anderson model, we have found that the abrupt variations

of adsorption energy at magic numbers can be understood from the location of adsorbate-induced states within the cluster relative to the Fermi level. For adsorbates that induce states only below the Fermi level, electrons will be transferred from the Fermi level down into the induced states, such that variations of the Fermi level directly correspond to variations of the adsorption energy. Adsorbates that only induce states above the Fermi level have the opposite behaviour. H displays a more complex behaviour, where a bonding state well below the Fermi level is cancelled by the elimination of one state from the cluster, which implies that H effectively adds an electron to the cluster.

We have performed simulated annealings of Au clusters with DFT using very coarse parameters. The shell structure is similar to the previously considered structures near the magic numbers, but differs markedly away far from magic numbers. Electronic gaps at the Fermi level are created for all clusters up to 150 atoms, which is the maximum size studied. The opening of gaps is facilitated by large geometric deformations of the clusters, with magic-number clusters being spherical and other clusters being mostly oblate. The complex relationship between electronic and geometric effects persists with deformations of 10–15% well beyond 100 atoms.

Bibliography

[1] P. Hohenberg and W. Kohn, "Inhomogeneous electron gas," *Phys. Rev.*, vol. 136, pp. B864–B871, Nov 1964.

[2] W. Kohn and L. J. Sham, "Self-consistent equations including exchange and correlation effects," *Phys. Rev.*, vol. 140, pp. A1133–A1138, Nov 1965.

[3] P. E. Blöchl, "Projector augmented-wave method," *Phys. Rev. B*, vol. 50, pp. 17953–17979, Dec 1994.

[4] P. E. Blöchl, C. J. Först, and J. Schimpl, "Projector augmented wave method: ab initio molecular dynamics with full wave functions," *Bulletin of Materials Science*, vol. 26, pp. 33–41, Jan. 2003.

[5] J. J. Mortensen, L. B. Hansen, and K. W. Jacobsen, "Real-space grid implementation of the projector augmented wave method," *Phys. Rev. B*, vol. 71, p. 035109, JAN 2005.

[6] J. Enkovaara, C. Rostgaard, J. J. Mortensen, J. Chen, M. Dułak, L. Ferrighi, J. Gavnholt, C. Glinsvad, V. Haikola, H. A. Hansen, H. H. Kristoffersen, M. Kuisma, A. H. Larsen, L. Lehtovaara, M. Ljungberg, O. Lopez-Acevedo, P. G. Moses, J. Ojanen, T. Olsen, V. Petzold, N. A. Romero, J. Stausholm-Møller, M. Strange, G. A. Tritsaris, M. Vanin, M. Walter, B. Hammer, H. Häkkinen, G. K. H. Madsen, R. M. Nieminen, J. K. Nørskov, M. Puska, T. T. Rantala, J. Schiøtz, K. S. Thygesen, and K. W. Jacobsen, "Electronic structure calculations with GPAW: a real-space implementation of the projector augmented-wave method," *Journal of Physics: Condensed Matter*, vol. 22, no. 25, p. 253202, 2010.

[7] A. H. Larsen, M. Vanin, J. J. Mortensen, K. S. Thygesen, and K. W. Jacobsen, "Localized atomic basis set in the projector augmented wave method," *Phys. Rev. B*, vol. 80, p. 195112, Nov 2009.

[8] E. Artacho, D. Sanchez-Portal, P. Ordejon, A. Garcia, and J. M. Soler, "Linear-scaling ab-initio calculations for large and complex systems," *arXiv:cond-mat/9904159*, Apr. 1999.

[9] J. M. Soler, E. Artacho, J. D. Gale, A. García, J. Junquera, P. Ordejón, and D. Sánchez-Portal, "The SIESTA method for ab initio order- n materials simulation," *Journal of Physics: Condensed Matter*, vol. 14, pp. 2745–2779, Mar. 2002.

[10] J. Chen, J. S. Hummelshøj, K. S. Thygesen, J. S. Myrdal, J. K. Nørskov, and T. Vegge, "The role of transition metal interfaces on the electronic transport in lithium–air batteries," *Catalysis Today*, vol. 165, no. 1, pp. 2 – 9, 2011.

[11] P. Pyykkö, "Theoretical chemistry of gold," *Angewandte Chemie International Edition*, vol. 43, no. 34, p. 4412–4456, 2004.

[12] P. Pyykkö, "Theoretical chemistry of gold. II," *Inorganica chimica acta*, vol. 358, no. 14, p. 4113–4130, 2005.

[13] P. Pyykkö, "Theoretical chemistry of gold. III," *Chemical Society Reviews*, vol. 37, no. 9, p. 1967–1997, 2008.

[14] P. Pyykkö and J. P. Desclaux, "Relativity and the periodic system of elements," *Accounts of Chemical Research*, vol. 12, no. 8, pp. 276–281, 1979.

[15] P. Pyykkö, "Relativistic effects in structural chemistry," *Chem. Rev.*, vol. 88, no. 3, pp. 563–594, 1988.

[16] H. Schmidbaur, S. Cronje, B. Djordjevic, and O. Schuster, "Understanding gold chemistry through relativity," *Chemical Physics*, vol. 311, pp. 151–161, Apr. 2005.

[17] H. Grönbeck and P. Broqvist, "Comparison of the bonding in Au_8 and Cu_8: A density functional theory study," *Phys. Rev. B*, vol. 71, p. 073408, Feb 2005.

[18] L. Xiao and L. Wang, "From planar to three-dimensional structural transition in gold clusters and the spin–orbit coupling effect," *Chemical Physics Letters*, vol. 392, no. 4-6, pp. 452 – 455, 2004.

[19] E. M. Fernández, J. M. Soler, and L. C. Balbás, "Planar and cagelike structures of gold clusters: Density-functional pseudopotential calculations," *Phys. Rev. B*, vol. 73, p. 235433, Jun 2006.

[20] W. D. Knight, K. Clemenger, W. A. de Heer, W. A. Saunders, M. Y. Chou, and M. L. Cohen, "Electronic shell structure and abundances of sodium clusters," *Physical Review Letters*, vol. 52, p. 2141, June 1984.

[21] M. Y. Chou, A. Cleland, and M. L. Cohen, "Total energies, abundances, and electronic shell structure of lithium, sodium, and potassium clusters," *Solid State Communications*, vol. 52, pp. 645–648, Nov. 1984.

[22] I. Katakuse, T. Ichihara, Y. Fujita, T. Matsuo, T. Sakurai, and H. Matsuda, "Mass distributions of copper, silver and gold clusters and electronic shell structure," *International Journal of Mass Spectrometry and Ion Processes*, vol. 67, pp. 229–236, Nov. 1985.

[23] M. Walter, J. Akola, O. Lopez-Acevedo, P. D. Jadzinsky, G. Calero, C. J. Ackerson, R. L. Whetten, H. Grönbeck, and H. Häkkinen, "A unified view of ligand-protected gold clusters as superatom complexes," *Proceedings of the National Academy of Sciences*, vol. 105, pp. 9157 –9162, July 2008.

[24] M. B. Knickelbein, "Reactions of transition metal clusters with small molecules1," *Annual Review of Physical Chemistry*, vol. 50, no. 1, pp. 79–115, 1999.

[25] M. Vanin, "Projector augmented wave calculations with localized basis sets," Master's thesis, 2007.

[26] A. H. Larsen, "Localized basis sets in the projector augmented wave method," Master's thesis, 2007.

[27] W. Kohn, "Nobel lecture: Electronic structure of matter—wave functions and density functionals," *Reviews of Modern Physics*, vol. 71, pp. 1253–1266, Oct. 1999.

[28] J. P. Perdew, K. Burke, and M. Ernzerhof, "Generalized gradient approximation made simple," *Physical Review Letters*, vol. 77, pp. 3865–3868, Oct. 1996.

[29] B. Hammer, L. B. Hansen, and J. K. Nørskov, "Improved adsorption energetics within density-functional theory using revised Perdew-Burke-Ernzerhof functionals," *Phys. Rev. B*, vol. 59, pp. 7413–7421, Mar 1999.

[30] C. Hartwigsen, S. Goedecker, and J. Hutter, "Relativistic separable dual-space Gaussian pseudopotentials from H to Rn," *Phys. Rev. B*, vol. 58, pp. 3641–3662, Aug 1998.

[31] L. Kleinman and D. M. Bylander, "Efficacious form for model pseudopotentials," *Physical Review Letters*, vol. 48, pp. 1425–1428, May 1982.

[32] M. Teter, "Additional condition for transferability in pseudopotentials," *Phys. Rev. B*, vol. 48, pp. 5031–5041, Aug 1993.

[33] X. Gonze, P. Käckell, and M. Scheffler, "Ghost states for separable, norm-conserving, ab initio pseudopotentials," *Physical Review B*, vol. 41, pp. 12264–12267, June 1990.

[34] D. Vanderbilt, "Soft self-consistent pseudopotentials in a generalized eigenvalue formalism," *Physical Review B*, vol. 41, pp. 7892–7895, Apr. 1990.

[35] G. Kresse and J. Furthmüller, "Efficient iterative schemes for ab initio total-energy calculations using a plane-wave basis set," *Physical Review B*, vol. 54, pp. 11169–11186, Oct. 1996.

[36] G. Kresse and D. Joubert, "From ultrasoft pseudopotentials to the projector augmented-wave method," *Physical Review B*, vol. 59, pp. 1758–1775, Jan. 1999.

[37] C. Rostgaard, "The projector augmented-wave method," *arXiv:0910.1921*, Oct. 2009.

[38] M. Kuisma, J. Ojanen, J. Enkovaara, and T. T. Rantala, "Kohn-sham potential with discontinuity for band gap materials," *Phys. Rev. B*, vol. 82, p. 115106, Sep 2010.

[39] P. Pulay, "Convergence acceleration of iterative sequences. The case of SCF iteration," *Chemical Physics Letters*, vol. 73, no. 2, pp. 393 – 398, 1980.

[40] T. Takeda, "The scalar relativistic approximation," *Zeitschrift für Physik B Condensed Matter and Quanta*, vol. 32, pp. 43–48, Mar. 1978.

[41] J. Junquera, O. Paz, D. Sánchez-Portal, and E. Artacho, "Numerical atomic orbitals for linear-scaling calculations," *Physical Review B*, vol. 64, p. 235111, Nov. 2001.

[42] S. R. Bahn and K. W. Jacobsen, "An object-oriented scripting interface to a legacy electronic structure code," *Comput. Sci. Eng.*, vol. 4, pp. 56–66, MAY-JUN 2002.

[43] S. Goedecker, "Linear scaling electronic structure methods," *Rev. Mod. Phys.*, vol. 71, pp. 1085–1123, Jul 1999.

[44] J. Choi, J. J. Dongarra, R. Pozo, and D. W. Walker, "ScaLAPACK: a scalable linear algebra library for distributed memory concurrent computers," in *Frontiers of Massively Parallel Computation, 1992., Fourth Symposium on the*, pp. 120–127, IEEE, Oct. 1992.

[45] L. Blackford, A. Cleary, J. Choi, E. D'Azevedo, J. Demmel, I. Dhillon, J. Dongarra, S. Hammarling, G. Henry, A. Petitet, *et al.*, *ScaLAPACK users' guide*, vol. 4. Society for Industrial Mathematics, 1997.

[46] E. Anderson, A. Benzoni, J. Dongarra, S. Moulton, S. Ostrouchov, B. Tourancheau, and R. van de Geijn, "Basic linear algebra communication subprograms," in *Distributed Memory Computing Conference, 1991. Proceedings., The Sixth*, pp. 287 –290, apr-1 may 1991.

[47] O. F. Sankey and D. J. Niklewski, "Ab initio multicenter tight-binding model for molecular-dynamics simulations and other applications in covalent systems," *Physical Review B*, vol. 40, no. 6, p. 3979, 1989.

[48] `https://wiki.fysik.dtu.dk/niflheim`.

[49] M. Haruta, T. Kobayashi, H. Sano, and N. Yamada, "Novel gold catalysts for the oxidation of carbon monoxide at a temperature far below 0.DEG.C.," *Chemistry Letters*, pp. 405–408, 1987.

[50] M. Haruta, S. Tsubota, T. Kobayashi, H. Kageyama, M. J. Genet, and B. Delmon, "Low-Temperature oxidation of CO over gold supported on TiO2, [alpha]-Fe2O3, and Co3O4," *Journal of Catalysis*, vol. 144, pp. 175–192, Nov. 1993.

[51] M. Valden, X. Lai, and D. W. Goodman, "Onset of catalytic activity of gold clusters on titania with the appearance of nonmetallic properties," *Science*, vol. 281, no. 5383, pp. 1647 –1650, 1998.

[52] H. Masatake, "Size- and support-dependency in the catalysis of gold," *Catalysis Today*, vol. 36, pp. 153–166, Apr. 1997.

[53] G. Mills, M. S. Gordon, and H. Metiu, "Oxygen adsorption on au clusters and a rough au(111) surface: The role of surface flatness, electron confinement, excess electrons, and band gap," *The Journal of Chemical Physics*, vol. 118, p. 4198, 2003.

[54] N. Lopez, T. Janssens, B. Clausen, Y. Xu, M. Mavrikakis, T. Bligaard, and J. Nørskov, "On the origin of the catalytic activity of gold nanoparticles for low-temperature CO oxidation," *Journal of Catalysis*, vol. 223, pp. 232–235, Apr. 2004.

[55] B. Hvolbæk, T. V. Janssens, B. S. Clausen, H. Falsig, C. H. Christensen, and J. K. Nørskov, "Catalytic activity of au nanoparticles," *Nano Today*, vol. 2, pp. 14–18, Aug. 2007.

[56] H. Falsig, B. Hvolbæk, I. S. Kristensen, T. Jiang, T. Bligaard, C. H. Christensen, and J. K. Nørskov, "Trends in the catalytic CO oxidation activity of nanoparticles," *Angewandte Chemie*, vol. 120, pp. 4913–4917, June 2008.

[57] A. S. Barnard, X. M. Lin, and L. A. Curtiss, "Equilibrium morphology of Face-Centered cubic gold nanoparticles >3 nm and the shape changes induced by temperature," *The Journal of Physical Chemistry B*, vol. 109, pp. 24465–24472, Dec. 2005.

[58] C. L. Cleveland, U. Landman, T. G. Schaaff, M. N. Shafigullin, P. W. Stephens, and R. L. Whetten, "Structural evolution of smaller gold nanocrystals: The truncated decahedral motif," *Phys. Rev. Lett.*, vol. 79, pp. 1873–1876, Sep 1997.

[59] F. Baletto, R. Ferrando, A. Fortunelli, F. Montalenti, and C. Mottet, "Crossover among structural motifs in transition and noble-metal clusters," *The Journal of Chemical Physics*, vol. 116, p. 3856, 2002.

[60] T. P. Martin, "Shells of atoms," *Physics Reports*, vol. 273, pp. 199–241, Aug. 1996.

[61] F. Baletto and R. Ferrando, "Structural properties of nanoclusters: Energetic, thermodynamic, and kinetic effects," *Rev. Mod. Phys.*, vol. 77, pp. 371–423, May 2005.

[62] C. L. Cleveland, W. D. Luedtke, and U. Landman, "Melting of gold clusters: Icosahedral precursors," *Phys. Rev. Lett.*, vol. 81, pp. 2036–2039, Sep 1998.

[63] C. L. Cleveland, W. D. Luedtke, and U. Landman, "Melting of gold clusters," *Physical Review B*, vol. 60, no. 7, p. 5065, 1999.

[64] A. P. Sutton and J. Chen, "Long-range finnis–sinclair potentials," *Philosophical Magazine Letters*, vol. 61, no. 3, pp. 139–146, 1990.

[65] R. P. Gupta, "Lattice relaxation at a metal surface," *Phys. Rev. B*, vol. 23, pp. 6265–6270, Jun 1981.

[66] X. Shao, X. Liu, and W. Cai, "Structural optimization of silver clusters up to 80 atoms with gupta and Sutton-Chen potentials," *Journal of Chemical Theory and Computation*, vol. 1, pp. 762–768, July 2005.

[67] M. Y. Chou and M. L. Cohen, "Electronic shell structure in simple metal clusters," *Physics Letters A*, vol. 113, pp. 420–424, Jan. 1986.

[68] M. P. Iñiguez, J. A. Alonso, and L. C. Balbas, "Magic numbers of sodium clusters," *Solid State Communications*, vol. 57, pp. 85–88, Jan. 1986.

[69] W. D. Knight, W. A. De Heer, W. A. Saunders, K. Clemenger, M. Y. Chou, and M. L. Cohen, "Alkali metal clusters and the jellium model," *Chemical Physics Letters*, vol. 134, pp. 1–5, Feb. 1987.

[70] Z. Penzar and W. Ekardt, "Electronic shell structure and metal clusters: the self-consistent spheroidal jellium model," *Zeitschrift für Physik D Atoms, Molecules and Clusters*, vol. 17, pp. 69–72, Mar. 1990.

[71] T. Hirschmann, M. Brack, and J. Meyer, "Spheroidally deformed sodium clusters in the selfconsistent jellium model," *Annalen der Physik*, vol. 506, no. 5, pp. 336–369, 1994.

[72] M. Brack, "The physics of simple metal clusters: self-consistent jellium model and semiclassical approaches," *Rev. Mod. Phys.*, vol. 65, pp. 677–732, Jul 1993.

[73] W. A. de Heer, W. Knight, M. Chou, and M. L. Cohen, "Electronic shell structure and metal clusters," in *Advances in Research and Applications* (H. Ehrenreich and D. Turnbull, eds.), vol. 40 of *Solid State Physics*, pp. 93 – 181, Academic Press, 1987.

[74] K. Clemenger, "Ellipsoidal shell structure in free-electron metal clusters," *Physical Review B*, vol. 32, p. 1359, July 1985.

[75] Z. Penzar and W. Ekardt, "The self-consistent spheroidal jellium model of open-shell monovalent metal clusters," *Zeitschrift für Physik D Atoms, Molecules and Clusters*, vol. 19, pp. 109–111, Mar. 1991.

[76] C. Yannouleas and U. Landman, "Electronic shell effects in triaxially deformed metal clusters: A systematic interpretation of experimental observations," *Physical Review B*, vol. 51, p. 1902, Jan. 1995.

[77] M. Koskinen, P. O. Lipas, and M. Manninen, "Electron-gas clusters: the ultimate jellium model," *Zeitschrift für Physik D Atoms, Molecules and Clusters*, vol. 35, pp. 285–297, Dec. 1995.

[78] S. M. Reimann, M. Koskinen, H. Häkkinen, P. E. Lindelof, and M. Manninen, "Magic triangular and tetrahedral clusters," *Physical Review B*, vol. 56, p. 12147, Nov. 1997.

[79] E. Hückel, "Quantentheoretische Beiträge zum Benzolproblem," *Zeitschrift für Physik A Hadrons and Nuclei*, vol. 70, pp. 204–286, 1931. 10.1007/BF01339530.

[80] E. Hückel, "Quantentheoretische Beiträge zum Problem der aromatischen und ungesättigten Verbindungen. III," *Zeitschrift für Physik A Hadrons and Nuclei*, vol. 76, pp. 628–648, 1932. 10.1007/BF01341936.

[81] Y. Wang, T. F. George, D. M. Lindsay, and A. C. Beri, "The Hückel model for small metal clusters. I. Geometry, stability, and relationship to graph theory," *The Journal of Chemical Physics*, vol. 86, p. 3493, 1987.

[82] H. Grönbeck and A. Rosén, "Chemisorption of molecular oxygen on small copper clusters and the Cu(100) surface," *Computational Materials Science*, vol. 2, no. 3-4, pp. 607 – 614, 1994.

[83] J. Mansikka-aho, M. Manninen, and E. Hammarén, "On the shell structure and geometry of monovalent metal clusters," *Zeitschrift für Physik D Atoms, Molecules and Clusters*, vol. 21, pp. 271–279, 1991. 10.1007/BF01426385.

[84] J. Mansikka-aho, M. Manninen, and E. Hammarén, "Level-spacing distribution in the tight-binding model of fcc clusters," *Physical Review B*, vol. 47, p. 10675, Apr. 1993.

[85] L. Xiao, B. Tollberg, X. Hu, and L. Wang, "Structural study of gold clusters," *The Journal of Chemical Physics*, vol. 124, no. 11, p. 114309, 2006.

[86] X. Xing, B. Yoon, U. Landman, and J. H. Parks, "Structural evolution of Au nanoclusters: From planar to cage to tubular motifs," *Phys. Rev. B*, vol. 74, p. 165423, Oct 2006.

[87] L. Ferrighi, B. Hammer, and G. K. H. Madsen, "2D-3D transition for cationic and anionic gold clusters: a kinetic energy density functional study.," *Journal of the American Chemical Society*, vol. 131, pp. 10605–10609, Aug. 2009.

[88] E. M. Fernández, J. M. Soler, I. L. Garzón, and L. C. Balbás, "Trends in the structure and bonding of noble metal clusters," *Physical Review B*, vol. 70, p. 165403, Oct. 2004.

[89] E. M. Fernández, J. M. Soler, I. L. Garzón, and L. C. Balbás, "Trends in the structure and bonding of neutral and charged noble metal clusters," *International Journal of Quantum Chemistry*, vol. 101, pp. 740–745, Jan. 2005.

[90] H.-Y. Zhao, H. Ning, J. Wang, X.-J. Su, X.-G. Guo, and Y. Liu, "Structural evolution of Au_n (n=20-32) clusters: Lowest-lying structures and relativistic effects," *Physics Letters A*, vol. 374, no. 8, pp. 1033 – 1038, 2010.

[91] W. Yin, X. Gu, and X. Gong, "Magic number 32 and 90 of metal clusters: A shell jellium model study," *Solid State Communications*, vol. 147, pp. 323–326, Aug. 2008.

[92] W. Huang, M. Ji, C. Dong, X. Gu, L. Wang, X. G. Gong, and L. Wang, "Relativistic effects and the unique Low-Symmetry structures of gold nanoclusters," *ACS Nano*, vol. 2, pp. 897–904, May 2008.

[93] H. Häkkinen, M. Moseler, O. Kostko, N. Morgner, M. A. Hoffmann, and B. v. Issendorff, "Symmetry and electronic structure of Noble-Metal nanoparticles and the role of relativity," *Physical Review Letters*, vol. 93, no. 9, p. 093401, 2004.

[94] H. Häkkinen and M. Moseler, "55-Atom clusters of silver and gold: Symmetry breaking by relativistic effects," *Computational Materials Science*, vol. 35, pp. 332–336, Mar. 2006.

[95] I. L. Garzón, K. Michaelian, M. R. Beltrán, A. Posada-Amarillas, P. Ordejón, E. Artacho, D. Sánchez-Portal, and J. M. Soler, "Lowest energy structures of gold nanoclusters," *Physical Review Letters*, vol. 81, no. 8, p. 1600, 1998.

[96] A. S. Barnard and L. A. Curtiss, "Predicting the shape and structure of Face-Centered cubic gold nanocrystals smaller than 3 nm," *ChemPhysChem*, vol. 7, pp. 1544–1553, July 2006.

[97] J. Kleis, J. Greeley, N. Romero, V. Morozov, H. Falsig, A. Larsen, J. Lu, J. Mortensen, M. Dułak, K. Thygesen, J. Nørskov, and K. Jacobsen, "Finite size effects in chemical bonding: From small clusters to solids," *Catalysis Letters*, vol. 141, pp. 1067–1071, 2011. 10.1007/s10562-011-0632-0.

[98] H. Boyen, G. Kästle, F. Weigl, B. Koslowski, C. Dietrich, P. Ziemann, J. P. Spatz, S. Riethmüller, C. Hartmann, M. Möller, G. Schmid, M. G. Garnier, and P. Oelhafen, "Oxidation-Resistant gold-55 clusters," *Science*, vol. 297, no. 5586, pp. 1533 –1536, 2002.

[99] M. Turner, V. B. Golovko, O. P. H. Vaughan, P. Abdulkin, A. Berenguer-Murcia, M. S. Tikhov, B. F. G. Johnson, and R. M. Lambert, "Selective oxidation with dioxygen by gold nanoparticle catalysts derived from 55-atom clusters," *Nature*, vol. 454, no. 7207, pp. 981–983, 2008.

[100] J. Mansikka-aho, E. Hammarén, and M. Manninen, "Shell structure in large nonspherical metal clusters," *Physical Review B*, vol. 46, p. 12649, Nov. 1992.

[101] L. Magaud, S. N. Khanna, and P. Jena, "Limitation on the success of the jellium model for metal clusters," *Chemical Physics Letters*, vol. 183, pp. 333–336, Sept. 1991.

[102] O. Genzken and M. Brack, "Temperature dependence of supershells in large sodium clusters," *Physical Review Letters*, vol. 67, p. 3286, Dec. 1991.

[103] T. P. Martin, T. Bergmann, H. Göhlich, and T. Lange, "Electronic shells and shells of atoms in metallic clusters," *Zeitschrift für Physik D Atoms, Molecules and Clusters*, vol. 19, pp. 25–29, Mar. 1991.

[104] J. Pedersen, S. Bjørnholm, J. Borggreen, K. Hansen, T. Martin, and H. Rasmussen, "Observation of quantum supershells in clusters of sodium atoms," *Nature*, vol. 353, no. 6346, p. 733–735, 1991.

[105] S. Buckart, G. Ganteför, Y. D. Kim, and P. Jena, "Anomalous behavior of atomic hydrogen interacting with gold clusters," *Journal of the American Chemical Society*, vol. 125, pp. 14205–14209, Nov. 2003.

[106] K. A. Kacprzak, O. Lopez-Acevedo, H. Häkkinen, and H. Grönbeck, "Theoretical characterization of cyclic thiolated copper, silver, and gold clusters," *The Journal of Physical Chemistry C*, vol. 114, no. 32, pp. 13571–13576, 2010.

[107] B. Hammer and J. K. Nørskov, "Why gold is the noblest of all the metals," *Nature*, vol. 376, pp. 238–240, July 1995.

[108] D. M. Newns, "Self-consistent model of hydrogen chemisorption," *Phys. Rev.*, vol. 178, pp. 1123–1135, Feb 1969.

[109] T. B. Grimley, "Overlap effects in the theory of adsorption using Anderson's Hamiltonian," *Journal of Physics C: Solid State Physics*, vol. 3, pp. 1934–1942, Sept. 1970.

[110] K. S. Thygesen, "Electron transport through an interacting region: The case of a nonorthogonal basis set," *Phys. Rev. B*, vol. 73, p. 035309, Jan 2006.

[111] J. K. Nørskov, A. Houmøller, P. K. Johansson, and B. I. Lundqvist, "Adsorption and Dissociation of H_2 on Mg Surfaces," *Physical Review Letters*, vol. 46, pp. 257–260, Jan. 1981.

[112] K. W. Jacobsen, J. K. Nørskov, and M. J. Puska, "Interatomic interactions in the effective-medium theory," *Phys. Rev. B*, vol. 35, pp. 7423–7442, May 1987.

[113] K. W. Jacobsen, P. Stoltze, and J. K. Nørskov, "A semi-empirical effective medium theory for metals and alloys," *Surface Science*, vol. 366, no. 2, pp. 394 – 402, 1996.

[114] `https://wiki.fysik.dtu.dk/asap`.

[115] Y. Wang, S. Teitel, and C. Dellago, "Melting and equilibrium shape of icosahedral gold nanoparticles," *Chemical Physics Letters*, vol. 394, pp. 257–261, Aug. 2004.

[116] J. Li, X. Li, H. Zhai, and L. Wang, "Au20: A tetrahedral cluster," *Science*, vol. 299, pp. 864 –867, Feb. 2003.

[117] E. S. Kryachko and F. Remacle, "The magic gold cluster Au20," *International Journal of Quantum Chemistry*, vol. 107, pp. 2922–2934, Jan. 2007.

[118] O. B. Christensen, K. W. Jacobsen, J. K. Nørskov, and M. Manninen, "Cu cluster shell structure at elevated temperatures," *Phys. Rev. Lett.*, vol. 66, pp. 2219–2222, Apr 1991.

[119] O. B. Christensen and K. W. Jacobsen, "The coupling between atomic and electronic structure in small Cu clusters," *Journal of Physics: Condensed Matter*, vol. 5, pp. 5591–5602, Aug. 1993.

[120] H. Häkkinen and M. Manninen, "Electronic-structure-induced deformations of liquid metal clusters," *Phys. Rev. B*, vol. 52, pp. 1540–1543, Jul 1995.

[121] R. G. Pearson, "The principle of maximum hardness," *Accounts of Chemical Research*, vol. 26, pp. 250–255, May 1993.

[122] M. K. Harbola, "Magic numbers for metallic clusters and the principle of maximum hardness," *Proceedings of the National Academy of Sciences*, vol. 89, pp. 1036 –1039, Feb. 1992.

[123] M. Manninen, J. Mansikka-aho, H. Nishioka, and Y. Takahashi, "Odd-even staggering in simple models of metal clusters," *Zeitschrift für Physik D Atoms, Molecules and Clusters*, vol. 31, pp. 259–267, Dec. 1994.

[124] H. Grönbeck and A. Rosén, "Analysis of the odd-even alternation in simple metal clusters," *Zeitschrift für Physik D Atoms, Molecules and Clusters*, vol. 36, pp. 153–157, 1996. 10.1007/BF01426630.

[125] E. M. Fernández, P. Ordejón, and L. C. Balbás, "Theoretical study of O_2 and CO adsorption on Au_n clusters (n = 5–10)," *Chemical Physics Letters*, vol. 408, pp. 252–257, June 2005.

[126] N. S. Phala, G. Klatt, and E. van Steen, "A dft study of hydrogen and carbon monoxide chemisorption onto small gold clusters," *Chemical Physics Letters*, vol. 395, no. 1-3, pp. 33 – 37, 2004.

[127] S. Klacar, A. Hellman, I. Panas, and H. Grönbeck, "Oxidation of small silver clusters: A density functional theory study," *The Journal of Physical Chemistry C*, vol. 114, no. 29, pp. 12610–12617, 2010.

Paper I: Localized atomic basis set in the projector augmented wave method

Localized atomic basis set in the projector augmented wave method

A. H. Larsen, M. Vanin, J. J. Mortensen, K. S. Thygesen, and K. W. Jacobsen
Center for Atomic-Scale Materials Design, Department of Physics, Technical University of Denmark, DK-2800 Kgs. Lyngby, Denmark
(Received 4 September 2009; revised manuscript received 9 October 2009; published 18 November 2009)

We present an implementation of localized atomic-orbital basis sets in the projector augmented wave (PAW) formalism within the density-functional theory. The implementation in the real-space GPAW code provides a complementary basis set to the accurate but computationally more demanding grid representation. The possibility to switch seamlessly between the two representations implies that simulations employing the local basis can be fine tuned at the end of the calculation by switching to the grid, thereby combining the strength of the two representations for optimal performance. The implementation is tested by calculating atomization energies and equilibrium bulk properties of a variety of molecules and solids, comparing to the grid results. Finally, it is demonstrated how a grid-quality structure optimization can be performed with significantly reduced computational effort by switching between the grid and basis representations.

DOI: 10.1103/PhysRevB.80.195112 PACS number(s): 71.15.Ap, 71.15.Dx, 71.15.Nc

I. INTRODUCTION

Density-functional theory (DFT) with the single-particle Kohn-Sham scheme is presently the most widely used method for electronic-structure calculations in both solid-state physics and quantum chemistry.[1–3] Its success is mainly due to a unique balance between accuracy and efficiency which makes it possible to handle systems containing hundreds of atoms on a single CPU with almost chemical accuracy.

At the fundamental level the only approximation of DFT is the exchange-correlation functional which contains the nontrivial parts of the kinetic and electron-electron interaction energies. However, given an exchange-correlation functional one is still left with the nontrivial numerical task of solving the Kohn-Sham equations. The main challenge comes from the very rapid oscillations of the valence electrons in the vicinity of the atom cores that makes it very costly to represent this part of the wave functions numerically. In most modern DFT codes the problem is circumvented by the use of pseudopotentials.[4–6] The pseudopotential approximation is, in principle, uncontrolled and is, in general, subject to transferability errors. An alternative method is the projector augmented wave (PAW) method invented by Blöchl.[7] An appealing feature of the PAW method is that it becomes exact if sufficiently many projector functions are used. In another limit the PAW method becomes equivalent to the ultrasoft pseudopotentials introduced by Vanderbilt.[5]

The representation of the Kohn-Sham wave functions is a central aspect of the numerics of DFT. High accuracy is achieved by using system-independent basis sets such as plane waves,[7–9] wavelets,[10,11] or real-space grids,[12,13] which can be systematically expanded to achieve convergence. Less accurate but computationally more manageable methods expand the wave function in terms of a system-dependent localized basis consisting of, e.g., Gaussians[14] or numerical atomic orbitals.[15,16] Such basis sets cannot be systematically enlarged in a simple way and consequently any calculated quantity will be subject to basis-set errors. For this reason the former methods are often used to obtain binding energies where accuracy is crucial while the latter are useful for structural properties which are typically less sensitive to the quality of the wave functions.

In this paper we discuss the implementation of a localized atomic basis set in the PAW formalism and present results for molecular atomization energies, bulk properties, and structural relaxations. The localized basis set, which we shall refer to as the linear combination of atomic orbitals (LCAO) basis, is similar to that of the well-known SIESTA pseudopotential code[16] but here it is implemented in our recently developed multigrid PAW code GPAW.[13] A unique feature of the resulting scheme is the possibility of using two different but complementary basis sets. On the one hand wave functions can be represented on a real-space grid which, in principle, facilitates an exact representation and on the other hand the wave functions can be represented in the efficient LCAO basis. This allows the user to switch seamlessly between the two representations at any point of a calculation. As a particularly powerful application of this "double-basis" feature, we demonstrate how accurate structural relaxations can be performed by first relaxing with the atomic basis set and then switching to the grid for the last part. Also adsorption energies, which are typically not very good in LCAO, can be obtained on the grid at the end of a relaxation.

While LCAO pseudopotential codes as well as plane-wave/grid PAW codes already exist and have been discussed extensively in the literature,[7,15,16] the combination of LCAO and PAW is different. Compared to the popular SIESTA method, which is based on norm-conserving pseudopotentials, the advantage of the present scheme (apart from the double-basis feature) is that PAW works with coarser grids to represent the density and effective potentials. As an example, Fig. 1 shows the atomic orbitals of iron calculated with the norm-conserving Hartwigsen-Goedecker-Hutter (HGH) pseudopotentials[6] as well as with PAW. Clearly the d wave function is much smoother in PAW. This is essential for larger systems where operations on the grid, i.e., solving the Poisson equation, evaluating the density, and calculating the potential matrix elements become computationally demanding.

II. PROJECTOR AUGMENTED WAVE METHOD

In this section we give a brief review of the PAW formalism. For simplicity we restrict the equations to the case of

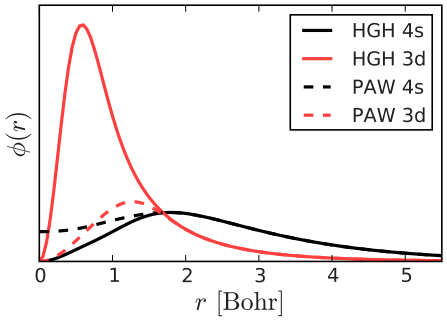

FIG. 1. (Color online) The pseudovalence states of iron calculated with PAW and the norm-conserving HGH pseudopotentials. Both methods produce smooth wave functions for the delocalized 4*s* state but the lack of norm conservation allows the short-ranged 3*d* state in PAW to be accurately sampled on a much coarser grid.

spin-paired finite systems but the generalizations to magnetic and periodic systems are straightforward. For a more comprehensive presentation we refer to Ref. 7.

A. PAW transformation operator

The PAW method is based on a linear transformation $\mathcal{T}$ which maps some computationally convenient "pseudo" or "smooth" wave functions $|\tilde{\psi}_n\rangle$ to the physically relevant "all-electron" wave functions $|\psi_n\rangle$,

$$|\psi_n\rangle = \mathcal{T}|\tilde{\psi}_n\rangle, \tag{1}$$

where n is a quantum state label, consisting of a band index and possibly a spin and $\mathbf{k}$-vector index.

The transformation is chosen as $\mathcal{T}=1+\Sigma_a\mathcal{T}^a$, i.e., the identity operator plus an additive contribution centered around each atom, which differs based on the species of atom. The atomic contribution for atom a is determined by choosing a set of smooth functions $\tilde{\phi}_i^a(\mathbf{r})$, called pseudopartial waves and requiring the transformation to map those onto the atomic valence orbitals $\phi_i^a(\mathbf{r})$ of that atom, called all-electron partial waves. This effectively allows the all-electron behavior to be incorporated by the smooth pseudowave functions. Since the all-electron wave functions are smooth sufficiently far from the atoms, we may require the pseudopartial waves to match the all-electron ones outside a certain cutoff radius, such that $\tilde{\phi}_i^a(\mathbf{r})=\phi_i^a(\mathbf{r})$ for $r>r_c$. This localizes the atomic contribution $\mathcal{T}^a$ to the *augmentation sphere* $r<r_c$. Finally a set of localized *projectors* $\tilde{p}_i^a(\mathbf{r})$ is chosen as a dual basis to the pseudopartial waves. We further want the partial-wave-projector basis to be complete within the augmentation sphere, in the sense that any pseudowave function should be expressible in terms of pseudopartial waves and therefore require

$$\sum_i |\tilde{\phi}_i^a\rangle\langle\tilde{p}_i^a| = 1, \quad \langle\tilde{\phi}_i^a|\tilde{p}_j^a\rangle = \delta_{ij}. \tag{2}$$

The transformation $\mathcal{T}$ is then defined by

$$\mathcal{T} = 1 + \sum_a \sum_i (|\phi_i^a\rangle - |\tilde{\phi}_i^a\rangle)\langle\tilde{p}_i^a|, \tag{3}$$

which allows the all-electron Kohn-Sham wave function $\psi_n(\mathbf{r})=\langle\mathbf{r}|\psi_n\rangle$ to be recovered from a pseudowave function through

$$\psi_n(\mathbf{r}) = \tilde{\psi}_n(\mathbf{r}) + \sum_a \sum_i [\phi_i^a(\mathbf{r}) - \tilde{\phi}_i^a(\mathbf{r})]\langle\tilde{p}_i^a|\tilde{\psi}_n\rangle. \tag{4}$$

We emphasize that the all-electron wave functions are never evaluated explicitly but all-electron values of observables are calculated through manipulations which rely only on coarse grids or one-dimensional radial grids. Using Eqs. (1) and (3), the all-electron expectation value for any semilocal operator O due to the valence states can be written as

$$\langle O\rangle = \sum_n f_n\langle\tilde{\psi}_n|O|\tilde{\psi}_n\rangle + \sum_{naij} f_n\langle\tilde{\psi}_n|\tilde{p}_i^a\rangle\langle\phi_i^a|O|\phi_j^a\rangle\langle\tilde{p}_j^a|\tilde{\psi}_n\rangle - \sum_{naij} f_n\langle\tilde{\psi}_n|\tilde{p}_i^a\rangle\langle\tilde{\phi}_i^a|O|\tilde{\phi}_j^a\rangle\langle\tilde{p}_j^a|\tilde{\psi}_n\rangle. \tag{5}$$

Inside the augmentation spheres the partial-wave expansion is ideally complete, so the first and third terms will cancel and leave only the all-electron contribution. Outside the augmentation spheres the pseudopartial waves are identical to the all-electron ones, so the two atomic terms cancel. The atomic matrix elements of O in the second and third terms can be pre-evaluated for the isolated atom on high-resolution radial grids, so operations on smooth quantities, such as $\langle\tilde{\psi}_n|O|\tilde{\psi}_n\rangle$ and $\langle\tilde{p}_i^a|\tilde{\psi}_n\rangle$, are the only ones performed during actual calculations.

It is convenient to define the *atomic density matrices*

$$D_{ij}^a = \sum_n \langle\tilde{p}_i^a|\tilde{\psi}_n\rangle f_n\langle\tilde{\psi}_n|\tilde{p}_j^a\rangle \tag{6}$$

since these completely describe the dependence of the atomic terms in Eq. (5) on the pseudowave functions. The expectation value can then be written as

$$\langle O\rangle = \sum_n f_n\langle\tilde{\psi}_n|O|\tilde{\psi}_n\rangle + \sum_{aij} D_{ji}^a(\langle\phi_i^a|O|\phi_j^a\rangle - \langle\tilde{\phi}_i^a|O|\tilde{\phi}_j^a\rangle). \tag{7}$$

Although the PAW method is an exact implementation of density-functional theory, some approximations are needed for realistic calculations. The frozen-core approximation assumes that the core states are localized within the augmentation spheres and that they are not modified by the chemical environment and hence taken from atomic reference calculations. The noncompleteness of the basis, or equivalently the finite grid spacing, will introduce an error in the evaluation of the PS contribution $\tilde{\psi}_n$ in Eq. (5). Finally, the number of partial waves and projector functions is obviously finite. This means that the completeness conditions of Eq. (2) we have required are not strictly fulfilled. This approximation can be controlled directly by increasing the number of partial waves and projectors.

B. Density

The electron density $n(\mathbf{r})$ is the expectation value of the real-space projection operator and, by Eq. (7), takes the form

$$n(\mathbf{r}) = \tilde{n}(\mathbf{r}) + \sum_a [n^a(\mathbf{r}-\mathbf{R}^a) - \tilde{n}^a(\mathbf{r}-\mathbf{R}^a)], \tag{8}$$

where

$$\tilde{n}(\mathbf{r}) = \sum_n f_n |\tilde{\psi}_n(\mathbf{r})|^2 + \sum_a \tilde{n}_c^a(|\mathbf{r}-\mathbf{R}^a|), \tag{9}$$

$$n^a(\mathbf{r}) = \sum_{ij} D_{ji}^a \phi_i^a(\mathbf{r}) \phi_j^a(\mathbf{r}) + n_c^a(r), \tag{10}$$

$$\tilde{n}^a(\mathbf{r}) = \sum_{ij} D_{ji}^a \tilde{\phi}_i^a(\mathbf{r}) \tilde{\phi}_j^a(\mathbf{r}) + \tilde{n}_c^a(r). \tag{11}$$

Here we have separated out the all-electron core density $n_c^a(r)$ and the pseudocore density $\tilde{n}_c^a(r)$, where the latter can be chosen as any smooth continuation of $n_c^a(r)$ inside the augmentation spheres since it will cancel out in Eq. (8). We omit conjugation of the partial waves since these can be chosen as real functions without loss of generality.

C. Compensation charges

In order to avoid dealing with the cumbersome nuclear point charges and to compensate for the lack of norm conservation, we introduce smooth localized *compensation charges* $\tilde{Z}^a(\mathbf{r})$ on each atom, which are added to $\tilde{n}(\mathbf{r})$ and $\tilde{n}^a(\mathbf{r})$, thus keeping the total charge neutral. This yields a total charge density that can be expressed as

$$\rho(\mathbf{r}) = \tilde{\rho}(\mathbf{r}) + \sum_a [\rho^a(\mathbf{r}-\mathbf{R}^a) - \tilde{\rho}^a(\mathbf{r}-\mathbf{R}^a)] \tag{12}$$

in terms of the neutral charge densities

$$\tilde{\rho}(\mathbf{r}) = \tilde{n}(\mathbf{r}) + \tilde{Z}(\mathbf{r}) = \tilde{n}(\mathbf{r}) + \sum_a \tilde{Z}^a(\mathbf{r}-\mathbf{R}^a), \tag{13}$$

$$\rho^a(\mathbf{r}) = n^a(\mathbf{r}) + \mathcal{Z}^a \delta(\mathbf{r}), \tag{14}$$

$$\tilde{\rho}^a(\mathbf{r}) = \tilde{n}^a(\mathbf{r}) + \tilde{Z}^a(\mathbf{r}), \tag{15}$$

where $\mathcal{Z}^a\delta(\mathbf{r})$ is the central nuclear point charge. The compensation charges are chosen to be localized functions around each atom of the form

$$\tilde{Z}^a(\mathbf{r}) = \sum_L Q_L^a \tilde{g}_L^a(\mathbf{r}) = \sum_{lm} Q_{lm}^a r^l \tilde{g}_l^a(r) Y_{lm}(\hat{\mathbf{r}}), \tag{16}$$

where $\tilde{g}_l^a(r)$ are fixed Gaussians and $Y_{lm}(\hat{\mathbf{r}})$ are spherical harmonics. We use $L=l,m$ as a composite index for angular and magnetic quantum numbers. The expansion coefficients Q_L^a are determined in terms of D_{ij}^a by requiring the compensation charges to cancel all the multipole moments of each augmentation region up to some order, generally $l_{\max}=2$. The charges will therefore dynamically adapt to the surroundings of the atom. For more details we refer to the original work by Blöchl.[7]

D. Total energy

The total energy can also be separated into smooth and atom-centered contributions

$$E = \tilde{E} + \sum_a (E^a - \tilde{E}^a), \tag{17}$$

where

$$\tilde{E} = \sum_n f_n \langle \tilde{\psi}_n | -\frac{1}{2}\nabla^2 | \tilde{\psi} \rangle_n + \sum_a \int \tilde{n}(\mathbf{r}) \bar{v}^a(|\mathbf{r}-\mathbf{R}^a|) d\mathbf{r} + \frac{1}{2}\int\int \frac{\tilde{\rho}(\mathbf{r})\tilde{\rho}(\mathbf{r}')}{|\mathbf{r}-\mathbf{r}'|} d\mathbf{r}d\mathbf{r}' + E_{\mathrm{xc}}[\tilde{n}], \tag{18}$$

$$E^a = \sum_{ij} D_{ji}^a \langle \phi_i^a | -\frac{1}{2}\nabla^2 | \phi_j^a \rangle + T_{\mathrm{core}}^a + \frac{1}{2}\int\int \frac{\rho^a(\mathbf{r})\rho^a(\mathbf{r}')}{|\mathbf{r}-\mathbf{r}'|} d\mathbf{r}d\mathbf{r}' + E_{\mathrm{xc}}[n^a], \tag{19}$$

$$\tilde{E}^a = \sum_{ij} D_{ji}^a \langle \tilde{\phi}_i^a | -\frac{1}{2}\nabla^2 | \tilde{\phi}_j^a \rangle + \tilde{T}_{\mathrm{core}}^a + \int \tilde{n}^a(\mathbf{r}) \bar{v}^a(r) d\mathbf{r} + \frac{1}{2}\int\int \frac{\tilde{\rho}^a(\mathbf{r})\tilde{\rho}^a(\mathbf{r}')}{|\mathbf{r}-\mathbf{r}'|} d\mathbf{r}d\mathbf{r}' + E_{\mathrm{xc}}[\tilde{n}^a]. \tag{20}$$

The terms T_{core}^a and $\tilde{T}_{\mathrm{core}}^a$ are the kinetic-energy contributions from the frozen-core states while $\bar{v}^a(r)$ is an arbitrary potential, vanishing for $r > r_c^a$. This potential is generally chosen to make the atomic potential smooth while its contribution to the total energy vanishes if the partial-wave expansion is complete.[13]

E_{xc} is the exchange-correlation functional, which must be local or semilocal as per Eq. (7) for the above expressions to be correct. While the functional is nonlinear, it remains true that

$$E_{\mathrm{xc}}[n] = E_{\mathrm{xc}}[\tilde{n}] + \sum_a (E_{\mathrm{xc}}[n^a] - E_{\mathrm{xc}}[\tilde{n}^a]) \tag{21}$$

because of the functional's semilocality: the energy contribution from $\tilde{n}(\mathbf{r})$ around every point inside the augmentation sphere is exactly canceled by that of $\tilde{n}^a(\mathbf{r})$ since $\tilde{n}(\mathbf{r})$ and $\tilde{n}^a(\mathbf{r})$ are exactly identical here, leaving only the contribution $E_{\mathrm{xc}}[n^a]$. Outside the augmentation region, a similar argument applies to $n^a(\mathbf{r})$ and $\tilde{n}(\mathbf{r})$, leaving only the energy contribution from $\tilde{n}(\mathbf{r})$ which is here equal to the all-electron density.

E. Hamiltonian and orthogonality

In generic operator form, the Hamiltonian corresponding to the total energy from Eq. (17) is

$$\tilde{H} = -\frac{1}{2}\nabla^2 + \tilde{v} + \sum_{aij} |\tilde{p}_i^a\rangle \Delta H_{ij}^a \langle p_j^a|, \tag{22}$$

where $\tilde{v} = \tilde{v}_{\mathrm{Ha}}[\tilde{\rho}] + \bar{v} + v_{\mathrm{xc}}[\tilde{n}]$ is the local effective potential, containing the Hartree, the arbitrary localized and the xc potentials, and where

$$\Delta H_{ij}^a = \frac{\partial E}{\partial D_{ji}^a} \tag{23}$$

are the *atomic Hamiltonians* containing the atom-centered contributions from the augmentation spheres. Since the all-

electron wave functions ψ_n must be orthonormal, the pseudowave functions $\tilde{\psi}_n$ must obey

$$\delta_{nm} = \langle \psi_n | \psi_m \rangle = \langle \tilde{\psi}_n | \mathcal{T}^\dagger \mathcal{T} | \tilde{\psi}_m \rangle = \langle \tilde{\psi}_n | S | \tilde{\psi}_m \rangle, \tag{24}$$

where we have defined the *overlap operator*

$$S = \mathcal{T}^\dagger \mathcal{T} = 1 + \sum_{aij} |\tilde{p}_i^a\rangle \Delta S_{ij}^a \langle \tilde{p}_j^a|. \tag{25}$$

The atomic contributions

$$\Delta S_{ij}^a = \langle \phi_i^a | \phi_j^a \rangle - \langle \tilde{\phi}_i^a | \tilde{\phi}_j^a \rangle \tag{26}$$

are constant for a given element.

Given the Hamiltonian and orthogonality condition, a variational problem can be derived for the pseudowave functions. This problem is equivalent to the generalized Kohn-Sham eigenvalue problem

$$\tilde{H} | \tilde{\psi}_n \rangle = S | \tilde{\psi}_n \rangle \epsilon_n, \tag{27}$$

which can then be solved self-consistently with available techniques.

III. LOCALIZED BASIS SETS IN PAW

We now introduce a set of basis functions $|\Phi_\mu\rangle$ which are fixed, strictly localized atomic-orbital-like functions represented numerically, following the approach by Sankey and Niklewski.[15] We furthermore consider the pseudowave functions $|\tilde{\psi}_n\rangle$ to be linear combinations of the basis functions

$$|\tilde{\psi}_n\rangle = \sum_\mu c_{\mu n} |\Phi_\mu\rangle, \tag{28}$$

where the coefficients $c_{\mu n}$ are variational parameters. It proves useful to define the density matrix

$$\rho_{\mu\nu} = \sum_n c_{\mu n} f_n c_{\nu n}^*. \tag{29}$$

The pseudodensity can be evaluated from the density matrix through

$$\tilde{n}(\mathbf{r}) = \sum_{\mu\nu} \Phi_\mu^*(\mathbf{r}) \Phi_\nu(\mathbf{r}) \rho_{\nu\mu} + \sum_a \tilde{n}_c^a(\mathbf{r}). \tag{30}$$

Ahead of a calculation, we evaluate the matrices

$$T_{\mu\nu} = \langle \Phi_\mu | -\frac{1}{2}\nabla^2 | \Phi_\nu \rangle, \tag{31}$$

$$P_{i\mu}^a = \langle \tilde{p}_i^a | \Phi_\mu \rangle, \tag{32}$$

$$\Theta_{\mu\nu} = \langle \Phi_\mu | \Phi_\nu \rangle, \tag{33}$$

which are used to evaluate most of the quantities of the previous sections in matrix form. The atomic density matrices from Eq. (6) become

$$D_{ij}^a = \sum_{\mu\nu} P_{i\mu}^a \rho_{\mu\nu} P_{j\nu}^{a*} \tag{34}$$

and the kinetic-energy contribution in the first term of Eq. (18) is

$$\sum_n f_n \langle \tilde{\psi}_n | -\frac{1}{2}\nabla^2 | \tilde{\psi}_n \rangle = \sum_{\mu\nu} T_{\mu\nu} \rho_{\nu\mu}. \tag{35}$$

We can then define the Hamiltonian matrix elements by taking the derivative of the total energy E with respect to the density-matrix elements, which eventually results in the discretized Hamiltonian

$$H_{\mu\nu} \equiv \frac{\partial E}{\partial \rho_{\nu\mu}} = T_{\mu\nu} + V_{\mu\nu} + \sum_{aij} P_{i\mu}^{a*} \Delta H_{ij}^a P_{j\nu}^a, \tag{36}$$

where

$$V_{\mu\nu} = \int \Phi_\mu^*(\mathbf{r}) \tilde{v}(\mathbf{r}) \Phi_\nu(\mathbf{r}) d\mathbf{r}. \tag{37}$$

The overlap operator of Eq. (25) has the matrix representation

$$S_{\mu\nu} = \langle \Phi_\mu | S | \Phi_\nu \rangle = \Theta_{\mu\nu} + \sum_{aij} P_{i\mu}^{a*} \Delta S_{ij}^a P_{j\nu}^a, \tag{38}$$

so orthogonality of the wave functions is now expressed by

$$\sum_{\mu\nu} c_{\mu m}^* S_{\mu\nu} c_{\nu n} = \delta_{mn}. \tag{39}$$

This is incorporated by defining a quantity Ω to be variationally minimized with respect to the coefficients, specifically

$$\Omega = E - \sum_{mn\mu\nu} \lambda_{nm} (c_{\mu m}^* S_{\mu\nu} c_{\nu n} - \delta_{mn}). \tag{40}$$

Setting the derivative of Ω with respect to $c_{\mu n}$ equal to 0, one obtains the generalized eigenvalue equation

$$\sum_\nu H_{\mu\nu} c_{\nu n} = \sum_\nu S_{\mu\nu} c_{\nu n} \epsilon_n, \tag{41}$$

which can be solved for the coefficients $c_{\mu n}$ and energies ϵ_n when the Hamiltonian $H_{\mu\nu}$ and the overlap matrix $S_{\mu\nu}$ are known.

A. Basis functions generation

The basis functions $|\Phi_\mu\rangle$ in Eq. (28) are atom-centered orbitals written as products of numerical radial functions and spherical harmonics,

$$\Phi_{nlm}(\mathbf{r}) = \varphi_{nl}(r) Y_{lm}(\hat{\mathbf{r}}). \tag{42}$$

In order to make the Hamiltonian and overlap matrices sparse in the basis-set representation, we use strictly localized radial functions, i.e., orbitals that are identically zero beyond a given radius, as proposed by Sankey and Niklewski[15] and successfully implemented in the SIESTA method.[16]

The first (single-zeta) basis orbitals $\varphi_{nl}^{\mathrm{AE}}(r)$ are obtained for each valence state by solving the radial all-electron Kohn-Sham equations for the isolated atom in the presence of a confining potential with a certain cutoff. If the confining potential is chosen to be smooth, the basis functions similarly become smooth. We use the same confining potential as proposed in Ref. 17. The smooth basis functions are then

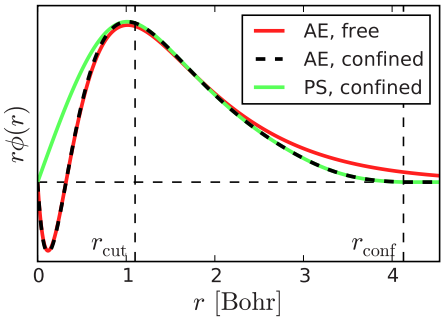

FIG. 2. (Color online) Basis function generation for the nitrogen 2*s* state: the all-electron orbital of the free atom, the confined all-electron orbital, and the corresponding pseudowave function after applying the inverse PAW transformation. The augmentation sphere and basis function cutoffs are indicated.

obtained using $\varphi_{nl}(r)=\mathcal{T}^{-1}\varphi_{nl}^{\mathrm{AE}}(r)$. The result of the procedure is illustrated in Fig. 2.

The cutoff radius is selected in a systematic way by specifying the energy shift ΔE of the confined orbital compared to the free-atom orbital. In this approach small values of ΔE will correspond to long-ranged basis orbitals.[16]

To improve the radial flexibility, extra basis functions with the same angular momentum l (multiple zeta) are constructed for each valence state using the split-valence technique.[16] The extra function is constructed by matching a polynomial to the tail of the atomic orbital, where the matching radius is determined by requiring the norm of the part of the atomic orbital outside that radius to have a certain value.

Finally, polarization functions (basis functions with l quantum number corresponding to the lowest unoccupied angular momentum) can be added in order to improve the angular flexibility of the basis. There are several approaches to generate these orbitals, such as perturbing the occupied eigenstate with the highest l quantum number with an electric field using first-order perturbation theory (like in Ref. 16) or using the appropriate unoccupied orbitals. As a first implementation we use a Gaussian-type function of the form $r^l \exp(-\alpha r^2)$ for the radial part, where l corresponds to the lowest unoccupied angular momentum. This produces reasonable polarization functions as demonstrated by the results presented in a following section.

A generator program is included in the GPAW code and it can produce basis sets for virtually any elements in the periodic table. Through our experiences with generating and using different basis sets, we have reached the following set of default parameters: we usually work with a double zeta polarized (DZP) basis. The energy shift for the atomic orbital is taken as 0.1 eV and the tail norm is 0.16 (in agreement with SIESTA (Ref. 16). The width of the Gaussian used for the polarization function is 1/4 of the cutoff radius of the first zeta basis function. Further information can be found in the documentation for the basis-set generator. At this point we have not yet systematically optimized the basis-set parameters, although we expect to do so by means of an automatic procedure.

B. Atomic forces

The force on some atom a is defined as the negative derivative of the total energy of the system with respect to the position of that atom,

$$\mathbf{F}^a = -\frac{\partial E}{\partial \mathbf{R}^a}. \tag{43}$$

The derivative is to be taken with the constraints that self-consistency and orthonormality according to Eq. (39) must be obeyed. This implies that the calculated force will correspond to the small-displacement limit of the finite-difference energy gradient one would obtain by performing two separate energy calculations, where atom a is slightly displaced in one of them.

The expression for the force is obtained by using the chain rule on the total energy of Eq. (17). The primary complication compared to the grid-based PAW force formula, Eq. (50) from Ref. 13, is that the basis functions move with the atoms, introducing extra terms in the derivative.

The complete formula for the force on atom a is

$$\begin{aligned}
\mathbf{F}^a = &-2\Re\sum_{\mu\in a;\nu}\frac{dT_{\mu\nu}}{d\mathbf{R}^a}\rho_{\nu\mu} + 2\Re\sum_{\mu\in a;\nu}\frac{d\Theta_{\mu\nu}}{d\mathbf{R}^a}E_{\nu\mu} \\
&- 2\Re\sum_{b;\mu\in a;\nu}\mathbf{Z}^b_{\mu\nu}E_{\nu\mu} + 2\Re\sum_{\mu\nu}\mathbf{Z}^a_{\mu\nu}E_{\nu\mu} \\
&+ 2\Re\sum_{b;\mu\in a;\nu}\mathbf{A}^b_{\mu\nu}\rho_{\nu\mu} - 2\Re\sum_{\mu\nu}\mathbf{A}^a_{\mu\nu}\rho_{\nu\mu} \\
&- 2\Re\sum_{\mu\in a;\nu}\left[\int\frac{d\Phi^*_\mu(\mathbf{r})}{d\mathbf{R}^a}\tilde{v}(\mathbf{r})\Phi_\nu(\mathbf{r})d\mathbf{r}\right]\rho_{\nu\mu} \\
&- \int\tilde{v}(\mathbf{r})\frac{d\tilde{n}^a_c(|\mathbf{r}-\mathbf{R}^a|)}{d\mathbf{R}^a}d\mathbf{r} - \int\tilde{n}(\mathbf{r})\frac{d\bar{v}^a(|\mathbf{r}-\mathbf{R}^a|)}{d\mathbf{R}^a}d\mathbf{r} \\
&- \int\tilde{v}_H(\mathbf{r})\sum_L Q^a_L\frac{d\tilde{g}^a_L(\mathbf{r}-\mathbf{R}^a)}{d\mathbf{R}^a}d\mathbf{r},
\end{aligned} \tag{44}$$

where

$$\mathbf{A}^b_{\mu\nu} = \sum_{ij}\frac{dP^{b*}_{i\mu}}{d\mathbf{R}^b}\Delta H^b_{ij}P^b_{j\nu}, \tag{45}$$

$$\mathbf{Z}^b_{\mu\nu} = \sum_{ij}\frac{dP^{b*}_{i\mu}}{d\mathbf{R}^b}\Delta S^b_{ij}P^b_{j\nu}, \tag{46}$$

$$E_{\mu\nu} = \sum_{\lambda\xi}S^{-1}_{\mu\lambda}H_{\lambda\xi}\rho_{\xi\nu}. \tag{47}$$

The notation $\mu\in a$ denotes that summation should be performed only over those basis functions that reside on atom a.

Equation (44) is derived in Appendix. The last three terms are basis set independent and inherited from the grid-based implementation.

IV. IMPLEMENTATION

The LCAO code is implemented in GPAW, a real-space PAW code. For the details of the real-space implementation

we refer to the original paper.[13] In this code the density, effective potential, and wave functions are evaluated on real-space grids.

In LCAO the matrix elements of the kinetic and overlap operators $T_{\mu\nu}$, $\Theta_{\mu\nu}$, and $P^a_{i\mu}$ in Eqs. (31)–(33) are efficiently calculated in Fourier space based on analytical expressions.[15] For each pair of different basis orbitals (i.e., independently of the atomic positions), the overlap can be represented in the form of radial functions and spherical harmonics. These functions are stored as splines which can in turn be evaluated for a multitude of different atomic separations.

The two-center integrals are thus calculated once for a given atomic configuration ahead of the self-consistency loop. This is equivalent to the SIESTA approach.[16] The matrix elements of the effective potential $V_{\mu\nu}$ are still calculated numerically on the three-dimensional (3D) real-space grid since the density is also evaluated on this grid.[13]

Because of the reduced degrees of freedom of a basis calculation compared to a grid-based calculation, the Hamiltonian from Eq. (36) is directly diagonalized in the space of the basis functions according to Eq. (41). This considerably lowers the number of required iterations to reach self-consistency, compared to the iterative minimization schemes used in grid-based calculations.

For each step in the self-consistency loop, the Hartree potential $\tilde{v}_{\mathrm{Ha}}(\mathbf{r})$ is calculated by solving the Poisson equation $\nabla^2\tilde{v}_{\mathrm{Ha}}(\mathbf{r})=-4\pi\tilde{\rho}(\mathbf{r})$ in real space using existing multigrid methods, such as the Gauss-Seidel and Jacobi methods. A solver based on the fast Fourier transform is also available in the GPAW code.

The calculations are parallelized over k points, spins, and real-space domains such as in the grid-based case.[13] We further distribute the orbital-by-orbital matrices such as $H_{\mu\nu}$ and $S_{\mu\nu}$, and use SCALAPACK for operations on these, notably the diagonalization of Eq. (41).

Localized functions on the grid

Quantities such as the density $\tilde{n}(\mathbf{r})$ and effective potential $\tilde{v}(\mathbf{r})$ are still stored on 3D grids. Matrix elements such as $V_{\mu\nu}$ in Eq. (37) and the pseudodensity given by Eq. (30) can therefore be calculated by loops over grid points.

Since each basis function is nonzero only in a small part of space, we only store the values of a given function within its bounding sphere. Each function value inside the bounding sphere is calculated as the product of radial and angular parts, viz., Eq. (42), where the radial part is represented by a spline and the spherical harmonic evaluated in Cartesian form, i.e., as a polynomial. The same method is used to evaluate derivatives in force calculations, although this involves the derivatives of these quantities aside from just their function values.

We initially compile a data structure to keep track of which functions are nonzero for each grid point. When looping over the grid, we maintain a list of indices μ for the currently nonzero basis functions by adding or removing, as appropriate, those functions whose bounding spheres we intersect. The locations of these bounding spheres are likewise precompiled into lists for efficient processing. The memory overhead due to this method is still much smaller than the storage requirements for the actual function values.

V. RESULTS

In this section we calculate common quantities using the localized basis set on different systems. The results are compared to the complete basis-set limit, i.e., a well-converged grid calculation. Note that this comparison can be done in a very systematic way since the calculations on the grid share the same approximations and mostly the same implementation as the calculations performed with the localized basis. All the results presented in this section have been obtained using PAW setups from the extensive GPAW library, freely available online.[18]

A. Molecules

In order to assess the accuracy of the LCAO implementation for small molecules, the Perdew-Burke-Ernzerhof (PBE) (Ref. 19) atomization energies for the G2-1 data set[20] are considered. The atomic coordinates are taken from MP2(full)/6-31G(d) optimized geometries. The error with respect to the grid results is shown in Fig. 3 for different basis sets. This error is defined as

$$\Delta E^{\mathrm{LCAO}} - \Delta E^{\mathrm{grid}} = E^{\mathrm{LCAO}}_{\mathrm{mol}} - \sum_{\mathrm{atoms}} E^{\mathrm{LCAO}}_{\mathrm{atoms}} - \left(E^{\mathrm{grid}}_{\mathrm{mol}} - \sum_{\mathrm{atoms}} E^{\mathrm{grid}}_{\mathrm{atoms}} \right). \quad (48)$$

The reference grid results are well-converged calculations in very good agreement with the VASP (Ref. 8) and Gaussian[14] codes. The figure shows that enlarging the basis set, i.e., including more orbitals per valence electron, systematically improves the results toward the grid energies.

It must be noted that some differences with respect to the grid atomization energies still remain, even in the case of large basis sets. This is mainly due to the two following reasons. First, the basis functions are generated from spin-paired calculations and hence they do not explicitly account for possible spin-polarized orbitals. This is in practice accounted for by using larger basis sets in order to include more degrees of freedom in the shape of the wave functions. Second, isolated atoms are difficult to treat because of their long-ranged orbitals. Actual basis functions are, in fact, obtained from atomic calculations with an artificial confining potential thus resulting in more confined orbitals.

B. Solids

The equilibrium bulk properties have been calculated for several crystals featuring different electronic structures: simple metals (Li, Na, and Al), semiconductors (AlP, Si, and SiC), ionic solids (NaCl, LiF, and MgO) transition metals (Fe, Cu, and Pt) as well as one insulator (C). The results are shown in Fig. 4. For comparison with grid-based calculations, the bar plots show the deviations from grid-based results for each basis set while the precise numbers are shown in each of the corresponding tables. All the calculations were

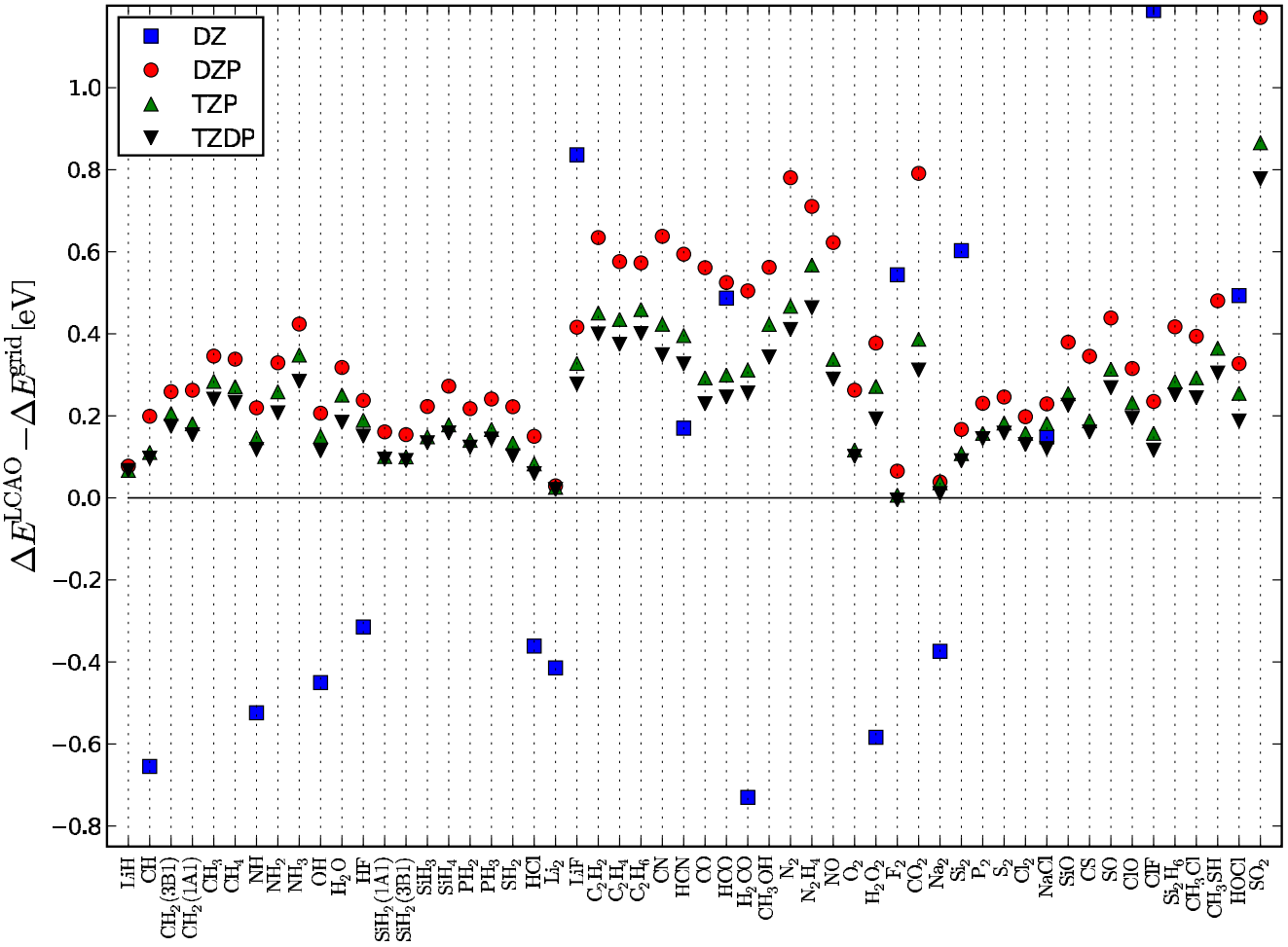

FIG. 3. (Color online) PBE atomization energies from the G2-1 data set, relative to the grid values. The corresponding mean absolute errors with respect to the grid values are: 1.71 eV (20.4%) for DZ; 0.36 eV (4.45%) for DZP; 0.25 eV (3.02%) for triple zeta polarized; and 0.20 eV (2.44%) for triple zeta double polarized.

performed with the solids in their lowest energy crystal structure, using the PBE functional for exchange and correlation.[19] The quantities were computed using the relaxed structures obtained with the default, unoptimized basis sets. The calculations were generally spin paired, i.e., nonmagnetic, with the exception of Fe and the atomic calculations used to get cohesive energies.

The overall agreement with the real-space grid is excellent: about 0.5% mean absolute error in the computation of lattice constants, 4% in cohesive energies, and 5–8 % for bulk moduli using double zeta polarized (DZP) basis sets. Notice that in many cases remarkably good results can be obtained even with a small single zeta polarized (SZP) basis, particularly for lattice constants. This shows that structure optimizations with the LCAO code are likely to yield very accurate geometries. This is probably due to the fact that calculations of equilibrium structures only involve energy differences between very similar structures, i.e., not with respect to isolated atoms, thus leading to larger error cancellations.

With DZP the primary source of error in cohesive energy comes from the free-atom calculation, where the confinement of each orbital raises the energy levels by around 0.1 eV. Thus, atomic energies are systematically overestimated, leading to stronger binding. This error can be controlled by using larger basis-set cutoffs, i.e., choosing smaller orbital energy shifts during basis generation.

C. Structure optimizations

LCAO calculations tend to reproduce geometries of grid-based calculations very accurately. In structure optimizations, the LCAO code can therefore be used to provide a high-quality initial guess for a grid-based structure optimization.

While it is trivial to reuse a geometry obtained in one code for a more accurate optimization in another, our approach is practical because the two representations share the exact same framework. Thus the procedure is seamless as well as numerically consistent, in the sense that most of the operations are carried out using the same approximations, finite-difference stencils, and so on. With quasi-Newton methods, the estimate of the Hessian matrix generated during the LCAO optimization can be reused as well. For most nontrivial systems, an LCAO calculation is between 25 and 30

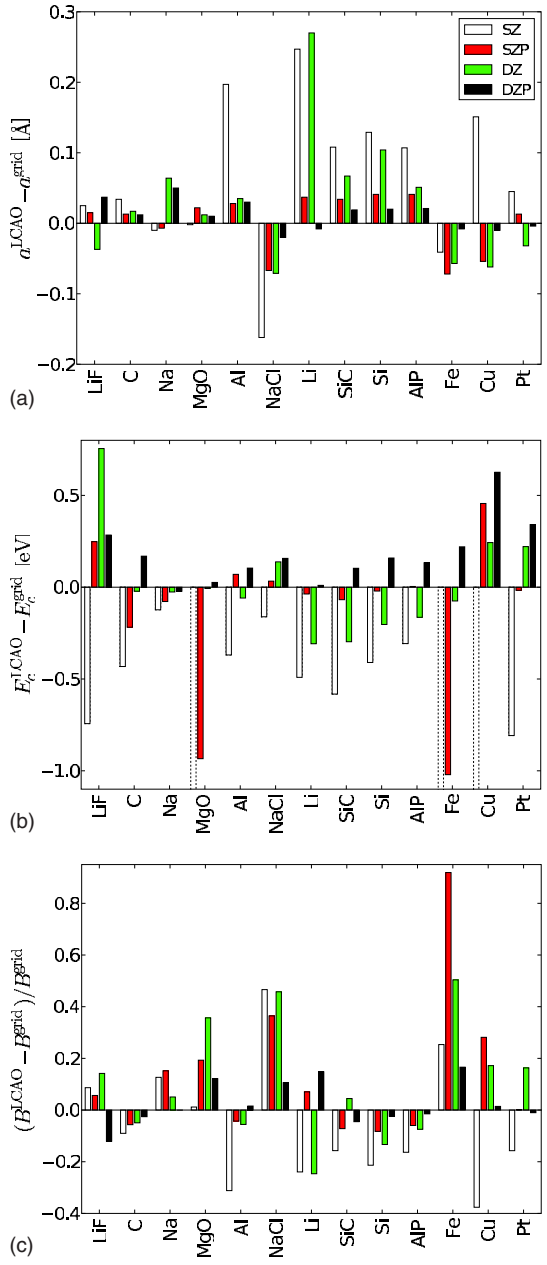

FIG. 4. (Color online) Deviations in lattice parameter (a), cohesive energy (b), and relative bulk modulus (c) from the converged results. The largest bars have been truncated and are shown with dotted edges. See Table I for the precise values.

times faster than a grid calculation, making the cost of the LCAO optimization negligible.

Figure 5 shows a performance comparison when reusing the positions and Hessian from a LCAO-based structure optimization for a grid-based one, using the default basis set. The system is a 38-atom truncated octahedral gold cluster with CO adsorbed, with the initial and final geometries shown in the inset.

A purely grid-based optimization takes 223 CPU hours while a purely LCAO-based one, requiring roughly the same number of steps, takes 8.4 CPU hours. A further grid-based optimization takes 45 CPU hours, for a total speedup factor

TABLE I. Lattice parameter (top), cohesive energy (middle), and bulk modulus (bottom) calculated using different basis sets.

a (Å)

	SZ	SZP	DZ	DZP	GRID
LiF	4.08	4.08	4.02	4.10	4.06
C	3.61	3.58	3.59	3.58	3.57
Na	4.18	4.19	4.26	4.24	4.19
MgO	4.26	4.28	4.27	4.27	4.26
Al	4.24	4.07	4.08	4.07	4.04
NaCl	5.52	5.62	5.61	5.67	5.69
Li	3.68	3.47	3.70	3.43	3.43
SiC	4.50	4.42	4.46	4.41	4.39
Si	5.60	5.52	5.58	5.49	5.48
AlP	5.62	5.55	5.56	5.53	5.51
Fe	2.80	2.77	2.78	2.83	2.84
Cu	3.80	3.59	3.58	3.64	3.65
Pt	4.02	3.99	3.95	3.98	3.98
MAE	0.097	0.034	0.068	0.019	
MAE %	2.33	0.84	1.70	0.45	

E_c (eV)

	SZ	SZP	DZ	DZP	GRID
LiF	3.49	4.48	4.99	4.52	4.24
C	7.29	7.51	7.70	7.89	7.72
Na	0.97	1.02	1.07	1.07	1.09
MgO	2.81	4.01	4.94	4.97	4.95
Al	3.07	3.51	3.38	3.54	3.43
NaCl	2.94	3.14	3.24	3.26	3.10
Li	1.13	1.58	1.31	1.63	1.62
SiC	5.80	6.31	6.08	6.48	6.38
Si	4.14	4.52	4.34	4.71	4.55
AlP	3.77	4.09	3.92	4.21	4.08
Fe	1.34	3.83	4.77	5.07	4.85
Cu	2.38	3.97	3.75	4.14	3.51
Pt	4.54	5.33	5.57	5.69	5.35
MAE	0.86	0.25	0.19	0.18	
MAE %	20.70	5.86	5.51	4.40	

B (GPa)

	SZ	SZP	DZ	DZP	GRID
LiF	87	84	91	70	80
C	394	408	411	422	433
Na	8.9	9.1	8.3	7.9	7.9
MgO	156	184	209	173	154
Al	53	74	73	79	77
NaCl	35	32	34	26	24

TABLE I. (*Continued.*)

Li	10.8	15.2	10.7	16.3	14.2
SiC	178	196	221	202	211
Si	70	81	77	86	88
AlP	69	77	76	81	82
Fe	248	379	297	231	198
Cu	88	181	166	143	141
Pt	224	266	309	263	266
MAE	22.9	24.8	23.2	7.4	
MAE %	20.4	18.2	18.8	6.3	

of 4. The value of an initial LCAO optimization is of course higher if the initial guess is worse. For systems where a large fraction of the time is spent close to the converged geometry, the speedup may not be as significant.

The energy reference corresponds to the separate cluster and molecule at optimized geometries—the total-energy difference between an LCAO and a grid calculation is otherwise around 30 eV. It is therefore important to choose an optimization algorithm which will handle such a shift well. The present plots use the L-BFGS algorithm[22,23] (limited memory Broyden-Fletcher-Goldfarb-Shanno) from the Atomic Simulation Environment.[21]

VI. CONCLUSIONS

We have described the implementation of a localized basis in the grid-based PAW code GPAW and tested the method on a variety of molecules and solids. The results for atomization energies, cohesive energies, lattice parameters, and bulk moduli were shown to converge toward the grid results as the size of the LCAO basis was increased. Structural properties were found to be particularly accurate with the LCAO basis. It has been demonstrated how the LCAO basis can be used to produce accurate initial guesses (both for the electron wave functions, atomic structure, and Hessian matrix) for subsequent grid-based calculations to increase efficiency of high-accuracy grid calculations.

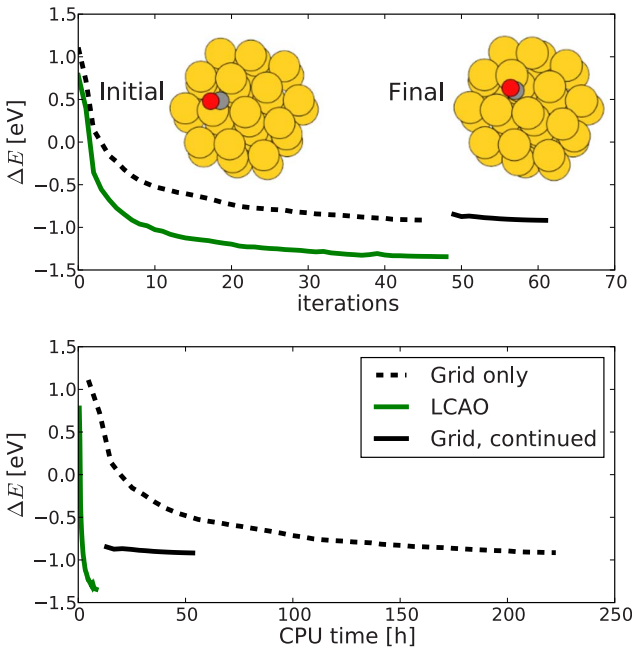

FIG. 5. (Color online) The energy as a function of iteration count (top) as well as CPU time (bottom) in structure optimizations. Shows a grid-based optimization and an LCAO-based structure optimization plus the continuation of the LCAO optimization after switching to the grid representation.

The combination of the grid-based and LCAO methods in one code provides a flexible, simple, and smooth way to switch between the two representations. Furthermore the PAW formalism itself presents significant advantages: it is an all-electron method, which eliminates pseudopotential errors and it allows the use of coarser grids than norm-conserving pseudopotentials, which increases efficiency.

Finally, the LCAO method enables GPAW to perform calculations involving Green's function, which intrinsically need a basis set with finite support. Current developments along these lines include electron-transport calculations, electron-phonon coupling, and scanning tunnel microscope simulations.

ACKNOWLEDGMENTS

The authors acknowledge support from the Danish Center for Scientific Computing through Grant No. HDW-1103-06. The Center for Atomic-scale Materials Design is sponsored by the Lundbeck Foundation.

APPENDIX: FORCE FORMULA

The force on atom a is found by taking the derivative of the total energy with respect to the atomic position $\mathbf{R}^a$. We shall use the chain rule on Eq. (17), taking $\rho_{\mu\nu}$, D^a_{ij}, $\tilde{n}(\mathbf{r})$, $\tilde{\rho}(\mathbf{r})$, $T_{\mu\nu}$, and $\bar{v}(\mathbf{r})$ to be *separate variables* for the purposes of partial derivatives,

$$\frac{\partial E}{\partial \mathbf{R}^a} = \sum_{\mu\nu} \frac{\partial E}{\partial \rho_{\nu\mu}} \frac{\partial \rho_{\nu\mu}}{\partial \mathbf{R}^a} + \sum_{bij} \frac{\partial E}{\partial D^b_{ji}} \frac{\partial D^b_{ji}}{\partial \mathbf{R}^a} + \int \frac{\delta E}{\delta \tilde{n}(\mathbf{r})} \frac{\partial \tilde{n}(\mathbf{r})}{\partial \mathbf{R}^a} d\mathbf{r} + \int \frac{\delta E}{\delta \tilde{\rho}(\mathbf{r})} \frac{\partial \tilde{\rho}(\mathbf{r})}{\partial \mathbf{R}^a} d\mathbf{r} + \sum_{\mu\nu} \frac{\partial E}{\partial T_{\mu\nu}} \frac{\partial T_{\mu\nu}}{\partial \mathbf{R}^a} + \int \frac{\delta E}{\delta \bar{v}(\mathbf{r})} \frac{\partial \bar{v}(\mathbf{r})}{\partial \mathbf{R}^a} d\mathbf{r}, \tag{A1}$$

where $\bar{v}(\mathbf{r}) = \Sigma_a \bar{v}^a(|\mathbf{r} - \mathbf{R}^a|)$. The remaining quantities in the energy expression pertain to isolated atoms and thus do not depend on atomic positions. The first term of Eq. (A1) is

$$\sum_{\mu\nu} \frac{\partial E}{\partial \rho_{\nu\mu}} \frac{\partial \rho_{\nu\mu}}{\partial \mathbf{R}^a} = 2\Re \sum_{\mu\nu n} H_{\mu\nu} c_{\nu n} f_n \frac{\partial c^*_{\mu n}}{\partial \mathbf{R}^a} = 2\Re \sum_{\mu\nu n} \frac{\partial c^*_{\mu n}}{\partial \mathbf{R}^a} S_{\mu\nu} c_{\nu n} \epsilon_n f_n, \tag{A2}$$

where we have used Eqs. (29) and (36) in the first step and Eq. (41) in the second. When the atoms are displaced (infinitesimally), the coefficients must change to accommodate the

orthogonality criterion. This can be incorporated by requiring the derivatives of each side of Eq. (39) to be equal, implying the relationship

$$-\sum_{\mu\nu} c^*_{\mu n}\frac{\partial S_{\mu\nu}}{\partial \mathbf{R}^a}c_{\nu n} = 2\Re\sum_{\mu\nu}\frac{\partial c^*_{\mu n}}{\partial \mathbf{R}^a}S_{\mu\nu}c_{\nu n}. \tag{A3}$$

Inserting this into Eq. (A2) yields

$$\sum_{\mu\nu}\frac{\partial E}{\partial \rho_{\nu\mu}}\frac{\partial \rho_{\nu\mu}}{\partial \mathbf{R}^a} = -\sum_{\mu\nu n}\frac{\partial S_{\mu\nu}}{\partial \mathbf{R}^a}c_{\nu n}\epsilon_n f_n c^*_{\mu n} = -\sum_{\mu\nu}\frac{\partial S_{\mu\nu}}{\partial \mathbf{R}^a}E_{\nu\mu}, \tag{A4}$$

where we have introduced the matrix

$$E_{\nu\mu} = \sum_n c_{\nu n}\epsilon_n f_n c^*_{\mu n} = \sum_{\lambda\xi} S^{-1}_{\nu\lambda}H_{\lambda\xi}\rho_{\xi\mu}. \tag{A5}$$

The equivalence of these forms follows from Eq. (41). The overlap matrix elements $S_{\mu\nu}$ depend on $\mathbf{R}^a$ through the two-center integrals $\Theta_{\mu\nu}$ and $P^b_{i\mu}$. The derivative of a two-center integral can be nonzero only if exactly one of the two involved atoms is a and for nonzero derivatives, the sign changes if the indices are swapped. Taking these issues into account, Eq. (A4) is split into those three terms in Eq. (44) which contain $E_{\nu\mu}$.

In the second term in Eq. (A1), we take the D^b_{ij}-dependent derivative for fixed $\rho_{\nu\mu}$, which by Eq. (23) evaluates to

$$\sum_{bij}\frac{\partial E}{\partial D^a_{ji}}\frac{\partial D^a_{ji}}{\partial \mathbf{R}^a} = 2\Re\sum_{bij\mu\nu} P^{b*}_{i\mu}\Delta H^b_{ij}\frac{\partial P^b_{j\nu}}{\partial \mathbf{R}^a}\rho_{\nu\mu}. \tag{A6}$$

Again most of the two-center integral derivatives are zero. A complete reduction yields the two terms in Eq. (44) which depend on the $\mathbf{A}^b_{\mu\nu}$ vectors.

Using Eq. (30), the third term of Eq. (A1) is

$$\int\frac{\delta E}{\delta \tilde{n}(\mathbf{r})}\frac{\partial \tilde{n}(\mathbf{r})}{\partial \mathbf{R}^a}d\mathbf{r} = \int \tilde{v}(\mathbf{r})\frac{\partial \tilde{n}(\mathbf{r})}{\partial \mathbf{R}^a}d\mathbf{r}$$
$$= 2\Re\sum_{\mu\nu}\left[\int\frac{\partial \Phi^*_\mu(\mathbf{r})}{\partial \mathbf{R}^a}\tilde{v}(\mathbf{r})\Phi_\nu(\mathbf{r})\right]\rho_{\nu\mu}$$
$$+\int \tilde{v}(\mathbf{r})\frac{\partial \tilde{n}^a_c(|\mathbf{r}-\mathbf{R}^a|)}{\partial \mathbf{R}^a}d\mathbf{r}. \tag{A7}$$

The sum over μ can be restricted to $\mu\in a$.

Consider the fourth term of Eq. (A1). Aside from $\tilde{n}(\mathbf{r})$ and D^b_{ij}, which are considered fixed as per the chain rule, the pseudocharge density $\tilde{\rho}(\mathbf{r})$ depends only on the locations of the compensation charge expansion functions $\tilde{g}^a_L(\mathbf{r})$ which move rigidly with the atom, so

$$\int\frac{\delta E}{\delta \tilde{\rho}(\mathbf{r})}\frac{\partial \tilde{\rho}(\mathbf{r})}{\partial \mathbf{R}^a}d\mathbf{r} = \int \tilde{v}_H(\mathbf{r})\frac{\delta\tilde{\rho}(\mathbf{r})}{\delta\tilde{Z}(\mathbf{r})}\sum_{bL}\frac{\delta\tilde{Z}(\mathbf{r})}{\delta\tilde{g}^b_L(\mathbf{r})}\frac{\partial\tilde{g}^b_L(\mathbf{r})}{\partial \mathbf{R}^a}d\mathbf{r}$$
$$= \int \tilde{v}_H(\mathbf{r})\sum_L Q^a_L\frac{\partial\tilde{g}^a_L(\mathbf{r})}{\partial \mathbf{R}^a}d\mathbf{r}. \tag{A8}$$

The kinetic term from Eq. (A1) is

$$\sum_{\mu\nu}\frac{\partial E}{\partial T_{\mu\nu}}\frac{\partial T_{\mu\nu}}{\partial \mathbf{R}^a} = \sum_{\mu\nu}\frac{\partial T_{\mu\nu}}{\partial \mathbf{R}^a}\rho_{\nu\mu} \tag{A9}$$

and can also be restricted to $\mu\in a$. Finally, the contribution from the local potential $\bar{v}^a(\mathbf{r})$ is simply

$$\int\frac{\delta E}{\delta \bar{v}(\mathbf{r})}\frac{\partial \bar{v}(\mathbf{r})}{\partial \mathbf{R}^a}d\mathbf{r} = \int \tilde{n}(\mathbf{r})\frac{\partial \bar{v}^a(\mathbf{r}-\mathbf{R}^a)}{\partial \mathbf{R}^a}d\mathbf{r}. \tag{A10}$$

By now we have considered all position-dependent variables in the energy expression and have obtained expressions for all terms present in Eq. (44).

[1] P. Hohenberg and W. Kohn, Phys. Rev. **136**, B864 (1964).
[2] W. Kohn and L. J. Sham, Phys. Rev. **140**, A1133 (1965).
[3] M. C. Payne, M. P. Teter, D. C. Allan, T. A. Arias, and J. D. Joannopoulos, Rev. Mod. Phys. **64**, 1045 (1992).
[4] L. Kleinman and D. M. Bylander, Phys. Rev. Lett. **48**, 1425 (1982).
[5] D. Vanderbilt, Phys. Rev. B **41**, 7892 (1990).
[6] C. Hartwigsen, S. Goedecker, and J. Hutter, Phys. Rev. B **58**, 3641 (1998).
[7] P. E. Blöchl, Phys. Rev. B **50**, 17953 (1994).
[8] G. Kresse and J. Hafner, Phys. Rev. B **47**, 558 (1993).
[9] B. Hammer, L. B. Hansen, and J. K. Nørskov, Phys. Rev. B **59**, 7413 (1999).
[10] L. Genovese, A. Neelov, S. Goedecker, T. Deutsch, A. Ghasemi, O. Zilberberg, A. Bergman, M. Rayson, and R. Schneider, J. Chem. Phys. **129**, 014109 (2008).
[11] T. A. Arias, Rev. Mod. Phys. **71**, 267 (1999).
[12] E. L. Briggs, D. J. Sullivan, and J. Bernholc, Phys. Rev. B **54**, 14362 (1996).
[13] J. J. Mortensen, L. B. Hansen, and K. W. Jacobsen, Phys. Rev. B **71**, 035109 (2005).
[14] Gaussian 03, Revision C.02, Gaussian, Inc., Wallingford CT, (2004).
[15] O. F. Sankey and D. J. Niklewski, Phys. Rev. B **40**, 3979 (1989).
[16] J. M. Soler, E. Artacho, J. D. Gale, A. García, J. Junquera, P. Ordejón, and D. Sanchez-Portal, J. Phys.: Condens. Matter **14**, 2745 (2002).
[17] J. Junquera, O. Paz, D. Sanchez-Portal, and E. Artacho, Phys. Rev. B **64**, 235111 (2001).
[18] http://wiki.fysik.dtu.dk/gpaw/setups/setups.html
[19] J. P. Perdew, K. Burke, and M. Ernzerhof, Phys. Rev. Lett. **77**, 3865 (1996).
[20] L. A. Curtiss, Krishnan Raghavachari, P. C. Redfern, and J. A. Pople, J. Chem. Phys. **106**, 1063 (1997).
[21] S. Bahn and K. W. Jacobsen, Comput. Sci. Eng. **4**, 56 (2002).
[22] D. Sheppard, R. Terrell, and G. Henkelman, J. Chem. Phys. **128**, 134106 (2008).
[23] J. Nocedal, Math. Comput. **35**, 773 (1980).

Paper II: Electronic structure calculations with GPAW: a real-space implementation of the projector augmented-wave method

J. Phys.: Condens. Matter **22** (2010) 253202 (24pp) doi:10.1088/0953-8984/22/25/253202

TOPICAL REVIEW

Electronic structure calculations with GPAW: a real-space implementation of the projector augmented-wave method

J Enkovaara[1], C Rostgaard[2], J J Mortensen[2], J Chen[2], M Dułak[2], L Ferrighi[3], J Gavnholt[4], C Glinsvad[2], V Haikola[5], H A Hansen[2], H H Kristoffersen[3], M Kuisma[6], A H Larsen[2], L Lehtovaara[5], M Ljungberg[7], O Lopez-Acevedo[8], P G Moses[2], J Ojanen[6], T Olsen[4], V Petzold[2], N A Romero[9], J Stausholm-Møller[3], M Strange[2], G A Tritsaris[2], M Vanin[2], M Walter[10], B Hammer[3], H Häkkinen[8], G K H Madsen[11], R M Nieminen[5], J K Nørskov[2], M Puska[5], T T Rantala[6], J Schiøtz[4], K S Thygesen[2] and K W Jacobsen[2]

[1] CSC—IT Center for Science Ltd, PO Box 405 FI-02101 Espoo, Finland
[2] Center for Atomic-scale Materials Design, Department of Physics, Technical University of Denmark, DK-2800 Kongens Lyngby, Denmark
[3] Interdisciplinary Nanoscience Center (iNANO) and Department of Physics and Astronomy, Aarhus University, DK-8000 Aarhus C, Denmark
[4] Danish National Research Foundation's Center for Individual Nanoparticle Functionality (CINF), Technical University of Denmark, DK-2800 Kongens Lyngby, Denmark
[5] Department of Applied Physics, Aalto University School of Science and Technology, PO Box 11000, FIN-00076 Aalto, Espoo, Finland
[6] Department of Physics, Tampere University of Technology, PO Box 692, FI-33101 Tampere, Finland
[7] FYSIKUM, Stockholm University, Albanova University Center, SE-10691 Stockholm, Sweden
[8] Departments of Physics and Chemistry, Nanoscience Center, University of Jyväskylä, PO Box 35 (YFL), FI-40014, Finland
[9] Leadership Computing Facility, Argonne National Laboratory, Argonne, IL, USA
[10] Freiburg Materials Research Center, Stefan-Meier-Strasse 21, 79104 Freiburg, Germany
[11] ICAMS, Ruhr Universität Bochum, 44801 Bochum, Germany

Received 6 April 2010, in final form 14 May 2010
Published 10 June 2010
Online at stacks.iop.org/JPhysCM/22/253202

Abstract
Electronic structure calculations have become an indispensable tool in many areas of materials science and quantum chemistry. Even though the Kohn–Sham formulation of the density-functional theory (DFT) simplifies the many-body problem significantly, one is still confronted with several numerical challenges. In this article we present the projector augmented-wave (PAW) method as implemented in the GPAW program package (https://wiki.fysik.dtu.dk/gpaw) using a uniform real-space grid representation of the electronic wavefunctions. Compared to more traditional plane wave or localized basis set approaches, real-space grids offer several advantages, most notably good computational scalability and systematic convergence properties. However, as a unique feature GPAW also facilitates a localized atomic-orbital basis set in addition to the grid. The efficient atomic basis set is complementary to the more accurate grid, and the possibility to seamlessly switch between the two representations provides great flexibility. While DFT allows one to study ground state properties, time-dependent density-functional theory (TDDFT) provides access to the excited

states. We have implemented the two common formulations of TDDFT, namely the linear-response and the time propagation schemes. Electron transport calculations under finite-bias conditions can be performed with GPAW using non-equilibrium Green functions and the localized basis set. In addition to the basic features of the real-space PAW method, we also describe the implementation of selected exchange–correlation functionals, parallelization schemes, ΔSCF-method, x-ray absorption spectra, and maximally localized Wannier orbitals.

(Some figures in this article are in colour only in the electronic version)

Contents

1. Introduction 2
2. General overview 3
   2.1. Projector augmented-wave method 3
   2.2. Atomic setups 5
   2.3. Uniform 3d real-space grids 5
   2.4. Localized functions and Fourier filtering 5
   2.5. Iterative solution of eigenproblem 6
   2.6. Density mixing 6
3. Exchange–correlation functionals in GPAW 6
   3.1. Meta-GGA 6
   3.2. Exact exchange 7
   3.3. GLLB approximation for the exact exchange 8
   3.4. van der Waals functional 9
4. Error estimation 11
5. Time-dependent density-functional theory 12
   5.1. Real-time propagation 12
   5.2. Linear-response formalism 12
   5.3. Optical absorption spectra 12
   5.4. Non-linear emission spectra 13
   5.5. Photoelectron spectra 13
6. Localized atomic-like basis functions 14
   6.1. Non-equilibrium electron transport 15
7. Additional features 16
   7.1. Δ*SCF* 16
   7.2. X-ray absorption spectra 17
   7.3. Wannier orbitals 18
   7.4. Local properties 19
8. Parallel calculations 20
9. Summary and outlook 21
Acknowledgments 21
References 22

1. Introduction

Electronic structure calculations have become an indispensable tool for simulations of condensed-matter systems. Nowadays systems ranging from atoms and small molecules to nanostructures with several hundreds of atoms are studied routinely with density-functional theory (DFT) [1, 2].

In principle, only ground state properties such as total energies and equilibrium geometries can be investigated with DFT. However, several interesting material properties such as excitation energies and optical spectra are related to the excited states of a system. These excited state properties can be studied with time-dependent density-functional theory (TDDFT) [3].

Even though the DFT equations are much easier to solve than the full many-body Schrödinger equation, several numerical approximations are usually made. The approximations can be related to the treatment of core electrons and the region near the atomic nuclei (pseudopotential versus all-electron methods) [4–8] or to the discretization of equations (plane waves, localized orbitals, real-space grids, finite elements) [9–19]. In this work, we present a real-space-based implementation of the projector augmented-wave (PAW) method in the open-source program package GPAW [20]. We note that there are several software packages that currently implement the PAW method using a plane-wave basis [21–23].

The PAW method [7, 24] is formally an all-electron method which provides an exact transformation between the smooth pseudo-wavefunctions and the all-electron wavefunctions. While in practical implementations the PAW method resembles pseudopotential methods, it addresses several shortcomings of norm-conserving or ultrasoft pseudopotentials. The PAW method offers a reliable description over the whole periodic table with good transferability of PAW potentials. The pseudo-wavefunctions in the PAW method are typically smoother compared to norm-conserving pseudopotential methods so that the wavefunctions can be represented with fewer degrees of freedom. The PAW approximation contains all the information about the nodal structure of wavefunctions near the nuclei, and it is always possible to reconstruct the all-electron wavefunctions from the pseudo-wavefunctions.

In the solid state community, plane-wave basis sets [9, 22, 25, 26] are the most popular choice for discretizing the density-functional equations while localized basis sets [11, 27] have been more popular in quantum chemistry. A more recent approach is the use of uniform real-space grids [13, 28–30]. Real-space methods provide several advantages over plane waves. A plane-wave basis imposes periodic boundary conditions, while a real-space grid can flexibly treat both free and periodic boundary conditions. The plane-wave method relies heavily on fast Fourier transforms, which are difficult to parallelize efficiently due to the non-local nature of the operations. On the other hand, in real space it is possible to work entirely with local and semi-local operations, which enables efficient parallelization with small communication overhead. The accuracy of a real-space representation can be increased systematically by decreasing the grid spacing, similar to increasing the kinetic energy cutoff in a plane-wave calculation. This systematic improvement of accuracy is also the main advantage of both real-space and plane-wave methods compared to localized basis sets, where the accuracy of representation cannot be controlled as systematically. However, as localized functions can provide a very compact basis set, we have also implemented atom-centered basis

functions for situations where the high accuracy of a real-space grid is not needed. The atom-centered basis is especially convenient in the context of electron transport calculations within the non-equilibrium Green function approach also implemented in GPAW. To our knowledge, GPAW is the first publicly available package to implement the PAW method with uniform real-space grids and atom-centered localized orbitals.

In tandem with numerical approximations, physical approximations are needed in DFT since the exact form of the exchange–correlation (XC) functional is unknown. The traditional local density and generalized gradient approximations have been surprisingly successful, but due to well-known shortcomings, there are continuing efforts to go beyond them. Some of the new developments in this field, such as meta-GGA and exact-exchange-based approximations are available in GPAW.

Time-dependent density-functional theory (TDDFT) can be realized in two different formalism. In the most general form, the time-dependent Kohn–Sham equations are integrated over the time-domain [31]. In the linear-response regime it is also possible to obtain excitation energies by solving a matrix equation in an electron–hole basis [32]. The real-time propagation and the linear-response approaches are complementary. For example, the linear-response scheme provides all the excitations in a single calculation, while the real-time formalism provides the excitations corresponding to a given initial perturbation. On the other hand, the real-time propagation scheme can also address non-linear effects. While the linear-response scheme is more efficient for small systems, the real-time propagation approach scales more favorably with system size. Both the linear-response and real-time forms are implemented in GPAW, to our knowledge for the first time within the PAW method.

In addition to the standard total energy calculations, GPAW contains several more specific features. For example, excitation energies can be estimated with the ΔSCF method [33] as an alternative to the TDDFT approaches. X-ray absorption spectra and maximally localized Wannier functions can also be calculated.

This article is organized as follows. First, the general features of the PAW method and the implementation on a real-space grid are described in section 2. In section 3 we give an overview of the different exchange–correlation functionals available, and in section 4 we discuss a recent method for error estimations within DFT. An overview of TDDFT is presented in section 5, and the localized basis set and its use in finite-bias transport calculations are described in section 6. In section 7, other features, such as ΔSCF, x-ray absorption spectra and Wannier functions are described. The parallelization strategy and parallel scaling are presented in section 8. Finally, we provide a summary and an outlook in section 9.

2. General overview

In this section, we present the main features of our PAW implementation. Some of the details have been published earlier [34], so we provide here a general overview and discuss in more detail only the parts where our approach has changed from the earlier publication. The notation is similar to the one used in the original references [7]. We use Hartree atomic units ($\hbar = m = e = \frac{4\pi}{\epsilon_0} = 1$) throughout the article. Generally, the equations are written for the case of a spin-paired and finite system of electrons and the spin and k-point indices are included when necessary.

2.1. Projector augmented-wave method

In the Kohn–Sham formulation of DFT, we work with single-particle all-electron wavefunctions to describe core, semi-core and valence states. The PAW method is a linear transformation between smooth valence (and semi-core) pseudo (PS) wavefunctions, $\tilde{\psi}_n$ (n is the state index) and all-electron (AE) wavefunctions, ψ_n. The core states of the atoms, $\phi_i^{a,\mathrm{core}}$, are fixed to the reference shape for the isolated atom. Here a is an atomic index and i is a combination index for the principal, angular momentum, and magnetic quantum numbers respectively (n, ℓ and m). Note, that the PAW method can be extended beyond the frozen core approximation [35], but we have not done that.

Given a smooth PS wavefunction, the corresponding AE wavefunction, which is orthogonal to the set of $\phi_i^{a,\mathrm{core}}$ orbitals, can be obtained through a linear transformation

$$\psi_n(\mathbf{r}) = \hat{\mathcal{T}}\tilde{\psi}_n(\mathbf{r}). \tag{1}$$

The transformation operator, $\hat{\mathcal{T}}$, is given in terms of atom-centered AE partial waves, $\phi_i^a(\mathbf{r})$, the corresponding smooth partial waves, $\tilde{\phi}_i^a(\mathbf{r})$, and projector functions, $\tilde{p}_i^a(\mathbf{r})$, as

$$\hat{\mathcal{T}} = 1 + \sum_a \sum_i (|\phi_i^a\rangle - |\tilde{\phi}_i^a\rangle)\langle\tilde{p}_i^a|, \tag{2}$$

where atom a is at the position $\mathbf{R}^a$. The defining properties of the atom-centered functions are that AE partial waves and smooth PS partial waves are equal outside atom-centered augmentation spheres of radii r_c^a,

$$\phi_i^a(\mathbf{r}) = \tilde{\phi}_i^a(\mathbf{r}), \qquad |\mathbf{r} - \mathbf{R}^a| > r_\mathrm{c}^a \tag{3}$$

and that the projector functions are localized inside the augmentation spheres and are orthogonal to the PS partial waves

$$\langle\tilde{p}_{i_1}^a|\tilde{\phi}_{i_2}^a\rangle = \delta_{i_1 i_2}. \tag{4}$$

In principle, an infinite number of atom-centered partial waves and projectors is required for the PAW transformation to be exact. However, in practical calculations it is usually enough to include one or two functions per angular momentum channel. The projectors and partial waves are constructed from an AE calculation for a spherically symmetric atom.

Inside the augmentation sphere of atom a, we can define one-center expansions of an AE and PS state as [7]

$$\psi_n^a(\mathbf{r}) = \sum_i P_{in}^a \phi_i^a(\mathbf{r}) \tag{5}$$

and

$$\tilde{\psi}_n^a(\mathbf{r}) = \sum_i P_{in}^a \tilde{\phi}_i^a(\mathbf{r}), \tag{6}$$

where the expansion coefficients are

$$P_{in}^a = \langle\tilde{p}_i^a|\tilde{\psi}_n\rangle. \tag{7}$$

For a complete set of partial waves, we have $\psi_n = \psi_n^a$ and $\tilde{\psi}_n = \tilde{\psi}_n^a$ for $|\mathbf{r} - \mathbf{R}^a| < r_c^a$, which leads to

$$\psi_n = \tilde{\psi}_n + \sum_a (\psi_n^a - \tilde{\psi}_n^a). \tag{8}$$

Here, the term in the parenthesis is a correction inside the augmentation spheres only.

We define a PS electron density

$$\tilde{n}(\mathbf{r}) = \sum_n f_n |\tilde{\psi}_n(\mathbf{r})|^2 + \sum_a \tilde{n}_c^a(\mathbf{r}), \tag{9}$$

where f_n are occupation numbers between 0 and 2, and $\tilde{n}_c^a$ is a smooth PS core density equal to the AE core density n_c^a outside the augmentation sphere. From the atomic density matrix $D_{i_1 i_2}^a$

$$D_{i_1 i_2}^a = \sum_n \langle \tilde{\psi}_n | \tilde{p}_{i_1}^a \rangle f_n \langle \tilde{p}_{i_2}^a | \tilde{\psi}_n \rangle, \tag{10}$$

we define one-center expansions of the AE and PS densities,

$$n^a(\mathbf{r}) = \sum_{i_1, i_2} D_{i_1 i_2}^a \phi_{i_1}^a(\mathbf{r}) \phi_{i_2}^a(\mathbf{r}) + n_c^a(\mathbf{r}), \tag{11}$$

and

$$\tilde{n}^a(\mathbf{r}) = \sum_{i_1, i_2} D_{i_1 i_2}^a \tilde{\phi}_{i_1}^a(\mathbf{r}) \tilde{\phi}_{i_2}^a(\mathbf{r}) + \tilde{n}_c^a(\mathbf{r}), \tag{12}$$

respectively.

From $\tilde{n}$, n^a and $\tilde{n}^a$, we can construct the AE density in terms of a smooth part and atom-centered corrections

$$n(\mathbf{r}) = \tilde{n}(\mathbf{r}) + \sum_a (n^a(\mathbf{r}) - \tilde{n}^a(\mathbf{r})). \tag{13}$$

The PAW total energy expression has three contributions: kinetic, Coulomb and XC energy, all of which are composed of a PS part and atomic corrections. For the kinetic energy, we get

$$\tilde{E}_{\text{kin}} = -\tfrac{1}{2} \sum_n f_n \int \mathrm{d}\mathbf{r}\, \tilde{\psi}_n(\mathbf{r}) \nabla^2 \tilde{\psi}_n(\mathbf{r}), \tag{14}$$

$$\Delta E_{\text{kin}}^a = -\tfrac{1}{2} 2 \sum_i^{\text{core}} \int \mathrm{d}\mathbf{r}\, \phi_i^a(\mathbf{r}) \nabla^2 \phi_i^a(\mathbf{r}) - \tfrac{1}{2} \sum_{i_1 i_2} D_{i_1 i_2}^a \int \mathrm{d}\mathbf{r}\, (\phi_{i_1}^a(\mathbf{r}) \nabla^2 \phi_{i_2}^a(\mathbf{r}) - \tilde{\phi}_{i_1}^a(\mathbf{r}) \nabla^2 \tilde{\phi}_{i_2}^a(\mathbf{r})). \tag{15}$$

Before we can write down the expression for the PAW Coulomb energy, we must define one-center AE and PS charge densities

$$\rho^a(\mathbf{r}) = n^a(\mathbf{r}) - \mathcal{Z}^a \delta(\mathbf{r} - \mathbf{R}^a), \tag{16}$$

$$\tilde{\rho}^a(\mathbf{r}) = \tilde{n}^a(\mathbf{r}) + \sum_{\ell m} Q_{\ell m}^a \hat{g}_{\ell m}^a(\mathbf{r}), \tag{17}$$

where $\mathcal{Z}^a$ is the atomic number of atom a, $\hat{g}_{\ell m}^a(\mathbf{r}) = \hat{g}_\ell^a(|\mathbf{r} - \mathbf{R}^a|) Y_{\ell m}(\mathbf{r} - \mathbf{R}^a)$ is a shape function localized inside the augmentation sphere fulfilling $\int r^2 \,\mathrm{d}r\, r^\ell \hat{g}_\ell^a(r) = 1$, and $Q_{\ell m}^a$ are multipole moments that we choose as described below. We define a PS charge density as

$$\tilde{\rho}(\mathbf{r}) = \tilde{n}(\mathbf{r}) + \sum_a \sum_{\ell m} Q_{\ell m}^a \hat{g}_{\ell m}^a(\mathbf{r}), \tag{18}$$

so that the AE charge density is $\rho = \tilde{\rho} + \sum_a (\rho^a - \tilde{\rho}^a)$. By choosing $Q_{\ell m}^a$ so that ρ^a and $\tilde{\rho}^a$ have the same multipole moments, augmentation spheres on different atoms will be electrostatically decoupled and the Coulomb energy is simply

$$\tilde{E}_{\text{coul}} = \frac{1}{2} \int \mathrm{d}\mathbf{r}\, \mathrm{d}\mathbf{r}'\, \frac{\tilde{\rho}(\mathbf{r}) \tilde{\rho}(\mathbf{r}')}{|\mathbf{r} - \mathbf{r}'|}, \tag{19}$$

$$\Delta E_{\text{coul}}^a = \frac{1}{2} \int \mathrm{d}\mathbf{r}\, \mathrm{d}\mathbf{r}'\, \frac{\rho^a(\mathbf{r}) \rho^a(\mathbf{r}') - \tilde{\rho}^a(\mathbf{r}) \tilde{\rho}^a(\mathbf{r}')}{|\mathbf{r} - \mathbf{r}'|}. \tag{20}$$

For local and semi-local XC functionals, the contributions to the XC energy is

$$\tilde{E}_{\text{xc}} = E_{\text{xc}}[\tilde{n}], \tag{21}$$

$$\Delta E_{\text{xc}}^a = E_{\text{xc}}[n^a] - E_{\text{xc}}[\tilde{n}^a]. \tag{22}$$

There is one extra term in the PAW total energy expression which does not have a physical origin

$$\tilde{E}_{\text{zero}} = \int \mathrm{d}\mathbf{r}\, \tilde{n}(\mathbf{r}) \sum_a \bar{v}^a(\mathbf{r}), \tag{23}$$

$$\Delta E_{\text{zero}}^a = -\int \mathrm{d}\mathbf{r}\, \tilde{n}^a(\mathbf{r}) \bar{v}^a(\mathbf{r}). \tag{24}$$

The only restriction in the choice of the so called zero potential (or local potential) $\bar{v}^a$ is that it must be zero outside the augmentation sphere of atom a. For a complete set of partial waves and projectors, $\tilde{E}_{\text{zero}} + \sum_a \Delta E_{\text{zero}}^a$ is exactly zero, but for practical calculations with a finite number of partial waves and projector functions, $\bar{v}^a$ can be used to improve the accuracy of a PAW calculation [36].

The final expression for the energy is

$$E = \tilde{E} + \sum_a \Delta E^a \tag{25}$$

$$= \tilde{E}_{\text{kin}} + \tilde{E}_{\text{coul}} + \tilde{E}_{\text{xc}} + \tilde{E}_{\text{zero}} + \sum_a (\Delta E_{\text{kin}}^a + \Delta E_{\text{coul}}^a + \Delta E_{\text{xc}}^a + \Delta E_{\text{zero}}^a). \tag{26}$$

The smooth PS wavefunctions $\tilde{\psi}_n$ are orthonormal only with respect to the PAW overlap operator $\hat{S}$: $\langle \tilde{\psi}_n | \hat{S} | \tilde{\psi}_m \rangle = \delta_{nm}$, where

$$\hat{S} = \hat{\mathcal{T}}^\dagger \hat{\mathcal{T}} = 1 + \sum_a \sum_{i_1 i_2} |\tilde{p}_{i_1}^a\rangle \Delta S_{i_1 i_2}^a \langle \tilde{p}_{i_2}^a|, \tag{27}$$

$$\Delta S_{i_1 i_2}^a = \langle \phi_{i_1}^a | \phi_{i_2}^a \rangle - \langle \tilde{\phi}_{i_1}^a | \tilde{\phi}_{i_2}^a \rangle. \tag{28}$$

This leads to the generalized eigenproblem

$$\hat{H} \tilde{\psi}_n = \epsilon_n \hat{S} \tilde{\psi}_n, \tag{29}$$

where

$$\hat{H} = -\tfrac{1}{2} \nabla^2 + \tilde{v} + \sum_a \sum_{i_1 i_2} |\tilde{p}_{i_1}^a\rangle \Delta H_{i_1 i_2}^a \langle \tilde{p}_{i_2}^a|, \tag{30}$$

$$\Delta H_{i_1 i_2}^a = \frac{\partial \Delta E^a}{\partial D_{i_1 i_2}^a} + \int \mathrm{d}\mathbf{r}\, \tilde{v}_{\text{coul}}(\mathbf{r}) \frac{\partial \tilde{\rho}(\mathbf{r})}{\partial D_{i_1 i_2}^a}, \tag{31}$$

and the effective potential

$$\tilde{v} = \frac{\delta \tilde{E}}{\delta \tilde{n}} = \tilde{v}_{\text{coul}} + \tilde{v}_{\text{xc}} + \sum_a \bar{v}^a, \tag{32}$$

where the Coulomb potential satisfies the Poisson equation $\nabla^2 \tilde{v}_{\text{coul}} = -4\pi \tilde{\rho}$ and $\tilde{v}_{\text{xc}}$ is the XC potential.

2.2. Atomic setups

For each type of atom, we construct an atomic setup consisting of the following quantities: ϕ_i^a, $\tilde{\phi}_i^a$, $\tilde{p}_i^a$, n_c^a, $\tilde{n}_c^a$, $\hat{g}_{\ell m}$, $\bar{v}^a$ and r_c^a. From a scalar-relativistic reference calculation for the isolated neutral spin-paired spherically symmetric atom, we calculate the required AE partial waves ϕ_i^a and the core density n_c^a. We choose a cutoff radius r_c^a for the augmentation sphere and a shape for $\hat{g}_{\ell m}$, which is usually a Gaussian. The smooth PS partial waves $\tilde{\phi}_i^a$ and the smooth PS core density $\tilde{n}_c^a$ are constructed by smooth continuation of ϕ_i^a and n_c^a, respectively, inside the augmentation sphere. The projector functions $\tilde{p}_i^a$ are constructed as described in [7] and $\bar{v}^a$ is chosen so that the effective potential $\tilde{v}$ becomes as smooth as possible or to produce good scattering of f-states [36]. For more details, see [34].

All the functions in an atomic setup are of the form of a radial function times spherical harmonics and each radial function is tabulated on a radial grid. Since ϕ_i^a and n_c^a can contain tightly bound localized electrons, the radial grid used has a higher grid density close to $r = 0$ than further from the nucleus (we use $r_i = \beta i/(N - i)$ for $i = 0, 1, \ldots, N$). All the functions comprising a setup need only be known for $r < r_c^a$, except for $\tilde{\phi}_i^a$ and $\tilde{n}_c^a$, which are used also for initialization of wavefunctions and density.

2.3. Uniform 3d real-space grids

Uniform real-space grids provide a simple discretization for the Kohn–Sham and Poisson equations. Physical quantities such as wavefunctions, densities, and potentials are represented by the values at the grid points. Derivatives are calculated using finite differences. The accuracy of discretization is determined by the grid spacing and the finite difference approximations used for the derivatives.

For a general unit cell with lattice vectors $\mathbf{a}_\alpha$ ($\alpha = 1, 2, 3$) and N_α grid points along the three directions, we define grid spacing vectors $\mathbf{h}_\alpha = \mathbf{a}_\alpha/N_\alpha$. For an orthorhombic unit cell, the Laplacian is discretized as

$$\nabla^2 f(\mathbf{r}) = \sum_{\alpha=1}^{D} \sum_{n=-N}^{N} b_\alpha c_n^N f(\mathbf{r} + n\mathbf{h}_\alpha) + \mathrm{O}(h^{2N}), \qquad (33)$$

where $D = 3$, $b_\alpha = 1/h_\alpha^2$ and c_n^N are the Nth order finite difference coefficients for the second derivative expansion.

In the case of a non-orthorhombic unit cell, we extend the set of grid spacing vectors with more nearest neighbor directions. The D coefficients b_α are determined by the conventional method of undetermined coefficients, inserting the six functions $f(\mathbf{r}) = x^2, y^2, z^2, xy, yz, zx$ in equation (33) and solving for b_α at $\mathbf{r} = (0, 0, 0)$. The number of directions needed to satisfy the six equations depends on the symmetry of the lattice: For hexagonal or body-centered cubic symmetry, $D = 4$ directions are needed, while $D = 6$ directions are used for a face-centered cubic cell or a general unit cell without any symmetry. This procedure allows for finite difference stencils with only $1 + 2DN$ points, which is similar to the stencils defined by Natan *et al* [37].

It must be noted that the performance of a given stencil is to an extent structure-dependent. For example, for calculations of individual molecules, where large gradients are present, a more compact stencil may outperform a higher accuracy but less compact one. However, good accuracy is typically obtained for a combination of a grid spacing of $h = 0.2$ Å and a finite difference stencil with $\mathrm{O(h^6)}$ error for the kinetic energy.

The PS electron density is evaluated on the same grid as the wavefunctions. It is then interpolated to a finer grid with a grid spacing of $h/2$, where the XC energy and potential are calculated. The fine grid is also used for constructing the PS charge density and for solving the Poisson equation. The discretization of the Poisson equation is done with a finite difference stencil like equation (33) with an error of $\mathrm{O(h^6)}$. For orthorhombic unit cells a more compact Mehrstellen-type stencil [16] can also be used for solving the Poisson equation. The effective potential, equation (32), is then restricted to the coarse grid where it can be applied to the wavefunctions.

Boundary conditions for the quantities represented on 3d grids can be zero for an isolated system or periodic for a periodic system (or any combination). When using **k**-point sampling, a wavefunction can also have Bloch-type boundary conditions

$$\tilde{\psi}_{n\mathbf{k}}(\mathbf{r} + \mathbf{R}) = \tilde{\psi}_{n\mathbf{k}}(\mathbf{r}) \mathrm{e}^{\mathrm{i}\mathbf{k}\cdot\mathbf{R}}, \qquad (34)$$

where $\mathbf{R}$ is any Bravais vector. For charged systems, the boundary condition for $\tilde{v}_{\mathrm{coul}}$ can be determined from a multipole expansion.

2.4. Localized functions and Fourier filtering

Special care is needed when dealing with integrals involving products of localized functions centered on an atom and functions spanning the whole simulation cell. As an example, consider the projection of a wavefunction onto a projector function $\tilde{p}_i^a(\mathbf{r}) = \tilde{p}_{n_i\ell_i}^a(|\mathbf{r}-\mathbf{R}^a|)Y_{\ell_i m_i}(\mathbf{r}-\mathbf{R}^a)$ centered on atom a. This integral is approximated by a sum over grid points:

$$\langle \tilde{p}_i^a | \tilde{\psi} \rangle = \sum_{\mathrm{g}} \tilde{p}_i^a(\mathbf{r}_\mathrm{g}) \tilde{\psi}(\mathbf{r}_\mathrm{g}) \Delta v, \qquad (35)$$

where Δv is the volume per grid point. In order to make the integration as accurate as possible, it is important that the radial function $\tilde{p}_{n_i\ell_i}^a(r)$ contains as few short wavelength components as possible. To achieve this, we Fourier filter our projector functions using the mask function technique [38]. Here, the radial function is divided by a mask function that goes smoothly to zero at approximately twice the original cutoff radius. We use $m(r) = \exp(-\gamma r^2)$. After a Fourier transform, the short wavelength components are cut off by multiplying the spectrum by a smooth cutoff function. Transforming back to real-space, the final result is obtained by multiplying by $m(r)$, which will remove the oscillating and decaying tail beyond the cutoff of the chosen mask function.

In the PAW formalism, there are four different types of localized functions that need to be evaluated on the grid points: projector functions $\tilde{p}_i^a$, the zero potential $\bar{v}^a$, the shape functions $\hat{g}_{\ell m}^a$ (for the compensation charges), and the PS core density $\tilde{n}_c^a$; we apply the mask function technique to $\tilde{p}_i^a$ and

$\bar{v}^a$. The radial part of the shape functions are chosen as $r^\ell e^{-\alpha^a r^a}$ and are therefore optimally smooth [39], and the PS core densities can always be chosen very smooth.

2.5. Iterative solution of eigenproblem

The Hamiltonian and overlap operators appearing in the generalized eigenvalue problem equation (29) are large sparse matrices in the real-space grid representation. Due to the large size of the matrices, direct diagonalization schemes which scale $O(N^3)$ with the matrix size are not tractable. On the other hand, sparsity of the matrices makes iterative diagonalization schemes [9, 40] appealing due to their dominant $O(N^2)$ scaling.

We have implemented three different iterative eigensolvers which share some common ingredients: the residual minimization method-direct inversion in iterative subspace (RMM-DIIS) [41, 40], the conjugate gradient method [9, 42], and Davidson's method [43, 40]. A basic concept in all the methods is the update of the eigenvectors $\tilde{\psi}_n$ with the residuals

$$R_n = (\hat{H} - \epsilon_n \hat{S})\tilde{\psi}_n. \tag{36}$$

The convergence of iterative methods can be accelerated with preconditioning, and we calculate preconditioned residuals $\tilde{R}_n = \hat{P} R_n$, by solving approximately a Poisson equation

$$\tfrac{1}{2}\nabla^2 \tilde{R}_n = R_n \tag{37}$$

with a multigrid method [16].

A subspace diagonalization is always performed before the iteration steps. The RMM-DIIS method does not conserve the orthonormality of eigenvectors, and thus explicit orthonormalization is done after each RMM-DIIS step. A good initial guess for the wavefunctions is especially important for the robustness of the RMM-DIIS algorithm. We take the initial guess from an atomic orbital basis calculation, the details of which are described in section 6.

2.6. Density mixing

During the self-consistency cycles both wavefunctions and the density are updated iteratively. New PS density $\tilde{n}(\mathbf{r})$ and atomic density matrices $D^a_{i_1 i_2}$ are calculated from the wavefunctions, equations (9) and (10) and mixed with the old densities using Pulay's method [44, 40].

Pulay's method requires a good metric $\hat{M}$ for measuring the change from input to output density $\langle \Delta\tilde{n}|\hat{M}|\Delta\tilde{n}\rangle$, where $\Delta\tilde{n} = \tilde{n}_{\text{out}} - \tilde{n}_{\text{in}}$, in order to determine the optimal linear combination of old output densities. It is important that $\hat{M}$ puts more weight on long wavelength changes, as these can introduce charge sloshing in systems with many states at the Fermi level [40], who, for example, use the metric

$$\hat{M} = \sum_q f_q |\mathbf{q}\rangle\langle\mathbf{q}|, \qquad \text{with } f_q = \frac{q^2 + q_1^2}{q^2}, \tag{38}$$

where $q_1 \sim 1$ and $|\mathbf{q}\rangle$ is a plane wave with wavevector $\mathbf{q}$. Expressed on a real-space grid, where $|\mathbf{R}\rangle$ is a grid point at $\mathbf{R}$, we have

$$\hat{M} = \sum_{\mathbf{R}\mathbf{R}'} M_{\mathbf{R}\mathbf{R}'} |\mathbf{R}\rangle\langle\mathbf{R}'|, \qquad \text{with } M_{\mathbf{R}\mathbf{R}'} = \sum_{\mathbf{q}} f_q e^{i\mathbf{q}\cdot(\mathbf{R}'-\mathbf{R})}. \tag{39}$$

We would like to calculate scalar products from the density on the real-space grid, but the non-locality of equation (39) makes this intractable. We therefore seek a more local metric $\hat{M}$, which can be represented as a finite difference operator

$$\hat{M} = \sum_{\mathbf{R}} \sum_{i=0}^{N} \sum_{\mathbf{v}\in\mathcal{V}_i} c_i |\mathbf{R}\rangle\langle\mathbf{R}+\mathbf{v}|, \tag{40}$$

where $\mathcal{V}_i$ is the set of vectors pointing to the ith nearest neighbors of a grid point. We enforce $\hat{M}$ to be semi-local by including only up to Nth nearest neighbors. In reciprocal space $\hat{M}$ has matrix elements

$$\tilde{f}_{\mathbf{q}} = \langle\mathbf{q}|\hat{M}|\mathbf{q}'\rangle = \sum_i c_i \sum_{\mathbf{v}\in\mathcal{V}_i} e^{i\mathbf{q}\cdot\mathbf{v}} \delta_{\mathbf{q},\mathbf{q}'}. \tag{41}$$

The coefficients c_i should be determined so that equation (41) mimics the behavior of f_q in equation (38). This means that $\tilde{f}_{\mathbf{q}}$ should decay monotonically from a weight factor $w > 1$ at $q = 0$–1 for the largest wavevectors at the zone boundary in reciprocal space: $\tilde{f}^{(3)}_{(\pi/h,q_y,q_z)} = 1$ for $|q_y| \leqslant \pi/h$ and $|q_z| \leqslant \pi/h$. For an orthorhombic grid with grid spacing h, including up to 3rd nearest neighbors, we can fulfil these boundary conditions with the coefficients

$$c_0 = \frac{w+7}{8}, \qquad c_1 = \frac{w-1}{16}, \qquad c_2 = \frac{w-1}{32}, \qquad c_3 = \frac{w-1}{64}. \tag{42}$$

We find the metric to improve convergence significantly when there are many states near the Fermi level. A value of $w = 100$ seems to be a good choice.

3. Exchange–correlation functionals in GPAW

The exact form of the exchange–correlation (XC) functional in the DFT is not known. Thus, it has to be approximated, which constitutes the fundamental physical approximation in practical calculations. GPAW provides several forms of XC functionals ranging from the basic local density (LDA) and generalized gradient (GGA) approximations to the more exotic hybrid functionals; a van der Waals density-functional and the Hubbard-corrected DFT + U are also available. For the basic functionals GPAW uses libxc [45], which is an open-source library of popular XC functionals: LDA, GGA, and meta-GGA. The exchange and correlation parts of libxc can be freely combined. In the following we describe the more advanced functionals implemented in GPAW.

3.1. Meta-GGA

Meta-GGAs use the kinetic energy density in addition to densities and density gradients in standard GGAs so that more

of the known properties of the exact XC functional can be fulfilled [46]. The kinetic energy density is defined as

$$\tau(\mathbf{r}) = \tfrac{1}{2}\sum_n f_n |\nabla\psi_n(\mathbf{r})|^2. \tag{43}$$

The MGGAs currently implemented in GPAW [47–49] depend on the reduced (dimensionless) quantities τ/τ^{HEG} and τ/τ^{vW}, where

$$\tau^{\mathrm{HEG}} = \tfrac{3}{10}(6\pi^2)^{2/3} n^{5/3} \tag{44}$$

is the kinetic energy density of the homogeneous electron gas (HEG), and

$$\tau^{\mathrm{vW}} = \frac{|\nabla n|^2}{8n} \tag{45}$$

is the von Weizsäcker (vW) kinetic energy density.

Just like the AE density, equation (13), the kinetic energy density can be written as $\tau = \tilde{\tau} + \sum_a(\tau^a - \tilde{\tau}^a)$, where the smooth part is

$$\tilde{\tau}(\mathbf{r}) = \tfrac{1}{2}\sum_n f_n |\nabla\tilde{\psi}_n(\mathbf{r})|^2 + \sum_a \tilde{\tau}_{\mathrm{c}}^a(\mathbf{r}), \tag{46}$$

and the atom-centered parts are

$$\tau^a(\mathbf{r}) = \tfrac{1}{2}\sum_{i_1 i_2} D^a_{i_1 i_2} \nabla\phi_{i_1}(\mathbf{r})\cdot\nabla\phi_{i_2}(\mathbf{r}) + \tau_{\mathrm{c}}^a(r), \tag{47}$$

$$\tilde{\tau}^a(\mathbf{r}) = \tfrac{1}{2}\sum_{i_1 i_2} D^a_{i_1 i_2} \nabla\tilde{\phi}_{i_1}(\mathbf{r})\cdot\nabla\tilde{\phi}_{i_2}(\mathbf{r}) + \tilde{\tau}_{\mathrm{c}}^a(r). \tag{48}$$

The AE and PS core kinetic energy densities $\tau_{\mathrm{c}}^a(r)$ and $\tilde{\tau}_{\mathrm{c}}^a(r)$ are simple radial functions that are calculated during atomic setup generation.

Currently, GPAW enables calculation of non-self-consistent TPSS [47], revTPSS [49] and M06-L [48] energies. The use of PBE orbitals in non-self-consistent calculations of atomization energies and bond lengths for small molecules has been determined to be accurate [50]. In figure 1 the GPAW atomization energies errors, with respect to experiments, are reported both for the PBE and MGGA functionals. The TPSS mean absolute error with respect to experimental values obtained with GPAW is 0.13 eV, and this is consistent with the value of 0.14 eV of [50]. All MGGA functionals employed improve over the PBE atomization energies whose mean absolute error is 0.33 eV.

3.2. Exact exchange

GPAW offers access to the Fock exchange energy (exact exchange), as well as fractional inclusion of the Fock operator in the hybrid XC functionals. The exact-exchange (EXX) functional was implemented within the PAW method in a plane-wave basis [51], but to the authors' knowledge this is the first implementation in a real-space PAW method. As the PAW related expressions are independent of the basis, we refer to [51] for their derivation, and sketch only the main features here.

The EXX energy functional is given by

$$E_{\mathrm{xx}} = -\tfrac{1}{2}\sum_{ij\sigma} f_{i\sigma} f_{j\sigma} K^{\mathrm{C}}_{ij\sigma,ij\sigma}, \tag{49}$$

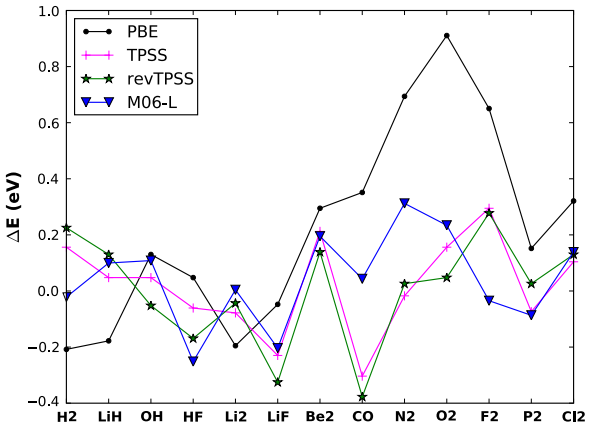

Figure 1. PBE, TPSS, revTPSS and M06-L non-self-consistent atomization energies errors, with respect to experiments, calculated with GPAW for small molecules, in eV. The MGGA GPAW values are obtained from PBE orbitals at experimental geometries. Experimental values are as in [50].

where i and j are the state indices, and σ is the spin index. The Coulomb matrix K^{C} is defined as

$$K^{\mathrm{C}}_{ij\sigma_1,kl\sigma_2} = (n_{ij\sigma_1}|n_{kl\sigma_2}) := \int \frac{\mathrm{d}\mathbf{r}\,\mathrm{d}\mathbf{r}'}{|\mathbf{r}-\mathbf{r}'|} n^*_{ij\sigma_1}(\mathbf{r}) n_{kl\sigma_2}(\mathbf{r}'), \tag{50}$$

where the orbital pair density is $n_{ij\sigma}(\mathbf{r}) = \psi^*_{i\sigma}(\mathbf{r})\psi_{j\sigma}(\mathbf{r})$.

When i, j both refer to valence states, the pair density can be partitioned into a smooth part and atom-centered corrections, similar to the AE density in equation (13), as

$$n_{ij\sigma} = \tilde{n}_{ij\sigma} + \sum_a (n^a_{ij\sigma} - \tilde{n}^a_{ij\sigma}). \tag{51}$$

Due to the non-local nature of the Coulomb kernel $1/|\mathbf{r}-\mathbf{r}'|$, direct insertion of equation (51) into (50) leads to cross terms between different augmentation spheres. The same problem appeared already in the evaluation of the PAW Coulomb energy, and it can be solved similarly by introducing compensation charges (from now on we drop the spin indices for brevity)

$$\tilde{Z}^a_{ij}(\mathbf{r}) = \sum_{\ell m} Q^a_{\ell m,ij}\hat{g}^a_{\ell m}(\mathbf{r}), \tag{52}$$

which are chosen to electrostatically decouple the smooth compensated pair densities

$$\tilde{\rho}_{ij} = \tilde{n}_{ij} + \sum_a \tilde{Z}^a_{ij}. \tag{53}$$

The Coulomb matrix now has a simple partitioning in terms of a smooth part and local corrections,

$$K^{\mathrm{C}}_{ij,kl} = (\tilde{\rho}_{ij}|\tilde{\rho}_{kl}) + \sum_a \Delta K^{\mathrm{C},a}_{ij,kl}. \tag{54}$$

We refer to [52] for the exact form of the correction term $\Delta K^{\mathrm{C},a}_{ij,kl}$, which is also used to evaluate equation (20). We note that the Coulomb matrix $K^{\mathrm{C}}_{ij,kl}$ appears also in the linear-response TDDFT (see section 5) and in the GW method [53].

The formally exact partitioning in equation (54) retains all information about the nodal structure of the AE wavefunctions

in the core region, which is important due to the non-local probing of the Coulomb operator. In standard pseudopotential schemes this information is lost, leading to an uncontrolled approximation to $K^{\mathrm{C}}_{ij,kl}$.

As a technical issue, we note that integration over the Coulomb kernel $1/|\mathbf{r}-\mathbf{r}'|$ is done by solving the associated Poisson equation, $\nabla^2\tilde{v}_{ij} = -4\pi\tilde{\rho}_{ij}$, for the Coulomb potential. However, the compensated pair densities $\tilde{\rho}_{ii}$ have a non-zero total charge, which leads to an integrable singularity in periodic systems. For periodic systems, the problem is solved by subtracting a homogeneous background charge from the pair densities and adding a correction term to the calculated potential afterward [51, 54]. For non-periodic systems, the Poisson equation is solved by adjusting the boundary values according to the multipole expansion of the pair density.

Terms in the Coulomb matrix, where either i or j refers to a core orbital, can be reduced to trivial functions of the expansion coefficients P^a_{in}, equation (7). Although the valence–core interaction is computationally trivial to include, it is not unimportant, and we will return to the effect of neglecting it, as it is unavailable in pseudopotential schemes. The core–core exchange is simply a constant energy that can be calculated once and for all for every atom given the frozen core orbitals.

The Fock operator $v^{\mathrm{F}}(\mathbf{r},\mathbf{r}')$ corresponding to the exact-exchange energy functional of equation (49) is non-local, and it is difficult to represent on any realistic grid. Fortunately, in the iterative minimization schemes used in GPAW the explicit form is never needed, but it suffices to evaluate only the action of the operator on a wavefunction. By taking into account the PAW transformation, the action on the PS wavefunction can be derived by the relation.

$$f_n\hat{\tilde{v}}^{\mathrm{F}}|\tilde{\psi}_n\rangle = \partial E_{\mathrm{xx}}/\partial\langle\tilde{\psi}_n|, \tag{55}$$

which results in

$$f_n\hat{\tilde{v}}^{\mathrm{F}}|\tilde{\psi}_n\rangle = -\sum_m f_m\tilde{v}_{nm}(\mathbf{r})|\tilde{\psi}_m\rangle + \sum_a\sum_i|\tilde{p}^a_i\rangle\Delta v^{\mathrm{F}a}[\tilde{v}_{nm},\{P^a_{jm}\}]. \tag{56}$$

The computationally demanding first term is related to smooth pseudo-quantities only, which can be accurately represented on coarse grids, making it possible to do converged self-consistent EXX calculations at a relatively modest cost. Applying the Fock operator is, however, still expensive, as a Poisson equation must be solved for all pairs of orbitals. The atomic correction $\Delta v^{\mathrm{F}a}$ depends both on $\tilde{v}_{nm}$ and on the set of expansion coefficients P^a_{in}. The details of the derivation as well as the exact form of the correction term can be found in [55].

As a benchmark of the implementation, and for comparing the PBE and hybrid PBE0 [56] functionals, we have computed the atomization energies of the G2-1 database of molecules [57] using these two functionals. The results are compared to the experimental values as well as to the results of the plane-wave PAW implementation VASP, and of the all-electron atomic orbital code Gaussian 03, as reported in [51].

The PBE0 functional includes a fraction (25%) of Fock exchange in PBE, which improves the agreement with experiments significantly, as shown in figure 2. The figure shows also that the different implementations deviate from one another by less than 0.05 eV on average. The GPAW PBE0 energies are all slightly too small because they have not been geometry optimized with the hybrid functional (they are evaluated at PBE geometries).

The importance of the valence–core exchange interaction for this test suite is typically a few tenths of eV for the atomization energy, but can induce a shift of several eV in the eigenvalues of the frontier orbitals.

The difference in atomization energy between EXX evaluated using PBE orbitals and self-consistent EXX orbitals is less than 13 meV on average suggesting that PBE and HF orbitals are very similar. The difference in self-consistency is even less for PBE0. Also, for the eigenvalues of the EXX (or PBE0) Hamiltonian the use of PBE orbitals has a small effect, differences being less than 0.1 eV in the worst case (CO_2).

3.3. GLLB approximation for the exact exchange

One drawback of the EXX approach is that the evaluation of the Fock operator is computationally quite expensive. Thus, it would be desirable to have computationally inexpensive approximations to the exact exchange. One such approximation (GLLB) is provided in [58], where the exchange potential v_{x} is separated into a screening part v_{S} and a response part v_{resp},

$$v_{\mathrm{x}}(\mathbf{r}) = v_{\mathrm{S}}(\mathbf{r}) + v_{\mathrm{resp}}(\mathbf{r}), \tag{57}$$

and the two parts are approximated independently.

In the original work v_{S} is approximated with the GGA exchange energy density $\epsilon_x^{\mathrm{GGA}}$ of Becke [59]

$$v_{\mathrm{S}}(\mathbf{r}) = \frac{2\epsilon_x^{\mathrm{GGA}}(\mathbf{r};n)}{n(\mathbf{r})}. \tag{58}$$

Using the common denominator approximation, exchange scaling relations and asymptotic behavior, the response part is approximated as

$$v_{\mathrm{resp}}(\mathbf{r}) = \sum_i^{\mathrm{occ}} K[n]\sqrt{\varepsilon_{\mathrm{r}}-\varepsilon_i}\frac{|\psi_i(\mathbf{r})|^2}{n(\mathbf{r})}, \tag{59}$$

where ε_{r} is the highest occupied eigenvalue. The coefficient $K[n]$ can be determined for the homogeneous electron gas, where it is a constant

$$K = \frac{8\sqrt{2}}{3\pi^2} \approx 0.382. \tag{60}$$

In addition to the above GLLB potential, we have implemented an extension (GLLB-SC) which contains also correlation and is targeted more to solids [60]. Instead of the exchange potential, the whole exchange–correlation potential $v_{\mathrm{xc}}(\mathbf{r})$ is separated into two parts. The screening part is approximated now with the PBEsol [61] exchange–correlation energy density and the response part contains also the contribution from the PBEsol response potential,

$$v_{\mathrm{resp}}(\mathbf{r}) = \sum_i^{\mathrm{occ}} K\sqrt{\varepsilon_{\mathrm{r}}-\varepsilon_i}\frac{|\psi_i(\mathbf{r})|^2}{n(\mathbf{r})} + v_{\mathrm{resp}}^{\mathrm{PBEsol}}(\mathbf{r}). \tag{61}$$

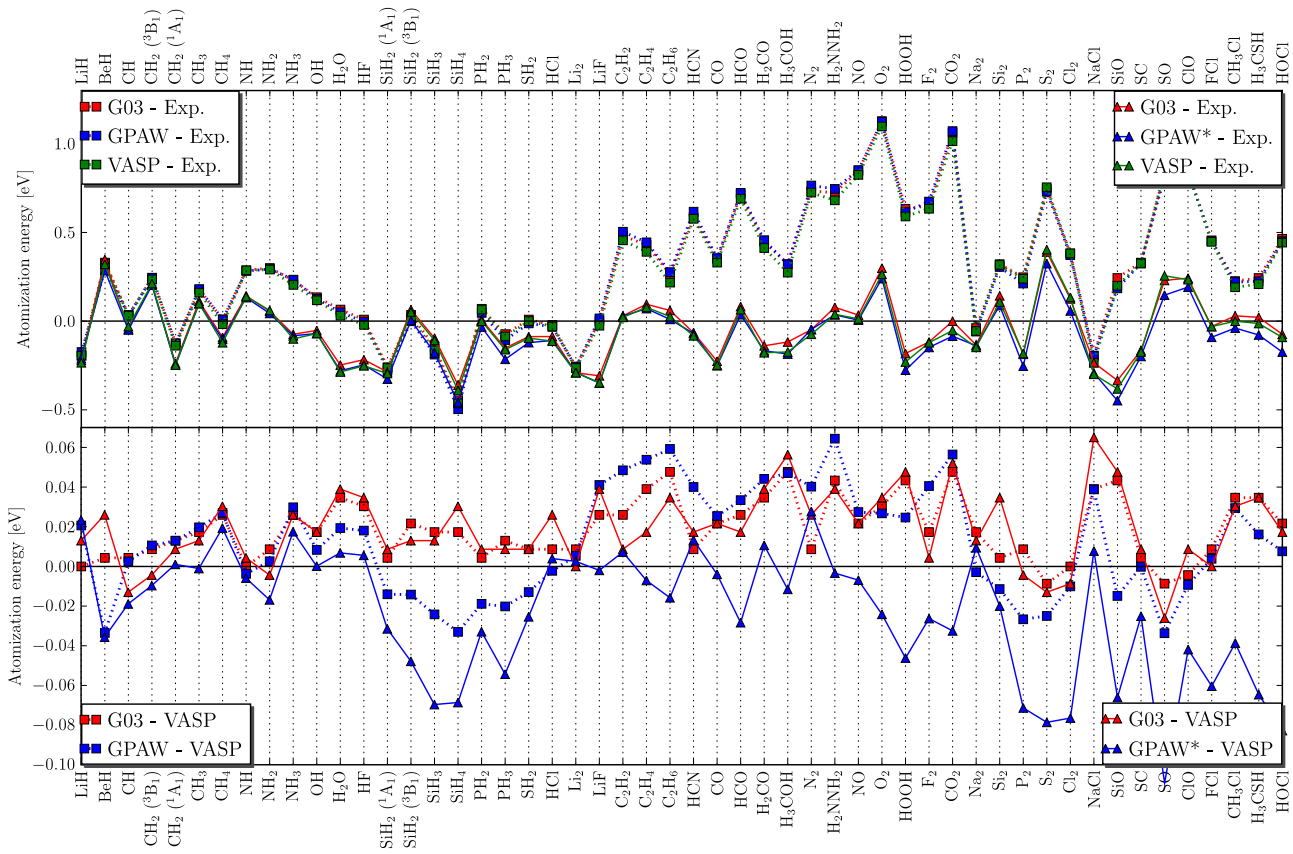

Figure 2. Calculated atomization energies using PBE (dotted) and PBE0 (solid) functionals compared to experimental values (top) and to VASP (bottom). GPAW PBE0 values are not geometry optimized (evaluated at PBE geometries).

An important property of the exact exchange–correlation potential is the discontinuity at integer occupation numbers N,

$$\Delta_{\mathrm{xc}} = \lim_{\delta\to 0}[v_{\mathrm{xc}}(\mathbf{r}; N+\delta) - v_{\mathrm{xc}}(\mathbf{r}; N-\delta)]. \qquad (62)$$

The derivative discontinuity is especially important for the band gaps of semiconductors and insulators, as the true quasiparticle band gap $E_{\mathrm{g}}^{\mathrm{QP}}$ is a sum of the Kohn–Sham band gap $E_{\mathrm{g}}^{\mathrm{KS}}$ and the discontinuity [62, 63]

$$E_{\mathrm{g}}^{\mathrm{QP}} = E_{\mathrm{g}}^{\mathrm{KS}} + \Delta_{\mathrm{xc}}. \qquad (63)$$

Neither LDA nor GGA potentials exhibit the discontinuity, which explains partly their failure in reproducing experimental band gaps. On the other hand, in the GLLB and GLLB-SC approximations one obtains an estimate for the discontinuity. The reference energy ε_{r} in the GLLB response part changes from ε_N to ε_{N+1} when approaching N from above, so that inserting equation (59) into (62) gives the discontinuity

$$\Delta_{x,\mathrm{resp}}(\mathbf{r}) = \sum_i^N K(\sqrt{\varepsilon_{N+1}-\varepsilon_i} - \sqrt{\varepsilon_N - \varepsilon_i})\frac{|\psi_i(\mathbf{r})|^2}{n(\mathbf{r})}. \qquad (64)$$

The above expression for Δ_x depends on spacial coordinates, however, a constant value can be obtained from the first order perturbation theory

$$\Delta_{x,\mathrm{resp}} = \langle\Psi_{N+1}|\Delta_{x,\mathrm{resp}}(\mathbf{r})|\Psi_{N+1}\rangle. \qquad (65)$$

Table 1. The minimum Kohn–Sham band gaps for LDA and GLLB-SC together with derivative discontinuity and the quasiparticle band gap of GLLB-SC. Experimental values are from [64]. All values are in eV.

Material	$E_{\mathrm{g}}^{\mathrm{KS}}$ (LDA)	$E_{\mathrm{g}}^{\mathrm{KS}}$	Δ_{xc}	$E_{\mathrm{g}}^{\mathrm{QP}}$	Exp.
C	4.09	4.14	1.27	5.41	5.48
Si	0.443	0.68	0.32	1.00	1.17
GaAs	0.36	0.79	0.25	1.04	1.63
AlAs	1.34	1.67	0.82	2.49	2.32
LiF	8.775	10.87	4.09	14.96	14.2
Ar	8.18	10.28	4.69	14.97	14.2

The calculated derivative discontinuities in the GLLB-SC approximation and their effect on the calculated quasiparticle band gaps are shown in table 1 for several materials. It can be seen that GLLB-SC clearly improves the description of band gaps in these systems.

3.4. van der Waals functional

van der Waals interactions are due to long range correlation effects that are not included in GGA-type XC functionals. The recently developed functional which includes van der Waals interactions [65] (vdW-DF) is available in GPAW.

The vdW-DF is a sum of a GGA exchange and a correlation term consisting of both short-ranged correlation (evaluated in the local density approximation) and longer-

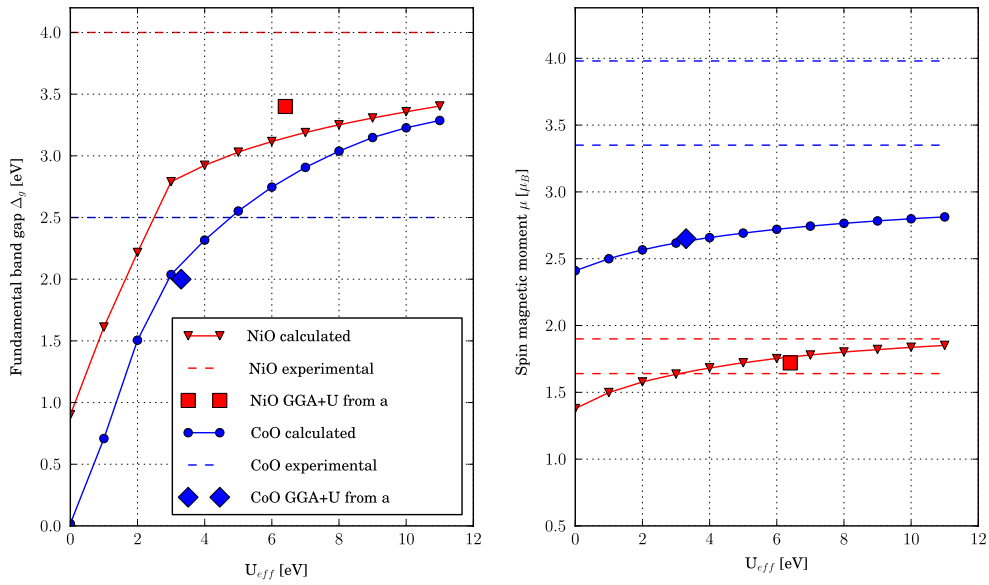

Figure 3. Fundamental band gap Δ_g (left) and the spin magnetic moment μ (right), for the AFMII phase of NiO and CoO as a function of the applied Hubbard U_{eff}. (a) Wang *et al* [70]. Experimental values are as cited in [71]. Two different experimental values are shown for the spin magnetic moment.

ranged correlation (depending non-locally on the electron density) [65]:

$$E_c^{nl}[n] = \tfrac{1}{2}\int d\mathbf{r}_1\, d\mathbf{r}_2\, n(\mathbf{r})\phi(q_1 r_{12}, q_2 r_{12})n(\mathbf{r}_2), \qquad (66)$$

where $\phi(d_1, d_2)$ is the vdW-DF kernel, $r_{12} = |\mathbf{r}_1 - \mathbf{r}_2|$ and q_1 and q_2 are the values of a universal function $q_0(n(\mathbf{r}), |\nabla n(\mathbf{r})|)$ evaluated at the two points $\mathbf{r}_1$ and $\mathbf{r}_2$. Instead of n, we use the PS valence density $\tilde{n}$ for the evaluation of equation (66). The justification for this choice is that $q_0(\mathbf{r})$ has very high values close to the nuclei, and the vdW kernel $\phi(d_1, d_2)$ in terms of the rescaled distances $d_1 = q_1 r_{12}$ and $d_2 = q_2 r_{12}$ will be quite short ranged and therefore not important for studying interactions between atoms.

Evaluation of $E_c^{nl}[\tilde{n}]$ by direct summation in real space has an operation count that scales as N_g^2 (N_g is the number of grid points), which is often too time consuming for typical calculations. We have therefore implemented the fast Fourier transformation (FFT) technique introduced by Román-Pérez and Soler [66], where the scaling is $N_g \log N_g$. As an example, a self-consistent vdW-DF calculation for water (64 molecules on 16 processors) takes only 80% longer than a self-consistent PBE calculation. Additional details of our implementation can be found in [67].

3.4.1. DFT + U. In strongly correlated materials, such as transition metal oxides, lanthanides or actinides, the strong on-site Coulomb interaction of the localized d or f electrons is not correctly described by LDA or GGA. The basic idea behind the DFT + U method is to treat this interaction with an additional Hubbard-like term. The strength of the on-site interactions are usually described by semi-empirical parameters U and J. The GPAW implementation is based on the particular branch of DFT + U suggested in [68], where only a single effective $U_{\text{eff}} = U - J$ accounts for the Coulomb interaction, neglecting thereby any higher multi-polar terms.

Following [68], the DFT + U total energy is

$$E_{\text{DFT+U}} = E_{\text{DFT}} + \sum_a \frac{U_{\text{eff}}}{2}\text{Tr}(\rho^a - \rho^a\rho^a), \qquad (67)$$

where ρ^a is the atomic orbital occupation matrix (AOOM).

In order to evaluate equation (67), a mapping between the wavefunctions and AOOM $\rho^a_{mm'}$ is required. This mapping can be written in terms of the density matrices $D^a_{n\ell m,n'\ell m'}$, equation (10), and the AE atomic orbitals $\phi^a_{n\ell m}$ as [69]

$$\rho^a_{mm'} = \sum_{n,n'} D^a_{n\ell m,n'\ell m'}\langle\phi^a_{n\ell m}|\phi^a_{n'\ell m'}\rangle.$$

The orbital quantum number ℓ is restricted to the orbital of interest and m is restricted to the associated magnetic quantum numbers. The n index refers to the nth projector of the particular ℓ-channel. GPAW atomic setups have typically $n \in (1, 2)$, where $n = 1$ is the bound state projector and $n = 2$ is unbound state projector. Because of the latter, we truncate the integration in $\langle\phi^a_{n\ell m}|\phi^a_{n'\ell m'}\rangle$ at the augmentation sphere radius. The DFT+U energy correction also adds a term to the Hamiltonian within the augmentation spheres, $\Delta H^a_{i_1 i_2}$ in equation (31), which is obtained by taking the derivative of equation (67) with respect to $D^a_{i_1 i_2}$.

As an example, we show in figure 3 the calculated spin magnetic moment μ and the fundamental band gap Δ_g of CoO and NiO with increasing values of the effective Hubbard U_{eff}. The figure shows clearly that the DFT+U scheme improves the description of the strongly correlated nature of the transition metal oxide. The calculations have been carried out using the PBE exchange–correlation functional, a grid spacing of 0.16 Å and $8 \times 8 \times 8$ k-points in the Brillouin zone. In all calculations, the lattice constants are optimized with pure PBE ($U_{\text{eff}} = 0$)

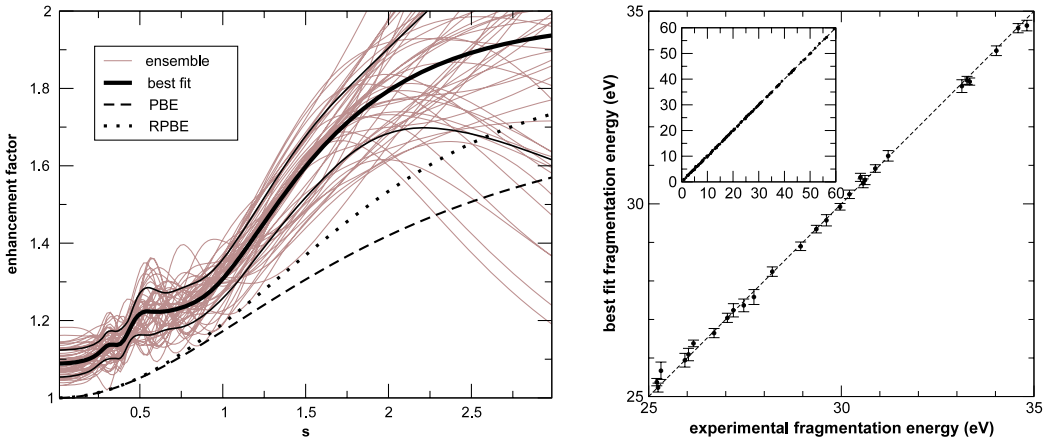

Figure 4. Left: ensemble of enhancement factors as optimized to the experimental fragmentation energies of 148 molecules. The thin black lines running parallel to the best-fit mark the width of the ensemble. The PBE and RPBE enhancement factors are also shown for comparison, s is the reduced density gradient. Right: fragmentation energies predicted with the best-fit enhancement factor versus the experimental values. The error bars are calculated from the ensemble in the left panel.

with a grid spacing of 0.16 Å, the obtained values are 4.19 Å for NiO and 4.24 Å for CoO. The corresponding experimental values are 4.17 Å and 4.25 Å for NiO and CoO, respectively.

4. Error estimation

Density-functional theory is used extensively to calculate binding energies of different atomic structures ranging from small molecules to extended condensed-matter systems. A number of different approximations to the exchange–correlation energy have been developed with different scopes in mind and with different virtues. When it comes to the practical use of DFT, it is therefore usually very much up to the user to obtain experience with the different xc functionals and gain insight into how accurate the calculations are for a particular application. This learning process can be rather slow and, also for other more general reasons, it would be advantageous to have a reliable and unbiased way to estimate errors on DFT calculations.

The error estimation implemented in GPAW is inspired by ideas from Bayesian statistics [72]. The ingredients in a typical statistical model construction consist of (1) a database with a number of (possibly noisy) data points which the model is supposed to reproduce as closely as possible and (2) the model which is described by a number of parameters which can be adjusted to improve the model. The quality of the model can for example be estimated by a least-squares cost which is a sum over all data points of the squared difference between the database value and the value predicted by the model. The cost thus becomes a function of the model parameters and minimization of the cost leads to the best-fit model. (An important issue here is to control the effective number of parameters in the model to avoid over-fitting, but we shall not go into this here.) So far we have described a common least-squares fit. What the Bayesian approach adds to this is the idea of not only a single best-fit model but an ensemble of models representing a probability distribution in model space. Using the ensemble, the model no longer predicts only a single value for a data point but a distribution of values which will be more or less scattered depending on the ability of the model to make an accurate prediction for that point.

In the case of GPAW, we have worked on providing error estimates for GGA-type calculations. The model space is defined by a suitable parametrization of the exchange enhancement factor f_x, which enters the exchange functional as (see [73] for details)

$$E_x[n] = \int f_x(s(\mathbf{r}); \boldsymbol{\theta}) n(\mathbf{r}) \varepsilon_x^{\mathrm{unif}}(n(\mathbf{r}))\, \mathrm{d}\mathbf{r}.$$

Here, s is the reduced density gradient $\sim|\nabla n|/n$, and $\boldsymbol{\theta}$ our parametrization. The database consists of the experimental fragmentation energies of 148 small molecules (from the G2 neutral test set [57]). The left panel in figure 4 displays the resulting Bayesian ensemble of enhancement factors in terms of some randomly drawn members. The enhancement factor for the best-fit model is seen to resemble other commonly used enhancement factors, such as PBE and RPBE. It should be noted that for a typical Bayesian ensemble the spread is governed mostly by the noise in the data points and the limitations in the number of data points. In our case the noise in the experimental fragmentation energies is quite small compared with a typical deviation between the experimental value and the best-fit value. This is an indication that our model space is incomplete, i.e. there is simply a limit to how accurate a GGA-type functional can be. The width of the ensemble shown in figure 4 is therefore controlled not so much by the noise as by the model incompleteness.

The ensemble can be used to estimate errors, as also shown in figure 4. Here the calculated fragmentation energies for the molecular database are shown together with the estimated error bars versus the experimental values. The average of the predicted error bars squared reproduces, by construction of the ensemble, the average value of the squared deviation between experiment and best-fit model. The detailed transferability of the best-fit model and the error predictions to other classes of systems is currently under investigation.

5. Time-dependent density-functional theory

Standard DFT is applicable only to the ground state properties of a system. However, there are many properties of great interest which are related to the excited states, e.g. optical absorption spectrum. Time-dependent density-functional theory (TDDFT) [3] is the extension of standard DFT into the time-domain enabling the study of excited state properties. There are two widely used formulations of TDDFT, the real-time propagation scheme [74] and the linear-response scheme [75]; both of these are available in GPAW. The details of the implementations are described in [52], and we present only a brief overview here.

5.1. Real-time propagation

The time-dependent AE Kohn–Sham equation is

$$\mathrm{i}\frac{\partial}{\partial t}\psi_n(t) = \hat{H}(t)\psi_n(t), \tag{68}$$

where the time-dependent Hamiltonian $\hat{H}(t)$ can include also an external time-dependent potential. Assuming that the overlap matrix $\hat{S}$ is independent of time, this equation can be written in the PAW formalism as

$$\mathrm{i}\hat{S}\frac{\partial}{\partial t}\tilde{\psi}_n(t) = \hat{H}(t)\tilde{\psi}_n(t). \tag{69}$$

This time-dependent equation can be solved using the Crank–Nicolson propagator with a predictor–corrector step as described in [52].

5.2. Linear-response formalism

Within the linear-response regime, the excitation energies can be calculated from the eigenvalue equation of the form

$$\mathbf{\Omega} F_I = \omega_I^2 F_I, \tag{70}$$

where ω_I is the transition energy from the ground state to the excited state I, and F_I denotes the associated eigenvector. The matrix $\mathbf{\Omega}$ can be expanded in Kohn–Sham single particle–hole excitations leading to

$$\Omega_{ij\sigma,kl\tau} = \delta_{ik}\delta_{jl}\delta_{\sigma\tau}\varepsilon_{ij\sigma}^2 + 2\sqrt{f_{ij\sigma}\varepsilon_{ij\sigma} f_{kl\tau}\varepsilon_{kl\tau}}K_{ij\sigma,kl\tau}, \tag{71}$$

where $\varepsilon_{ij\sigma} = \varepsilon_{j\sigma} - \varepsilon_{i\sigma}$ are the energy differences and $f_{ij\sigma} = f_{i\sigma} - f_{j\sigma}$ are the occupation number differences of the Kohn–Sham states. The indices i, j, k, l are state indices, whereas σ, τ denote spin indices. The coupling matrix can be split into two parts $K_{ij\sigma,kl\tau} = K^{\mathrm{C}}_{ij\sigma,kl\tau} + K^{\mathrm{xc}}_{ij\sigma,kl\tau}$. The former Coulomb matrix has exactly the same form as in the context of exact exchange, equation (50)

$$K^{\mathrm{C}}_{ij\sigma,kl\tau} = (n_{ij\sigma}|n_{kl\tau}) \tag{72}$$

and is often called the random phase approximation part. It describes the effect of the linear density response via the classical Hartree energy. The second contribution is the exchange–correlation part

$$K^{\mathrm{xc}}_{ij\sigma,kq\tau} = \int \mathrm{d}\mathbf{r}_1\,\mathrm{d}\mathbf{r}_2\, n^*_{ij\sigma}(\mathbf{r}_1)\frac{\delta^2 E_{\mathrm{xc}}}{\delta n_\sigma(\mathbf{r}_1)\delta n_\tau(\mathbf{r}_2)}n_{kq\tau}(\mathbf{r}_2), \tag{73}$$

Table 2. Calculated excitation energies of the CO molecule within the LDA approximation in eV. Bond length is 1.128 Å.

State	Spin	GPAW	AE [76]
a $^3\Pi$	Triplet	5.95	6.03
A $^1\Pi$	Singlet	8.36	8.44
a′ $^3\Sigma^+$	Triplet	8.58	8.57
b $^3\Sigma^+$	Triplet	9.01	9.02
B $^1\Sigma^+$	Singlet	9.24	9.20
d $^3\Delta$	Triplet	9.25	9.23
I $^1\Sigma^-$	Singlet	9.87	9.87
e $^3\Sigma^-$	Triplet	9.87	9.87
D $^1\Delta$	Triplet	10.35	10.36

where n_σ is the spin density. The functional derivative can be calculated with a finite difference scheme.

Diagonalization of the linear-response equation (70) gives directly all the excitation energies in the linear-response regime. As an example, table 2 shows the calculated excitation energies of a CO molecule together with reference calculations. The agreement between our results and numerically accurate AE results [76] is generally good.

Within the time propagation scheme, one obtains only the excitations corresponding to a particular initial perturbation. Thus, different types of perturbations would be needed to reach different excited states. In the case of a singlet ground state molecule like CO, the often applied delta pulse perturbation (as introduced in section 5.3) can lead only to dipole allowed singlet–singlet excitations. Therefore the triplet excitations and dipole forbidden singlet excitation at 9.87 eV do not appear in the time propagation scheme.

5.3. Optical absorption spectra

In the real-time formalism the linear absorption spectrum can be obtained by exciting the system first with a weak delta pulse,

$$\mathbf{E}(t) = \epsilon\mathbf{k}^{\mathbf{o}}\delta(t), \tag{74}$$

where ϵ is a unitless perturbation strength parameter and $\mathbf{k}^{\mathbf{o}}$ is a unit vector giving the polarization direction of the field. The delta pulse changes the initial wavefunctions to

$$\psi(t = 0^+) = \exp\left(\mathrm{i}\frac{\epsilon}{a_0}\mathbf{k}^{\mathbf{o}}\cdot\mathbf{r}\right)\psi(t = 0^-). \tag{75}$$

The system is then allowed to evolve freely and during the time-evolution the time-dependent dipole moment $\boldsymbol{\mu}(t)$ is recorded. At the end of the calculation, the dipole strength tensor and oscillator strengths are obtained via a Fourier transform.

In the linear-response formalism one also needs the eigenvectors of equation (70) when calculating the absorption spectrum. Together with the Kohn–Sham transition dipoles

$$\boldsymbol{\mu}_{ij\sigma} = \langle\psi_{i\sigma}|\mathbf{r}|\psi_{j\sigma}\rangle \tag{76}$$

the oscillator strengths are given by

$$f_{I\alpha} = \left|\sum_{ij\sigma}^{f_{i\sigma}>f_{j\sigma}} (\boldsymbol{\mu}_{ij\sigma})_\alpha\sqrt{f_{ij\sigma}\varepsilon_{ij\sigma}}(F_I)_{ij\sigma}\right|^2. \tag{77}$$

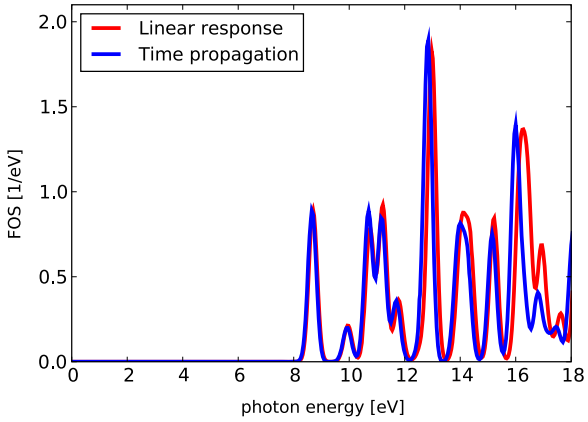

Figure 5. Calculated optical absorption spectra of the CH_4 molecule presented as folded oscillator strengths (FOS). The calculation is performed both with the time propagation and the linear-response method.

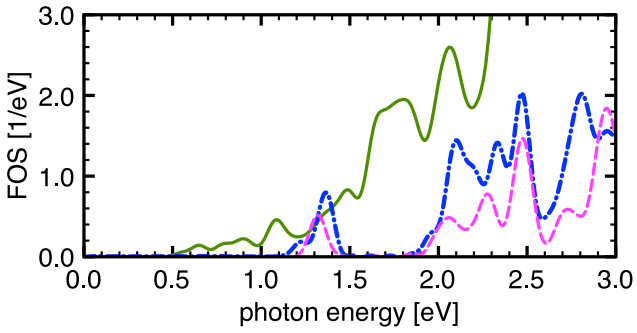

Figure 6. Optical absorption spectra of $Au_{25}(S\text{-}CH_3)_{18}^-$ (dashed magneta), $Au_{25}(S\text{-}CH_2\text{–}CH_2\text{–}C_6H_5)_{18}^-$ (dash-dotted blue), and $Au_{102}(S\text{-}CH_3)_{44}$ (solid green).

The discrete oscillator strengths can be folded by a Gaussian (as an example) for comparison with the time propagation calculation and experiments.

Figure 5 shows the calculated linear absorption spectra of a CH_4 molecule. The agreement between the completely different numerical schemes is remarkable.

Even though the time propagation scheme is relatively time consuming in small systems, the favorable scaling with system size as well as the good parallelization possibilities (described in more detail in section 8) enable calculations also for large systems. As an example, figure 6 shows the calculated optical spectra of $Au_{25}(S\text{-}CH_3)_{18}^-$, $Au_{25}(S\text{-}CH_2\text{–}CH_2\text{–}C_6H_5)_{18}^-$, and $Au_{102}(S\text{-}CH_3)_{44}$. The shapes of $Au_{25}(SR)_{18}^-$ spectra are similar to experimental spectra in [77]. However, all features appear systematically at too low energy. This is most probably due to ALDA approximation. The $Au_{102}(S\text{-}CH_3)_{44}$ spectrum has less structure than the smaller clusters and it also shows a significant red shift of 0.6 eV.

5.4. Non-linear emission spectra

The time propagation approach can also be used in the non-linear regime where the linear-response scheme is no longer

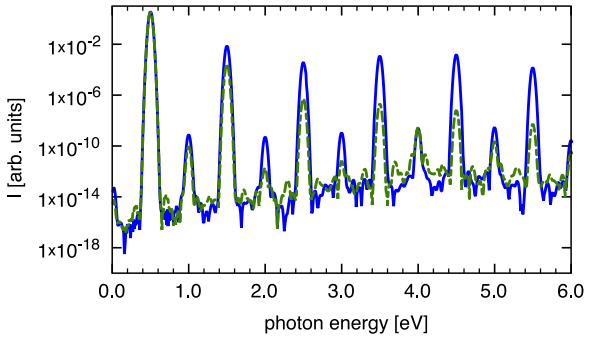

Figure 7. Non-linear emission spectra of Mg atom in a laser field of frequency 0.5 eV and strength of 0.01 (solid blue) and 0.05 (dashed green) atomic units. Strong harmonic frequency generation is observed at odd multiples of the laser field frequency.

applicable. For example, a strong laser field can introduce non-linear terms in the polarizability of an atom or molecule. Figure 7 shows the emission spectra of Mg atom in a laser field with frequency 0.5 eV and strength 0.01 and 0.05 atomic units. Due to non-linear effects, harmonics of the laser field frequency appear at odd integer multiples of the driving field. The intensity depends non-linearly on the strength of the field. The harmonics at even integer multiples are forbidden by the symmetry. In the simulated spectrum, weak even harmonics are observed due to numerical inaccuracies. Compared to our earlier calculation with beryllium [52], the Mg spectra has less numerical noise, which is because of the imaginary potential absorbing boundary conditions [78] used in the calculation of the Mg spectra.

5.5. Photoelectron spectra

The process of photoionization may be viewed in two different ways. In the simplest interpretation, the single-particle states of Kohn–Sham DFT are directly connected to the observed electrons in the experiment. Even though the orbital energies (except for the highest occupied orbital) do not have rigorous physical meaning, they often give a very reasonable description of the experimentally observed electron binding energies E_{bind} [79].

A more rigorous description of the photoelectron spectrum (PES) is available in the many-body picture. The 'daughter' system, after emitting the electron, is left either in the electronic ground state or in an electronically excited state when the released electron has reached the detector. The measured kinetic energy distribution of the ejected electron is given by the difference between the ground state energy of the 'mother' system E_0^N and the excited state energies of the daughter system E_I^{N-1}

$$E_{\text{bind}} = E_I^{N-1} - E_0^N, \tag{78}$$

where N denotes the number of electrons. The ground state energy and excitation energies can be calculated with DFT and TDDFT, respectively. However, it is not only the energies that determine the number of electrons in the detector, but also the probability for ionization, i.e. not all excited states of the daughter system can be reached by ionizing the mother system.

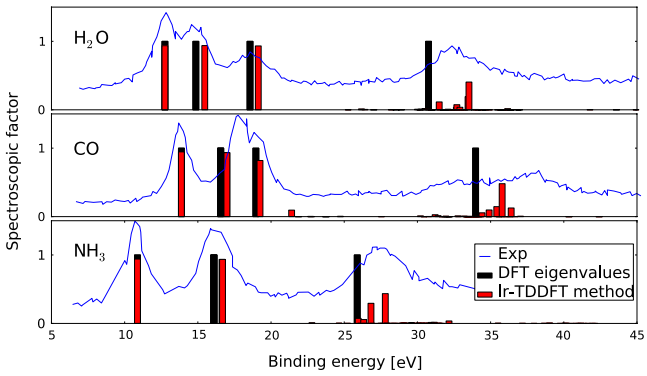

Figure 8. Experimental photoelectron cross sections (adapted from [81]) compared with spectroscopic factors from TDDFT and Kohn–Sham approaches.

In principle, one would need many-particle wavefunctions to be able to calculate the transition probabilities, but these are not available in DFT. One can nevertheless create an approximate scheme to calculate the overlaps [80]: the ground state wavefunctions of the daughter and mother systems are approximated by a single Slater determinant of the occupied Kohn–Sham orbitals. The excited state wavefunctions of the daughter states are constructed via the weights F_I (equation (70)) of the Kohn–Sham single orbital excitations. With these approximations one can evaluate the spectroscopic factor f_I, the energy independent probability for the daughter system to end up in a given excited state I due to photoemission.

We have implemented this scheme in GPAW. As an example, we have calculated the resultant PES spectrum of H_2O, CO and NH_3. Figure 8 shows the comparison of the spectroscopic factors with experiments and the single-particle Kohn–Sham approach, where the spectroscopic factor is unity for each occupied orbital. Both the Kohn–Sham approach and the linear-response TDDFT scheme give good agreement with experiment for lower bound electrons. For peaks at high binding energies, there is a clear improvement by the new scheme. In particular the 'broadening' of the highest energy peak cannot be described by the Kohn–Sham single-particle picture. Here many excitations of the daughter system contribute to the peak.

6. Localized atomic-like basis functions

As an alternative to the grid-based finite difference approach described above, GPAW offers also the possibility to work with atomic-like basis functions, or linear combinations of atomic orbitals (LCAO) [82, 11, 83]. A detailed description of GPAW's LCAO implementation is available in [84]. An LCAO basis function centered at atom a has the form

$$\Phi^a_{n\ell m}(\mathbf{r}) = R^a_{n\ell}(|\mathbf{r} - \mathbf{R}^a|)Y_{\ell m}(\mathbf{r} - \mathbf{R}^a), \tag{79}$$

where $R^a_{n\ell}$ is a radial function which vanishes beyond a certain cutoff radius, and $Y_{\ell m}$ is a spherical harmonic. By defining ν as the composite a, n, ℓ, m, a general PAW state i can then be expanded as

$$\tilde{\psi}_i = \sum_\nu C_{i\nu}\Phi_\nu(\mathbf{r}), \tag{80}$$

where $C_{i\nu}$ are expansion coefficients.

The grid method and the localized basis complement each other very well. With the grid-based scheme the complete basis set limit can be systematically reached while the localized basis allows for fast calculations in situations where efficiency is more important than high accuracy. Moreover, the localized basis is well suited for quantum transport calculations, linear scaling computation schemes, molecular dynamics simulations, as well as for analysis purposes. The 'multi-basis' feature of GPAW allows the user to switch seamlessly between the accurate grid mode and the efficient LCAO mode at any point of a computation. For example, the first part of a structural optimization could be performed efficiently using the minimal localized basis while the final steps could be performed in the 'grid mode'. To our knowledge GPAW is the first code combining localized basis functions with the PAW method, *and* the first code supporting two different representations for the Kohn–Sham orbitals within the same unifying DFT framework, that is, with exactly the same set of approximations.

The LCAO implementation reuses most of what is implemented in the finite difference PAW method: calculation of electrostatic interactions, evaluation of the XC potential, atomic PAW energy corrections, density mixing and also most of the contributions to the atomic forces are the same. It is only the evaluation of overlap integrals and matrix elements of the kinetic energy operator that are done differently. Instead of calculating integrals like $\langle\tilde{\psi}_n|\hat{S}|\tilde{\psi}_m\rangle$, $\langle\tilde{\psi}_n|\hat{T}|\tilde{\psi}_m\rangle$, and $\langle\tilde{p}^a_i|\tilde{\psi}_n\rangle$ on a 3d grid and using a finite difference representation for $\hat{T}$, we express these integrals in terms of two-center integrals of the type: $\langle\Phi_\mu|\Phi_\nu\rangle$, $\langle\Phi_\mu|\hat{T}|\Phi_\nu\rangle$, and $\langle\tilde{p}^a_i|\Phi_\nu\rangle$, where Φ_μ are the atomic-like basis functions. These integrals can be pre-calculated as described in [11].

Because of the much smaller number of degrees of freedom in a LCAO calculation compared to a grid-based calculation, we can do a complete diagonalization in the subspace of our basis set instead of being forced to use iterative diagonalization techniques.

A minimal atomic basis set consists of one modified atomic orbital for each valence state—the single-zeta basis functions. First, localized atomic-like orbitals Φ^{AE} are obtained for each valence state by solving the radial AE Kohn–Sham equations for the isolated atom. In order to ensure that the wavefunction vanishes beyond a certain cutoff radius, the atom is placed in a suitably defined confining potential well [82]. The basis functions are then obtained using $\Phi(\mathbf{r}) = \mathcal{T}^{-1}\Phi^{\mathrm{AE}}(\mathbf{r})$. The cutoff radius is selected in a systematic way by specifying the energy shift ΔE of the confined orbital compared to the free-atom orbital [85]. In this approach small values of ΔE will correspond to long-ranged basis orbitals [84].

In order to improve the radial flexibility, extra basis functions with the same angular momentum ℓ (multiple-zeta) are constructed for each valence state using the split-valence technique [11]. The extra function is constructed by matching a polynomial to the tail of the atomic orbital, where the matching radius is determined by requiring the norm of the part of the atomic orbital outside that radius to have a certain value.

Finally, polarization functions (basis functions with ℓ quantum number corresponding to the lowest unoccupied

Table 3. Lattice constants, a, cohesive energies, E_c, and bulk moduli, B, for selected solids. MAE denotes the mean absolute error of the double-zeta polarized (DZP) basis set with respect to the grid-based results.

	a (Å)		E_c (eV)		B (GPa)	
	DZP	GRID	DZP	GRID	DZP	GRID
LiF	4.10	4.06	4.52	4.24	70	80
C	3.58	3.57	7.89	7.72	422	433
Na	4.24	4.19	1.07	1.09	7.9	7.9
MgO	4.27	4.26	4.97	4.95	173	154
Al	4.07	4.04	3.54	3.43	79	77
NaCl	5.67	5.69	3.26	3.10	26	24
Li	3.43	3.43	1.63	1.62	16.3	14.2
SiC	4.41	4.39	6.48	6.38	202	211
Si	5.49	5.48	4.71	4.55	86	88
AlP	5.53	5.51	4.21	4.08	81	82
Fe	2.83	2.84	5.07	4.85	231	198
Cu	3.64	3.65	4.14	3.51	143	141
Pt	3.98	3.98	5.69	5.35	263	266
MAE	0.019	0.0	0.18	0.0	7.4	0.0

angular momentum) can be added in order to improve the angular flexibility of the basis. There are several approaches for generating these orbitals, such as perturbing the occupied eigenstate with the highest ℓ quantum number with an electric field using first order perturbation theory or using the appropriate unoccupied orbitals. In GPAW we use a Gaussian-like function of the form $r^\ell \exp(-\alpha r^2)$ for the radial part, where ℓ corresponds to the lowest unoccupied angular momentum.

One of the most time consuming parts of a basis set calculation is the evaluation of matrix elements of the effective pseudopotential $\langle\Phi_\mu|\tilde{v}|\Phi_\nu\rangle$, which is done on a 3d grid. For an efficient evaluation of these matrix elements, it is important to have as short-ranged basis functions as possible and to use as coarse grids as possible. For the latter, the PAW method helps to make the basis functions and potentials smooth.

As an example, table 3 shows the lattice constant, cohesive energy, and bulk modulus for a range of solids calculated with double-zeta polarized (DZP) basis sets and compared to the grid-based results. The cutoff radii of the basis orbitals correspond to an energy shift of 0.1 eV. The DZP values are in good agreement with the grid-based values, in particular for the structural properties, i.e. lattice constants and bulk moduli. Cohesive energies are more difficult to describe with a localized basis set. The primary source of error in cohesive energies comes from the free-atom calculation, where the confinement of each orbital raises the energy levels by around 0.1 eV. Thus, atomic energies are systematically overestimated, leading to stronger binding.

6.1. Non-equilibrium electron transport

Driven by the prospects of nano-scale electronics, the field of quantum transport has developed rapidly over the last decade. In support of this development, GPAW supports open-boundary finite-bias electron transport calculations with the LCAO basis. The basic setting is that of a central device region (C) connected to two semi-infinite leads (L) and (R). The leads are kept at fixed chemical potentials, μ_L and μ_R, to simulate an applied bias voltage of $V = (\mu_L - \mu_R)/e$ across the device region. Due to electronic screening the electron potential inside the leads converges rapidly to the bulk value and this defines the boundary conditions for the electrostatic potential inside C. Rather than obtaining the wavefunctions from the eigenvalue equation we work with the Green function (GF) of the central region defined by

$$G(z) = (zS - H_C - \Sigma_L(z) - \Sigma_R(z))^{-1}, \tag{81}$$

where S and H_C are, respectively, the overlap and Kohn–Sham Hamiltonian matrix of the central region in the LCAO basis. The self-energies, $\Sigma_{L/R}$, represent the coupling to the leads and are obtained using the efficient decimation technique [86]. The electron density matrix is given by

$$D = \frac{1}{2\pi i}\int_{-\infty}^{\infty} G^<(\varepsilon)\,d\varepsilon = \frac{1}{2\pi i}\int_C G^<(z)\,dz \tag{82}$$

with the lesser GF defined by

$$G^<(z) = G(z)(\Sigma_L^<(z) + \Sigma_R^<(z))G(z)^\dagger. \tag{83}$$

As indicated in the last equality of equation (82) the integral is performed along a complex contour C. The equivalence of the two expressions follows from the analytical properties of the Green function and residue calculus [87]. Away from the real axis the Green function varies slowly with z and the integral can be efficiently evaluated using a Gauss–Kronrod quadrature [88]. The non-equilibrium density is obtained from

$$\tilde{n}(\mathbf{r}) = \sum_{\nu\mu} D_{\nu\mu}\Phi_\nu(\mathbf{r})^*\Phi_\mu(\mathbf{r}) + \sum_a \tilde{n}_c^a, \tag{84}$$

where Φ_ν and Φ_μ are the LCAO orbitals in the central region and $D_{\nu\mu}$ are the corresponding matrix elements of the density matrix. The Poisson equation is solved on the real-space grid to obtain the electrostatic contribution to the effective potential $\tilde{v}$ in region C. The boundary conditions for the Poisson equation at the C–L and C–R interfaces are given by the bulk potential of the leads (shifted by the applied bias voltage $\pm eV/2$), while periodic boundary conditions are used in the plane perpendicular to the direction of transport.

The cycle $D \to \tilde{n}(\mathbf{r}) \to \tilde{v}(\mathbf{r}) \to H_C \to D$ is iterated until self-consistency using Pulay density mixing. At self-consistency the current of a spin-degenerate system can be calculated from [89, 90]

$$I(V) = \frac{1}{\pi}\int_{-\infty}^{\infty}(f_L(\varepsilon) - f_R(\varepsilon)) \times \mathrm{Tr}[\Gamma_L(\varepsilon)G(\varepsilon^+)\Gamma_R(\varepsilon)G(\varepsilon^+)^\dagger]\,d\varepsilon, \tag{85}$$

where $\varepsilon^+ = \varepsilon + i0^+$ and $\Gamma_{L/R}(\varepsilon) = i(\Sigma_{L/R}(\varepsilon^+) - \Sigma_{L/R}(\varepsilon^+)^\dagger)$ and the trace is taken over the central region basis functions.

As an example, figure 9 shows the IV curve of a molecular junction consisting of a benzene dithiol molecule attached to gold electrodes (see inset). We have used a DZP basis set for the molecule and a SZ basis for the Au, a total of 84 Au atoms in the central region, and 4×4 k-points in the surface plane (8 irreducible). A 2d plot of the average effective potential at

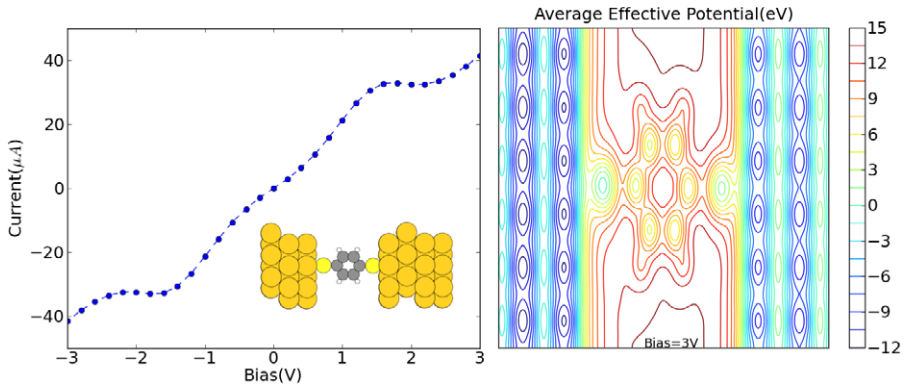

Figure 9. Left: calculated IV curve for the Au/benzene-dithiolate junction shown in the inset. Right: effective potential at a bias voltage of 3 V.

a bias of 3 V is shown in the right panel. Although four Au layers are included in the central region on both sides of the molecule, electronic screening limits the potential drop to the molecule and outermost Au surface layer.

Let us finally mention some of the limitations of the DFT-based transport approach. It has recently been shown that the energetic position of molecular electronic levels at a solid–molecule interface can be substantially wrong in DFT due to self-interaction errors [91] and the lack of dynamical screening [92–94]. This circumstance is expected to influence the calculated conductance, in particular when the transport mechanism is off-resonant tunneling, which is the most commonly encountered case. In such cases DFT must be considered to be only qualitatively correct, while quantitative predictions require a many-body description such as the GW approximation [95]. More fundamental problems are encountered for weakly coupled and strongly correlated systems dominated by Coulomb blockade and Kondo physics, where the single-particle approximation breaks down [96, 97]. In the opposite regime, characterized by strong molecule–lead couplings, DFT has been found to work surprisingly well and provides results in quantitative agreement with experiments [98, 99].

7. Additional features

7.1. ΔSCF

ΔSCF [100, 101, 33] is a simple method for estimating excitation energies within DFT. The acronym refers to the fact that the excitation energy is calculated as the difference between two self-consistent calculations, one traditional ground state calculation and one where an electron is constrained to a certain Kohn–Sham orbital as the system reaches self-consistency. The method is formally justified only when the constrained orbital is the lowest lying of its symmetry [102], but it is often applied in other situations with reasonable success [33, 103–106]. GPAW implements a generalized version of ΔSCF, where it is possible to constrain an electron to any linear combination of Kohn–Sham orbitals, which is desirable for molecules on surfaces where the molecular orbitals hybridize with substrate states. A molecular orbital $|\alpha\rangle$ can always be represented by a linear combination of Kohn–Sham orbitals if a sufficient number of unoccupied Kohn–Sham orbitals is included in the calculation:

$$|\alpha\rangle = \sum_n c_n |\psi_n\rangle, \qquad c_n = \langle\psi_n|\alpha\rangle. \tag{86}$$

The contribution to the PS electron density from this molecular orbital is then:

$$\Delta\tilde{n}_\alpha(\mathbf{r}) = \sum_{m,n} c_m^* c_n \tilde{\psi}_m^*(\mathbf{r})\tilde{\psi}_n(\mathbf{r}), \tag{87}$$

and the corrections to the atomic density matrices equation (10) are

$$\Delta D^a_{i_1 i_2} = \sum_{m,n} c_m^* c_n \langle\tilde{\psi}_m|\tilde{p}^a_{i_1}\rangle\langle\tilde{p}^a_{i_2}|\tilde{\psi}_n\rangle. \tag{88}$$

The extra electron is usually taken from the Fermi level by simply requiring that the Fermi distribution integrates to the number of valence electrons minus one, but it is possible to introduce any specified hole according to the above description.

The contribution to the band energy from the excited state is given by

$$\langle\alpha|\hat{H}|\alpha\rangle = \sum_{m,n} c_m^* c_n \langle\psi_m|\hat{H}|\psi_n\rangle = \sum_n |c_n|^2 \varepsilon_n. \tag{89}$$

The linear combination in equation (86) is found by projecting the Kohn–Sham orbitals onto a desired orbital in the self-consistency cycle. In GPAW this can be done in the two different ways as described below.

7.1.1. Projector–pseudo-wavefunction overlap. If the orbital to be kept occupied is an atomic orbital corresponding to a partial wave ($|\alpha\rangle = |\phi^a_i\rangle$), then the overlaps in equation (86) can be approximated by

$$\langle\psi_n|\phi^a_i\rangle \approx \langle\tilde{\psi}_n|\tilde{p}^a_i\rangle, \tag{90}$$

which follows from equation (5) if we neglect overlap between atomic sites. This is a quick and efficient way of obtaining the expansion coefficients c_n, since the projector overlaps equation (90) are calculated in each step of the self-consistence cycle anyway. The method is easily extended to molecular orbitals by taking appropriate linear combinations of $\langle\tilde{\psi}_n|\tilde{p}^a_i\rangle$.

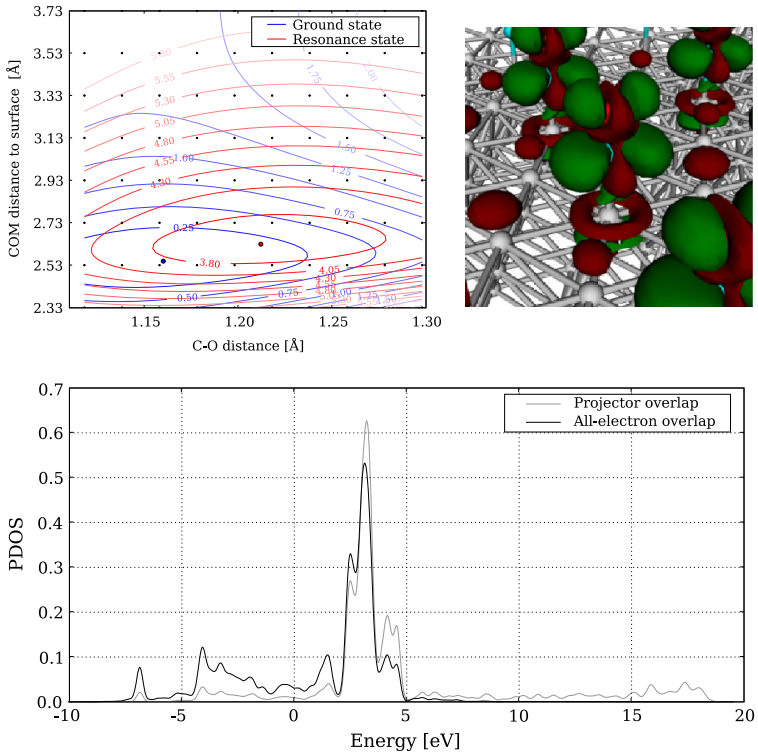

Figure 10. CO on Pt(111). Top left: potential energy surfaces in the ground state and the $2\pi^*$ resonance as a function of the CO binding distance and the molecule's center of mass distance to the surface. Top right: the change in charge distribution due to the excitation. Green: more charge (0.02 au contour), red: less charge (-0.02 au contour). Lower: density of states projected onto the $2\pi^*$ orbital of CO using the two projection methods described in sections 7.1.1 and 7.1.2.

7.1.2. AE wavefunction overlap. In principle one has access to the AE wavefunctions in the PAW formalism and thus it is possible to resolve any molecular orbital exactly into Kohn–Sham orbitals. However, the DFT PAW formalism works with the PS wavefunctions and these are the ones which are immediately available in the GPAW code.

To find the overlaps $c_n = \langle\psi_n|\alpha\rangle$ one should start by performing a gas-phase calculation of the molecule or atom which is to be used in an ΔSCF calculation. The PS wavefunction $|\tilde{\psi}_\alpha\rangle$ corresponding to the orbital to be occupied is then saved along with the its projector overlaps $\langle\tilde{p}^a_k|\tilde{\psi}_\alpha\rangle$ and the ΔSCF calculation is initialized. In each step of the calculation the AE overlap c_n can then be obtained by

$$c_n = \langle\psi_n|\psi_\alpha\rangle = \langle\tilde{\psi}_n|\tilde{\psi}_\alpha\rangle + \sum_{a,i_1,i_2}\langle\tilde{\psi}_n|\tilde{p}^a_{i_1}\rangle\Delta S^a_{i_1 i_2}\langle\tilde{p}^a_{i_2}|\tilde{\psi}_\alpha\rangle. \tag{91}$$

Note that there is only a single sum over atoms (and only the ones in the molecule) and that the cross terms of PS/AE wavefunctions do not contribute. Since the AE wavefunctions are orthonormal, the squared norm of the coefficients sums to one, $\sum_n |c_n|^2 = 1$, if the Kohn–Sham orbitals span the molecular orbital $|\alpha\rangle$. If this is not the case, one has to increase the number of unoccupied states in the calculation.

The expansion in equation (86) holds for each point in k-space, so one has to use the same k-points in the gas-phase calculation and then calculate the overlaps for each k-point.

7.1.3. Application to CO on Pt(111). In figure 10 we show the potential energy surfaces of CO on a Pt surface (1/4 monolayer) in the ground state and in an excited state where the $2\pi^*$ resonance is occupied. This demonstrates how the minimum energy configuration in the resonance state is shifted with respect to the ground state, which is interesting in relation to molecular motion induced by hot electrons [103]. Figure 10 also compares the projected density of states using the two projection methods described in sections 7.1.1 and 7.1.2, and clearly shows that the methods have the same qualitative features. However, the long high energy tail of the projector overlap method is a symptom of the lower accuracy of this method and indicates that the excitation energy will depend on the number of unoccupied bands included in the calculation. In contrast, the AE overlaps approach zero for high lying states and this method can be converged in the number unoccupied bands. Finally, figure 10 shows the charge redistribution due to the excitation. The $2\pi^*$ orbital of the molecule is clearly seen as well as an induced image charge on the surface.

7.2. X-ray absorption spectra

In a one-particle picture, x-ray absorption (XAS) can be viewed as exciting a core electron to an unoccupied orbital [107]. The absorption cross section is given by Fermi's golden rule:

$$\sigma(\omega) \propto \sum_f |\langle\psi_f|\mathbf{e}\cdot\boldsymbol{\mu}|\phi^a_c\rangle|^2\delta(E_{fc}-\omega), \tag{92}$$

where $|\phi^a_c\rangle$ is the core orbital, $|\psi_f\rangle$ are unoccupied orbitals, E_{fc} is the eigenvalue difference between orbitals c and f, $\mathbf{e}$ is the

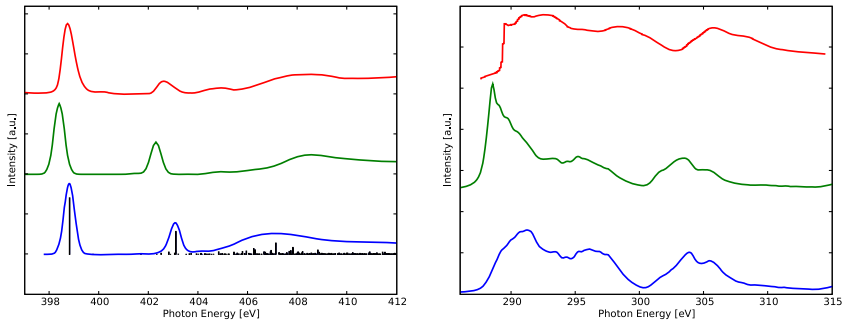

Figure 11. Left: half core hole K-edge nitrogen spectrum of Pyridine. Spectra shown are for GPAW (blue), StoBe (green), and experiment (red). The GPAW spectrum shows the individual oscillator strengths. Right: K-edge carbon spectrum of diamond. Spectra shown are the half core hole (blue), full core hole (green), and experiment (red).

polarization vector of the incoming photon and $\boldsymbol{\mu}$ is the dipole operator. To account for core hole effects we use specially constructed PAW setups with half or a full electron removed from the core orbital. The wavefunctions are then relaxed in this potential [108]. Using the PAW transformation we can rewrite the expression for the cross section [109]

$$\sigma(\omega) \propto \sum_f |\langle \tilde{\psi}_f | \tilde{\phi}_c^a \rangle|^2 \delta(E_{fc} - \omega), \tag{93}$$

where $|\tilde{\phi}_c^a\rangle = \sum_i |\tilde{p}_i^a\rangle\langle\phi_i^a|\mathbf{e}\cdot\boldsymbol{\mu}|\phi_c^a\rangle$. In the above expression for the cross section many unoccupied states must be determined, which is computationally demanding. This can be avoided with the Haydock recursion scheme [110], which we have also implemented. Due to the non-orthogonal PS wavefunctions in the PAW method, the calculation of the recursion coefficients involves the inverse overlap $\hat{S}^{-1}$, which cannot be explicitly computed. Instead, the equation $\hat{S}x = y$ is solved with the conjugate gradient method using an approximate $\hat{S}^{-1}$ as a preconditioner [111]. The absolute energy scale is determined separately in a ΔSCF procedure where the total energy difference is computed between the ground state and the first core excited state using a full core hole setup and an extra electron in the valence band. ΔSCF transition energies depend strongly on the functional used [112], mostly due to differing descriptions of the core electrons. The spectra discussed in the following were calculated using the LDA functional, with the ΔSCF shifts computed using the BLYP functional.

In figure 11 we show the calculated half core hole XAS spectrum for the pyridine nitrogen K-edge. A cubic box with 20 Å sides and a grid spacing of 0.2 Å was used with open-boundary conditions. The agreement with experiment and a calculation using the StoBe code [113, 114] is good. Comparing the GPAW calculation to experiment the first peak is 0.8 eV too low and the relative energy between the first peak and the sigma resonance (408 eV in experiment) is about one electron volt too low.

Figure 11 shows also the calculated carbon K-edge XAS spectrum of diamond both for half and full core hole. A cubic super-cell with 216 atoms was used with periodic boundary conditions and the Brillouin zone was sampled at the Γ point. The grid spacing was set to 0.2 Å. The spectrum was calculated with the recursion method using $6 \times 6 \times 6$ k-points and 2000 recursion coefficients. The full core hole spectrum is in good agreement with [109], but has too much intensity near the onset of the spectrum compared to the experiment [115]. Neither the half or the full core hole reproduces the first excitonic peak of the experiment.

7.3. Wannier orbitals

The partly occupied maximally localized Wannier functions (WF) [116] are constructed by doing an unitary rotation for the lowest states (*fixed space*), and using a dynamically optimized linear combination of the remaining orbitals (*active space*). Both linear combinations are chosen such as to minimize the spread of the resulting Wannier functions. The unitarity of the rotation in the fixed spaces implies that the eigenvalues of the Bloch states contained in the fixed space can all be exactly reproduced by the resulting WF, whereas the largest eigenvalues of the WF will not necessarily correspond to any 'real' eigenvalues.

When constructing Wannier functions, the only quantities that need to be supplied from the DFT calculation are the integrals $Z^{\mathbf{G}}_{n_1 n_2} = \langle\psi_{n_1}|e^{-i\mathbf{G}\cdot\mathbf{r}}|\psi_{n_2}\rangle$, where $\mathbf{G}$ is one of at most six possible (three in an orthorhombic cell) vectors connecting nearest neighbor cells in the reciprocal lattice. When introducing the PAW transformation, this quantity can be expressed as [116, 117]

$$Z^{\mathbf{G}}_{n_1 n_2} = \langle\tilde{\psi}_{n_1}|e^{-i\mathbf{G}\cdot\mathbf{r}}|\tilde{\psi}_{n_2}\rangle + \sum_a \sum_{i_1 i_2} P^{a*}_{i_1 n_1} P^a_{i_2 n_2} (\langle\phi^a_{i_1}|e^{-i\mathbf{G}\cdot\mathbf{r}}|\phi^a_{i_2}\rangle - \langle\tilde{\phi}^a_{i_1}|e^{-i\mathbf{G}\cdot\mathbf{r}}|\tilde{\phi}^a_{i_2}\rangle). \tag{94}$$

Even for small systems, the phase of the exponential of the last integral does not vary significantly over the augmentation spheres where ϕ_i^a and $\tilde{\phi}_i^a$ differ. The integrals in the last two terms can therefore safely be approximated by taking the exponential outside the integrals as $e^{-i\mathbf{G}\cdot\mathbf{R}^a}$.

An example of partly occupied Wannier functions constructed using the GPAW code is shown in figure 12 (left) for a benzene molecule.

One can also, in the same sense as for the partly occupied Wannier functions, form a linear combination of the Kohn–Sham Bloch states, spanning the occupied space exactly, where the unitary rotation in the fixed space, and the linear

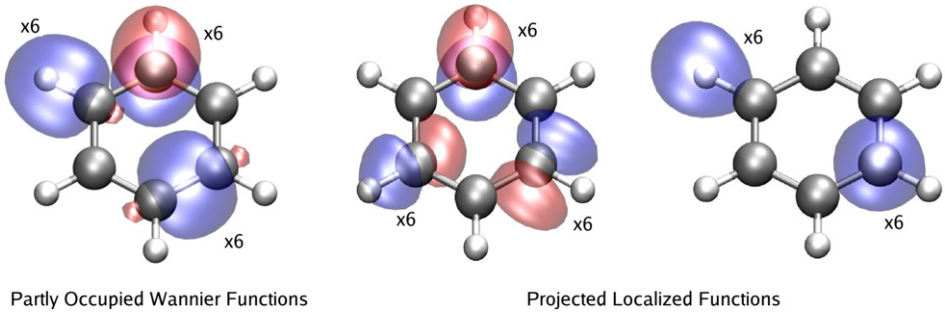

Figure 12. Left: partly occupied WF; 6 C–H σ bonds, 6 C–C σ bonds, and 6 p_z orbitals on C. Right: projected localized functions; 12 s orbitals on C and H respectively, and 3 p-type orbitals on each C, one p_z, one along the C–H bond, and one perpendicular to the C–H bond.

combination of the active space are chosen such that the overlap of the resulting wavefunctions with the projector functions or the PS LCAO orbitals is maximized. This will result in a optimized single-zeta numerical basis set, which can be used for minimal basis set calculations. An example of such localized optimized orbitals for benzene is shown in figure 12 (right). In this case the resulting orbitals have been rotated to diagonalize the Hamiltonian in the subspaces spanned by orbitals on the same atom. In GPAW, these functions are used as an efficient minimal basis set for performing computationally demanding GW calculations [53].

The algorithm for constructing such localized functions is much faster, and more robust than the one for constructing the partly occupied WF, as it only involves some linear algebra on the pre-calculated projections, and not an iterative maximization of a spread functional. The procedure is described in more detail in [118].

An exact representation of the Kohn–Sham eigenstates in a minimal and maximally localized basis can facilitate orbital analysis [116].

7.4. Local properties

This section describes quantities that can somehow be related to a specific atom. As the PAW transform utilizes an inherent partitioning of space into atomic regions, such quantities are usually extractable from already determined atomic attributes, such as the atomic density matrices or the projector overlaps.

The projector overlaps P^a_{in} are simultaneous expansion coefficients of the PS and the AE wavefunctions inside the augmentation spheres (see equations (5) and (6)). They can therefore be used both for reconstruction of AE wavefunction or densities, and for making a local expansion in atomic orbitals.

7.4.1. Density partitioning. Charge redistribution during a chemical reaction can often be studied by assigning the density distribution to the individual atoms. Formally, it is easy to reconstruct the true AE density from the PS density and the atom projected density matrix via equation (13).

In GPAW, charge assignment can be done in several ways. One choice is to apply a Wigner–Seitz scheme, where $\tilde{n}(\mathbf{r})$ at each grid point is assigned to the closest atom. The atomic PAW corrections in equation (13) can then be integrated on the radial grid, and added for each atom.

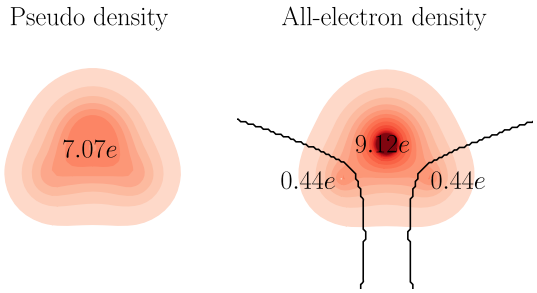

Figure 13. Contour lines for the PS (left) and reconstructed AE (right) densities of a water molecule. While the PS density only has a single maximum, the AE density has one distinct local maximum per atom, and a Bader partitioning scheme can be used to analyze charge transfer. The AE density integrates to the total number of electrons.

In the Bader analysis [119], it is not possible to apply the algorithm to the PS density and corrections separately, as the dividing surfaces might intersect the augmentation spheres. Thus, the AE density should be reconstructed on a single regular grid, which can also be useful for other post-processing purposes. To accurately represent the peaked features of the AE density, the PS density is interpolated to a grid with reduced grid spacing before transferring the density corrections from the radial grid to the uniform grid.

For the purpose of studying charge transfer, it can be advantageous to adjust the value of the atomic corrections on the uniform grid at the grid point closest to each nucleus, such that these integrate to the same value as on the more accurate radial grid. This does not affect the determination of the dividing surfaces, but enforces the integral properties of the reconstructed AE density within each domain.

In pseudopotential schemes, a reconstruction of the AE density is not possible, which can cause problems if the dividing surfaces and pseudization regions intersect. This is the case for water, as illustrated in figure 13, showing the dividing surfaces of a water molecule determined using the Bader program [120] and the reconstructed AE density from GPAW.

7.4.2. Projected density of states. Given a set of states $|\psi_n\rangle$ with eigenenergies ε_n, the density of states projected onto a

state $|\alpha\rangle$ is defined by

$$\rho_\alpha(\varepsilon) = \sum_n |\langle\alpha|\psi_n\rangle|^2 \delta(\varepsilon - \varepsilon_n). \quad (95)$$

If $|\alpha\rangle$ is an atomic orbital which can be represented by a partial wave $|\phi_i^a\rangle$, the simplest way to obtain the overlaps is to use the single-center expansion of the AE wavefunction equation (5), which gives $\langle\alpha|\psi_n\rangle \approx \langle\tilde{p}_i^a|\tilde{\psi}_n\rangle$ when neglecting the overlap of ϕ_i^a with neighboring augmentation spheres. The method is easily extended to molecular orbitals by considering superpositions of partial waves.

If the state $|\alpha\rangle$ can be represented by a Kohn–Sham state $|\psi_\alpha\rangle$ from a different calculation, the PAW formalism allows one to obtain the AE overlaps exactly from equation (91). The difference in the two methods is illustrated for the case of the $2\pi^*$ orbital of CO adsorbed on Pt(111) in figure 10. A major advantage of the AE overlap method is that the projected density of states is correctly normalized and one can obtain the fraction of an orbital located below a given energy by truncating the sum in (95) at that energy.

8. Parallel calculations

Drastic performance improvements in desktop computers and supercomputers are nowadays being achieved through new CPU designs with a high density of processing elements (PEs). (Here we will use the terms cores, processors, and processing elements interchangeably.) Thus, parallel computing is needed for utilizing this kind of hardware. The benefits of parallelization are two-fold: firstly, a reduction in the time-to-solution, and secondly, the capability to study larger problems. At present, parallelization of GPAW is accomplished using MPI; though with the advent of multicore CPUs fine-grained parallelism with OpenMP or Posix threads is a likely future enhancement.

The real-space representation allows seamless distribution of the PS wavefunction $\tilde{\psi}_{n\mathbf{k}\sigma}(\mathbf{r}_g)$ over all wavefunction indices: band n, $\mathbf{k}$-point, spin σ, as well as the grid point g index. This is in sharp contrast to plane-wave basis codes which rely on the dual-space technique [121] for iterative diagonalization, and are thus complicated by representing the PS wavefunction in both real and reciprocal space. Parallelization over k-points and spin is almost trivial as these degrees are normally only coupled through electron density (except in the case of EXX). The generalized eigenvalue problem, equation (29) can be solved independently for each k-point and spin. However, as there are significant number of k-points only in small periodic systems and spin only in magnetic systems, the scalability accessible via k-point and spin parallelization is of limited benefit for large systems.

The primary parallelization scheme in GPAW is the domain decomposition of the real-space grid. The simulation box is divided among the PEs so that each subdomain has approximately the same number of grid points. Due to the local nature of the finite difference Laplacian, communication is needed only between neighboring PEs when evaluating derivatives. The non-local parts of the PAW Hamiltonian also require only nearest neighbor communication: calculating an integral involving a projector function, $\langle\tilde{p}_i^a|\tilde{\psi}_n\rangle$, only involves contributions from those PEs that have grid points inside the augmentation sphere of atom a.

The computation of the dense matrix diagonalization and Cholesky decomposition needed for subspace diagonalization and orthogonalization scales as N_e^3, where N_e is the number of electronic states. For large systems with many electrons ($N_e > 2000$), these operations can be excessively slow in serial and must be performed in a parallel. In GPAW, we use ScaLAPACK [122] to perform these dense linear algebra operations. In practice, a small subset of the PEs is used for ScaLAPACK parallelization. As an example, in a 2048 core calculation with $N_e \sim 1800$, ScaLAPACK diagonalizations are performed with only 16 cores and take a few per cent of the total computing time. In our most recent release of GPAW, the associated dense linear algebra matrices, requiring $O(N_e^2)$ storage, are fully distributed so that very large problems ($N_e > 10\,000$) can be treated.

Even though the real-space domain decomposition scales well, the ratio of computation to communication decreases when the number of PEs is increased (for a fixed problem size). The limiting factor is the ratio N_g/P_d, where N_g is the total number of grid points (proportional to system size N) and P_d is the number of PEs used for domain decomposition. The computational workload of the entire calculation scales as $O(N^3)$ (due to orthonormality constraints and subspace diagonalization), so that in large systems additional parallelization levels are necessary.

For large systems, domain decomposition is combined with parallelization over the band index. This is ideal in the case of real-time propagation TDDFT because different electronic states can be propagated independently of each other and communication is needed only when summing for the electron density, similar to k-point and spin parallelization. However, for a ground state DFT calculation, the subspace diagonalization and orthogonalization steps necessitate communication of all the electronic states on co-subdomains (g index). The amount of data to communicate per PE is proportional to $N_g N_e/(P_d P_e)$. On the other hand, the relevant computational workload is proportional to $N_g N_e^2/(P_d P_e)$ (where P_e is the number of band groups and $P_d P_e$ equals to the total number of PEs). In sharp contrast to the domain decomposition, where the communication is proportional to the surface area of the subdomain, parallelization over the band index introduces communication which is proportional to the *volume* of the subdomain. P_e must be carefully chosen so that the computation to communication ratio can be kept reasonable. Part of the communication overhead can often be hidden by overlapping communication and computation.

Optimal values of N_g/P_d and N_e/P_e depend a lot on the underlying hardware, but our experience has shown that typical minimum values are $N_g/P_d = 1000$–8000 and $N_e/P_e = 250$ for ground state calculations, and $N_e/P_e = 20$–40 for real-time propagation. This enables scaling to thousands of processors for large systems, as shown in figure 14. The ground state DFT calculation is a 102 Au atom cluster surrounded by 44 p-MBA molecules [123] and the dimension of the system is ~3 nm. There are total of 762 atoms on a 160^3 real-space grid

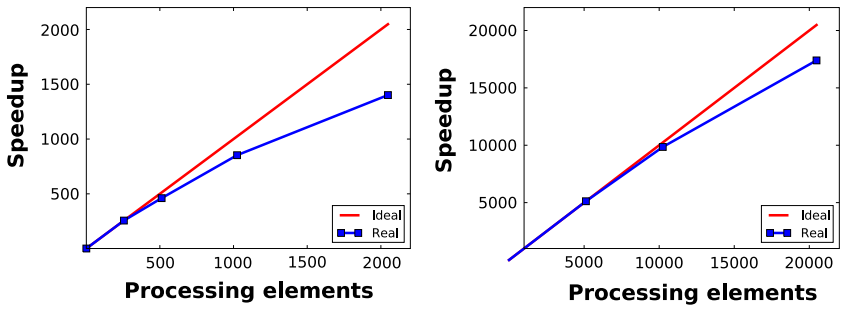

Figure 14. Parallel scaling for ground state total energy calculation (left) and for real-time propagation (right). The calculations are performed on a Cray XT5 systems at CSC and at Oak Ridge National Laboratory. The speedup is normalized so that at the first data point (256 PEs on left and 5000 PEs on right) the speedup equals the number of PEs.

and ∼1800 electronic states are included in the calculation. The real-time propagation TDDFT is performed for a silicon cluster with 702 atoms on a 160^3 real-space grid, the number of electronic states in the calculation is ∼1600.

When using the LCAO basis, the real-space domain decomposition is used when solving the Poisson equation and in the evaluation of two-center integrals. Dense matrix diagonalizations can also be performed with the help of ScaLAPACK, and parallelization over basis functions (equivalent of state parallelization in grid calculations) has been implemented. Generally, the parallel scaling of LCAO calculations is not as good as that of grid calculations, on the other hand the more modest memory requirement and computational workload enable large LCAO-type calculations with a smaller number of CPUs.

In some special cases, it is possible to introduce further parallelization levels. For example, in nudged elastic band calculations, the total energies of the images are independent and can hence be calculated in parallel. Also, when calculating optical spectra with real-time propagation, the calculations over different polarization directions (if required by the symmetry of the system) can be performed in parallel. Finally, in linear-response TDDFT, the construction of the Ω matrix, equation (71), can be performed parallel over the electron–hole pairs. All these additional parallelization schemes are trivial and therefore scale ideally.

9. Summary and outlook

As described in this article, GPAW is now a stable and fairly mature real-space realization of DFT and TDDFT, based on the PAW method. In addition to the grid-based description, a localized atomic orbital basis is available for fast computations of more limited accuracy. Many features have been implemented, including a wide range of exchange–correlation functionals. The code is currently developed by an expanding group of developers situated primarily in Denmark, Finland, Sweden, and Germany, with users from all over the world.

GPAW is an open-source project with only a loose organization behind it and, therefore, there exists no single long-term master plan for the further development of the code. The implementations that take place are exclusively based on the needs of the researchers working with the code and the whole project is therefore in the end carried by the enthusiasm of researchers at all levels. Among the features which are currently implemented, we mention the calculation of static response functions using density-functional perturbation theory and more general calculations of dynamical response functions within TDDFT. The calculation of forces as well as adiabatic and Ehrenfest dynamics are also being implemented within TDDFT. Furthermore, there is ongoing-work to extend the number of atomic setups to include all elements through atomic number 86.

The GPAW code builds upon the Atomistic Simulation Environment (ASE) [124], which is a set of Python modules to facilitate setting up, running, and analyzing atomistic/electronic calculations. The tight integration with ASE is expected to be maintained in the future. This seems natural also from the point of view that the interest in ASE has increased considerably in the past few years such that ASE now supports about 12 different force and energy calculators.

There are of course a number of other open-source projects focused on DFT/TDDFT, such as ABINIT, Quantum ESPRESSO, and Octopus. How does GPAW fit into this 'market' of codes? The main feature which distinguishes GPAW is the combination of real-space description with the PAW method. The PAW allows for an accurate, essentially all-electron, frozen core description, which leads to soft pseudo-wavefunctions even for transition metals. The real-space description allows for easy and very scalable parallelization through real-space decomposition, making it possible to perform accurate calculations for large systems. Only time can tell which future developments will make their way into the GPAW code, but almost certainly they will benefit from the PAW accuracy and the real-space parallelization.

Acknowledgments

This work has been supported by the Academy of Finland (Project 110013 and the Center of Excellence program) and Tekes MASI-program. We acknowledge support from the Danish Center for Scientific Computing (DCSC). The Center for Atomic-scale Materials Design (CAMD) is sponsored by the Lundbeck Foundation. We thank John Levesque from Cray Inc. for parallel calculations on the Cray XT5 Jaguar at Oak Ridge National Laboratory. The Argonne Leadership Computing Facility at Argonne National

Laboratory is supported by the Office of Science of the US Department of Energy under contract DE-AC02-06CH11357.

References

[1] Hohenberg P and Kohn W 1964 Inhomogeneous electron gas *Phys. Rev.* **136** B864–71

[2] Kohn W and Sham L J 1965 Self-consistent equations including exchange and correlation effects *Phys. Rev.* **140** A1133–8

[3] Runge E and Gross E K U 1984 Density-functional theory for time-dependent systems *Phys. Rev. Lett.* **52** 997–1000

[4] Phillips J C and Kleinman L 1959 New method for calculating wavefunctions in crystals and molecules *Phys. Rev.* **116** 287–94

[5] Kleinman L and Bylander D M 1982 Efficacious form for model pseudopotentials *Phys. Rev. Lett.* **48** 1425–8

[6] Vanderbilt D 1990 Soft self-consistent pseudopotentials in a generalized eigenvalue formalism *Phys. Rev.* B **41** 7892–5

[7] Blöchl P E 1994 Projector augmented-wave method *Phys. Rev.* B **50** 17953–79

[8] Wimmer E, Krakauer H, Weinert M and Freeman A J 1981 Full-potential self-consistent linearized-augmented-plane-wave method for calculating the electronic structure of molecules and surfaces: O_2 molecule *Phys. Rev.* B **24** 864–75

[9] Payne M C, Teter M P, Allan D C, Arias T A and Joannopoulos J D 1992 Iterative minimization techniques for *ab initio* total-energy calculations: molecular dynamics and conjugate gradients *Rev. Mod. Phys.* **64** 1045–96

[10] Hehre W J, Stewart R F and Pople J A 1969 Self-consistent molecular-orbital methods. i. Use of Gaussian expansions of Slater-type atomic orbitals *J. Chem. Phys.* **51** 2657–64

[11] Soler J M, Artacho E, Gale J D, García A, Junquera J, Ordejón P and Sánchez-Portal D 2002 The SIESTA method for *ab initio* order-*N* materials simulation *J. Phys.: Condens. Matter* **14** 2745

[12] Blum V, Gehrke R, Hanke F, Havu P, Havu V, Ren X, Reuter K and Scheffler M 2009 *Ab initio* molecular simulations with numeric atom-centered orbitals *Comput. Phys. Commun.* **180** 2175–96

[13] Chelikowsky J R, Troullier N and Saad Y 1994 Finite-difference-pseudopotential method: electronic structure calculations without a basis *Phys. Rev. Lett.* **72** 1240–3

[14] Beck T L 2000 *Rev. Mod. Phys.* **72** 1041

[15] Junquera J, Paz Ó, Sánchez-Portal D and Artacho E 2001 Numerical atomic orbitals for linear-scaling calculations *Phys. Rev.* B **64** 235111

[16] Briggs E L, Sullivan D J and Bernholc J 1996 Real-space multigrid based approach to large scale electronic structure calculations *Phys. Rev.* B **54** 14362–75

[17] Tsuchida E and Tsukada M 1995 Electronic-structure calculations based on the finite-element method *Phys. Rev.* B **52** 5573–8

[18] Pask J E and Sterne P A 2005 Finite element methods in *ab initio* electronic structure calculations *Modelling Simul. Mater. Sci. Eng.* **13** R71–96

[19] Lehtovaara L, Havu V and Puska M 2009 All-electron density functional theory and time-dependent density functional theory with high-order finite elements *J. Chem. Phys.* **131** 054103

[20] https://wiki.fysik.dtu.dk/gpaw

[21] Kresse G and Joubert D 1999 From ultrasoft pseudopotentials to the projector augmented-wave method *Phys. Rev.* B **59** 1758

[22] Gonze X *et al* 2002 First-principle computation of material properties: the ABINIT software project *Comput. Mater. Sci.* **25** 478

[23] Holzwarth N A W, Matthews G E, Dunning R B, Tackett A R and Zeng Y 1997 Comparison of the PAW, pseudopotential, and LAPW formalisms for density functional calculations of solids *Phys. Rev.* B **55** 2005

[24] Blöchl P E, Först C J and Schimpl J 2003 The projector augmented wave method: *ab initio* molecular dynamics with full wavefunctions *Bull. Mater. Sci.* **26** 33

[25] Kresse G and Furthmüller J 1996 Efficiency of *ab initio* total energy calculations for metals and semiconductors using a plane-wave basis set *Comput. Mater. Sci.* **6** 15–50

[26] Giannozzi P *et al* 2009 QUANTUM ESPRESSO: a modular and open-source software project for quantum simulations of materials *J. Phys.: Condens. Matter* **21** 395502

[27] Ahlrichs R, Bär M, Häser M, Horn H and Kölmel C 1989 Electronic structure calculations on workstation computers: the program system turbomole *Chem. Phys. Lett.* **162** 165–9

[28] Briggs E L, Sullivan D J and Bernholc J 1995 Large-scale electronic-structure calculations with multigrid acceleration *Phys. Rev.* B **52** R5471–4

[29] Marques M A L, Castro A, Bertsch G F and Rubio A 2003 Octopus: a first-principles tool for excited electron–ion dynamics *Comput. Phys. Commun.* **151** 60–78

[30] Heiskanen M, Torsti T, Puska M J and Nieminen R M 2001 Multigrid method for electronic structure calculations *Phys. Rev.* B **63** 245106

[31] Yabana K and Bertsch G F 1996 Time-dependent local-density approximation in real time *Phys. Rev.* B **54** 4484

[32] Casida M E 1996 Time-dependent density functional response theory of molecular systems: theory, computational methods, and functionals *Recent Developments and Applications in Modern Density-Functional Theory* ed J M Seminario (Amsterdam: Elsevier) p 391

[33] Gavnholt J, Olsen T, Engelund M and Schiøtz J 2008 Δ self-consistent field method to obtain potential energy surfaces of excited molecules on surfaces *Phys. Rev.* B **78** 075441

[34] Mortensen J J, Hansen L B and Jacobsen K W 2005 Real-space grid implementation of the projector augmented wave method *Phys. Rev.* B **71** 035109

[35] Marsman M and Kresse G 2006 Relaxed core projector-augmented-wave method *J. Chem. Phys.* **125** 104101

[36] Kiejna A, Kresse G, Rogal J, De Sarkar A, Reuter K and Scheffler M 2006 Comparison of the full-potential and frozen-core approximation approaches to density-functional calculations of surfaces *Phys. Rev.* B **73** 035404

[37] Natan A, Benjamini A, Naveh D, Kronik L, Tiago M L, Beckman S P and Chelikowsky J R 2008 Real-space pseudopotential method for first principles calculations of general periodic and partially periodic systems *Phys. Rev.* B **78** 075109

[38] Tafipolsky M and Schmid R 2006 A general and efficient pseudopotential Fourier filtering scheme for real space methods using mask functions *J. Comput. Phys.* **124** 174102

[39] Hartwigsen C, Goedecker S and Hutter J 1998 Relativistic separable dual-space Gaussian pseudopotentials from H to Rn *Phys. Rev.* B **58** 3641–62

[40] Kresse G and Furthmüller J 1996 Efficient iterative schemes for *ab initio* total-energy calculations using a plane-wave basis set *Phys. Rev.* B **54** 11169–86

[41] Wood D M and Zunger A 1985 A new method for diagonalising large matrices *J. Phys. A: Math. Gen.* **18** 1343

[42] Feng Y T and Owen D R J 1996 Conjugate gradient methods for solving the smallest eigenpair of large symmetric eigenvalue problems *Int. J. Num. Methods Eng.* **39** 2209–29

[43] Davidson E R 1975 The iterative calculation of a few of the lowest eigenvalues and corresponding eigenvectors of large real-symmetric matrices *J. Comput. Phys.* **17** 87–94

[44] Pulay P 1980 Convergence acceleration of iterative sequences. The case of SCF iteration *Chem. Phys. Lett.* **73** 393–8

[45] http://www.tddft.org/programs/octopus/wiki/index.php/Libxc
[46] Perdew J P, Ruzsinszky A, Tao J, Staroverov V N, Scuseria G E and Csonka G I 2005 Prescription for the design and selection of density functional approximations: more constraint satisfaction with fewer fits *J. Chem. Phys.* **123** 062201
[47] Tao J, Perdew J P, Staroverov V N and Scuseria G E 2003 Climbing the density functional ladder: nonempirical meta generalized gradient approximation designed for molecules and solids *Phys. Rev. Lett.* **91** 146401
[48] Zhao Y and Truhlar D G 2006 A new local density functional for main-group thermochemistry, transition metal bonding, thermochemical kinetics, and noncovalent interactions *J. Chem. Phys.* **125** 194101
[49] Perdew J P, Ruzsinszky A, Csonka G I, Constantin L A and Sun J 2009 Workhorse semilocal density functional for condensed matter physics and quantum chemistry *Phys. Rev. Lett.* **103** 026403
[50] Perdew J P, Tao J, Staroverov V N and Scuseria G 2004 Meta-generalized gradient approximation: explanation of a realistic nonempirical density functional *J. Chem. Phys.* **120** 6898–911
[51] Paier J, Hirschl R, Marsman M and Kresse G 2005 The Perdew–Burke–Ernzerhof exchange–correlation functional applied to the G2-1 test set using a plane-wave basis set *J. Chem. Phys.* **122** 234102
[52] Walter M, Häkkinen H, Lehtovaara L, Puska M, Enkovaara J, Rostgaard C and Mortensen J J 2008 Time-dependent density-functional theory in the projector augmented-wave method *J. Chem. Phys.* **128** 244101
[53] Rostgaard C, Jacobsen K W and Thygesen K S 2010 Fully self-consistent GW calculations for molecules *Phys. Rev.* B **81** 085103
[54] Massidda S, Posternak M and Baldereschi A 1993 Hartree–Fock LAPW approach to the electronic properties of periodic systems *Phys. Rev.* B **48** 5058–68
[55] Rostgaard C 2009 The projector augmented-wave method arXiv:0910.1921 [cond-mat.mtrl-sci]
[56] Adamo C and Barone V 1999 Towards reliable density functional methods without adjustable parameters: the PBE0 model *J. Chem. Phys.* **110** 6158–70
[57] Curtiss L A, Raghavachari K, Redfern P C and Pople J A 1997 Assessment of Gaussian-2 and density functional theories for the computation of enthalpies of formation *J. Chem. Phys.* **106** 1063–79
[58] Gritsenko O, van Leeuwen R, van Lenthe E and Jan Baerends E 1995 Self-consistent approximation to the Kohn–Sham exchange potential *Phys. Rev.* A **51** 1944–54
[59] Becke A D 1988 Density-functional exchange-energy approximation with correct asymptotic behavior *Phys. Rev.* A **38** 3098–100
[60] Kuisma M, Ojanen J, Enkovaara J and Rantala T T 2010 arXiv:1003.0296
[61] Perdew J P, Ruzsinszky A, Csonka G I, Vydrov O A, Scuseria G E, Constantin L A, Zhou X and Burke K 2008 Restoring the density-gradient expansion for exchange in solids and surfaces *Phys. Rev. Lett.* **100** 136406
[62] Perdew J P and Levy M 1983 Physical content of the exact Kohn–Sham orbital energies: band gaps and derivative discontinuities *Phys. Rev. Lett.* **51** 1884–7
[63] Sham L J and Schlüter M 1983 Density-functional theory of the energy gap *Phys. Rev. Lett.* **51** 1888–91
[64] Levinshtein M, Rumyantsev S and Shur M 1996 *Handbook Series on Semiconductor Parameters* (Singapore: World Scientific)
[65] Dion M, Rydberg H, Schroder E, Langreth D C and Lundqvist B I 2004 Van der Waals density functional for general geometries *Phys. Rev. Lett.* **92** 246401
[66] Román-Pérez G and Soler J M 2009 Efficient implementation of a van der Waals density functional: application to double-wall carbon nanotubes *Phys. Rev. Lett.* **103** 096102
[67] Wellendorff J, Kelkkanen A, Mortensen J J, Lundqvist B I and Bligaard T 2010 RPBE-vdW description of benzene adsorption on Au(111) *Top. Catal.* **53** 378–83
[68] Dudarev S L, Botton G A, Savrasov S Y, Humphreys C J and Sutton A P 1998 Electron-energy-loss spectra and the structural stability of nickel oxide: an LSDA + U study *Phys. Rev.* B **57** 1505–9
[69] Rohrbach A, Hafner J and Kresse G 2004 Molecular adsorption on the surface of strongly correlated transition-metal oxides: a case study for Co/NiO(100) *Phys. Rev.* B **69** 075413
[70] Maxisch T, Wang L and Ceder G 2006 Oxidation energies of transition metal oxides within the GGA + U framework *Phys. Rev.* B **73** 195107
[71] Tran F, Blaha P, Schwarz K and Novák P 2006 Hybrid exchange–correlation energy functionals for strongly correlated electrons: applications to transition-metal monoxides *Phys. Rev.* B **74** 155108
[72] Mortensen J J, Kaasbjerg K, Frederiksen S L, Nørskov J K, Sethna J P and Jacobsen K W 2005 Bayesian error estimation in density-functional theory *Phys. Rev. Lett.* **95** 216401
[73] Perdew J P, Burke K and Ernzerhof M 1996 Generalized gradient approximation made simple *Phys. Rev. Lett.* **77** 3865–8
[74] Yabana K and Bertsch G F 1999 Time-dependent local-density approximation in real time: application to conjugated molecules *Int. J. Quantum Chem.* **75** 55–66
[75] Casida M E 1995 Time-dependent density-functional response theory for molecules *Recent Advances in Density Functional Methods, Part I* ed D P Chong (Singapore: World Scientific) p 155
[76] Grabo T, Petersilka M and Gross E K U 2000 Molecular excitation energies from time-dependent density functional theory *J. Mol. Struct.: THEOCHEM* **501/502** 353–67
[77] Negishi Y, Chaki N K, Whetten R L and Tsukuda T 2007 Origin of magic stability of thiolated gold clusters: case study on Au25(Sc6h13)18 *J. Am. Chem. Soc.* **129** 11322
[78] Neuhasuer D and Baer M 1989 The time-dependent Schrodinger equation: application of absorbing boundary conditions *J. Chem. Phys.* **90** 4351–5
[79] Chong D P, Gritsenko O V and Baerends E J 2002 Interpretation of the Kohn–Sham orbital energies as approximate vertical ionization potentials *J. Chem. Phys.* **116** 1760–72
[80] Walter M and Häkkinen H 2008 Photoelectron spectra from first principles: from the many-body to the single-particle picture *New J. Phys.* **10** 043018
[81] Allison D A and Cavell R G 1978 Photoelectron spectroscopy with Zr $M\zeta$ (151 eV) radiation. A study of the variation of relative photoionization cross sections of molecules containing first row atoms (C, N, O) with exciting radiation from He^{I} to K_{α} limits *J. Chem. Phys.* **68** 593–601
[82] Sankey O F and Niklewski D J 1989 *Phys. Rev.* B **40** 3979
[83] Delley B 2000 From molecules to solids with the Dmol3 approach *J. Chem. Phys.* **113** 7756
[84] Larsen A H, Vanin M, Mortensen J J, Thygesen K S and Jacobsen K W 2009 Localized atomic basis set in the projector augmented wave method *Phys. Rev.* B **80** 195112
[85] Anglada E, Soler J M, Junquera J and Artacho E 2002 *Phys. Rev.* B **66** 205101
[86] Guinea F, Tejedor C, Flores F and Louis E 1983 Effective two-dimensional Hamiltonian at surfaces *Phys. Rev.* B **28** 4397
[87] Brandbyge M, Mozos J L, Ordejón P, Taylor J and Stokbro K 2002 Density-functional method for nonequilibrium electron transport *Phys. Rev.* B **65** 165401
[88] Patterson T N L 1968 Optimum addition of points to quadrature formulae *Math. Comput.* **22** 847
[89] Meir Y and Wingreen N S 1992 Landauer formula for the current through an interacting electron region *Phys. Rev.* B **68** 2512
[90] Thygesen K S 2006 Electron transport through an interacting region: the case of a nonorthogonal basis set *Phys. Rev.* B **73** 035309
[91] Toher C and Sanvito S 2008 Effects of self-interaction corrections on the transport properties of phenyl-based molecular junctions *Phys. Rev.* B **77** 155402

[92] Neaton J B, Hybertsen M S and Louie S G 2006 Renormalization of molecular electronic levels at metal–molecule interfaces *Phys. Rev. Lett.* **97** 216405

[93] Garcia-Lastra J M, Rostgaard C, Rubio A and Thygesen K S 2009 Polarization-induced renormalization of molecular levels at metallic and semiconducting surfaces *Phys. Rev.* B **80** 245427

[94] Thygesen K S 2008 Impact of exchange–correlation effects on the IV characteristics of a molecular junction *Phys. Rev. Lett.* **100** 166804

[95] Thygesen K S and Rubio A 2008 Conserving GW scheme for nonequilibrium quantum transport in molecular contacts *Phys. Rev.* B **77** 115333

[96] Wang X, Spataru C D, Hybertsen M S and Millis A J 2008 Electronic correlation in nanoscale junctions: comparison of the gw approximation to a numerically exact solution of the single-impurity anderson model *Phys. Rev.* B **77** 045119

[97] Jacob D, Haule K and Kotliar G 2009 Kondo effect and conductance of nanocontacts with magnetic impurities *Phys. Rev. Lett.* **103** 016803

[98] Scheer E, Agrait N, Cuevas J C, Yeyati A L, Ludoph B, Martin-Rodero A, Bollinger G R, van Ruitenbeek J M and Urbina C 1998 The signature of chemical valence in the electrical conduction through a single-atom contact *Nature* **394** 154–7

[99] Djukic D, Thygesen K S, Untiedt C, Smit R H M, Jacobsen K W and van Ruitenbeek J M 2005 Stretching dependence of the vibration modes of a single-molecule pt-h-2-pt bridge *Phys. Rev.* B **71** 161402

[100] Jones R O and Gunnarsson O 1989 The density functional formalism, its applications and prospects *Rev. Mod. Phys.* **61** 689–746

[101] Hellman A, Razaznejad B and Lundqvist B I 2004 Potential-energy surfaces for excited states in extended systems *J. Chem. Phys.* **120** 4593–602

[102] Gunnarsson O and Lundqvist B I 1976 Exchange and correlation in atoms, molecules, and solids by the spin-density-functional formalism *Phys. Rev.* B **13** 4274–98

[103] Olsen T, Gavnholt J and Schiøtz J 2009 Hot-electron mediated desorption rates calculated from excited-state potential energy surfaces *Phys. Rev.* B **79** 035403

[104] Olsen T 2009 Inelastic scattering in a local polaron model with quadratic coupling to bosons *Phys. Rev.* B **79** 235414

[105] Olsen T and Schiøtz J 2009 Origin of power laws for reactions at metal surfaces mediated by hot electrons *Phys. Rev. Lett.* **103** 238301

[106] Olsen T and Schiøtz J 2010 Vibrationally mediated control of single-electron transmission in weakly coupled molecule–metal junctions *Phys. Rev.* B **81** 115443

[107] Stöhr J 1992 *NEXAFS Spectroscopy* (Berlin: Springer)

[108] Triguero L, Pettersson L G M and Ågren H 1998 Calculations of near-edge x-ray-absorption spectra of gas-phase and chemisorbed molecules by means of density-functional and transition-potential theory *Phys. Rev.* B **58** 8097–110

[109] Taillefumier M, Cabaret D, Flank A-M and Mauri F 2002 X-ray absorption near-edge structure calculations with the pseudopotentials: application to the k edge in diamond and α-quartz *Phys. Rev.* B **66** 195107

[110] Haydock R, Heine V and Kelly M J 1972 Electronic structure based on the local atomic environment for tight-binding bands *J. Phys. C: Solid State Phys.* **5** 2845–58

[111] Hasnip P J and Pickard C J 2006 Electronic energy minimisation with ultrasoft pseudopotentials *Comput. Phys. Commun.* **174** 24–9

[112] Takahashi O and Pettersson L G M 2004 Functional dependence of core-excitation energies *J. Chem. Phys.* **121** 10339–45

[113] Kolczewski C *et al* 2001 Detailed study of pyridine at the C 1s and N 1s ionization thresholds: the influence of the vibrational fine structure *J. Chem. Phys.* **115** 6426–37

[114] http://w3.rz-berlin.mpg.de/∼hermann/StoBe/

[115] Ma Y, Wassdahl N, Skytt P, Guo J, Nordgren J, Johnson P D, Rubensson J-E, Boske T, Eberhardt W and Kevan S D 1992 Soft-x-ray resonant inelastic scattering at the C k edge of diamond *Phys. Rev. Lett.* **69** 2598–601

[116] Thygesen K S, Hansen L B and Jacobsen K W 2005 Partly occupied Wannier functions: construction and applications *Phys. Rev.* B **72** 125119

[117] Ferretti A, Calzolari A, Bonferroni B and Di Felice R 2007 Maximally localized Wannier functions constructed from projector-augmented waves or ultrasoft pseudopotentials *J. Phys.: Condens. Matter* **19** 036215

[118] Quek S Y, Venkataraman L, Choi H J, Louie S G, Hybertsen M S and Neaton J B 2007 Amine-gold linked single-molecule circuits: experiment and theory *Nano Lett.* **7** 3477–82

[119] Tang W, Sanville E and Henkelman G 2009 A grid-based Bader analysis algorithm without lattice bias *J. Phys.: Condens. Matter* **21** 084204

[120] http://theory.cm.utexas.edu/henkelman/research/bader/

[121] Martins J L and Cohen M L 1988 Diagonalization of large matrices in pseudopotential band-structure calculations: dual-space formalism *Phys. Rev.* B **37** 6134

[122] Blackford L S *et al* 1997 *ScaLAPACK Users' Guide* (Philadelphia, PA: Society for Industrial and Applied Mathematics)

[123] Walter M, Akola J, Lopez-Acevedo O, Jadzinsky P D, Calero G, Ackerson C J, Whetten R L, Grönbeck H and Häkkinen H 2008 A unified view of ligand-protected gold clusters as superatom complexes *Proc. Natl Acad. Sci.* **105** 9157–62

[124] Bahn S and Jacobsen K W 2002 *Comput. Sci. Eng.* **4** 56 https://wiki.fysik.dtu.dk/ase

Paper III: Finite Size Effects in Chemical Bonding: From Small Clusters to Solids

Catal Lett
DOI 10.1007/s10562-011-0632-0

Finite Size Effects in Chemical Bonding: From Small Clusters to Solids

J. Kleis · J. Greeley · N. A. Romero · V. A. Morozov · H. Falsig · A. H. Larsen · J. Lu · J. J. Mortensen · M. Dułak · K. S. Thygesen · J. K. Nørskov · K. W. Jacobsen

Received: 17 May 2011 / Accepted: 21 May 2011

Abstract We address the fundamental question of which size a metallic nano-particle needs to have before its surface chemical properties can be considered to be those of a solid, rather than those of a large molecule. Calculations of adsorption energies for carbon monoxide and oxygen on a series of gold nanoparticles ranging from 13 to 1,415 atoms, or 0.8–3.7 nm, have been made possible by exploiting massively parallel computing on up to 32,768 cores on the Blue Gene/P computer at Argonne National Laboratory. We show that bulk surface properties are obtained for clusters larger than ca. 560 atoms (2.7 nm). Below that critical size, finite-size effects can be observed, and we show those to be related to variations in the local atomic structure augmented by quantum size effects for the smallest clusters.

Keywords Nano-particle · Size effects · DFT

Electronic supplementary material The online version of this article (doi:10.1007/s10562-011-0632-0) contains supplementary material, which is available to authorized users.

J. Kleis · H. Falsig · A. H. Larsen · J. Lu · J. J. Mortensen · M. Dułak · K. S. Thygesen · J. K. Nørskov · K. W. Jacobsen (✉)
Department of Physics, Center for Atomic-Scale Materials Design, Technical University of Denmark, Building 307, 2800 Lyngby, Denmark
e-mail: kwj@fysik.dtu.dk

J. Greeley
Center for Nanoscale Materials, Argonne National Laboratory, Argonne, IL 60439, USA

N. A. Romero · V. A. Morozov
Leadership Computing Facility, Argonne National Laboratory, Argonne, IL 60439, USA

J. K. Nørskov
SUNCAT Center for Interface Science and Catalysis, SLAC National Accelerator Laboratory, 2575 Sand Hill Road, Menlo Park, CA 94025, USA

J. K. Nørskov (✉)
Department of Chemical Engineering, Stanford University, Stanford, CA 94305, USA
e-mail: norskov@stanford.edu

Most catalysts used in industry consist of nano-particles, typically 3–20 nm in diameter, of the catalytic material [1]. The small size maximizes the area of the catalytically active surface but may also affect the catalytic properties [2]; the most striking example is gold nano-particles, which can have substantial catalytic activity for a number of reactions, including CO oxidation, while larger gold particles are essentially inactive [3–5]. The existence of finite-size effects challenges the widely used surface science approach to understanding heterogeneous catalysis [6–8]. In this approach, extended single-crystal surfaces are used as models of the facets of nano-particle catalysts. Close-packed surfaces are models of the larger facets of the catalyst particles, while steps and kinks have been used to model edges and corners (as well as surface defects). For sufficiently large particles, this must clearly be a good model. In the present Letter, we set out to investigate theoretically the critical size at which the surface chemical properties converge to the infinite particle limit.

We will concentrate here on the particle size effects of freestanding metallic particles. We are focusing, in particular, on changes in the electronic structure of the particles with size. One such effect is that the electronic spectra of small metallic particles become discrete, as in a molecule, as opposed to the continuous spectrum of bulk metals. For real catalysts there are additional finite-size effects due to the interaction of the metal particles with the support. Such

Published online: 07 June 2011

effects can best be properly addressed, however, when the intrinsic particle size effects are understood. It is the study of the latter effects that is the purpose of the present Letter. We calculate the adsorption energy of CO and O on different size Au clusters and use that as a measure of the variation of the chemical properties of the surface with particle size [9]. While there are many theoretical studies of adsorption properties of small metal particles (see e.g. [10–17]) we know of no previous studies of systems large enough to reach the bulk limit. Rösch et al. have studied chemisorption on Pd clusters in the size range 55–260 atoms [17]. This study did not show convergence, but they suggested that for unrelaxed clusters, the bulk limit is reached in this size range.

The gold particles we have considered are the closed-shell cuboctahedra shown in Fig. 1 [18]. The smallest of these structures were found to be slightly less stable than corresponding closed-shell twenty-faced icosahedra. However, their construction from fcc-bulk by cutting (111) and (100) planes gives the closed shell cuboctahedra a unique resemblance with the model surfaces usually applied to study surface reactivity. The cuboctahedra therefore provide well-defined bulk limits that make them ideal candidates for the study of intrinsic finite-size effects.

The total energy of the clusters with and without adsorbates is determined from density functional theory (DFT) calculations using the GPAW code [19, 20]. This real-space grid code, which applies Projector Augmented Wave (PAW) [21] potentials to deal with the ionic cores, permits the massive parallelization on the Blue Gene/P supercomputer needed to treat up to 1,415 Au atoms. To describe the exchange and correlation effects, we apply the RPBE functional [22]. For further details of the calculations we refer to the electronic supplementary material.

In the following we consider adsorption on two fundamentally different sites: a "facet" site with a geometry similar to the close-packed (111) surface of Au and an

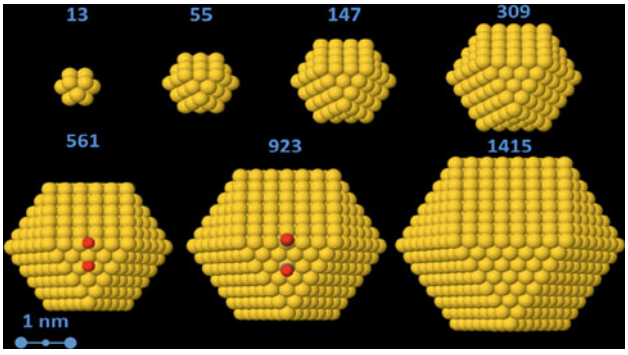

Fig. 1 All closed shell cuboctahedra up to 1,415 gold atoms [1–7] shells) are shown. We have studied adsorption of CO and O on all clusters, and the two considered adsorption sites for the two adsorbates are shown (O fcc site or edge site on the 561 atom cluster and CO top site on the 923 atom cluster, as close to the center of the edge/facet as possible)

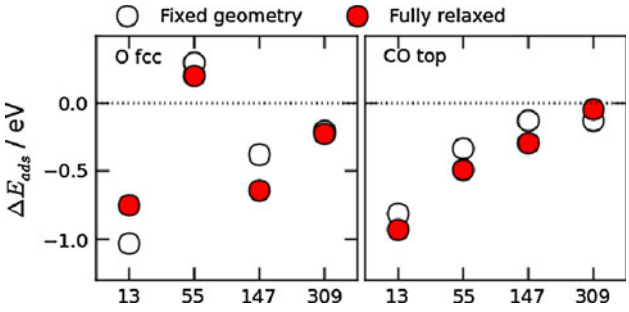

Fig. 2 Adsorption energies of O and CO at their most stable sites on the (111)-type facets, referenced to the adsorption energy on the bulk (111) surface (*dotted line*), are shown for fixed-geometry clusters and adsorbates (*white circles*) and for systems where all degrees of freedoms are allowed to relax (*red circles*)

"edge" site at one of the edges of the particle which in the bulk limit is analogous to a step site on a (211) surface.

Figure 2 compares the calculated adsorption energies for the two probe adsorbates as a function of cluster size up to 309 atoms for the case where the adsorbate has been placed in the same local geometry (same distance to the nearest neighbour Au atoms) and the case where the complete system has been allowed to relax with and without the adsorbate. The former measures the purely electronic effects of varying the size, whereas the latter includes the effect of coupling to the lattice. It is clear from Fig. 2 that there are non-negligible lattice effects and that they depend somewhat on size, but it is also clear that the electronic effects totally dominate the size effects. In the following, we therefore concentrate on the systems with fixed geometry. We also note that our calculations do not support the notion of Rösch et al. [17] that the unrelaxed clusters should reach the bulk limit much faster than the relaxed ones.

Figure 3 shows the size dependence of the adsorption energy for fixed-geometry structures for all sizes up to 1,415 atoms (3.7 nm). For the facet-type sites of both adsorbates, we find that clusters smaller than 561 atoms (2.7 nm) show clear finite-size effects. The general effect is that the adsorption becomes stronger as the particle becomes smaller. On top of this general trend, we find an anomaly at Au_{55}, which is found to be uniquely unreactive towards oxygen. This is in excellent agreement with experimental evidence [23].

At and above 561 atoms (2.7 nm), on the other hand, the value of the adsorption energy is identical to the one we calculate for an infinite surface within the numerical accuracy of our methods (estimated to be $\sim$50 meV).[1] The same is true for the edge sites although here the finite-size

[1] An estimate of the numerical errors in solving the Kohn–Sham equations can be obtained by noting that the variation of molecular atomization energies calculated by different codes (GPAW, VASP and Gaussian03) in Ref. [19] is found to be uncorrellated and of the order of 50 meV.

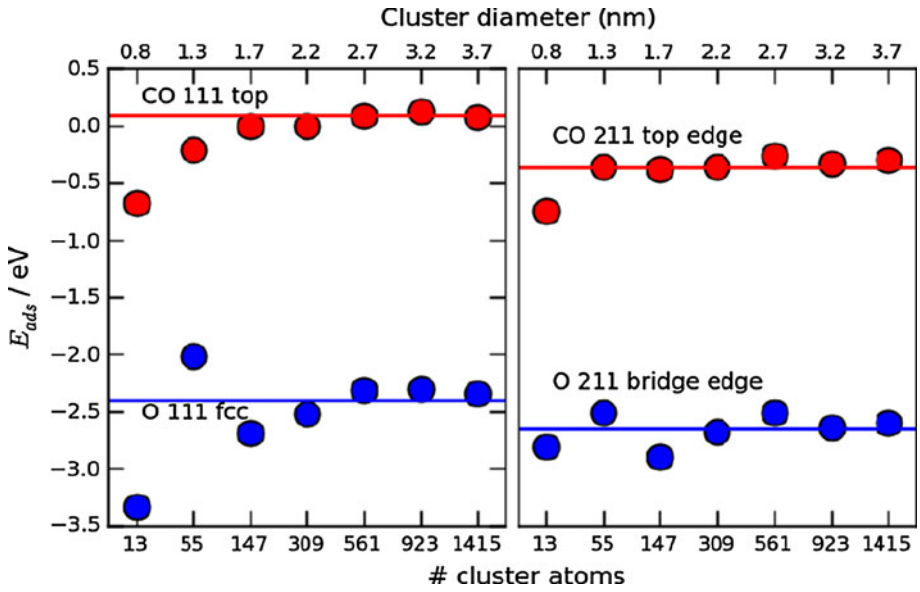

Fig. 3 Adsorption energies of CO and O on the (111) facet and at the edge of fixed-geometry clusters as a function of cluster size. The horizontal lines denote the adsorption energies for (111) and (211) slab surface calculations

effects appear to be smaller for both adsorbates. As a main conclusion of the present work, we have therefore identified the critical size above which finite size-effects disappears for Au clusters to be of the order of 560 atoms (2.7 nm). In the following we analyze the origin of the transition.

First, consider the charge density response of the cluster to the adsorption. We will illustrate this for O adsorption on the (111) facets (data for CO adsorption can be found in the electronic supplementary material). The main effect of coupling the O 2p states to the Au 6 s states is to transfer electrons into the oxygen states (a Bader analysis [24] gives that $\sim$0.7 electrons are transferred to the oxygen atom). Figure 4 shows charge density difference plots $[n(\text{metal} + \text{O}) - n(\text{metal}) - n(\text{O})]$ for O adsorption on the (111)-type sites on the clusters as well as on the Au(111) surface.[2]

Figure 4 shows that the adsorbate-induced perturbation is quite local. For clusters with 561 atoms and larger, the charge density response is very similar to that found for the (111) surface. Convergence in the adsorption energy thus coincides with convergence in the electron density response to the adsorption. For the 309-atom cluster, the electron density response extends along the surface to include the edge of the cluster, and for the smaller ones it extends all the way to the other side of the particle. The extent of the screening cloud is such that the nearest neighbour Au atoms are affected as well as the next nearest neighbours. For the extended surface, Fig. 4 shows the extent of charge density perturbation, λ, to be of the order 1 nm. The finite-size effect can be related to the value of λ relative to the size, L, of the facets on the particle. For comparison, the 561-atom cluster of diameter 2.7 nm has (111) facets of diameter 1 nm. It is therefore the smallest cluster for which the adsorbate-induced electron density is not affected by the size of the facets.

To test the nature of the finite-size effects further we plot in Fig. 5 the calculated adsorption energy for CO and O as a function of the average coordination number of the Au atoms to which the adsorbate binds. In the plot we include the adsorption on extended surfaces with different structures.

It can be seen that to a first approximation the cluster data follow the data for extended surfaces: The lower the metal coordination number, the stronger the bond. This trend is clearly not related to quantum-size effects. Rather, the main effect of varying the cluster size is to vary the environment (ligands) of the Au atoms to which the adsorbate bonds. On top of this general effect there are variations which we ascribe to quantum-size effects. They are most pronounced for the smallest clusters where the charge density response is covering the whole cluster, see Fig. 4.

One parameter which characterizes the electronic structure of a cluster is the size of the one-electron level spacings in the vicinity of the Fermi level. If the level spacings become comparable to the adsorbate-cluster coupling matrix element one would expect strong effects on the bonding strength. For O adsorption the coupling matrix element to the Au *s* and *d* electrons is of the order of 3.4 eV [25, 26]. That means that gaps in the cluster density of states that are much smaller than that will have limited influence on the adsorption energy. We find that for the 147

[2] The chosen contour of 0.001 e/Å^3 ensures that the electrostatic energy of the density-difference distribution is converged to 10 meV compared to the electrostratic energy of the full density difference, and that the sum of the absolute value of the redistributed charge enclosed in these contours is at least 70% of the total redistributed charge.

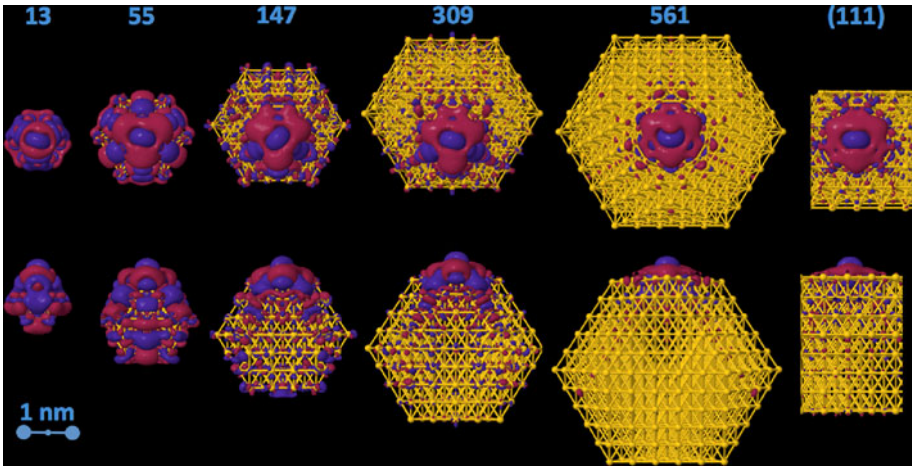

Fig. 4 Charge redistribution upon oxygen adsorption seen from the *top* (*upper*) and the *side* (*lower*). *Blue* (*red*) contours signify areas of accumulated (depleted) electron density. The contours are chosen to be 0.001 e/Å^3, enclosing $\sim$70% of the charge redistribution

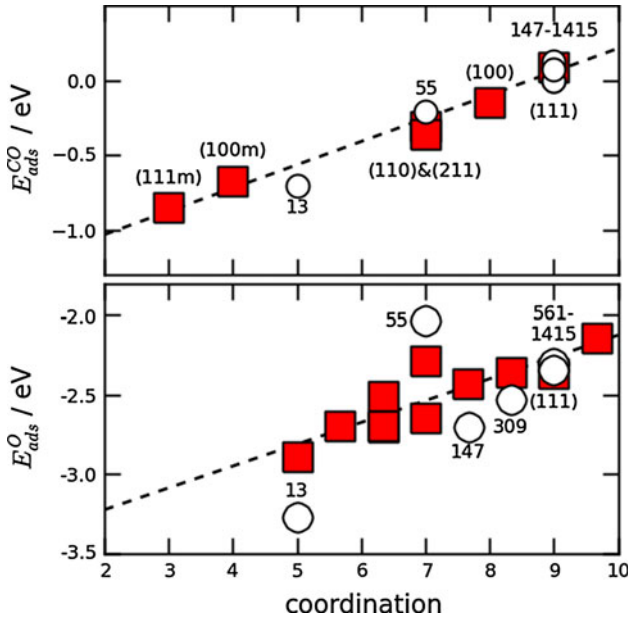

Fig. 5 Facet adsorption energy of CO (*top*) and O (*bottom*) as a function of the average coordination number of the gold atoms in the nearest proximity. Cluster calculations are denoted by *white circles*. Bulk-like calculations (marked with *red squares*) have been performed to separate size-effects due to the electronic structure of clusters from effects that can be attributed to the local geometry. The *dashed line fits* the coordination trend for the bulk-like systems. For CO, the surface type is indicated for each bulk-like calculation. An appended m refers to adatom calculations that model local monomer systems. For O, the bulk-like calculations correspond to 3-fold coordinated sites on (211) surfaces as well as steps and adatom plateaus on (111) surfaces

atom and larger clusters the typical level spacings are less than 10 meV. For the 55 and 13 atom clusters we find it to be ca. 0.25 and 0.7 eV, respectively. We therefore see that only for the smallest clusters the discreeteness of the one-electron spectrum can be expected to influence the bonding significantly. We note that there may be other properties of metal clusters (such as stability) where there is no external perturbation setting the energy scale of the interactions and where the shell structure of the clusters' electronic structure manifests itself more clearly [27].

Finally, we comment on the influence of the quantum-size effects on the rate of the CO oxidation reaction. For this discussion we will use the finding that, to a good approximation, the energies of all important surface intermediates and transition states in the CO oxidation process scale with the O and CO adsorption energies [9]. These two parameters can therefore be used to characterize the catalyst surface. As would be expected, the close-packed Au surface binds both O and CO too weakly to be a good catalyst. The optimal catalyst for low temperature (300 K) CO oxidation has CO binding which is $\sim$1 eV and O binding which is $\sim$0.5 eV stronger than Au(111) [9]. Figure 3 shows that the finite-size effects move the small Au particles towards the optimum, that is, the particles are better catalysts the smaller they are. We also note from Fig. 3 that the edge sites are intrinsically closer to the optimum than the (111)-type sites, all the way down to sizes around 55 atoms (1 nm).

To summarize, we identify three distinct intrinsic (that is, without including the possible effect of the support) finite-size effects in the surface properties of Au clusters:

1. The "trivial" effect of varying the relative number of edge and corner sites with varying particle size—the smaller the particle, the larger the number of highly active edge and corner sites per mass unit of catalyst.
2. For particles less than 2.7 nm, an additional effect sets in. Facets become small enough that the screening cloud of the adsorbate starts feeling the edges, or, equivalently, the metal atoms in the center of the facets have a number of metal nearest neighbours less than on an infinite surface. This effect is still local.
3. For the smallest clusters quantum-size effects also begin to play a role, as seen from the large deviations

of the binding energies at small clusters compared to the surface structures in Fig. 5.

In conclusion, we have identified the transition of surface chemical activity of Au clusters from molecular behaviour to bulk behaviour to be around 560 atoms, corresponding to a diameter of ca 2.7 nm. Above this size, the surface chemistry of two probe adsorbates, O and CO, is indistinguishable from that of an extended surface. Below this threshold, there are strong finite-size effects, which we identify as being related to the spatial extent of the charge density response to the adsorption event relative to the size of the cluster. Our results indicate that for supported metal catalysts above ca. 2.5 nm the surface science model of heterogeneous surfaces should work well, when proper care has been taken to include the effect of high pressure and temperature on the state of the surface. Additional effects of supports can be included on top of the intrinsic metal effects that can be extracted from planar surface models.

Acknowledgement This research used resources of the Argonne Leadership Computing Facility at Argonne National Laboratory, which is supported by the Office of Science of the U.S. Department of Energy under contract DE-AC02-06CH11357. The researchers' use of Argonne's Center for Nanoscale Materials was supported by the U.S. Department of Energy, Office of Science, Office of Basic Energy Sciences, also under contract No. DE-AC02-06CH11357. Additional support from the Office of Science of the U.S. Department of Energy to the SUNCAT Center for Interface Science and Catalysis at SLAC/Stanford, the NABIIT program under the Danish Strategic Research Council, and from the Lundbeck Foundation to the Center for Atomic-scale Materials Design at DTU is gratefully acknowledged.

References

1. Thomas JM, Thomas WJ (1997) Principle and practice of heterogeneous catalysis. VCH, Weinheim
2. Li Y, Somorjai GA (2010) Nano Lett 10:2289
3. Valden M, Lai X, Goodman DW (1998) Science 281:1647
4. Bond GC, Thompson DT (1994) Catal Rev Sci Eng 41:319
5. Haruta M, Kobayashi T, Sano H, Yamada N (1987) Chem Lett 2:405
6. Ertl G (2008) Angew Chem Int Ed 47:3524
7. Somorjai GA, Park JY (2008) Chem Soc Rev 37:2155
8. Honkala K, Hellman A, Remediakis IN, Logadottir A, Carlsson A, Dahl S et al (2005) Science 307:555
9. Jiang T, Mowbray D, Dobrin S, Falsig H, Hvolbaek B, Bligaard T et al (2009) J Phys Chem C 113:10548
10. Sanchez A, Abbet S, Heiz U, Schneider WD, Hakkinen H, Barnett RN et al (1999) J Phys Chem A. 103:9573
11. Chretien S, Gordon MS, Metiu H (2004) J Chem Phys 121:3756
12. Lopez-Acevedo O, Kacprzak KA, Akola J, Hakkinen H (2010) Nat Chem 2:329
13. Pyykko P (2008) Chem Soc Rev 37:1967
14. Mpourmpakis G, Andriotis AN, Vlachos DG (2010) Nano Lett 10:1041
15. Xie Y-P, Gong X-G (2010) J Chem Phys 132:244302
16. Roldan A, Manel Ricart J, Illas F, Pacchioni G (2010) Phys Chem Chem Phys 12:10723
17. Yudanov I, Metzner M, Genest A, Rosch N (2008) J Phys Chem C 112:20269
18. Martin TP (1996) Phys Rep 273:199
19. Enkovaara J, Rostgaard C, Mortensen JJ, Chen J, Dulak M, Ferrighi L et al (2010) J Phys Condens Matter 22:1
20. Mortensen JJ, Hansen LB, Jacobsen KW (2005) Phys Rev B 71:035109
21. Blocl P (1994) Phys Rev B 50:17953
22. Hammer B, Hansen LB, Norskov JK (1999) Phys Rev B 59:7413
23. Boyen HG, Kastle G, Weigl F, Koslowski B, Dietrich C, Ziemann P et al (2002) Science 297:1533
24. Bader RFW (1990) Atoms in molecules: a quantum Theory Oxford University Press, Oxford
25. Kitchin JR, Norskov JK, Barteau MA, Chen JG (2004) Phys Rev Lett 93:156801
26. Inoglu N, Kitchin JR (2010) Phys Rev B 82:045414
27. von Issendorff B, Cheshnovsky O (2005) Annu Rev Phys Chem 56:549

Paper IV: Electronic shell structure and chemisorption on gold nanoparticles

Electronic shell structure and chemisorption on gold nanoparticles

A. H. Larsen,[1] J. Kleis,[1] K. S. Thygesen,[1] J. K. Nørskov,[2] and K. W. Jacobsen[1]

[1] *Center for Atomic-scale Materials Design, Department of Physics Technical University of Denmark, DK - 2800 Kgs. Lyngby, Denmark*

[2] *SUNCAT Center for Interface Science and Catalysis, SLAC National Accelerator Laboratory 2575 Sand Hill Road, Menlo Park, CA 94025, USA*

(Dated: October 13, 2011)

We use density functional theory (DFT) to investigate the electronic structure and chemical properties of gold nanoparticles. Different structural families of clusters are compared. For up to 60 atoms we optimize structures using DFT-based simulated annealing. Cluster geometries are found to distort considerably, creating large band gaps at the Fermi level. For up to 200 atoms we consider structures generated with a simple EMT potential and clusters based on cuboctahedra and icosahedra. All types of cluster geometry exhibit jellium-like electronic shell structure. We calculate adsorption energies of several atoms on the cuboctahedral clusters. Adsorption energies are found to vary abruptly at magic numbers. Using a Newns-Anderson model we find that the effect of magic numbers on adsorption energy can be understood from the location of adsorbate-induced states with respect to the cluster Fermi level.

PACS numbers: 36.40.Cg, 36.40.Mr, 36.40.Jn, 34.35.+a

I. INTRODUCTION

A major theme in advanced materials design today is the possibility to modify and change materials properties through structuring at the nanoscale. The applications can be as diverse as optimizing the size of metal nanoparticles to catalyze certain chemical reactions[1] or the structuring of surfaces and interfaces for optimal light absorption in photovoltaic devices[2]. In very broad terms the interesting possibilities arise when the structures reach a scale comparable to the wavelengths of the relevant quantum particles (electrons, plasmons or photons).

In this work we investigate theoretically the properties of freestanding metal nanoparticles made of gold in particular. The purpose is to improve our understanding of the relationship between cluster size and a range of electronic and chemical properties. Different aspects of this has been investigated in numerous studies. See for example the review by Baletto and Ferrando.[3] What is special here is that we investigate the cluster properties over an – for electronic structure calculations – unusually large size range and for many different cluster structures. The hope is thereby to get a more complete picture of the general trends in the cluster behavior.

For transition metals with partially filled d-bands, cohesive energies will be dominated by the effect of the d-states[4]. Because of the short range of the d-states, their contribution to the cluster energy is determined mostly by the local arrangement of neighboring atoms. Facet types and local atomic packing can therefore be expected to be particularly important factors in the structures of transition metal clusters with partially filled d-bands.

The effect of the partially occupied d-band disappears for noble metals and alkali metals. Instead the long-range s-electrons, which hybridize in a more complex manner, yield the primary contribution to the cluster energy. The optimal structure will not be determined by optimizing the local structure around each atom, but rather by optimizing the global geometric structure to obtain the most desirable electronic structure of the delocalized electron cloud. The result is a much more complicated interplay between electronic and geometric structure.

Small free-standing gold clusters have been theoretically shown to possess very diverse ground-state geometries depending on cluster size. Examples are planar, cage-like and tube-like structures[5–8].

The s-electron hybridization can be interpreted in terms of a jellium model which regards the whole cluster as a spherical superatom. The s electrons organize into global shells, resulting in electronic "magic numbers" when shells are filled. Magic numbers at 2, 8, 18, 20, 34, 40, 58, ..., have been observed as particularly stable alkali metal clusters[9,10] with large band gaps in agreement with theory. For alkali metals, magic numbers attributed to both electronic and geometric shell structures have been observed for clusters with thousands of atoms, with geometric shells dominating beyond 2000 atoms[11]. Larger Au clusters are believed to form icosahedra, decahedra or truncated octahedra depending on size and temperature[12–14].

In this work we consider several series of clusters based on different generation procedures and structural motifs. We calculate structures of smaller clusters using simulated annealing with density functional theory (DFT) and for larger clusters using effective medium theory[15,16] (EMT). Using DFT we compare the energy and electronic structure of optimized clusters with the commonly considered regular icosahedral and cuboctahedral structures. For the cuboctahedra we identify trends in reactivity by considering adsorption of different atoms. The geometric similarity of clusters based on cuboctahedra and icosahedra allows us to isolate and study size-dependent effects on chemistry. The price of this simplification is that individual calculations do not represent globally op-

timal structures. Hence we focus on trends that are general enough to be significant outside the model systems.

II. COMPUTATIONAL METHODS

All electronic structure calculations are performed with the real-space DFT code GPAW[17,18] using the RPBE[19] functional for exchange and correlation. GPAW uses the projector augmented wave (PAW) method[20], and offers an accurate real-space representation of the Kohn-Sham orbitals along with an efficient basis set of localized atomic orbitals[21]. The calculations presented here are performed with the atomic orbitals using a double-zeta polarized (DZP) basis set. All calculations on clusters are spin-paired and use the scalar-relativistic atomic PAW setups and basis sets supplied with GPAW. The Au setup contains 11 valence electrons.

In our calculations the cluster is centered in a non-periodic orthorhombic cell with 5.0 Å vacuum along each axis. We use a grid-spacing of 0.2 Å.

We do not apply any basis set superposition error correction, so the values of adsorption energies are not necessarily accurate. However in comparing the bonding of an adsorbate to clusters of different sizes, the local structure around the adsorbate highly similar for all clusters, and the basis set error is consequently roughly the same for all clusters. Therefore variations in adsorption energies are subject to a much smaller error.

Pulay density mixing[22] is used to speed up convergence of the self-consistency loop. Electron occupations are smeared by a small Fermi temperature of 0.01 eV, which helps speed up convergence.

Structure optimizations are performed using the BFGS algorithm as implemented in the Atomic Simulation Environment[23] (ASE), and terminate when no force on any atom is larger than 0.075 eV/Å.

III. CLUSTER GEOMETRY

Systematic calculation of lowest-energy structures from first principles is computationally very expensive. Previous studies of structures and properties of Au clusters have therefore usually been limited to a few dozens of atoms.[8,24–26] Here we focus mainly on larger clusters which are quite challenging to systematically optimize and characterize, but which are clearly of interest both from a conceptual point of view and in applications like catalysis. The transition from smaller clusters over larger clusters to bulk-like behavior has been studied recently by Kleis *et al.*[27] and the results presented here can be seen as a supplement and expansion of this study.

In this work we compare clusters generated by several different procedures. For the smallest clusters we perform simulated annealings using DFT to obtain realistic structures. This is clearly the most realistic and theoretically satisfactory method since the same energy landscape is used to define the cluster geometry or shape as is used to subsequently study the bonding of the cluster and the chemical properties. However, for reasons of computer time this approach cannot be generally applied for larger clusters.

Larger clusters are studied using DFT, but with the structures being determined by simulated annealing with a classical EMT potential. As this EMT potential does not incorporate explicit electronic structure, the structures generated by this method will have no information about potential electronic shell effects but only of atomic shell effects related to atomic packing of the clusters.

We finally construct clusters based on prescribed cuboctahedral and icosahedral shapes. The simplicity of the fcc-based cuboctahedral structures allows us to study adsorption of atoms in a way which preserves the local geometry around the adsorbate for different cluster sizes. This allows us to separate the effect of local geometry from that of the electronic structure of the cluster, which would not generally be possible if the cluster were based on a global minimum search. The comparison of distinct types of structures will help determine how properties of clusters depend on structure versus size.

A. Simulated annealing with DFT

For the smallest clusters (N=6–60) we calculate realistic geometries using DFT with coarse parameters.

For each size of cluster we perform a rough simulated annealing based on molecular dynamics (MD) to find the optimal structure. We use a Langevin thermostat to regulate the temperature from 750 K to 300 K. For a cluster of size N we lower the temperature by 1 K for every $5 + N/2$ timesteps of length 24 fs. The timestep is too large to have accurate energy conservation during the optimization. This can cause unrealistic behavior when the atoms move quickly, but is not likely to affect the results of an annealing where the result is mostly determined at lower temperatures. The optimization is performed with a very coarse grid spacing of 0.24 Å.

At the end of the MD simulation we perform a structure optimization with normal DFT parameters using the BFGS algorithm such that the structure is guaranteed to be a local minimum.

These optimizations produce planar and tetrahedral structures in qualitative agreement with previous findings[6,28–30], while larger structures tend to be irregular but with some well-formed facets. Due to the short annealing times, the larger structures are unlikely to be global optima. Figure 1 shows the 20-atom tetrahedron and the 58-atom cluster obtained with this method. Notice on the 58-atom cluster the imperfect five-fold symmetry center reminiscent of those found on icosahedral clusters.

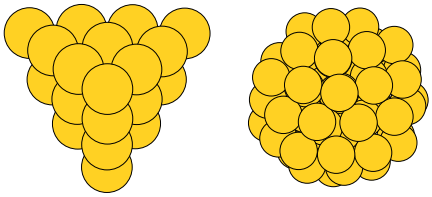

FIG. 1: (Color online) 20 (left) and 58-atom (right) clusters obtained by simulated annealing with DFT.

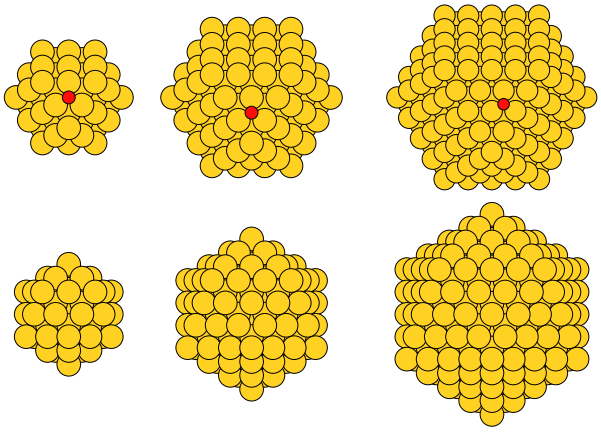

FIG. 2: (Color online) Cuboctahedra (top) and icosahedra (bottom) with 55, 147 and 309 atoms. For the cuboctahedra, an O atom is shown at the fcc site closest to the center of an 111 facet.

B. Simulated annealing with EMT

For a larger range of clusters (N=6–200) we calculate structures using a simple EMT potential[15,16] implemented in ASAP[31]. This potential is designed to provide reasonable descriptions of elastic and cohesive properties. It is a classical potential and as such contains no explicit description of electronic behavior.

For each size of cluster we perform a simulated annealing wherein the temperature varies from above the melting point (1337 K for Au) to 200 K with 600 MD steps of 6.0 fs for each 1 K decrease in temperature. The resulting structures frequently have 5-fold symmetry centers surrounded by 111 facets, resembling partially formed icosahedra or decahedra. Again, at the end of the simulated annealing we perform a BFGS structure optimization with the usual DFT parameters.

C. Atomic shell structures

Finally we consider the cuboctahedral and icosahedral series of structures. Each cluster can be constructed geometrically from the previous one by adding one complete shell of atoms. The cuboctahedra and icosahedra have closed atomic shells at the same numbers. The first few geometric shell closings are N=13, 55, 147, 309 and 561.

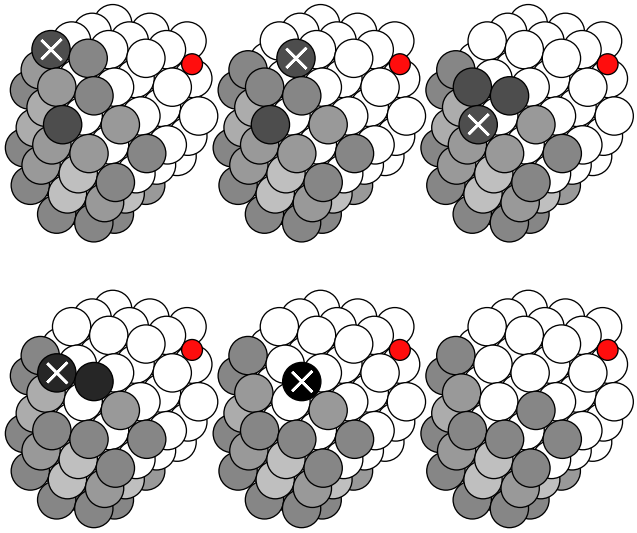

FIG. 3: (Color online) Generation of regular clusters with different numbers of atoms. The white atoms belong to the 55-atom cuboctahedron, while the grey atoms are stripped off one by one as marked with a cross. Removable atoms with lower coordination numbers have darker shades of grey, and at each step one of the lowest-coordinated atoms is removed at random. An oxygen atom is shown at the adsorption site.

We would like to study the chemical properties of clusters by calculating adsorption energies of atoms on clusters of different sizes. A systematic comparison can be made if we ensure that the local geometry around the adsorbate remains identical for all clusters independent of size.

For the cuboctahedra we generate clusters with different numbers of atoms by stripping off atoms one by one from one cuboctahedron until only the next smaller cuboctahedron remains. For each step, the next atom to be removed is chosen at random amongst those that have the lowest coordination numbers and are not part of the smaller cuboctahedron. This procedure is shown on Figure 3.

As mentioned, to obtain adsorption energies that can be meaningfully compared across the different clusters, we must avoid changing the immediate environment of the adsorbate when removing atoms. For this reason we do not simply remove the outermost shell. Instead we choose an adsorption site on a particular facet, then remove atoms as necessary on the other sides of the cluster such that the local facet is changed only minimally.

This method preferentially strips off corner atoms and atoms on the most open facet, opening a new facet only when necessary. This avoids very unphysical geometries. We run the calculations multiple times using a pseudo-random number generator with different random seeds,

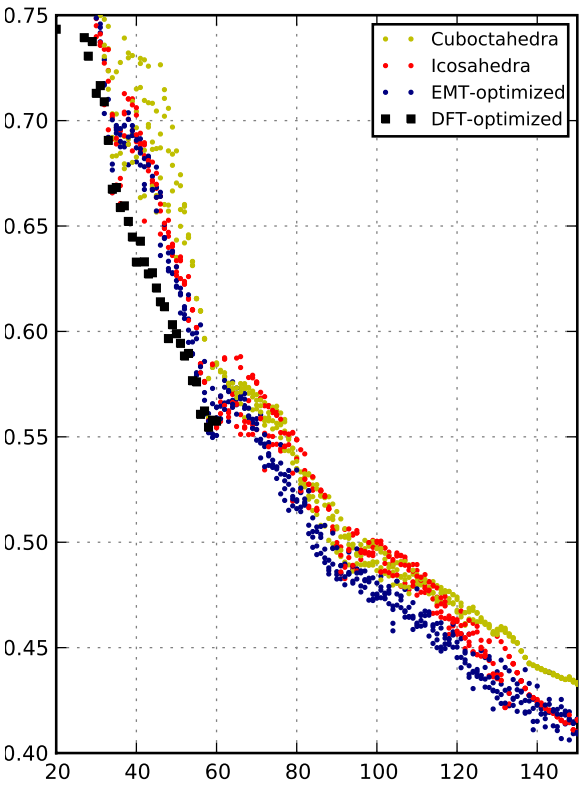

FIG. 4: (Color online) Energy per atom for different Au cluster types as a function of cluster size. The energy reference corresponds to bulk Au.

yielding a small ensemble that shows the dependence of cluster properties on the randomization.

A similar procedure can be applied to the icosahedra. However in the icosahedra, the distance between atoms in successive layers is different from the distance between atoms within the same layer, which means the local geometry around an adsorbate cannot always be preserved as for the cuboctahedra.

IV. INTRINSIC PROPERTIES OF CLUSTERS

In the following we study energies and electronic properties of the different types of clusters. Note that all clusters have been relaxed using DFT such that all structures are local minima corresponding to the same force method, and have directly comparable total energies.

A. Cluster structure and stability

Figure 4 compares the energy per atom for Au clusters of the different types. EMT-optimized and regular clusters have been generated multiple times from different pseudorandom number sequences, yielding four datapoints for each cluster size. The DFT-optimized structures generally have energies lower than or equal to the other methods followed by EMT. Among the regular structures, icosahedra usually have lower energies than cuboctahedra. Even where the regular clusters have closed geometric shells (N=55 and 147), they are less stable than the structures obtained by simulated annealing with EMT.

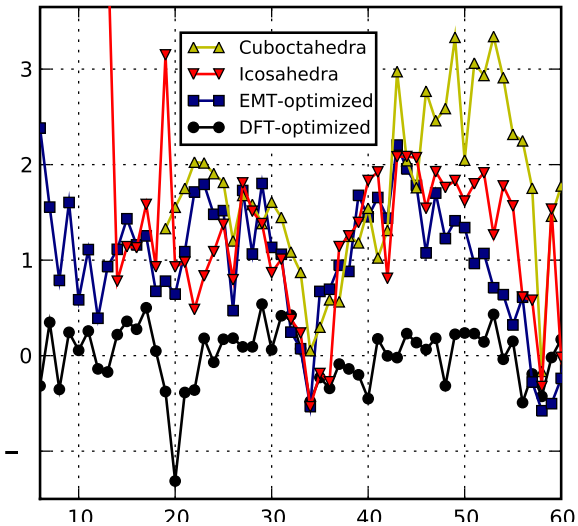

FIG. 5: (Color online) Energy for different Au cluster types as a function of cluster size N. A smooth function of N cf. Eq. 1 has been subtracted from all datapoints for legibility.

Prominent kinks in the energy are visible around N=34, 58 and 92 atoms. These are "magic numbers" corresponding to major electronic shell closings. They are well known in the jellium cluster models of simple metals[32–34], and have also been observed in mass spectra of noble metal clusters[35]. The kinks in energy due to electronic shell structure are robust enough to be visible for all types of clusters considered. Figure 5 provides a closer view of the energies of smaller clusters. To improve legibility, a smooth function of N of the form

$$E_{\mathrm{fit}}(N) = a_0 + a_1 N^{1/3} + a_2 N^{2/3} + a_3 N, \qquad (1)$$

is subtracted from all energies. The coefficients (a_0, a_1, a_2, a_3) are obtained by fitting the energies of the DFT-optimized clusters. For the other kinds of clusters, only the lowest-energy datapoint found among four attempts is shown for each N.

The DFT-optimized clusters up to 13 atoms are planar except for N=10 and 11. The predicted transition between planar and three-dimensional structures depends strongly on the approximation of exchange and correlation, and has been studied more systematically by several authors[28,29].

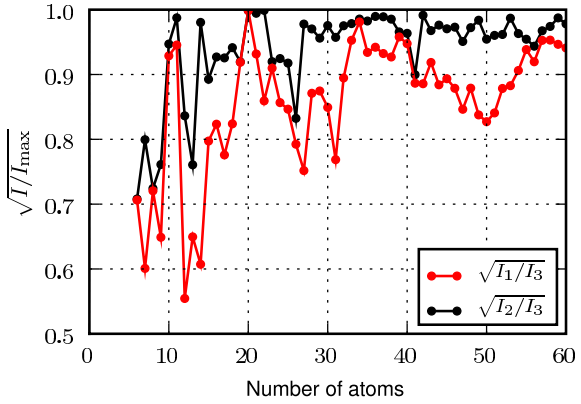

FIG. 6: (Color online) Square roots of ratios I_1/I_3 and I_2/I_3 of the three principal moments of inertia $I_1 \leq I_2 \leq I_3$ as a function of cluster size, showing deformations of the structures.

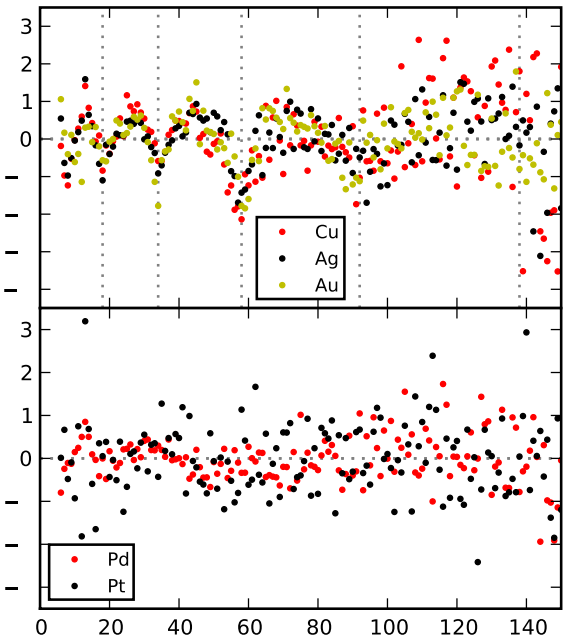

FIG. 7: (Color online) Energy minus fitted trend line for noble metal clusters (top) and d-band metals (bottom). Electronic magic numbers at N=18, 34, 58, 92 and 138 are indicated.

The particularly visible feature at N=20 is the well-known tetrahedron[36]. Aside from this, particularly stable clusters are N=34, 40, 48 and 56/58. The EMT-based and regular structures tend to obtain comparable energies only around the major magic numbers N=34 and 58. In between the magic numbers, the EMT-based structures have higher energies than the DFT-optimized ones by typically 1–2 eV.

The main structural difference between the DFT-optimized clusters and other types is that the DFT-optimized clusters systematically deviate from spherical shapes when doing so is favorable to the electronic structure. A rough measure of how spherical a cluster is can be obtained by considering the moments of inertia. For each cluster the three principal moments of inertia $I_1 \leq I_2 \leq I_3$ are calculated. Figure 6 shows the ratio $\sqrt{I_1/I_3}$ and $\sqrt{I_2/I_3}$, i.e. the square root of the inverse ratio between the largest principal moment and each of the smaller ones, as a function of cluster size. The most symmetric clusters are found around the magic numbers N=20, 34, 40 and 58, while intermediate clusters are deformed considerably. A similar variation has been predicted for Cu clusters[37,38] and in several deformable-background jellium models[39,40]. Clusters just above magic numbers are from jellium models expected to be prolate while clusters below magic numbers are expected to be oblate. Such a trend is not clearly visible from our results. This is most likely due to the roughness of the optimization procedure combined with the presence of a physical atomic lattice, modifying the simple model picture.

Figure 7 compares the stabilities of Cu, Ag, and Au (top). For comparison two other transition metals Pd and Pt are also shown (bottom). For each species, the energy is calculated using simulated annealing with EMT followed by a local geometry optimization with DFT for N=6–200. A smooth function is then subtracted by fitting the energies for each element according to Eq. 1, such that the figure shows the deviation from a smooth trend line.

As for Au, the other noble metal clusters are particularly stable close to the magic numbers 18, 34, 58 and 92, and to a lesser extent at 138. Deviations from the trend line oscillate with a peak-to-peak variation of around 3 eV. Beyond 138, the periodic trend is gradually obscured by fluctuations which are probably caused by imperfections in the optimization procedure.

The three noble metals exhibit roughly identical behaviour except in the region $N < 18$, where Au differs noticeably from Cu and Ag. In this case the Au clusters deform considerably from the geometries found by EMT, tending towards flat structures. Cu and Ag clusters remain round. The tendency of small Au clusters to form planar structures has been well documented and has been attributed to relativistic effects causing a contraction of the s-orbitals compared to the d-orbitals.[41–43] The differences in behavior between noble metals here appear to be caused exclusively by the relativistic behavior of Au, and not e.g. the location of the d-band in relation to the Fermi level, which would set Cu and Ag apart.

For Pd and Pt, no magic numbers are observed. Deviations from the trend line instead appear to depend on how well-formed the clusters are, i.e. the type and regularity of their facets as seen from visual inspection of the cluster structures. Thus the stability of non-noble transition metal clusters is determined mostly by local atomic

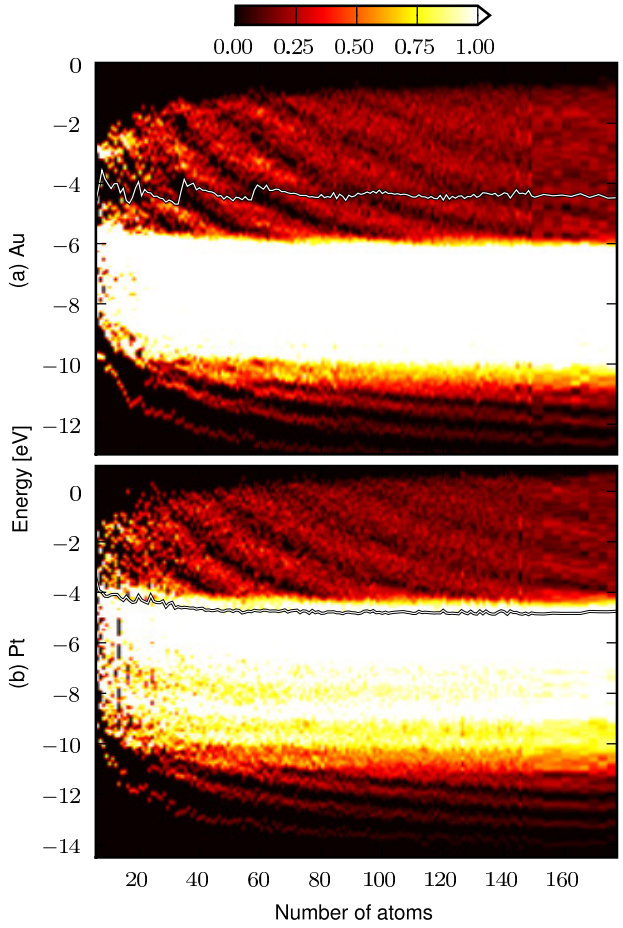

FIG. 8: (Color online) DOS of EMT-optimized Au clusters (top) and Pt clusters (bottom) as a function of cluster size and energy. The line indicates the Fermi level. The color scale is arbitrary. Values larger than 1.0 are truncated to 1.0.

arrangement, corresponding to interactions between the short-ranged d-electrons.

B. Electronic structure

Figure 9 compares the density of states (DOS) per atom of Au (top) and Pt (bottom) clusters optimized with EMT as a 2-variable function of cluster size and energy. For each cluster, the DOS is approximated as a sum of Gaussians of width 0.07 eV centered on each energy eigenvalue.

For both Au and Pt the d-states very quickly form the usual continuous, narrow band which beyond N=20 changes only very little. The s-states split up into multiple electronic shells which are separated by gaps as in the jellium shell model. As N increases the shells gradually broaden to form a continuous band. Oscillations in the DOS originating from the shell structure are still clearly visible even for the largest clusters.

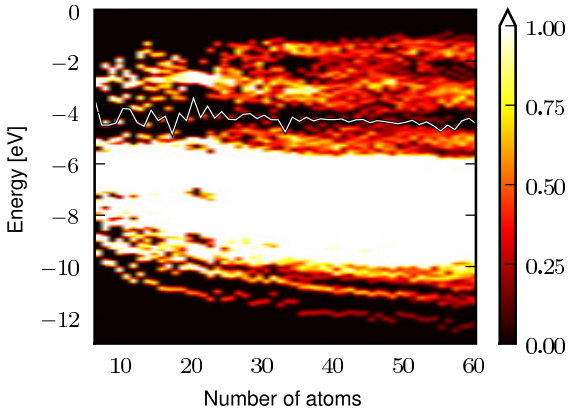

FIG. 9: (Color online) DOS of DFT-optimized clusters. The line indicates the Fermi level. The color scale is arbitrary. DOS values larger than 1.0 are truncated to 1.0.

For Au, where the Fermi level is located well above the d-band, the electronic shells due to the s-electrons are filled one by one as cluster size increases. When one shell is full, the Fermi level jumps to the next higher shell, causing the abrupt shifts in Fermi level and large band gaps.

The Fermi level for Pt is lodged at the top of the d-band where the DOS is extremely high. Therefore no gaps or jumps in the Fermi level are possible, and the cluster will not exhibit any electronic magic numbers even though the s-electrons form shells exactly like Au.

Comparing to the DOS of the DFT-optimized clusters on Fig. 9, the DFT-based optimization consistently creates very large gaps around the Fermi level for all small clusters. For clusters with an odd number of electrons (where the gap is zero because of spin-degeneracy), a single singly-occupied state is located at the middle of a symmetric gap. Similar behavior has been reported for Cu clusters[37]. A significant difference compared to the roughly spherical clusters obtained with EMT is that the shell structure cannot easily be seen as distinct shells that move down in energy as the cluster size increases. Rather there is an accumulation of states some way above as well as below the Fermi level. Only close to the shell closings does the DOS resemble that of the EMT-optimized clusters. A consequence of this is that the abrupt jumps in Fermi level ϵ_F seen for EMT-optimized clusters are less visible for the DFT-optimized ones. However a significant change in ionization potential I and electron affinity A still accompanies a magic number. Figure 10a shows the difference $-(I + A)/2 \approx \epsilon_F$. The value increases sharply at each magic number.

It is easy to understand that gaps at the Fermi level are associated with an increase in stability. The gap is created so that occupied states are pushed down in energy while pushing unoccupied ones up, resulting in a

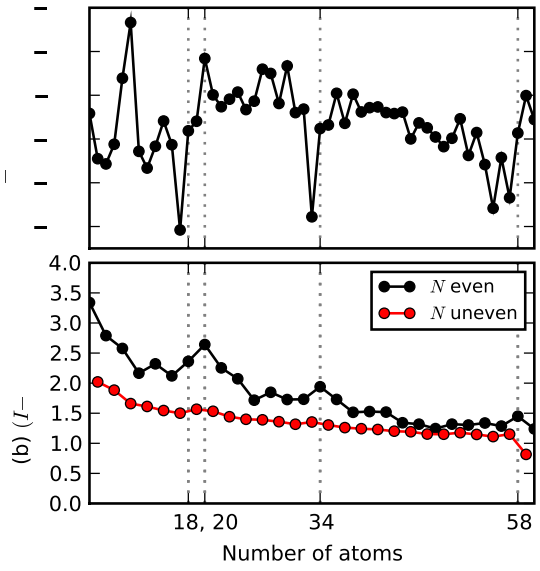

FIG. 10: (Color online) Fermi level (top) and chemical hardness (bottom) calculated from ionization potential I and electron affinity A for DFT-optimized Au clusters as a function of cluster size.

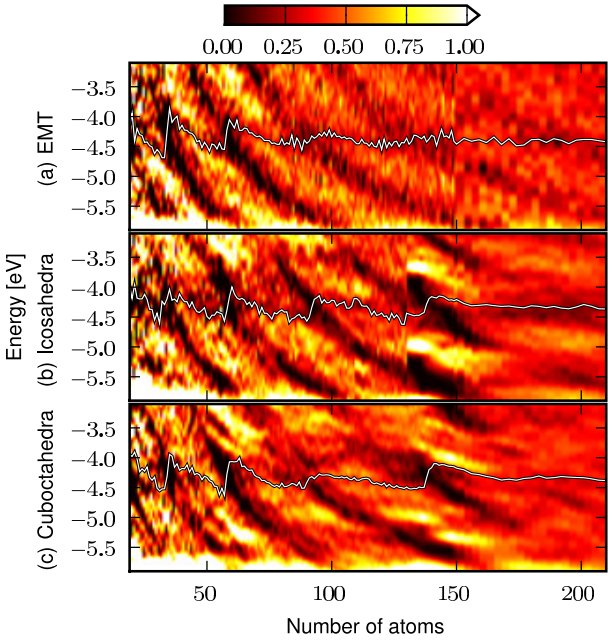

FIG. 11: (Color online) DOS near Fermilevel for different types of clusters. (a) Clusters optimized using the EMT potential. (b) Clusters based on icosahedra. (c) Clusters based on cuboctahedra.

decrease of band structure energy.

For larger clusters that are not close to magic numbers (e.g. $N \approx 45$) the gap becomes small, but a significant depletion of states around the Fermi level persists (a similar depletion of states close to the Fermi level is also seen for the EMT-optimized clusters e.g. for $N \approx 45$ and 70. This is a product of the local structure optimization with DFT after the EMT-annealing). The combined structural and electronic trends of the DFT-optimized clusters thus point to a picture where clusters far from magic numbers will deform significantly, maximizing the gap at the Fermi level. In a sense this deformation creates a new magic number for every size of cluster provided the clusters are small enough. As long as such a gap remains, strong even–odd oscillations of the electronic properties will persist due to the singly-filled state in uneven clusters. Figure 10b shows the band gap calculated as $(I - A)/2$ as a function of cluster size. Even and odd clusters are plotted as separate lines. The structure optimization tends to obtain larger gaps close to the spherical shell closings, and so the even–odd alternations are larger close to these. The even–odd alternations become small compared to the 0.1 eV smearing for clusters larger than ≈ 40 atoms except at the electronic shell closings.

Figure 11 compares the calculated DOS near the Fermi level for EMT-optimized, icosahedral and cuboctahedral structures. The structures yield remarkably similar electronic shells separated by gaps.

Similarities between the electronic shell structures of spherical and faceted structures with hundreds of electrons have previously been found in the context of well potentials.[44]. Our results show that the inclusion of a d-band, as well as the inclusion of an atomic lattice with various irregularies as per the different cluster generation procedures used here have limited effect on the shell structure in this size range.

The highly visible change for icosahedra close to N=130 happens when a sufficiently large number of atoms have been removed from the same side of the cluster, causing a substantial collective movement of the surrounding atoms (this is therefore just an artifact of the cluster generation method).

V. CHEMICAL PROPERTIES OF CLUSTERS

In this section we consider the chemisorption of various atoms on cuboctahedral clusters.

Adsorption energies are calculated as follows. A series of cuboctahedral clusters is generated by the procedure described in Section III C, so as to preserve the local geometry around the desired adsorption site. A structure optimization is then performed on the entire cluster plus adsorbate, yielding a total energy of the combined system. From this energy we subtract the energies of the isolated adsorbate and the isolated cluster. Ideally the energy of the isolated cluster should be calculated by removing the adsorbate, then re-relaxing the structure. However this is likely to cause atoms to move significantly for at least some of the smaller clusters, obscuring

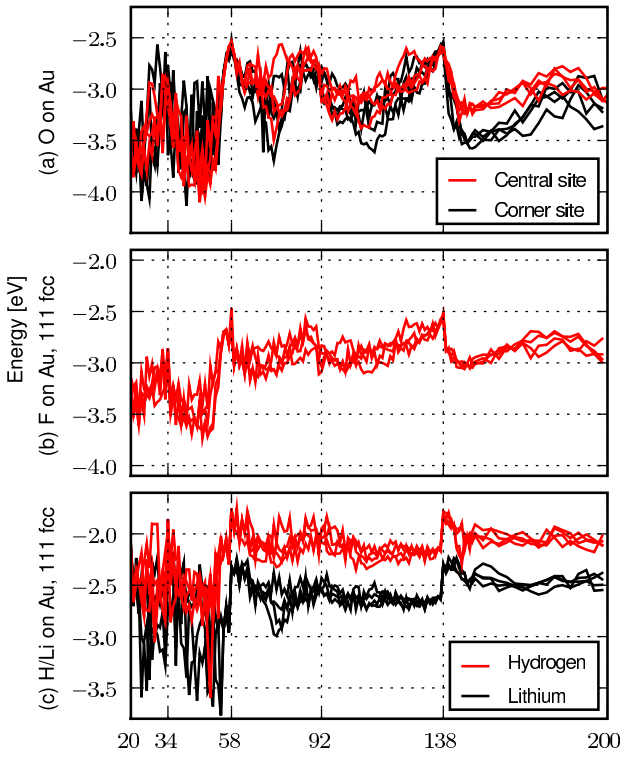

FIG. 12: (Color online) Adsorption energies as a function of Au cluster size. (a) O on the fcc site closest to the center of an (111) facet and the hcp site at the corner of an (111) facet. (b) F on the central (111) fcc site. (c) H and Li

the general trends that we are trying to examine without providing any insight. For this reason we instead neglect to re-relax the clusters after removing the adsorbate. Calculated binding energies therefore tend to be overestimated.

Figure 12a shows the adsorption energy of oxygen on cuboctahedral clusters as a function of cluster size for two different adsorption sites. One is the fcc site as close as possible to the center of an (111) facet, which locally resembles a (111) surface. The other is the hcp site closest to the corner of a (111) facet, where O frequently binds more strongly. For each site there are four series of datapoints corresponding to different random seeds in the cluster generation procedure.

Adsorption energies on both sites are related to the distribution of the electronic shell closings N=34, 58, 92 and 138 where binding energies are particularly low. Near the geometric shell closings 55 and 147, where the clusters are regular and closer to being spherical, this behaviour is most pronounced. The change near 92 is less abrupt, and we attribute this to the less symmetric structures generated far from geometric shell closings (we believe that 92 would stand out more clearly for clusters with more realistic geometry).

Consider the behavior at the magic number 138. The binding gradually weakens until 138, after which it abruptly changes from very weak to very strong. The same effect is seen to a smaller extent at 58 (the preceding weakening of binding energy is in this case not gradual, but coincides with the completion of a local facet as discussed below).

Clusters slightly larger than a magic number will have one or more loosely bound electrons which can easily be donated to O. Clusters can in this sense be characterized as alkali-like, noble or halogen-like depending on their location relative to magic numbers. What the comparison between the two adsorption sites shows is that the main variation of adsorption energy due to the electronic shell structure is not strongly affected by local geometry around the adsorbate. While there are intriguing differences between the binding on the central site and the corner site, such details are probably too specific to make predictions about more realistic geometries.

The alkali-like or halogen-like behavior of clusters near magic numbers is demonstrated on Figures 12b and 12c which show the adsorption energy of F, H and Li on the central (111) fcc site as a function of cluster size.

The variation of F adsorption energy (Figure 12b) around magic numbers is qualitatively similar to that of O. Since F is more electronegative, the increase in binding energy past a magic number is more abrupt and is clearly visible for all the magic numbers 34, 58, 92 and 138. However F can accept only one electron, and so the total magnitude of the increase in energy near N=58 and 138 (0.5 eV) is smaller than in the case of O (up to 1.0 eV). The variation of F binding energy at magic numbers is roughly equal to the increase in Fermi energy of the cluster (0.6 eV).

The electropositive Li shows the opposite trend: a steep decrease in binding energy follows a magic number. Again, the change in binding energy is close to 0.5 eV corresponding to the sharing of one electron. Hydrogen somewhat surprisingly follows the same trend as Li even though the H 1s-state is approximately as low-lying as the O 2p-states. We shall analyze this further in the next section.

Apart from the variation due to magic numbers, binding energies of all species tend to be stronger for the smallest clusters ($N < 50$). The very steep change in binding energy around N=50 which is seen for all adsorbates can be attributed to geometric changes of the local facet. The triangular 6-atom (111) facet of the 55-atom cuboctahedron appears to be generally unreactive, as all four adsorbates bind weakly to it, including O on both the central site and the corner site. Several previous works have noted that a lower overall coordination of nearby Au atoms has been found to increase binding strengths.[27,45,46] The effects due to local geometry are however comparatively small for Au clusters larger than

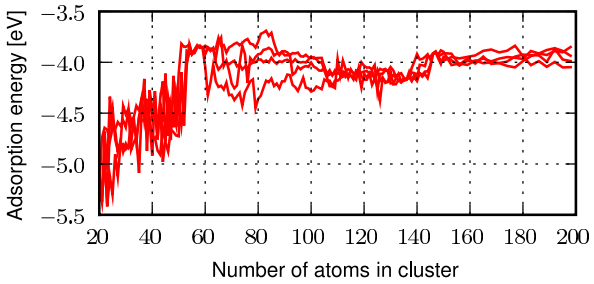

FIG. 13: (Color online) Adsorption energy of O on Pt as a function of cluster size.

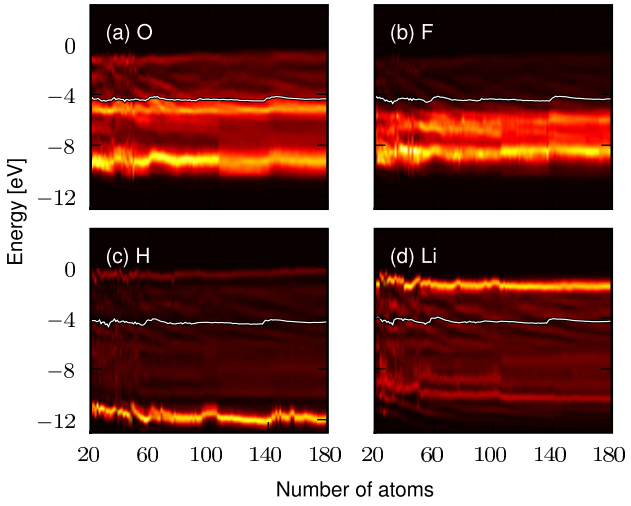

FIG. 14: (Color online) Projected density of states on O, F, H and Li adsorbed on Au clusters as a function of cluster size and energy calculated using the PAW projection operator. The white line indicates the Fermi level.

55 atoms. The global electronic shell structure is responsible for most of the variation in adsorption energy, as evidenced by the consistent oscillating trend.

For comparison, adsorption energies of O on Pt clusters are shown on Figure 13. The clusters have the same initial structures as the Au clusters in Figure 12a. Instead of a smooth oscillating trend, the binding energy can vary significantly when nearby facets are modified, even though the modification takes place several sites away. This causes the adsorption energy to depend much more sensitively on the geometry of the nearby facets. Apart from the strongly geometry-dependent variations, an overall decrease in O binding energy with size is also observed, which resembles that of Au. We note that the changes in adsorption energy on Au clusters occur even when atoms are added on the directly opposite side of the cluster as seen from the adsorption site.

Let us return to the Au clusters. The projected density of states (PDOS) on the adsorbate reveals useful information on how the atomic states hybridize with the clusters. The PDOS as a function of energy ϵ on atom A is calculated from the atomic expansion of the Kohn-Sham eigenstates $|\tilde{\psi}_n\rangle$ and eigenvalues ϵ_n as

$$\rho_A(\epsilon) = \sum_n \langle\tilde{\psi}_n|P_A|\tilde{\psi}_n\rangle\,\delta(\epsilon-\epsilon_n), \tag{2}$$

where

$$P_A = \sum_{a\in A, b\in A} |\Phi_a\rangle\,(S_A^{-1})_{ab}\,\langle\Phi_b| \tag{3}$$

is a projection operator onto the subspace spanned by the basis functions $|\Phi_a\rangle$ on atom A, and $(S_A)_{ab} = \langle\Phi_a|\Phi_b\rangle$ is the overlap matrix within that subspace.

Figure 14 shows the PDOS on the O, F, H and Li atoms adsorbed on Au cuboctahedra of varying size. For O the p-states split into bonding and antibonding states at the top and bottom of the d-band (see also Ref. 47 on hybridization on Au surfaces). Both bonding and antibonding states are occupied, and they remain qualitatively similar for all sizes of clusters although some variation is seen around the magic numbers. The weights of bonding and antibonding states can change drastically when the local geometry is modified, but for clusters larger than 55 atoms these changes are not reflected strongly in the adsorption energy and do not explain the trends (for example the most visible change, around $N = 105$, occurs when the last two second-nearest neighbor atoms are added. This causes the adsorption energy to change by 0.15 eV). The behavior of F resembles that of O except the coupling is weaker. For H a very low-lying state is created at the bottom of the s-band. The surprising formation of such a low-lying state at the bottom of the band has been described previously for H adsorption on Mg surfaces.[48] Finally Li has a high-lying state which is above the Fermi level.

VI. NEWNS-ANDERSON MODEL

The peculiar properties of metal nanoparticles are sometimes attributed to the discrete spectrum causing the nanoparticle to behave like a molecule rather than a bulk material characterized by a continuous spectrum. However the DOS quickly ($N >$ a few dozen atoms) becomes effectively continuous on any reasonable energy scale (~ 0.1 eV). The primary feature distinguishing clusters with a few dozens to a few hundred atoms compared to bulk is not whether the DOS is discrete or continuous, but rather the fact that the approximately continuous DOS remains grouped into shells separated by gaps. The size-dependent variation in this effectively continuous DOS, and in particular the distribution of magic numbers, are the significant factors that make clusters with many hundreds of atoms still differ from bulk Au. Since the DOS of an Au cluster larger than a few dozen atoms can effectively be regarded as continuous, we will in the following apply the Newns-Anderson model[49] to understand chemisorption on Au clusters. The Newns-Anderson model considers a single state $|a\rangle$ on an atom

which hybridizes with a continuum of states $\{|k\rangle\}$ of the metal surface described by a Hamiltonian of the form

$$H = H_0 + V, \tag{4}$$

where H_0 is the Hamiltonian of the uncoupled cluster plus adsorbate, and V describes the coupling. In the basis consisting of metal eigenstates $\{|k\rangle\}$ plus adsorbate eigenstate $|a\rangle$, the uncoupled Hamiltonian H_0 is diagonal, and the Newns-Anderson Hamiltonian can be written in block form as

$$H = \left[\begin{array}{ccc|c} \ddots & & 0 & \vdots \\ & \epsilon_k & & v_{ka}^* \\ 0 & & \ddots & \vdots \\ \hline \cdots & v_{ak} & \cdots & \epsilon_a \end{array}\right]. \tag{5}$$

Here ϵ_a and ϵ_k are the uncoupled energy eigenvalues on the atom and in the metal while $v_{ak} = \langle a|V|k\rangle$ are coupling matrix elements.

Our idea now is to perform a DFT calculation to obtain a Hamiltonian matrix of the composite system consisting of both cluster and adsorbate, then transform it to Newns-Anderson form cf. Eq. (5). In the basis of atomic orbitals used by GPAW, the Kohn-Sham equations are solved as a generalized eigenvalue problem[21]

$$\sum_\nu H_{\mu\nu} c_{\nu n} = \sum_\nu S_{\mu\nu} c_{\nu n} \epsilon_n. \tag{6}$$

The overlap matrix $S_{\mu\nu}$ is present because the basis is non-orthogonal. The Hamiltonian can be regarded as a blocked matrix

$$H^{\mathrm{DFT}} = \begin{bmatrix} H^M & H^{MA} \\ H^{AM} & H^A \end{bmatrix} \tag{7}$$

with one block H^M corresponding to the metal or cluster, one block H^A corresponding to the atom and the off-diagonal blocks H^{MA}, H^{AM} corresponding to the interaction. We diagonalize each of the metallic and atomic submatrices according to

$$\sum_\nu H^M_{k'\nu} c^M_{\nu k} = \sum_\nu S^M_{k'\nu} c^M_{\nu k} \epsilon_k, \tag{8}$$

$$\sum_\nu H^A_{a'\nu} c^A_{\nu a} = \sum_\nu S^A_{a'\nu} c^A_{\nu a} \epsilon_a, \tag{9}$$

to obtain values for the energies ϵ_k and ϵ_a of the uncoupled systems. Clearly these are approximate, as the real energy values could be evaluated selfconsistently on each of the uncoupled systems using a separate DFT calculation. However the Hamiltonian and eigenvalues from one selfconsistent calculation cannot be expected to be "compatible" with those from a different selfconsistent calculation. Indeed it is known from the force theorem[15,50] that the first-order change in energy due to a small perturbation of the Hamiltonian is equal to the change in band structure energy, keeping the potential and density fixed. Different Hamiltonian matrices based on DFT can therefore be expected to contain all information provided that they are constructed from the same potential and density.

Using the matrices c^M and c^A, coupling elements can be obtained through the transformation

$$v_{ak} = \sum_{a'k'} c^{A*}_{a'a} H^{AM}_{a'k'} c^M_{k'k}, \tag{10}$$

$$s_{ak} = \sum_{a'k'} c^{A*}_{a'a} S^{AM}_{a'k'} c^M_{k'k}. \tag{11}$$

Thereby we have all the parameters in the Newns-Anderson Hamiltonian (Eq. (5)), although the adsorbate state has an overlap $s_{ak} = \langle a|k\rangle$ with each of the metallic eigenstates, meaning the basis set is non-orthogonal. Below we will use expressions derived by Grimley[51] for the non-orthogonal case.

If the adsorption induces a change $\delta\rho(\epsilon)$ in the metallic density of states, the adsorption energy can be written as

$$E_{\mathrm{ads}} = 2\int_{-\infty}^{\epsilon_F} \delta\rho(\epsilon)\epsilon \,\mathrm{d}\epsilon - \Delta N \epsilon_F + n_a(\epsilon_F - \epsilon_a), \tag{12}$$

where ϵ_F is the Fermi level. The first term is the contribution to the binding energy from hybridization with the adsorbate (the factor of 2 assumes that each spin hybridizes equally and independently). The integral of the induced density of states

$$\Delta N = 2\int_{-\infty}^{\epsilon_F} \delta\rho(\epsilon)\,\mathrm{d}\epsilon \tag{13}$$

is the change in number of electrons below the Fermi level. If this integral is nonzero, either too much or too little charge will be counted in the integration up to the Fermi level, and the extra or missing electrons must then be deposited onto or taken from the Fermi level. This electron count correction is the second term, $\Delta N \epsilon_F$. Finally if the atom contributes n_a electrons which come from the adsorbate level ϵ_a, this amount of extra charge must in turn be deposited on the Fermi level ϵ_F (last term). In the Newns-Anderson model, the first two terms of Eq. (12) are expressed as the integral over a function $\eta(\epsilon)$ such that

$$E_{\mathrm{ads}} = \frac{2}{\pi}\int_{-\infty}^{\epsilon_F} \eta(\epsilon)\,\mathrm{d}\epsilon + n_a(\epsilon_F - \epsilon_a), \tag{14}$$

where

$$\tan\eta(\epsilon) = \frac{\Delta(\epsilon,\epsilon)}{\epsilon - \epsilon_a - \Lambda(\epsilon)}, \tag{15}$$

$$\Lambda(\epsilon) = \frac{1}{\pi}\int_{-\infty}^{\infty} \frac{\Delta(\epsilon,\epsilon')}{\epsilon - \epsilon'}\,\mathrm{d}\epsilon', \tag{16}$$

$$\Delta(\epsilon,\epsilon') = \pi \sum_k |\epsilon s_{ak} - v_{ak}|^2 \delta(\epsilon' - \epsilon_k). \tag{17}$$

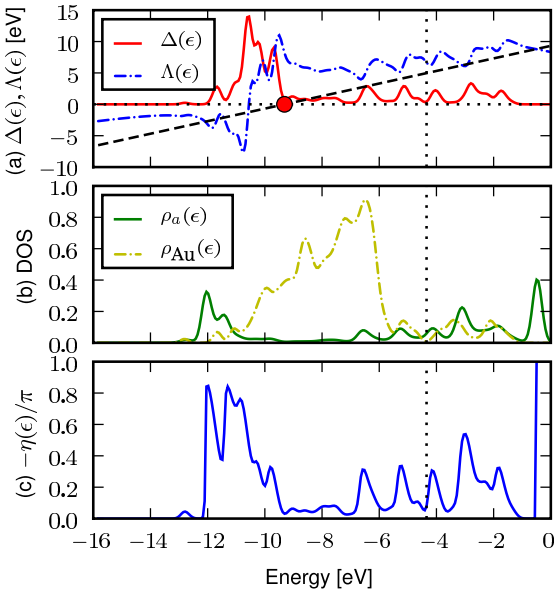

FIG. 15: (Color online) (a) $\Delta(\epsilon)$, $\Lambda(\epsilon)$ and $\epsilon - \epsilon_a$ for H on 58-atom Au cluster. The dotted line indicates the Fermi level. (b) Projected DOS on atom and total DOS of isolated cluster. (c) Cumulative induced DOS.

The one-variable function $\Delta(\epsilon) \equiv \Delta(\epsilon, \epsilon)$ is referred to as the *chemisorption function* and plays the role of a continuous coupling matrix element. $\eta(\epsilon)$ is the phase shift of the complex self-energy $\Lambda(\epsilon) - i\Delta(\epsilon)$ and is related to the the induced density of states by

$$-\frac{1}{\pi}\frac{\mathrm{d}\eta(\epsilon)}{\mathrm{d}\epsilon} = \delta\rho(\epsilon). \tag{18}$$

The PDOS on the adsorbate can be written as

$$\rho_a(\epsilon) = \frac{1}{\pi}\frac{\Delta(\epsilon)}{(\epsilon - \epsilon_a - \Lambda(\epsilon))^2 + \Delta^2(\epsilon)}. \tag{19}$$

Because of the approximations used in this method, calculated binding energies are by themselves not useful (or accurate) compared to the DFT results. The strength of this method lies in the conceptual simplification that the binding energy can be understood from continuous functions such as $\Delta(\epsilon)$ and $\eta(\epsilon)$. This allows the origin of the coupling and binding energy to be attributed to particular states in the cluster. Next we will apply this to H, O, Li and F on a 58-atom Au cluster to understand the effect of magic numbers on chemisorption.

A. Adsorption of H

We perform a DFT calculation on a 58-atom Au cluster with H adsorbed to obtain the Hamiltonian and overlap matrix. In this calculation, only the 1s basis function is included on H, but otherwise the parameters are identical to those used in earlier calculations. For the 1s basis function we calculate $\Delta(\epsilon)$ and $\Lambda(\epsilon)$ which is shown on Figure 15a together with the line $\epsilon - \epsilon_a$. When $\epsilon - \epsilon_a = \Lambda(\epsilon)$ and $\Delta(\epsilon)$ is small, there will be resonances in $\rho_a(\epsilon)$ (as per Eq. (19)) corresponding to states on the atom. The adsorbate level ϵ_a (circle) and Fermi level (dotted line) are indicated. The resulting PDOS is shown on Figure 15b together with the total DOS of the Au cluster. This reveals that it is the strong coupling to low-lying metallic states ($\epsilon \approx -11\,\mathrm{eV}$) which gives rise to a bonding, localized state at the bottom of the Au s-band, at $-12\,\mathrm{eV}$, and an antibonding state consisting of several peaks mostly above the Fermi level.

On a side note, the very high PDOS at the antibonding state may seem surprising. Given that the adsorbate level $\epsilon_a \approx -9$ is much closer to the bonding state, the bonding state would be expected to be similar to $|a\rangle$, and thus have a high PDOS on the atom, while the antibonding state should be more similar to the metallic states and therefore have a low PDOS on the atom. However the inclusion of overlap s_{ak} in the model causes part of the states on the neighboring metal atoms to be counted in the adsorbate PDOS, contributing to the prominence of the antibonding peak. While the overlap affects the calculated PDOS, the overlap is correctly taken into account in binding energies and other parts of the formalism.

In the creation of bonding and antibonding states the original adsorbate state has been eliminated, and a change $\delta\rho(\epsilon)$ in DOS has been induced in the cluster. The cumulative induced DOS $-\eta(\epsilon)/\pi$ is shown on Figure 15c. While the newly created bonding state at $-12\,\mathrm{eV}$ can accept a certain amount of charge, a similar amount of charge has been removed from the remainder of the cluster DOS (mostly around $-10\,\mathrm{eV}$) such that the total integral of the induced DOS up to the Fermi level is zero. The extra electron from the H atom is therefore deposited on the Fermi level. A higher-lying Fermi level implies a weaker adsorption energy, since the electron is deposited at a higher energy. This is why clusters just past a magic number, characterized by a higher Fermi level but an otherwise similar spectrum, adsorb H more weakly than clusters just before a magic number. We can also see how the induced DOS integrates to zero only because the Fermi level is located at a gap between electronic shells: Within each electronic subshell there are fluctuations in the induced DOS which correspond to slight movements of the electronic shells but without the introduction of any extra charge. These cause $\eta(\epsilon)$ to locally deviate from 0. The adsorption energy therefore may not depend simply on the Fermi energy in general, but must do so at the magic numbers. These results are consistent with previous findings for very small clusters, that H atoms effectively contribute their electron to the LUMO, behaving like an extra Au atom.[52,53]

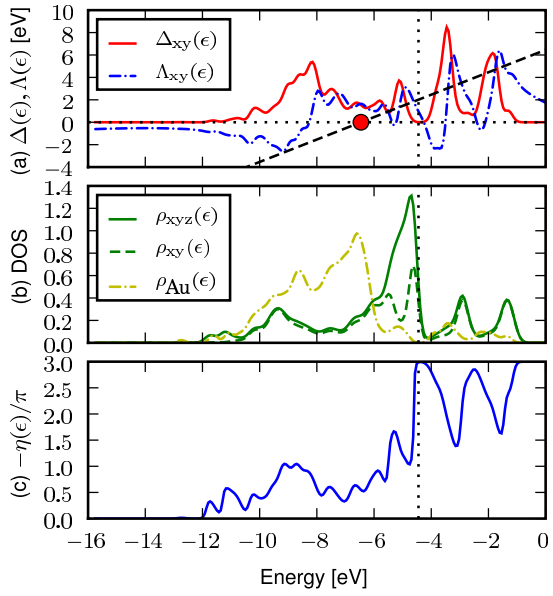

FIG. 16: (Color online) (a) $\Delta(\epsilon)$, $\Lambda(\epsilon)$ and $\epsilon - \epsilon_a$ for O p_x or p_y on 58-atom Au cluster. ϵ_a is indicated on the energy axis. (b) Projected DOS on all O 2p states (solid line), on p_x and p_y only (dashed line), and total DOS of isolated cluster. (c) Cumulative induced DOS.

B. Adsorption of O

Since the Newns-Anderson model only takes a single state into account while O has three p-states, we will assume that each of the states hybridizes independently and contributes to the adsorption energy as per Eq. (14). Thus we consider one Hamiltonian of the form (5) for each p-state with varying v_{ak} and s_{ak}.

The $2p_x$ and $2p_y$-states are close to degenerate and have almost identical chemisorption functions. Figure 16a shows the average $\Delta(\epsilon)$ and $\Lambda(\epsilon)$ from the O $2p_x$ and $2p_y$-states. In this case the weaker splitting leads to greater smearing of the states close to the d-band and between the electronic shells. The higher-lying peaks in $\Delta(\epsilon)$ correspond to coupling with of the electronic shells. Figure 16b shows the total PDOS $\rho_{xyz}(\epsilon)$ due to all three p-states (full lines) along with the contribution $\rho_{xy}(\epsilon)$ from p_x and p_y (dashed). The most profound feature is the state between the top of the d-band and the Fermi level, which therefore is filled. The induced DOS integrates to 3.0 at the Fermi level (Figure 16c), allowing space for six electrons counting spin-degeneracy. Since only four electrons are contributed, a total of two electrons are taken from the Fermi level into available lower-lying states. An upward shift in Fermi level therefore implies that more energy is gained from this transfer, causing a change in binding energy opposite that for H adsorption as seen from the DFT calculations.

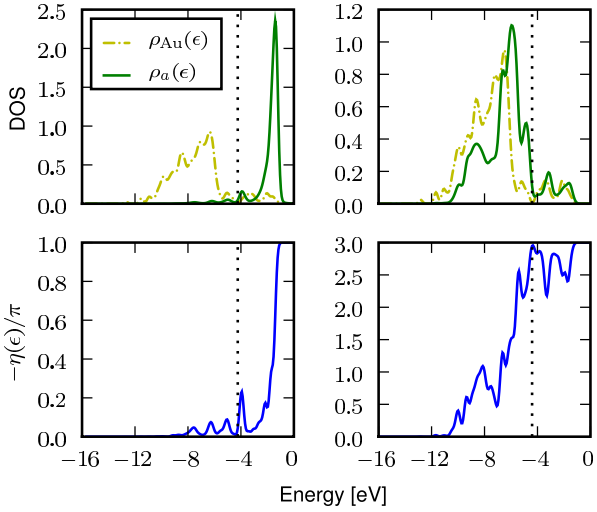

FIG. 17: (Color online) Projected density of states (top) on adsorbate and cumulative induced density of states (bottom) for Li (left) and F (right).

C. Adsorption of Li and F

Li is the simplest of the four cases. Here the bonding is weak enough that no significant splitting occurs. The adsorbate state instead broadens into a resonance far above the Fermi level, see the left part of Figure 17, without inducing any states below the Fermi level. The electron contributed by the Li atom therefore moves down to the Fermi level causing the same dependence of adsorption energy on Fermi level as for H.

F couples more weakly than O, and the bonding states are therefore split up less than for O (right part of Figure 17). Since both bonding and antibonding states are occupied, F behaves like O except only one electron can be transferred from the Fermi level, meaning that the change in adsorption energy at magic-number clusters is generally smaller than for O.

D. Comparison to Pt clusters

Finally we shall briefly consider the binding of O to the 58-atom Pt cluster. Again the p_x and p_y states are close to degenerate, and the average of their chemisorption functions is shown on Figure 18a. Two primary features appear in the chemisorption function: a strong coupling within the d-band around $\epsilon = -8\,\mathrm{eV}$, and a number of higher-lying peaks corresponding to electronic shells like those of Au clusters. Due to the broader and higher-lying d-band, the adsorbate state splits into peaks over a wider energy range as seen on Figure 18b. The increase in binding on Pt compared to Au manifests itself as an increase in area below the curve in Figure 16c cf. Eq. (14). The overall upward shift of the coupling leads to an upward shift of the induced density of states, and so only approx-

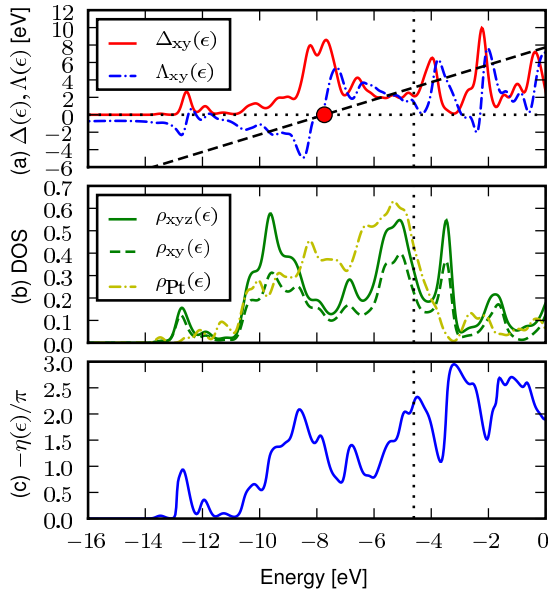

FIG. 18: (Color online) Chemisorption of O on 58-atom Pt cluster in comparison with Au from Figure 16.

imately 2.2 out of the 3 states contributed by O are in this case located below the Fermi level. The partial occupation of O 2p-states has been studied and confirmed experimentally.[54] Recall that for Au, essentially all of the adsorbate-induced states were located below the Fermi level (Figure 16c).

The s-electron shell structure is mostly visible in the chemisorption function well above the Fermi level. Further, since the location of the Fermi level within the d-band prevents abrupt changes in the Fermi level with cluster size, the s-electron shell structure – as expected – cannot exert a strong influence on the chemical binding on Pt clusters.

VII. CONCLUSIONS

The structure of very small Au clusters is intricately dependent on the s electron hybridization, with clusters at magic numbers having very large band gaps. Clusters with different numbers of atoms deform considerably to minimize the band structure energy by creating gaps at the Fermi level. For odd-numbered clusters this results in a singly-filled state in the middle of the gap, causing strong even–odd oscillations of HOMO and LUMO.

Clusters based on regular geometries or a simple EMT potential show a more clear electronic shell structure and have large band gaps only at the major shell closings. These structures are less realistic, but are computationally feasible to optimize for larger cluster sizes.

Adsorption energies of atoms on regular Au clusters oscillate with the electronic magic numbers. While local geometry is known to be important, the variation in binding energy of O due to magic numbers alone may be up to 1 eV. Clusters just before or after magic numbers are found to exhibit roughly halogen-like and alkali-like behavior while magic-number clusters are, as expected, universally unreactive.

A more detailed analysis attributes the increase or decrease in binding energy of specific adsorbates at magic numbers to properties of the adsorbate-induced density of states. Adsorption of O or F induces states below the Fermi level, allowing the transfer of electrons from the Fermi level into the lower-lying states. In contrast H and Li, despite having very different adsorbate levels and electronegativity, only induce states above the Fermi level, and the electron contributed by these atoms is therefore transferred to the Fermi level.

Center for Atomic-scale Materials Design is funded by the Lundbeck Foundation. The Catalysis for Sustainable Energy initiative is funded by the Danish Ministry of Science, Technology and Innovation. We acknowledge support from the Danish Center for Scientific Computing.

[1] M. Valden, X. Lai, and D. Goodman, Science (New York, NY) **281**, 1647 (1998).
[2] H. A. Atwater and A. Polman, Nature Materials **9**, 205 (2010).
[3] F. Baletto and R. Ferrando, Rev. Mod. Phys. **77**, 371 (2005).
[4] D. G. Pettifor, Journal of Physics F: Metal Physics **8**, 219 (1978).
[5] H. Häkkinen, B. Yoon, U. Landman, X. Li, H. Zhai, and L. Wang, The Journal of Physical Chemistry A **107**, 6168 (2003).
[6] E. M. Fernández, J. M. Soler, I. L. Garzón, and L. C. Balbás, Phys. Rev. B **70**, 165403 (2004), URL `http://link.aps.org/doi/10.1103/PhysRevB.70.165403`.
[7] X. Xing, B. Yoon, U. Landman, and J. H. Parks, Phys. Rev. B **74**, 165423 (2006).
[8] H.-Y. Zhao, H. Ning, J. Wang, X.-J. Su, X.-G. Guo, and Y. Liu, Physics Letters A **374**, 1033 (2010), ISSN 0375-9601.
[9] W. D. Knight, K. Clemenger, W. A. de Heer, W. A. Saun-

ders, M. Y. Chou, and M. L. Cohen, Phys. Rev. Lett. **52**, 2141 (1984).
[10] G. Wrigge, M. A. Hoffmann, and B. v. Issendorff, Phys. Rev. A **65**, 063201 (2002), URL http://link.aps.org/doi/10.1103/PhysRevA.65.063201.
[11] T. P. Martin, Physics Reports **273**, 199 (1996).
[12] A. S. Barnard, X. M. Lin, and L. A. Curtiss, The Journal of Physical Chemistry B **109**, 24465 (2005).
[13] A. S. Barnard, N. P. Young, A. I. Kirkland, M. A. van Huis, and H. Xu, ACS Nano **3**, 1431 (2009).
[14] J. P. K. Doye and F. Calvo, Physical Review Letters **86**, 3570 (2001).
[15] K. W. Jacobsen, J. K. Norskov, and M. J. Puska, Phys. Rev. B **35**, 7423 (1987).
[16] K. W. Jacobsen, P. Stoltze, and J. K. Nørskov, Surface Science **366**, 394 (1996), ISSN 0039-6028.
[17] J. J. Mortensen, L. B. Hansen, and K. W. Jacobsen, Physical Review B **71**, 035109 (2005).
[18] J. Enkovaara, C. Rostgaard, J. J. Mortensen, J. Chen, M. Dułak, L. Ferrighi, J. Gavnholt, C. Glinsvad, V. Haikola, H. A. Hansen, et al., Journal of Physics: Condensed Matter **22**, 253202 (2010).
[19] B. Hammer, L. B. Hansen, and J. K. Nørskov, Phys. Rev. B **59**, 7413 (1999).
[20] P. E. Blöchl, Phys. Rev. B **50**, 17953 (1994).
[21] A. H. Larsen, M. Vanin, J. J. Mortensen, K. S. Thygesen, and K. W. Jacobsen, Physical Review B **80**, 195112 (2009).
[22] P. Pulay, Chemical Physics Letters **73**, 393 (1980), ISSN 0009-2614.
[23] S. R. Bahn and K. W. Jacobsen, Comput. Sci. Eng. **4**, 56 (2002), ISSN 1521-9615.
[24] L. Xiao, B. Tollberg, X. Hu, and L. Wang, The Journal of Chemical Physics **124**, 114309 (2006), ISSN 00219606.
[25] B. Yoon, P. Koskinen, B. Huber, O. Kostko, B. von Issendorff, H. Häkkinen, M. Moseler, and U. Landman, ChemPhysChem **8**, 157 (2007), ISSN 1439-7641.
[26] A. W. Snow and H. Wohltjen, Chemistry of Materials **10**, 947 (1998).
[27] J. Kleis, J. Greeley, N. Romero, V. Morozov, H. Falsig, A. Larsen, J. Lu, J. Mortensen, M. Dułak, K. Thygesen, et al., Catalysis Letters pp. 1–5 (2011), ISSN 1011-372X, 10.1007/s10562-011-0632-0.
[28] L. Ferrighi, B. Hammer, and G. K. H. Madsen, Journal of the American Chemical Society **131**, 10605 (2009).
[29] E. M. Fernández, J. M. Soler, and L. C. Balbás, Phys. Rev. B **73**, 235433 (2006), URL http://link.aps.org/doi/10.1103/PhysRevB.73.235433.
[30] L. Xiao and L. Wang, Chemical Physics Letters **392**, 452 (2004).
[31] ASAP, URL https://wiki.fysik.dtu.dk/asap.
[32] W. A. de Heer, W. Knight, M. Chou, M. L. Cohen, H. Ehrenreich, and D. Turnbull, in *Advances in Research and Applications* (Academic Press, 1987), vol. Volume 40, pp. 93–181, ISBN 0081-1947.
[33] M. Brack, Reviews of Modern Physics **65**, 677 (1993).
[34] O. Genzken and M. Brack, Physical Review Letters **67**, 3286 (1991).
[35] I. Katakuse, T. Ichihara, Y. Fujita, T. Matsuo, T. Sakurai, and H. Matsuda, International Journal of Mass Spectrometry and Ion Processes **67**, 229 (1985), ISSN 0168-1176.
[36] J. Li, X. Li, H. Zhai, and L. Wang, Science **299**, 864 (2003).
[37] O. B. Christensen, K. W. Jacobsen, J. K. Nørskov, and M. Manninen, Phys. Rev. Lett. **66**, 2219 (1991).
[38] O. B. Christensen and K. W. Jacobsen, Journal of Physics: Condensed Matter **5**, 5591 (1993), ISSN 0953-8984.
[39] Z. Penzar and W. Ekardt, Zeitschrift für Physik D Atoms, Molecules and Clusters **17**, 69 (1990), ISSN 0178-7683.
[40] M. Koskinen, P. O. Lipas, and M. Manninen, Zeitschrift für Physik D Atoms, Molecules and Clusters **35**, 285 (1995), ISSN 0178-7683.
[41] M. Moseler, H. Häkkinen, and B. Issendorff, in *High Performance Computing in Science and Engineering' 04*, edited by E. Krause, W. Jäger, and M. Resch (Springer Berlin Heidelberg, Berlin, Heidelberg, 2005), pp. 95–105, ISBN 978-3-540-22943-8.
[42] P. Pyykko and J. P. Desclaux, Accounts of Chemical Research **12**, 276 (1979).
[43] H. Häkkinen, M. Moseler, and U. Landman, Phys. Rev. Lett. **89**, 033401 (2002).
[44] J. Mansikka-aho, E. Hammarén, and M. Manninen, Phys. Rev. B **46**, 12649 (1992).
[45] N. Lopez and J. K. Nørskov, Journal of the American Chemical Society **124**, 11262 (2002).
[46] H. Falsig, B. Hvolbæk, I. S. Kristensen, T. Jiang, T. Bligaard, C. H. Christensen, and J. K. Nørskov, Angewandte Chemie **120**, 4913 (2008), ISSN 1521-3757.
[47] B. Hammer and J. K. Nørskov, Nature **376**, 238 (1995).
[48] J. K. Nørskov, A. Houmøller, P. K. Johansson, and B. I. Lundqvist, Physical Review Letters **46**, 257 (1981).
[49] D. M. Newns, Phys. Rev. **178**, 1123 (1969).
[50] A. Mackintosh and O. Andersen, ed. M. Springford, Cambridge Univ. Press, London p. 149 (1980).
[51] T. B. Grimley, Journal of Physics C: Solid State Physics **3**, 1934 (1970), ISSN 0022-3719.
[52] S. Buckart, G. Ganteför, Y. D. Kim, and P. Jena, Journal of the American Chemical Society **125**, 14205 (2003).
[53] N. S. Phala, G. Klatt, and E. van Steen, Chemical Physics Letters **395**, 33 (2004), ISSN 0009-2614.
[54] P. Strasser, S. Koh, T. Anniyev, J. Greeley, K. More, C. Yu, Z. Liu, S. Kaya, D. Nordlund, H. Ogasawara, et al., Nat Chem **2**, 454 (2010), ISSN 1755-4330.

Paper V: In situ XAS of Pt monolayer model fuel cell catalysts: balance of nanostructure and bimetallic interactions

In situ XAS of Pt monolayer model fuel cell catalysts: balance of nanostructure and bimetallic interactions

Daniel Friebel,[1,2,*] Daniel J. Miller,[1,2] Toyli Anniyev,[1,2] Hirohito Ogasawara,[1,2] Venkat Viswanathan,[3] Ask H. Larsen[4], Christopher P. O'Grady, Jens Nørskov,[3] Anders Nilsson[1,2,3,*]

[1]Stanford Institute for Materials and Energy Science, SLAC National Accelerator Laboratory, Menlo Park, CA 94025

[2]Stanford Synchrotron Radiation Lightsource, SLAC National Accelerator Laboratory, Menlo Park, CA 94025

[3]SUNCAT Center for Interface Science and Catalysis, SLAC National Accelerator Laboratory, Menlo Park, CA 94025

[4]Center for Atomic-scale Materials Design, Department of Physics, Building 311, Technical University of Denmark, DK-2800 Lyngby, Denmark

KEYWORDS (Word Style "BG_Keywords"). If you are submitting your paper to a journal that requires keywords, provide significant keywords to aid the reader in literature retrieval.

Supporting Information Placeholder

ABSTRACT: We have studied the effect of nanostructuring in Pt monolayer model electrocatalysts on a Rh(111) single-crystal substrate on the adsorption strength of chemisorbed species. *In situ* high energy resolution fluorescence detection x-ray absorption spectroscopy (HERFD XAS) at the Pt L_3 edge reveals characteristic changes of the shape and intensity of the "white-line" due to chemisorption of atomic hydrogen (H_{ad}) at low potentials and oxygen-containing species (O/OH_{ad}) at high potentials. On a uniform, two-dimensional Pt monolayer grown by Pt evaporation in ultrahigh vacuum (UHV), we observe a significant destabilization of both H_{ad} and O/OH_{ad} due to strain and ligand effects induced by the underlying Rh(111) substrate. When Pt is deposited via a wet-chemical route, by contrast, three-dimensional Pt islands are formed. In this case, strain and Rh ligand effects are balanced with higher local thickness of the Pt islands as well as higher defect density, shifting H and OH adsorption energies back towards pure Pt.

1. INTRODUCTION

Bimetallic catalyst materials are of great interest due to their wide variability of electronic structure that allows for "tuning" of the catalyst affinity to reaction intermediates. Such a tuning is needed in particular for the oxygen reduction reaction (ORR) in fuel cells, where a significant reduction of Pt loading is essential for economic viablility. While volcano-type relations between adsorption strength and electrocatalytic activity have been successfully predicted using density functional theory (DFT),[1,2] it remains challenging to confirm the underlying assumptions regarding structure and bonding at the catalyst surface with *in situ* experiments in a condensed electrolyte. Recently, we demonstrated that high energy resolution fluorescence detection x-ray absorption spectroscopy (HERFD XAS) at the Pt L_3 edge, applied to a well-defined Pt monolayer on a Rh(111) substrate, is a surface sensitive probe of Pt–O surface interactions that can unambiguously differentiate between the chemisorption of oxygen-containing species and surface oxide formation.[3] Moreover, the nature of Pt oxides and their formation mechanism at high potentials was found to be strongly influenced by the underlying metal support.[4]

By systematically studying Pt monolayers on a variety of M(111) substrates with HERFD XAS, we can directly probe the oxygen affinity of Pt "skin" layers under different strain and ligand effects; this is an important experimental complement on adsorption enthalpy calculations used in Nørskov's volcano plot. In comparison of the latter with experimentally determined ORR activities for a number of bimetallic systems including Pt monolayer catalysts,[2] we note two important characteristics: first, with the exception of the more recent development of Pt_3Sc and Pt_3Y catalysts, the materials near the top of the volcano are alloys of Pt with late 3*d* transition metals, which can be unstable under fuel cell operating conditions due to dissolution of the non-noble component. Second, it is remarkable that some model catalysts, i.e. Pt/Au(111), Pt/Ir(111), Pt/Rh(111) and Pt/Ru(0001),[5] appear much more active than predicted. This raises the question whether an additional catalyst design criterion besides ligand and strain effects affects the oxygen adsorption energy, enhancing the ORR activity for these systems. Here, we show that such an enhancement can be due to three-dimensional nanostructuring of the Pt monolayer, which has not been accounted for in the previous studies. Using the example of Pt/Rh(111), we compare electrochemical and *in situ* HERFD XAS measurements in 0.01 M $HClO_4$ electrolyte of two samples obtained with different Pt deposition techniques resulting in a uniform two-dimensional (2D) Pt layer and three-dimensional (3D) Pt islands, respectively.

2. METHODS

2.1. Sample preparation. An 8 mm diameter commercial Rh(111) single-crystal (Surface Preparation Laboratory, Zaandam, The Netherlands) was cleaned under ultrahigh vacuum by repeated sputtering and annealing cycles. A home-built evaporator with resistive heating was used to deposit the Pt film while the sample temperature was held at ~600 K. The Pt coverage was monitored using the changes in CO thermal desorption spectra from the Pt/Rh(111) surface. It has been previously shown[6] that, during the deposition, Pt atoms are incorporated into the topmost Rh layer to form a surface alloy with increasing Pt content and, eventually, a two-dimensional Pt overlayer.

For the redox displacement of a Cu monolayer, the Rh(111) single crystal was prepared by flame annealing and subsequent cooling in a H_2/N_2 (5:95) atmosphere. The crystal was then transferred into a nitrogen-filled glovebag where it was mounted in a hanging meniscus flow cell which allows for a rapid exchange of the electrolyte under potential control. A Cu deposition voltammogram in 1 mM $CuSO_4$ + 0.05 M H_2SO_4 solution was then recorded at a cathodic potential sweep rate of 10 mV/s starting from +400 mV (Ag/AgCl). Immediately after the completion of the Cu upd peak, the cell was flushed with the Cu-free supporting electrolyte (0.05 M H_2SO_4. Meanwhile, the cathodic potential sweep was continued to a final value of -400 mV in order to prevent any dissolution of the Cu monolayer. In analogy to previous experiments[7,8] which used the stabilization of a Cu upd layer on Au(111) in Cu-free electrolyte, we are able to verify with cyclic voltammetry that the Cu layer remains stable and has the desired coverage of 1 ML. After the deposition of 1 ML Cu and its stabilization in Cu-free supporting electrolyte, the Rh(111) sample was quickly transferred to a glass beaker where the polished surface was exposed to the Pt deposition solution (1 mM K_2PtCl_4 + 0.05 M H_2SO_4) for ca. 30 s.

2.2. In situ x-ray electrochemical cell. Subsequent to the Pt deposition, the sample was mounted into an *in situ* x-ray electrochemical cell. Two different setups have been used in this study. A "thin layer" cell similar to setups which have been used earlier for electrochemical surface x-ray diffraction studies[9] was used with 6 μm mylar foil (Goodfellow) as x-ray window. The cell can be deflated to minimize the x-ray path length through the electrolyte solution. A disadvantage of this setup is the limitation of mass transport due to the thin electrolyte layer. We circumvented this problem by limiting the potential window to a range where the electrochemical currents under potentiostatic conditions are low. Furthermore, for every change of the potential the cell was inflated in order to provide a thick electrolyte layer above the sample. At each new potential value, the cell was kept inflated for at least 15 min in order to allow for potential-induced phase transitions to complete under thick-layer conditions before returning to the thin-layer mode for the next XAS measurement. Faster potential changes and higher electrochemical currents can be achieved in our "droplet" hanging meniscus cell,[3] where a thick electrolyte layer is provided throughout the x-ray measurement. Both cells provide a three-electrode configuration with Pt wire as the counter electrode and a leak-free Ag/AgCl reference electrode. All electrode potentials were converted to the scale of the reversible hydrogen electrode (RHE).

All electrolytes were made from high-purity chemicals (70% $HClO_4$, Trace Select Ultra, Sigma-Aldrich and 95% H_2SO_4, Trace Select, Sigma-Aldrich; 99.999% $CuSO_4 \cdot 5\ H_2O$, Sigma-Aldrich) and ultrapure water from a Millipore Gradient system.

2.3. X-ray absorption spectroscopy. All *in situ* x-ray absorption spectra were measured at the Stanford Synchrotron Radiation Lightsource (SSRL). At Beam Line 11-2, EXAFS measurements were carried out with conventional fluorescence detection using a large 30-element Ge solid state detector. HERFD-XANES measurements were performed at SSRL Beam Line 6-2 using a Si(111) monochromator in combination with a Rowland circle analyzer spectrometer[10] consisting of three spherically bent Ge perfect crystals (R=1 m). The crystals were aligned in a backscattering geometry using the (660) Bragg reflection at 80.0 °to select the Pt $L\alpha_1$ fluorescence line (9442 eV). The combined resolution of the monochromator and analyzer as determined by measuring the elastic scattering was 1.6 eV. Assuming an intrinsic monochromator resolution of ~1.3 eV the analyzer resolution is estimated to be ~1 eV.

For all XAS measurements, the incidence angle of the x-ray beam to the Pt/Rh(111) surface was adjusted to the critical angle for total external reflection, thereby enhancing the fluorescence intensity up to fourfold.[11] The orientation of the electric field vector of the incident beam was perpendicular to the surface normal.

For the EXAFS data analysis, SIXPack[12] was used for background subtraction, spline fitting and least-square fitting of the Fourier-transformed EXAFS signal. Backscattering phase and amplitude functions required for fitting of spectra were obtained from FEFF 6.[13]

2.4. Computational methods. All HERFD XAS calculations were carried out using the FEFF 8.4 program, which employs a full multiple-scattering formalism.[14] By using the "NOHOLE" card, potentials and phase shifts were calculated assuming complete screening of the core-hole, resulting in better agreement with experimental white-line intensities. This is fully consistent with previously reported FEFF results on transition metal L_2 and L_3 edges.[15–19] The line-sharpening effect observed in HERFD was modeled by reducing the theoretical lifetime broadening by 1.75 eV using the "EXCHANGE" card. This value was determined by comparing the computed XANES spectrum of a clean Pt/Rh(111) surface with an experimental spectrum at a potential corresponding to the double-layer region, namely E=+0.4 V. More detailed information about the model structures and input parameters for the FEFF8 calculations are provided in the Supporting Information.

3. RESULTS

It is well-known that the fabrication of well-defined metal monolayers can be challenging, especially in the case of Pt which in general, due to its high surface energy,[20] is likely to tend towards a Volmer-Weber growth mode rather than the desired fully two-dimensional growth of one monolayer. However, on substrates with higher surface energies than Pt, such as Rh, Ru or Ir,[20] one would expect a growth mode of either the Frank-van der Merwe or Stranski-Krastanov type to be favored, *i.e.* at least up to a coverage of 1 ML, Pt would grow in a single 2D layer. The latter has been confirmed for the growth of Pt under UHV conditions on Rh(111)[6]

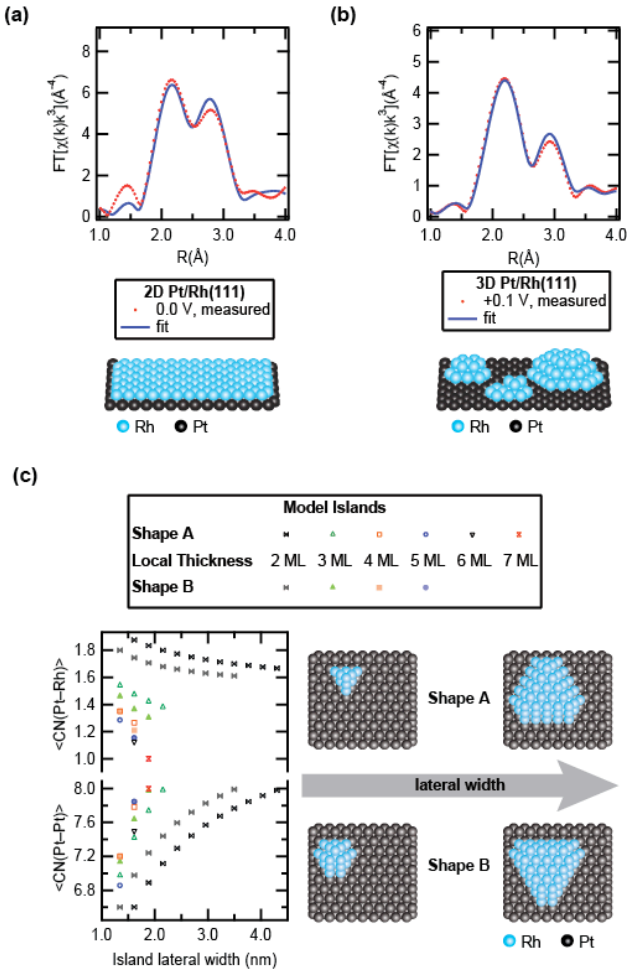

Figure 1. Morphology determination for Pt/Rh(111) using EXAFS. Fourier transforms of measured in situ EXAFS, fitting results for a) evaporated Pt/Rh(111), b) Pt/Rh(111) prepared by redox displacement of a Cu upd layer. Insets: schematic structure models. c) Pt–Pt and Pt–Rh coordination numbers for series of 3D islands with different local coverages (as indicated in the legend) as function of lateral width. Only islands where both coordination numbers agree with the EXAFS fit in (b) are shown. For each island shape A and B, two representative structure models with 3 ML local thickness are shown.

and Ru(0001).[21] While a well-defined 2D Pt monolayer was successfully prepared in ultrahigh vacuum (UHV) by Pt vapor deposition, we discovered that 3D island growth occurs when an electrochemical preparation is chosen, which consists of the redox displacement of an underpotential deposited (upd) Cu monolayer.[5,22]

The morphology of the deposited Pt layers on Rh(111) was determined for both samples using *in situ* extended x-ray absorption fine structure (EXAFS), recorded at potentials close to hydrogen evolution. The Fourier transformed EXAFS magnitudes for both samples are shown in Figure **Error! Reference source not found.** a and b. Least-square fitting with Pt–Pt and Pt–Rh nearest-neighbor coordination shells gives coordination numbers (Table 1) that can be used to determine the film morphology. For the vapor deposited sample, we found very good agreement with a pseudomorphic Pt layer of 1 ML thickness which uniformly covers the Rh surface. In contrast, the significantly smaller Pt–Rh coordination number in the redox-displacement sample indicates the three-dimensional nature of the deposit where only ~50% of the Pt atoms are in direct contact with the Rh substrate. Since the Pt–Pt coordination number, at the same time, is also significantly below values that would be expected for a uniform bilayer or multilayers, there must be a large number of undercoordinated Pt atoms. The observed coordination numbers can be explained with a model structure consisting of three-dimensional islands. For such islands, we calculated the average Pt–Pt and Pt–Rh coordination numbers (Figure **Error! Reference source not found.**c). For each local thickness above 1 ML, the Pt–Pt (Pt–Rh) coordination numbers monotonically increase (decrease) with increasing island size. Agreement with the EXAFS results for 3D Pt/Rh(111) within experimental error bars is found for islands of which the most range from two to four layers thickness and ~1 to ~4 nm lateral width. Note that two idealized shapes of islands with threefold symmetry were tested, with either all (111) facets confined to take a triangular shape and variable width of (100) facets (Type A in Figure 1c), or with variable (111) facets and a fixed width of (100) facets at 0.38 nm (Type B). Different ratios between (100) and (111) facet sizes merely result in subtle deviations of the coordination numbers that do not change our finding of island thicknesses and sizes. The range of island widths determined with our EXAFS analysis is in very good agreement with the sizes of Pt islands that can be seen in an *in situ* STM measurement[22] of Pt/Rh(111), where the same redox-displacement technique was employed.

Table 1: *In situ* EXAFS fitting results

	Pt–Pt	Pt–Rh	*R* factor
2D Pt/Rh(111)[a]			0.0282
N	6.5±0.8	3.2±0.7	
R(Å)	2.72±0.02	2.72±0.02	
σ^2(Å^2)	0.005	0.005	
3D Pt/Rh(111)[b]			0.0238
N	7.3±0.7	1.4±0.5	
R(Å)	2.74±0.02	2.68±0.05	
σ^2(Å^2)	0.005	0.005	

[a]Data range: k=3.0–9.8 Å^{-1}.

[b]Data range: k=3.0–9.5 Å^{-1}.

The near-edge region (XANES) of Pt L_3 spectra shows a characteristic absorption maximum ("white-line") due to $2p \rightarrow 5d$ transitions and thus provides a probe of the unoccupied part of the Pt $5d$ band.[23,24] The information about the energy distribution of unoccupied d states is limited by the Pt $2p$ core hole lifetime broadening, but significantly sharpened spectral features can be obtained in the High Energy Resolution Fluorescence Detection (HERFD) mode[15,25] which we used in our experiment. This resolution enhancement, together with the use of well-defined single crystal samples and sufficiently large model structures in the multiple-scattering computations, eliminates uncertainties in the interpretation of *in situ* XAS, in particular at high electrochemical potentials where contradictory models of Pt–O interactions have been proposed.[26–35]

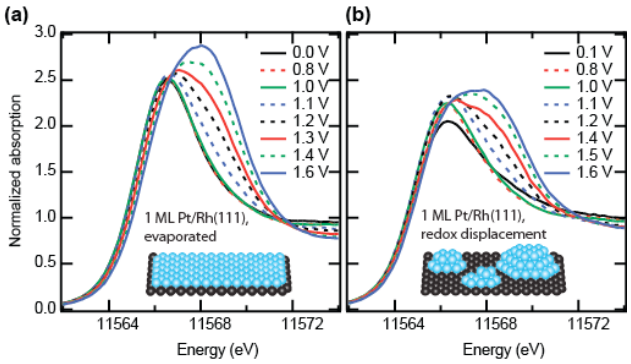

Figure 2. In situ Pt L_3 HERFD XAS for 1 ML Pt/Rh(111) in 0.01 M $HClO_4$: a) 2D Pt film, b) 3D Pt islands. Spectra were recorded in the order of increasing electrochemical potentials.

HERFD XAS spectra of both samples in N_2-saturated 0.01 M $HClO_4$ (Figure **Error! Reference source not found.**) were recorded in order of increasing potential with respect to the reversible hydrogen electrode (RHE). After increasing the potential to 1.1 V and higher values, both samples consistently show a strong broadening and intensity increase of the white-line and intensity decrease at energies just above the white-line region, which we identified earlier as unambiguous signature of Pt oxide formation.[3] Besides, the two samples show significant differences, both in the overall white-line intensities that are generally larger for the 2D Pt layer (Figure **Error! Reference source not found.**a), as well as in the potential-dependent changes of white-line shape and intensity. Additional changes can be seen for the 3D Pt islands in two potential regions: at potentials close to hydrogen evolution, a reduction of the peak intensity together with a significant shoulder on the high energy side of the white-line is caused by chemisorbed H, and a subtle increase of the peak intensity occurs at potentials just below 1.1 V, which is due to O or OH adsorption (Figure **Error! Reference source not found.**b). This interpretation of the spectral changes can be qualitatively confirmed with *ab initio* multiple-scattering calculations on model structures of H/Pt/Rh(111) and O/Pt/Rh(111) using the FEFF8 code.[14] The assignment of the Pt–H signature is also in agreement with previous studies where Pt nanoparticles were used in the measurements, although the corresponding FEFF calculations were employing a very small Pt_6 cluster.[36] In order to represent the measured spectral changes quantitatively, we performed a deconvolution using an arctangent function to model the absorption edge and two Gaussian profiles to represent the white-line peak, respectively. We kept the energy position of each component and the width and step height of the arctangent function at fixed values and allowed only the widths and intensities of the Gaussian functions to vary with the potential. For all spectra, good fitting results with reduced χ^2 values better than 0.0006 could thus be obtained. The results for both samples are shown in Figure **Error! Reference source not found.**. The white line for both samples at potentials below 1.1 V can be fitted with a sharp "main" peak at ~11566 eV and a broad "satellite" at ~11568.4 eV. At 1.1 V, Pt oxide formation causes the higher energy component to become significantly sharper and more intense, and upon further potential increase it eventually exceeds the intensity of the component at lower energy.

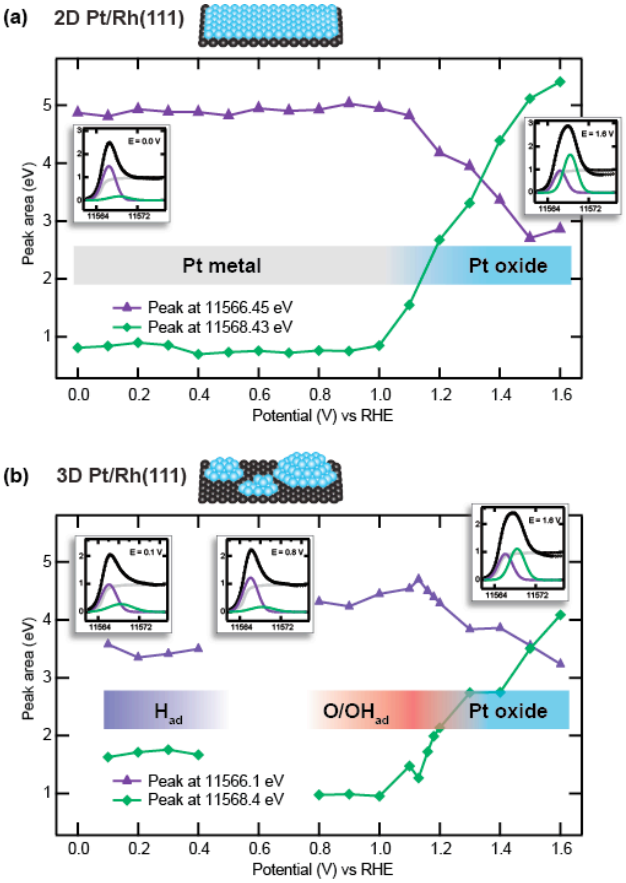

Figure 3. Deconvolution of *in situ* HERFD XAS of Pt/Rh(111) in 0.01 M $HClO_4$. While only the Pt metal-to-oxide transition can be identified for the 2D Pt layer, the 3D deposit shows additional spectral signatures due to H_{ad} and O/OH_{ad}.

Two additional phase transitions with more subtle spectral features appear on the 3D Pt islands: the signature of chemisorbed hydrogen can be clearly seen in the depressed main peak and stronger satellite at low potentials, and a subtle increase of the main peak as the potential is raised from 0.8 V to 1.13 V indicates O/OH chemisorption.

Both these changes are virtually absent for the 2D Pt sample. The suppression of features induced by Pt–H and Pt–O can only be explained when we assume significantly lower adsorbate coverages on the 2D Pt layer.

This interpretation is further supported by the comparison of cyclic voltammetry (CV) curves for 2D Pt/Rh(111) and 3D Pt/Rh(111) (Figure **Error! Reference source not found.**). In the CV of 2D Pt/Rh(111), we observe that both onsets of H_{ad} and O/OH_{ad} formation are significantly shifted outwards with respect to the potential window between 0 and 1.0 V, resulting in strongly reduced adsorbate coverages as compared to Pt(111). By contrast, the CV of 3D Pt/Rh(111) has much more pronounced features towards both ends of the potential window. The broad shape of the anodic current increase due to O/OH_{ad} formation indicates the presence of (100) or (110) facets, further supporting the proposed 3D island model. The large width of the potential range of O/OH adsorption can also explain why the

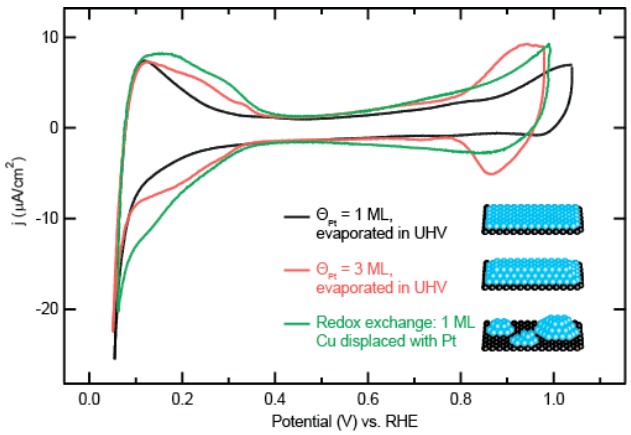

Figure 4. Cyclic voltammograms of UHV-evaporated Pt/Rh(111) samples with two different thicknesses (2D Pt/Rh(111), Θ_{Pt}=1 ML, and Θ_{Pt}=3 ML), and 3D Pt/Rh(111).

corresponding changes in HERFD XAS are much harder to detect than the spectral signature of H_{ad}.

In order to further elucidate the effect of nanostructure and local coverage on the shape of the CVs, we prepared an additional Rh(111) sample in UHV with a coverage of 3 ML Pt. In this case, also shown in Figure **Error! Reference source not found.**, the inward shift of both H_{ad} and O/OH_{ad} features at the cost of the double layer range can be clearly seen, without significant additional features from the contribution of (100) or (110) facets. Even for 3 ML Pt/Rh(111), however, the double layer range with an adsorbate-free or H_2O-covered Pt surface is wider than for pure Pt(111);[37] this can be attributed to the strain effect.

Our voltammetry results for UHV-prepared Pt/Rh(111) samples with different Pt layer thickness are in very good agreement with a combined *ex situ* STM and voltammetry study of similar Pt layers where a Ru(0001) substrate was used.[21] Both these experimental findings strongly confirm the DFT-based prediction that 1 ML Pt on Rh(111) and Ru(0001) adsorb O ~0.6 and ~0.7 eV more weakly than Pt(111), respectively.[2]

In order to estimate the average O adsorption energy on 3D/Pt(111), extensive DFT calculations were carried out using 12 model structures (Figure 5) representing different local Pt coverage, as well as different proximity of the O fcc threefold hollow adsorption site to surrounding Pt and Rh atoms and vacancy sites. To disentangle ligand, strain and local undercoordination effects, we carried out a simple linear regression analysis to correlate the O binding energy with the coordination environment of the three Pt atoms that constitute the adsorption site. We found the binding energy of O to scale linearly with an effective coordination number given by $CN_{eff}^{*} = CN_{Pt}^{*} + 1.08\ CN_{Rh}^{*}$. The coefficient for CN_{Rh}^{*} represents the ligand effect which in the case of Rh weakens the metal-oxygen bond more strongly than Pt. This relation also serves as a guiding principle to determine the electrocatalytic activity for different morphologies of nanostructures as it gives a simple way to correlate the oxygen binding energy to an easily calculable geometric parameter. Although this linear relationship is surprisingly simple, its validity becomes evident when we consider that (i) it predicts approximately the same gain in adsorption energy near

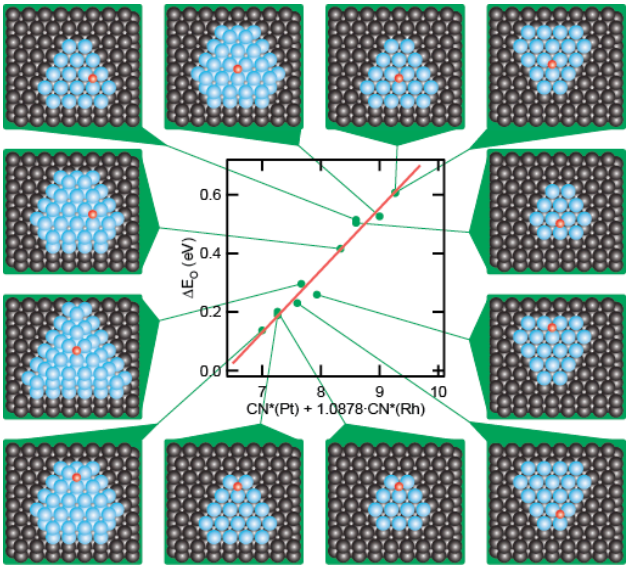

Figure 5. Model structures employed in DFT calculations of O adsorption energies. The corresponding adsorption energy for each structure is plotted as a function of the effective coordination number around the O adsorption site, and a linear fit (red line) is shown.

island edges as an earlier model for O adsorption near step edges on Pt(111);[38] (ii) it predicts no significant ligand effect beyond 1 ML local Pt thickness; this result is similar to the calculation of H adsorption energies on Pt/Ru(0001) where the ligand effect becomes very small already for 2 ML Pt.

The linear correlation in Figure 5 can be applied to the two series of 3D Pt islands already considered for the EXAFS analysis in Figure 1, and for each island we can predict the ORR current density as compared to pure Pt(111) using the volcano relationship[2] with ΔE_O and averaging over all different types of fcc threefold hollow sites. The current density is then normalized by the Pt loading (i. e., the island volume) and can thus be directly compared with the previous RDE measurement on Pt/Rh(111).[5]

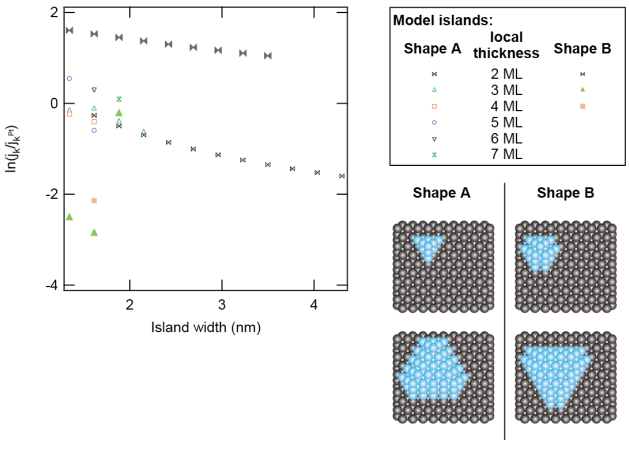

Figure 6. Predicted individual ORR activities of 3D Pt model islands on Rh(111) using the linear correlation between ΔE_O and the local coordination environment for each contributing fcc threefold hollow site.

4. DISCUSSION

Our *in situ* XAS measurements on Pt/Rh(111) monolayer electrocatalysts clearly and consistently show significant differences in surface morphology and chemisorption behaviour as a result of the two sample preparation techniques employed here. Three-dimensional Pt islands on Rh(111) show a significantly higher affinity to chemisorbed H at low potentials and O/OH at high potentials than the two-dimensional monolayer on the same substrate. This can be explained with two cooperative effects that both cause an up-shift of the Pt 5*d*-band and a corresponding increase of adsorption enthalpies for both H and O/OH. DFT calculations have predicted before that atomic oxygen is bound to a Pt monolayer supported on Rh(111) ~0.6 eV more weakly than to the surface of pure Pt;[2] this is due to a shift of the *d*-band center to lower energy caused by strain and vertical ligand effects. Compared to a two-dimensional Pt monolayer, three-dimensional islands formed with the redox-exchange procedure have higher local thickness (2−4 ML as determined from EXAFS) and, in addition, a significant fraction of Pt atoms in under-coordinated edge and corner sites. It can be expected that the higher local Pt thickness shifts the *d*-band center back from the calculated position for 2D Pt/Rh(111) towards that for pure Pt, thus increasing both Pt–O and Pt–H bond strengths. Furthermore, it is well known that oxygen adsorbs more strongly on edges and corners than on extended Pt terraces.

Since cyclic voltammetry on Pt(111) shows an onset of O/OH adsorption at ~ 0.6 V vs. RHE,[37] we can expect this value to shift on the 2D Pt/Rh(111) surface to ~ 1.2 V, which is beyond the onset potential of surface oxide formation. This DFT-based prediction is in perfect agreement with our observation of the complete absence of the spectral features for chemisorbed oxygen-containing species. On 3D Pt/Rh(111), the signature of O/OH chemisorption appears, but remains hard to detect since several different onset potentials exist due to the presence of (100) facets and defects. We estimate that, on average, fcc three-fold hollow sites on 3D Pt/Rh(111) adsorb oxygen ~ 0.3 eV more weakly than pure Pt(111), and that the agreement of a previous ORR activity measurement with such a sample[5] would no longer disagree with the predicted volcano plot[2] if nanostructuring is taken into account.

We conclude that HERFD-XAS applied to well-defined bimetallic model electrocatalysts is a valuable technique that can directly detect chemisorbed oxygen as a descriptor species for the oxygen reduction reaction and thus validate DFT-based predictions.

FIGURES (Word Style "VA_Figure_Caption"). Each figure must have a caption that includes the figure number and a brief description, preferably one or two sentences. The caption should follow the format "Figure 1. Figure caption." All figures must be mentioned in the text consecutively and numbered with Arabic numerals. The caption should be understandable without reference to the text. Whenever possible, place the key to symbols in the artwork, not in the caption. To insert the figure into the template, be sure it is already sized appropriately and paste before the figure caption. For formatting double-column figures, see the instructions at the end of the template. Do NOT modify the amount of space before and after the caption as this allows for the rules, space above and below the rules, and space above and below the figure to be inserted upon editing.

SCHEMES (Word Style "VC_Scheme_Title"). Groups of reactions that show action are called schemes. Schemes may have brief titles describing their contents. The title should follow the format "Scheme 1. Scheme Title". Schemes may also have footnotes (use Word Style "FD_Scheme_Footnote"). To insert the scheme into the template, be sure it is already sized appropriately and paste after the scheme title. For formatting double-column schemes, see the instructions at the end of the template. Do NOT modify the amount of space before and after the title as this allows for the rules, space above and below the rules, and space above and below the scheme to be inserted upon editing.

CHARTS (Word Style "VB_Chart_Title"). Groups of structures that do not show action are called charts. Charts may have brief titles describing their contents. The title should follow the format "Chart 1. Chart Title". Charts may also have footnotes (use Word Style "FC_Chart_Footnote"). To insert the chart into the template, be sure it is already sized appropriately and paste after the chart title. For formatting double-column charts, see the instructions at the end of the template. Do NOT modify the amount of space before and after the title as this allows for the rules, space above and below the rules, and space above and below the chart to be inserted upon editing.

TABLES. Each table must have a brief (one phrase or sentence) title that describes its contents. The title should follow the format "Table 1. Table Title" (Word Style "VD_Table_Title"). The title should be understandable without reference to the text. Put details in footnotes, not in the title (use Word Style "FE_Table_Footnote"). Do NOT modify the amount of space before and after the title as this allows for the space above and below the table to be inserted upon editing.

Use tables (Word Style "TC_Table_Body") when the data cannot be presented clearly as narrative, when many precise numbers must be presented, or when more meaningful interrelationships can be conveyed by the tabular format. **Do not use Word Style "TC_Table_Body" for tables containing artwork**. Tables should supplement, not duplicate, text and figures. Tables should be simple and concise. It is preferable to use the Table Tool in your word-processing package, placing one entry per cell, to generate tables.

Displayed equations can be inserted where desired making sure they are assigned Word Style "Normal". Displayed equations can only be one column wide. If the artwork needs to be two columns wide, it must be relabeled as a figure, chart, or scheme and mentioned as such in the text.

ASSOCIATED CONTENT

(Word Style "TE_Supporting_Information**"). Supporting Information**. A brief statement in nonsentence format listing the contents of material supplied as Supporting Information should be included, ending with "This material is available free of charge via the Internet at http://pubs.acs.org." For instructions on what should be included in the Supporting Information as well as how to prepare this material for publication, check the Instructions for Authors at (http://pubs.acs.org/page/jacsat/submission/authors.html).

AUTHOR INFORMATION

Corresponding Author

* (Word Style "FA_Corresponding_Author_Footnote"). Give contact information for the author(s) to whom correspondence should be addressed.

Present Addresses

†If an author's address is different than the one given in the affiliation line, this information may be included here.

Author Contributions

The manuscript was written through contributions of all authors. / All authors have given approval to the final version of the manuscript. /

Funding Sources

This work is supported [in part] by the Department of Energy, Office of Basic Energy Sciences, Division of Materials Sciences and Engineering, under contract DE-AC02-76SF00515.

Notes

Any additional relevant notes should be placed here.

ACKNOWLEDGMENT

(Word Style "TD_Acknowledgments"). Generally the last paragraph of the paper is the place to acknowledge people (dedications), places, and financing (you may state grant numbers and sponsors here).

ABBREVIATIONS

CCR2, CC chemokine receptor 2; CCL2, CC chemokine ligand 2; CCR5, CC chemokine receptor 5; TLC, thin layer chromatography.

REFERENCES

(1) Nørskov, J. K.; Rossmeisl, J.; Logadottir, A.; Lindqvist, L.; Kitchin, J. R.; Bligaard, T.; Jónsson, H. *J. Phys. Chem. B* **2004**, *108*, 17886–17892.
(2) Greeley, J.; Stephens, I. E. L.; Bondarenko, A. S.; Johansson, T. P.; Hansen, H. A.; Jaramillo, T. F.; Rossmeisl, J.; Chorkendorff, I.; Nørskov, J. K. *Nature Chem.* **2009**, *1*, 552–556.
(3) Friebel, D.; Miller, D. J.; O'Grady, C. P.; Anniyev, T.; Bargar, J.; Bergmann, U.; Ogasawara, H.; Wikfeldt, K. T.; Pettersson, L. G. M.; Nilsson, A. *Phys. Chem. Chem. Phys.* **2011**, *13*, 262–266.
(4) Friebel, D.; Miller, D. J.; Nordlund, D.; Ogasawara, H.; Nilsson, A. *Angew. Chem. Int. Ed.*
(5) Zhang, J. L.; Vukmirovic, M. B.; Xu, Y.; Mavrikakis, M.; Adzic, R. R. *Angew. Chem. Int. Ed.* **2005**, *44*, 2132–2135.
(6) Duisberg, M.; Dräger, M.; Wandelt, K.; Gruber, E. L. D.; Schmid, M.; Varga, P. *Surf. Sci.* **1999**, *433*, 554–558.
(7) Friebel, D.; Schlaup, C.; Broekmann, P.; Wandelt, K. *Surf. Sci.* **2006**, *600*, 2800–2809.
(8) Friebel, D.; Schlaup, C.; Broekmann, P.; Wandelt, K. *Phys. Chem. Chem. Phys.* **2007**, *9*, 2142–2145.
(9) Ocko, B. M.; Wang, J.; Davenport, A.; Isaacs, H. *Phys. Rev. Lett.* **1990**, *65*, 1466–1469.
(10) Glatzel, P.; Bergmann, U. *Coord. Chem. Rev.* **2005**, *249*, 65–95.
(11) Waychunas, G. A. In *Rev. Mineral. Geochem.*; Mineralogical Soc America, 2002; Vol. 49, pp. 267–315.
(12) Webb, S. M. *Phys. Scr.* **2005**, *T115*, 1011–1014.
(13) Rehr, J. J.; Albers, R. C.; Zabinsky, S. I. *Phys. Rev. Lett.* **1992**, *69*, 3397–3400.
(14) Ankudinov, A. L.; Ravel, B.; Rehr, J. J.; Conradson, S. D. *Phys. Rev. B* **1998**, *58*, 7565–7576.
(15) Safonova, O. V.; Tromp, M.; Bokhoven, J. A. van; Groot, F. M. F. de; Evans, J.; Glatzel, P. *J. Phys. Chem. B* **2006**, *110*, 16162–16164.
(16) Glatzel, P.; Singh, J.; Kvashnina, K. O.; Bokhoven, J. A. van *J. Am. Chem. Soc.* **2010**, *132*, 2555–2557.
(17) Ankudinov, A. L.; Rehr, J. J.; Low, J.; Bare, S. R. *Phys. Rev. Lett.* **2001**, *86*, 1642–1645.
(18) Ankudinov, A. L.; Rehr, J. J.; Low, J. J.; Bare, S. R. *J. Synchrotron Rad.* **2001**, *8*, 578–580.
(19) Teliska, M.; Murthi, V. S.; Mukerjee, S.; Ramaker, D. E. *J. Electrochem. Soc.* **2005**, *152*, A2159–A2169.
(20) Bauer, E.; van der Merwe, J. H. *Phys. Rev. B* **1986**, *33*, 3657–3671.
(21) Hoster, H. E.; Alves, O. B.; Koper, M. T. M. *ChemPhysChem* **2010**, *11*, 1518–1524.
(22) Lima, F. H. B.; Zhang, J.; Shao, M. H.; Sasaki, K.; Vukmirovic, M. B.; Ticianelli, E. A.; Adzic, R. R. *J. Phys. Chem. C* **2007**, *111*, 404–410.
(23) Horsley, J. A. *J. Chem. Phys.* **1982**, *76*, 1451–1458.
(24) Mansour, A. N.; Cook, J. W.; Sayers, D. E. *J. Phys. Chem.* **1984**, *88*, 2330–2334.
(25) Hämäläinen, K.; Siddons, D. P.; Hastings, J. B.; Berman, L. E. *Phys. Rev. Lett.* **1991**, *67*, 2850–2853.
(26) Vukmirovic, M. B.; Zhang, J.; Sasaki, K.; Nilekar, A. U.; Uribe, F.; Mavrikakis, M.; Adzic, R. R. *Electrochim. Acta* **2007**, *52*, 2257–2263.
(27) Zhang, J.; Mo, Y.; Vukmirovic, M. B.; Klie, R.; Sasaki, K.; Adzic, R. R. *J. Phys. Chem. B* **2004**, *108*, 10955–10964.
(28) Zhang, J.; Sasaki, K.; Sutter, E.; Adzic, R. R. *Science* **2007**, *315*, 220–222.
(29) Teliska, A.; O'Grady, W. E.; Ramaker, D. E. *J. Phys. Chem. B* **2005**, *109*, 8076–8084.
(30) Mukerjee, S.; Srinivasan, S.; Soriaga, M. P.; Mcbreen, J. *J. Electrochem. Soc.* **1995**, *142*, 1409–1422.
(31) Mukerjee, S.; McBreen, J. *J. Electroanal. Chem.* **1998**, *448*, 163–171.
(32) Tada, M.; Murata, S.; Asakoka, T.; Hiroshima, K.; Okumura, K.; Tanida, H.; Uruga, T.; Nakanishi, H.; Matsumoto, S.; Inada, Y.; Nomura, M.; Iwasawa, Y. *Angew. Chem. Int. Ed.* **2007**, *46*, 4310–4315.
(33) Imai, H.; Izumi, K.; Matsumoto, M.; Kubo, Y.; Kato, K.; Imai, Y. *J. Am. Chem. Soc.* **2009**, *131*, 6293–6300.
(34) Allen, P. G.; Conradson, S. D.; Wilson, M. S.; Gottesfeld, S.; Raistrick, I. D.; Valerio, J.; Lovato, M. *J. Electroanal. Chem.* **1995**, *384*, 99–103.
(35) Principi, E.; Witkowska, A.; Dsoke, S.; Marassi, R.; Cicco, A. D. *Phys. Chem. Chem. Phys.* **2009**, *11*, 9987–9995.
(36) Teliska, M.; O'Grady, W. E.; Ramaker, D. E. *J. Phys. Chem. B* **2004**, *108*, 2333–2344.
(37) Garcia-Araez, N.; Climent, V.; Herrero, E.; Feliu, J. M.; Lipkowski, J. *Electrochim. Acta* **2006**, *51*, 3787–3793.
(38) Feibelman, P. J.; Esch, S.; Michely, T. *Phys. Rev. Lett.* **1996**, *77*, 2257.

(Word Style "TF_References_Section"). References are placed at the end of the manuscript. Authors are responsible for the accuracy and completeness of all references. Examples of the recommended formats for the various reference types can be found at http://pubs.acs.org/page/jacsat/submission/authors.html. Detailed information on reference style can be found in The ACS Style Guide, available from Oxford Press.